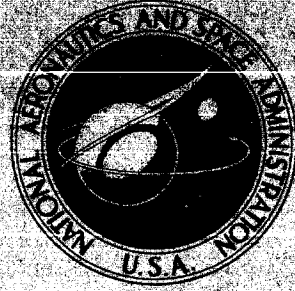


N71-24651/68

**NASA TECHNICAL  
MEMORANDUM**



**NASA TM X-2274**

NASA TM X-2274

**CASE FILE  
COPY**

**NASA SPACE SHUTTLE  
TECHNOLOGY CONFERENCE**

**Volume III - Dynamics and Aeroelasticity**

Held at

Langley Research Center

Hampton, Virginia

March 2-4, 1971

**NATIONAL AERONAUTICS AND SPACE ADMINISTRATION • WASHINGTON, D. C. • APRIL 1971**

1. Report No. NASA TM X-2274	2. Government Accession No.	3. Recipient's Catalog No.	
4. Title and Subtitle NASA SPACE SHUTTLE TECHNOLOGY CONFERENCE Volume III - Dynamics and Aeroelasticity		5. Report Date April 1971	
		6. Performing Organization Code	
7. Author(s)		8. Performing Organization Report No. L-7739	
9. Performing Organization Name and Address		10. Work Unit No.	
		11. Contract or Grant No.	
12. Sponsoring Agency Name and Address National Aeronautics and Space Administration Washington, D.C. 20546		13. Type of Report and Period Covered Technical Memorandum	
		14. Sponsoring Agency Code	
15. Supplementary Notes Held at the NASA Langley Research Center, March 2-4, 1971.			
16. Abstract The conference encompassed three technology efforts, each published as a separate NASA Technical Memorandum.  Volume I - Aerothermodynamics, Configurations, and Flight Mechanics (includes aerodynamics; atmospheric operations; and aerodynamic heating). NASA TM X-2272, 1971.  Volume II - Structures and Materials (includes structural design technology; thermal protection systems; and materials technology). NASA TM X-2273, 1971.  Volume III - Dynamics and Aeroelasticity (includes dynamic loads and response; aeroelasticity; and flight dynamics and environment). NASA TM X-2274, 1971.			
17. Key Words (Suggested by Author(s)) Space shuttle Aerothermodynamics Dynamics Aeroelasticity Structural design Thermal protection		18. Distribution Statement Unclassified - Unlimited  STAR Category 32	
19. Security Classif. (of this report) Unclassified	20. Security Classif. (of this page) Unclassified	21. No. of Pages 462	22. Price* \$6.00

\* For sale by the National Technical Information Service, Springfield, Virginia 22151

## FOREWORD

A significant factor in the development of new technology is the timely exchange of information to highlight areas of progress and to establish areas in need of greater emphasis - in short, to provide both program management and technical contributors an opportunity to review their work and plans in the context of the requirements and constraints of the total program.

During the past two years, the Langley Research Center has made a concerted effort to support the NASA objectives for development of a low-cost space transportation system - the space shuttle. The Langley effort covers a broad base of technology including electronics and life support systems, but its primary focus has been in the areas of Aerothermodynamics, Configurations, and Flight Mechanics; Structures and Materials; and Dynamics and Aeroelasticity.

Thus it was in the context of the need for a technology status review and our own active involvement in the aforementioned areas of technology that the Langley Research Center was pleased to host the Shuttle Technology Conference which culminated in this document. As the reader will recognize, the development and presentation of this information was largely achieved by very busy people doing an additional job. Nevertheless, I believe the results of the conference reflect a highly motivated and cooperative effort on the part of industry and NASA centers to provide the best information available for technical review and assessment. This effort is deeply appreciated by those of us involved in the implementation of the conference. Thus, to the authors, session chairmen, and numerous individuals involved in the logistic support of this conference, I offer my thanks both for your effort and for your cooperation. A job well done!

George W. Brooks  
General Chairman

## CONTENTS

### VOLUME III.- DYNAMICS AND AEROELASTICITY

Chairman - H. L. Runyan

GLOSSARY . . . . .	vii
--------------------	-----

#### DYNAMIC LOADS AND RESPONSES

Chairman - D. J. Martin, LaRC  
Co-Chairman - H. Wayne Leonard, LaRC

1. RECENT STUDIES OF SPACE SHUTTLE MULTIBODY DYNAMICS . . . . .	1
by Sumner A. Leadbetter (LaRC) and Larry A. Kiefling (MSFC)	
2. SPACE SHUTTLE TPS PANEL VIBRATION STUDIES . . . . .	27
by Huey D. Carden, Barbara J. Durling, and William C. Walton, Jr. (LaRC)	
3. APPROXIMATE ANALYSIS AND DYNAMIC TESTS FOR A THERMAL PROTECTION SYSTEM PANEL . . . . .	49
by I. U. Ojalvo and N. Arcas (GAC)	
4. SPACE SHUTTLE LIQUID DYNAMICS . . . . .	95
by Frank M. Bugg (MSFC) and Norman S. Land (LaRC)	
5. SOME LANDING-GEAR CONSIDERATIONS FOR SPACE SHUTTLE VEHICLES . . . . .	121
by Brantley R. Hanks and Trafford J. W. Leland (LaRC)	

#### AEROELASTICITY

Chairman - W. H. Reed III, LaRC  
Co-Chairman - C. F. Coe, ARC

6. RECENT STUDIES OF EFFECTS OF GROUND WINDS ON SPACE SHUTTLE VEHICLES . . . . .	155
by Robert W. Hess, Wilmer H. Reed III, and Jerome T. Foughner, Jr. (LaRC)	
7. EFFECTS OF SPACE SHUTTLE CONFIGURATION ON WING BUFFET AND FLUTTER  PART I - LAUNCH VEHICLE WING WITH TIP FIN . . . . .	181
by Robert C. Goetz (LaRC)	
Part II - THICK HIGH-ASPECT-RATIO WING . . . . .	201
by Larry L. Erickson, Bruno J. Gambucci, and Phillip R. Wilcox (ARC)	

8. APPLICATION OF RECENT PANEL FLUTTER RESEARCH TO THE SPACE SHUTTLE	
PART I - BOUNDARY LAYER AND HYPERSONIC EFFECTS . . . . .	231
by Peter A. Gaspers, Jr. (ARC)	
PART II - INFLUENCE OF EDGE CLIPS AND FLOW ANGULARITY . . . . .	247
by Herman L. Bohon and Charles P. Shore (LaRC)	
9. BUFFET RESPONSE OF SPACE SHUTTLE LAUNCH CONFIGURATIONS AS DETERMINED BY TESTS OF AN AEROELASTIC MODEL . . . . .	265
by Lado Muhlstein, Jr. (ARC)	
10. PRELIMINARY MEASUREMENTS AND FLOW VISUALIZATION STUDIES OF PRESSURE FLUCTUATIONS ON SPACE SHUTTLE CONFIGURATIONS . . . . .	293
by Charles F. Coe, Jules B. Dods, Jr., Robert C. Robinson (ARC), and William H. Mayes (LaRC)	

#### LOADS AND ENVIRONMENT

Chairman - R. W. Schock, MSFC

11. THE EFFECTS OF PARAMETER VARIATION ON INFILIGHT WIND LOADING . . . . .	315
by Alden C. Mackey (MSC)	
12. TECHNOLOGY - PRELIMINARY INVESTIGATION OF LOAD AND MODAL SUPPRESSION FOR SPACE SHUTTLE . . . . .	333
by Bernard J. Kuchta (GD/C)	
13. SHUTTLE POGO REVIEW . . . . .	359
by John E. Harbison (MSFC)	
14. SPACE SHUTTLE ACOUSTICS . . . . .	401
by Stanley H. Guest (MSFC)	
15. PRELIMINARY VIBRATION DESIGN AND TEST CRITERIA CONSIDERATIONS FOR THE SPACE SHUTTLE . . . . .	423
by Harry J. Bandgren (MSFC)	

## GLOSSARY

AC	aerodynamic center
ACLS	air cushion landing system
ACPS	attitude control propulsion system
ADV	advanced
AEM	acoustical emission monitoring
AFFDL	Air Force Flight Dynamics Laboratory
AFML	Air Force Materials Laboratory
APU	auxiliary power unit
ARC	Ames Research Center
ASCEP	Advanced Structural Concepts Experimental Program
ASOP	Automated Structural Optimization Program
AS-REC	as received
ATT	attitude
ATTACH	attachment
BEN	Bolt, Beranek, and Newman
BL	boundary layer
BPR	bypass ratio
BS	body station
BST	booster
CDC	Control Data Corporation
CER	cost estimating relationship
CONT	control
CONV	conventional
CPU	central processing unit
C.R.	cross range

CRIT	critical
CRT	cathode ray tube
CTI	cryogenic insulation
CW	cold worked
DB	dead band
DIA	diameter
DISP	dispersion; displacement
DSM	dispersion-strengthened metals
DW	double wall
EB	electron beam
ECS	environmental control system
ELONG	elongation
EMR	electromagnetic radiation
FLT	flight
FPL	fluctuating pressure level
FSW	flyback system weight
GAC; GAEC	Grumman Aerospace Corporation
GDC; GD/C	General Dynamics/Convair
GDLSWT	General Dynamics low speed wind tunnel
GE	General Electric Co.
GEN	generator; generated
GE-RESD	General Electric Reentry and Environmental Systems Division
HABP	hypersonic arbitrary-body program
HASP	hypersonic aerospace structures program
h. c.	honeycomb
HCF	hardened compacted fibers

RW	right wing
SAT	Saturn
SBC	single body canard
s/c	skin corrugation
SEP	separated
SF	safety factor
SL	sea level
SLA	spacecraft lunar module adapter
SPL	sound pressure level
SR&T	space research and technology
s.s.	simple support
SSV	space shuttle vehicle
STR	strengthened
SUB	subsonic
SW	single wall
T	transverse
T'COUPLES	thermocouples
TECH	technology
TPS	thermal protection system
TURB	turbulent
TWT	transonic wind tunnel
UB	underbody
u.i.s.	unidirectional
ULT	ultimate
VMSC	Vought Missiles and Space Corporation
WL	water line
WT	wind tunnel

MMC	Martin Marietta Corporation
MRP	moment reference point
MSC	Manned Spacecraft Center
MSFC	Marshall Space Flight Center
MTF	Mississippi Test Facility
NAR; NR	North American Rockwell
NDE	nondestructive evaluation
NDI	nondestructive inspection
NDT	nondestructive testing
NPSH	nominal positive suction head
OA FPL	overall fluctuating pressure level
OA PWL	overall acoustic power level
OART	Office Advanced Research and Technology
OA SPL	overall sound pressure level
OMSF	Office Manned Space Flight
ORB	orbiter
POS	positive
ppm	parts per million
PS	post support
PSD	power spectral density
PWR	power
R <sub>CR</sub>	cruise range
RCS	reaction control system
RDT&E	Research, Development, Tests, and Engineering
REI	reusable external insulation
REQ'D	required
RT	room temperature

HDWE	hardware
HMG	high-modulus graphite
HS	heat sink
HSG	high-strength graphite
HT	high temperature
HX	heat exchanger
HYP	hypersonic
IMU	inertial measurement unit
INSUL	insulation
INT	internal
i. s.	isogrid
IU	instrument unit
L	longitudinal
LaRC; LRC	Langley Research Center
LCR	low cross range
LE	leading edge
LeRC	Lewis Research Center
L. LOAD	limit load
LMSC	Lockheed Missiles and Space Company
LW	left wing
MAC	mean aerodynamic chord
MARL	Mobile Acoustic Research Laboratory
MDAC	McDonnell-Douglas Astronautics Corporation
MDC	McDonnell Douglas Corporation
MEAS	measured
MGMT	management
MIN	minimum

## RECENT STUDIES OF SPACE SHUTTLE MULTIBODY DYNAMICS

By Sumner A. Leadbetter  
NASA Langley Research Center, Hampton, Virginia

and

Larry A. Kiefling  
NASA George C. Marshall Space Flight Center  
Marshall Space Flight Center, Alabama

### SUMMARY

The parallel-staged space shuttle vehicle poses new dynamics problems in addition to those that in the past have been associated with launch vehicles and aircraft. Of fundamental importance to solve many of these pertinent dynamic problems is an adequate knowledge of vibration modes and frequencies of the launch vehicle structure. Not only must improved and new analytical methods be verified with experimental data but also existing computer programs must be modified to enable handling of complex and large mathematical models by techniques such as modal synthesis. In addition, the presently used and somewhat inaccurate method of using engineering judgment as well as intuitive values in defining mathematical model parameters must be placed on a sounder basis. This paper discusses preliminary results from vibration studies of a 1/15-scale space shuttle dynamic model to indicate some parametric trends, presents an analytical substructuring technique that will enable handling more complex structures with existing computer capability, and presents some results from a study to improve the mathematical model input data.

## INTRODUCTION

The current parallel-staged space shuttle configuration concept will involve classical launch-vehicle dynamics problems as well as other vibratory response problems that are not yet defined such as effects of a large asymmetric mass as is represented by the orbiter vehicle. Since the dynamic-response properties of flight-vehicle structures are essential ingredients to understanding the problems associated with unwanted vibrations, the structural dynamic characteristics must be accurately determined in order to predict vehicle response to unsteady loadings and to insure adequate stability and control design data. Analysis of calculated and measured data from full-scale and model studies of launch vehicles have indicated that an improved understanding of dynamic behavior and coupled interaction of structural components must be realized. In addition to the need for data to verify analytical results, there exists a need for a method to eliminate excessive engineering judgment when assigning values to key structural elements of the mathematical model. Also, with the involved large and complex shuttle structure, some representative synthesis method should be developed to maintain mathematical models within current computer capability.

This paper presents some preliminary results from a 1/15-scale space shuttle dynamic model analytical and experimental study, some information from a study to improve accuracy of mathematical models and discussion of a study of substructuring techniques to develop the capability to handle larger structures with existing computers.

## SPACE SHUTTLE DYNAMIC PROBLEMS

(Figure 1)

The space shuttle multibody configuration involves many dynamic problems. Some of these problems have received extensive treatment during earlier studies of aircraft and launch vehicles, but will require further specific attention relative to the complex shuttle structure. Among these problems are the classic acoustic, aeroelastic, and dynamic-response characteristics. Some of the newer shuttle configuration associated problems include thermal protection system (TPS) panel response, interference flutter, and staging dynamics. For many of the potential dynamics problems, the response characteristics of the involved structures must be known. To obtain parametric data, a 1/15-scale dynamic model of an early shuttle concept (MSC) has been designed and fabricated as a part of a LaRC study.\* Some preliminary results from this analytical and experimental study have been obtained and are presented in this paper. Of primary interest are some comparisons of analytical and experimental results from a study of the two-body configurations, some frequency content trends, and some examples of asymmetric modes.

---

\*MSC NASA Manned Spacecraft Center  
LaRC NASA Langley Research Center

# SPACE SHUTTLE DYNAMIC PROBLEMS

CREW ENVIRONMENT  
SEPARATED FLOW

DYNAMIC RESPONSE  
GUSTS  
LIFT-OFF  
STAGING  
LANDING

CLASSICAL FLUTTER  
STALL FLUTTER  
BUFFETING

TPS PANEL RESPONSE

SEPARATION PLUME

INTERFERENCE FLUTTER

BUFFETING

LAUNCH NOISE  
 $\approx 170$  dB

POGO  
BOUNDARY LAYER NOISE

Figure 1

## 1/15-SCALE SPACE SHUTTLE DYNAMIC MODEL

(Figure 2)

A 1/15-scale dynamic model of an early space shuttle concept has been fabricated and is currently undergoing vibration studies to obtain structural dynamic data needed to evaluate analytical procedures and to study parametric trends of coupled multibody structures. The model is a parallel beam-type structure that is dynamically representative of the stiffness and mass properties of an early MSC mini-shuttle version. Scaled simulated propellant masses can be varied on the booster and the orbiter to simulate desired flight times. Either straight or delta wings are available for the studies. The interface connecting springs between the booster and the orbiter, although not representative of full-scale hardware, can be varied over a wide range of stiffness and with different restraints at the forward and aft connecting joints as well as in pitch and yaw direction for parametric studies of the effects of the booster-orbiter interface spring connection. A unique two-cable suspension system is employed to support the model and to simulate flight conditions. The cables are attached at the top to springs that allow longitudinal freedom. At the bottom, the cable passes through pulleys and supports the vehicle weight while allowing motion in the transverse plane. The cable restraint located at the forward interface spring provides lateral stability and aligns the model center of gravity with the support system. With this system, the model rigid-body frequencies are quite low. At simulated lift-off conditions, the equivalent full-scale pendulum frequency is 0.018 Hz; the rocking frequency, 0.033 Hz; the torsional frequency, 0.028 Hz; and the longitudinal frequency, 0.082 Hz.

## 1/15 - SCALE SPACE SHUTTLE DYNAMIC MODEL

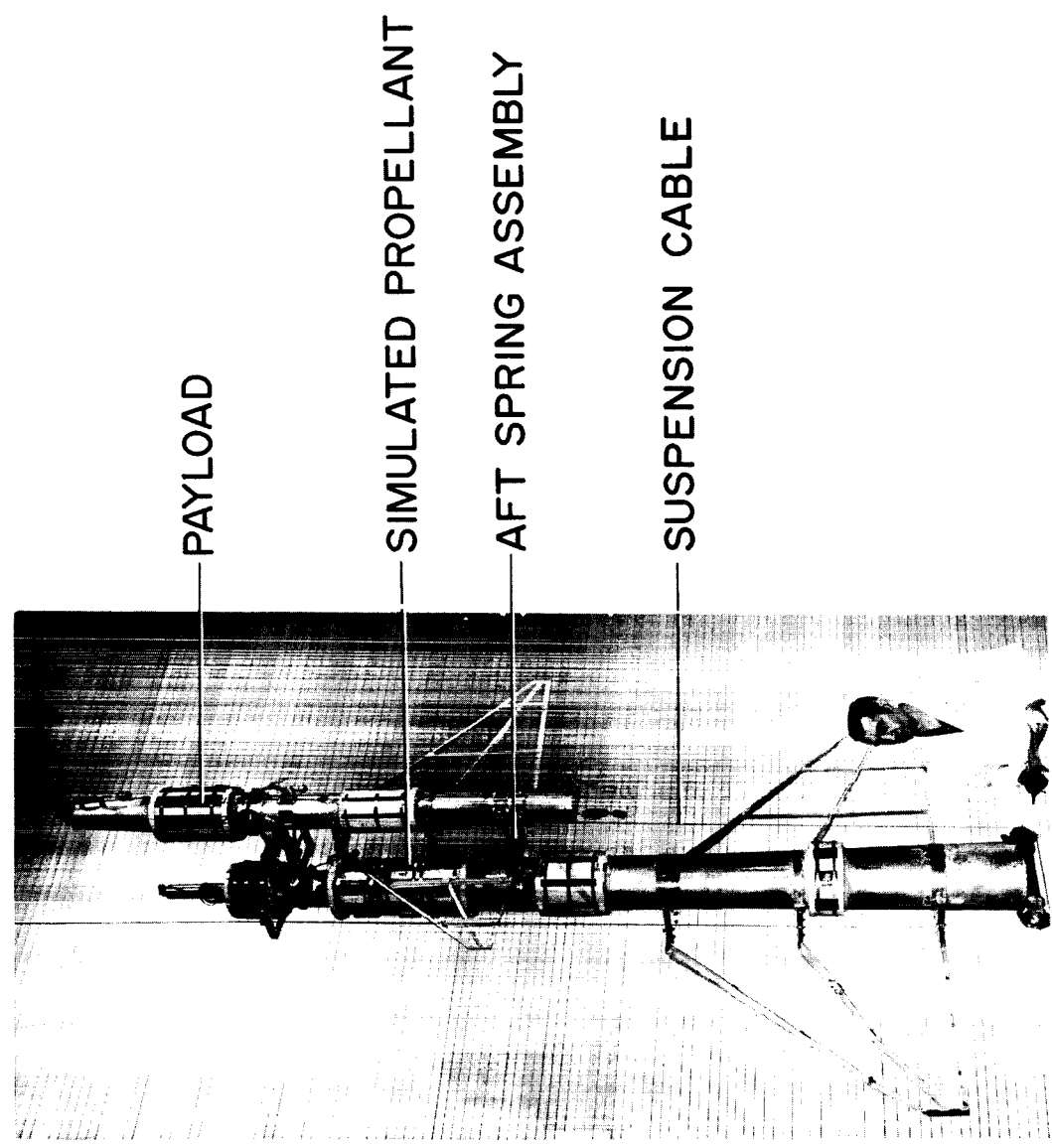


Figure 2

## SPRING ASSEMBLY DETAIL

(Figure 3)

At the time the model was designed, the type or method of attaching the orbiter and booster together had not been established and the approach used was to design an interconnecting spring assembly that would provide the degree of variability needed during the ensuing parametric investigation to study interconnecting spring effects and yet would not violate the integrity of the model. The resulting spring assembly (the companion assembly is identical to the one shown) is such that the orbiter can be mounted either in a forward or aft position and, in addition, the spring restraint in either or both the pitch or the yaw plane can be varied over several orders of magnitude. The two yaw springs and the four pitch springs act as compound cantilevers in their respective direction and are independently replaceable to obtain different values of stiffness in the pitch and yaw planes.

SPRING ASSEMBLY DETAIL

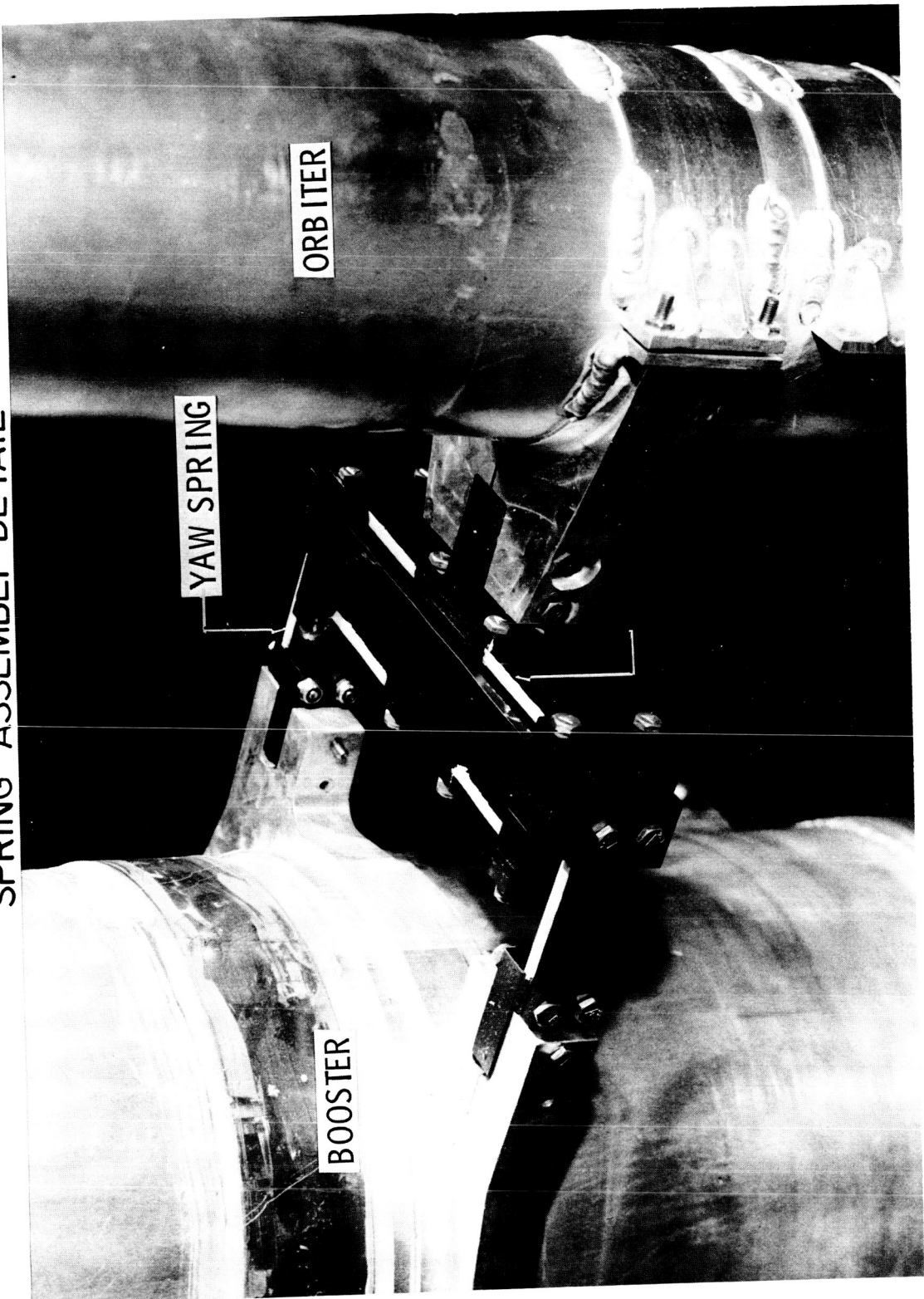


Figure 3

## ANALYTICAL APPROACH

(Figure 4)

The analytical approach used to obtain the calculated results presented in this paper is based on the finite-element method as implemented by the NASA Structural Analysis Program (NASTRAN). The booster fuselage was represented as an assembly of nine beam elements and ten concentrated masses. The concentrated masses modeled local distributions of masses, propellant mass, and nonstructural masses. All beam elements were assumed to have uniform properties. The mass moment of inertia about the roll axis of the fuselages was represented by concentrations at each grid point and included inertias of bulkhead, added weights, and each element of the fuselage. The orbiter fuselage was idealized in a manner similar to the booster fuselage but having seven beam elements and eight concentrated masses. The payload was modeled as a concentrated mass.

Each elastic interface was modeled as two linear springs where one spring resists a relative displacement in the pitch plane and the other spring resists a relative displacement in the yaw plane. The interface was assumed to be infinitely stiff with regard to roll rotation and longitudinal displacement. The assembled mathematical model of the two fuselages had 72 degrees of freedom.

## **ANALYTICAL APPROACH**

### **NASTRAN**

### **MATHEMATICAL MODEL**

- BOOSTER - 9 ELEMENTS, 10 MASSES
- ORBITER - 7 ELEMENTS, 8 MASSES
- FUSELAGE INTERFACE - LINEAR SPRINGS  
IN PITCH AND YAW PLANES
- 72 DEGREES OF FREEDOM

Figure 4

## BENDING-FREQUENCY VARIATION WITH SPRING STIFFNESS

(Figure 5)

A new structural dynamics problem introduced by the parallel-staged space shuttle configuration is the effects of asymmetry resulting from the large eccentric mass, the orbiter, attached to the side of the booster. Significant factors to be delineated in defining the coupled vehicle response characteristics will be the method of attaching the components and the stiffness of the joints between the two vehicles. To study the structural dynamic effects of elastically connected fuselages, an analytical parametric study of the interface joint stiffness has been conducted by utilizing a wingless two-body model configuration and, for comparison, some preliminary results, along with experimentally determined data for one value of model interface spring restraint, are presented. The data represent only the response in the pitch plane with the frequencies corrected to equivalent full-scale values. The trends for the first six calculated pitch modes are shown. The experimental data, given for an intermediate interface spring restraint condition, agree very well with the lower three modes. However, a mode, at a frequency of 3.3 Hz, is noted from the experimental data where there is no comparable calculated response having a similar mode shape. The existence of such an unpredicted mode is significant and indicates further studies must be made. For the higher modes the correlation is not so good; in fact, the fifth analytically determined mode is 14 percent greater than its experimentally determined counterpart.

SHADING - FREQUENCY VARIATION WITH CONNECTING SPRING  
STIFFNESS  
PITCH RESPONSE

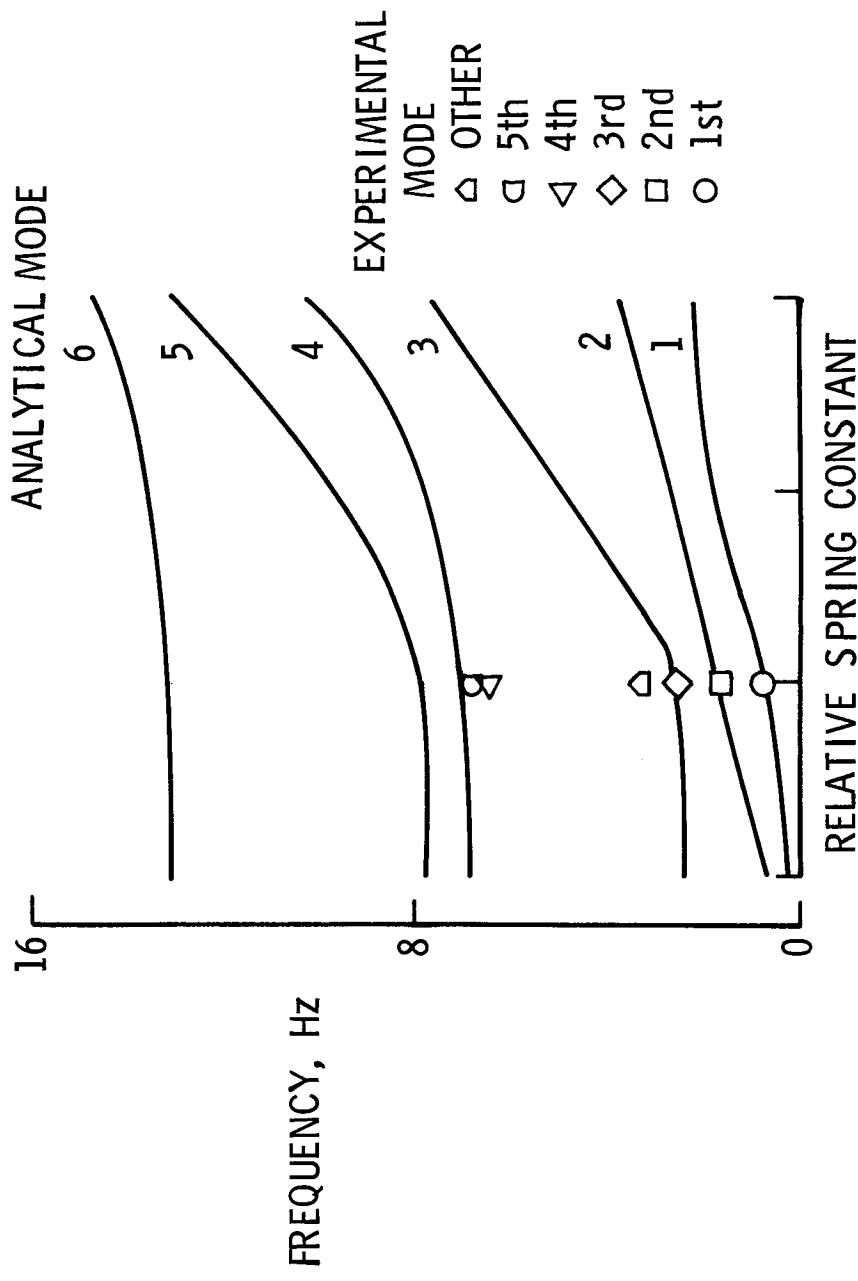


Figure 5

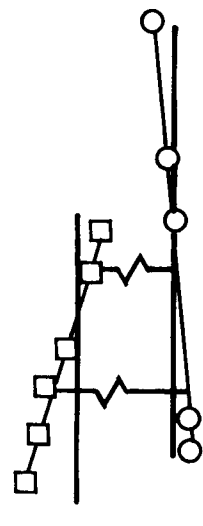
## SOME BENDING MODES OF ELASTICALLY CONNECTED FUSELAGES

(Figure 6)

A comparison of selected mode shapes and frequencies from the elastically connected fuselage analytical and experimental data presented in figure 5 is given. Presented are a rigid-body (scissors) mode, a booster first bending mode, and a booster second bending mode coupled with an orbiter first bending mode.

There exists very good agreement for the lower frequencies and corresponding mode shapes, some deviation occurring for the higher response. For this higher frequency, the mode shapes dictated a comparison of the fourth measured mode with the fifth calculated mode. Likewise, the fifth measured mode shape is similar to the fourth calculated mode shape. For both responses, the mode shapes are the same, but the relative phase between the booster and orbiter has changed. These results would suggest that the analytical procedure is satisfactory over a large part of the frequency range investigated.

## SOME BENDING MODES OF ELASTICALLY CONNECTED FUSELAGES NO WINGS



□ ORBITER   } EXPERIMENT  
○ BOOSTER   } ANALYSIS

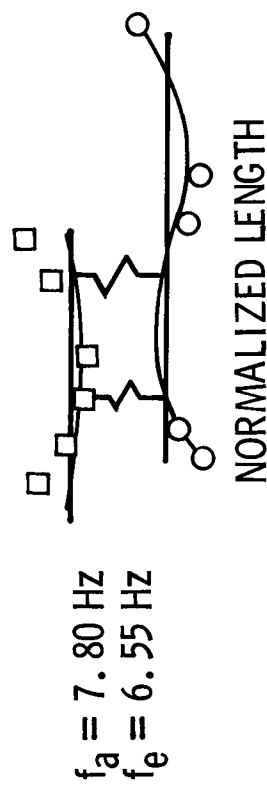
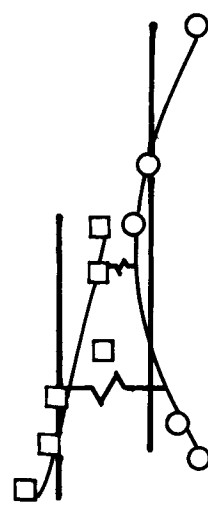


Figure 6

## (Figure 7)

Some preliminary experimental data for the winged model have been obtained and indicate that the parallel-staged space shuttle vehicle introduces new and complex responses that require extensive investigation. An illustration of the complexity that can be anticipated is exemplified by these data where the number of resonances for various components and for the assembled model are presented. The frequencies are given as equivalent full-scale values and all tests were conducted in a manner to simulate flight boundary conditions. From tests of the orbiter by itself, only one response is noted below 10 Hz; for the booster tested by itself, two resonances are noted. However, when these two components are elastically coupled, there are 11 resonant conditions recorded. With the delta-wing representations added to the parallel-staged configuration, the number of responses are increased to 31 over the same frequency range. The taller markings represent identified bending modes and include asymmetric modes; the shorter markings are due to wing responses or other modes not yet identified. For example, the mode at 0.8 Hz is known to be a "scissors" mode in the yaw direction. Data from another model, the 1/40-scale Apollo-Saturn V dynamic model, is presented for comparison. Data above a frequency of 3.5 Hz were not measured. It is seen that the shuttle model is more complex than the Saturn model and it can be noted that, even with a relatively simple model such as the 1/15-scale space shuttle model, the response characteristics are many and complex.

# FREQUENCY CONTENT COMPARISON OF VARIOUS MODELS

FREE-FREE BOUNDARY RESTRAINT

1/15 - SCALE ORBITER  
BODY

1/15 - SCALE BOOSTER  
BODY

1/15 - SCALE BOOSTER ORBITER  
WITHOUT WINGS

1/15 - SCALE BOOSTER ORBITER  
WITH DELTA WINGS

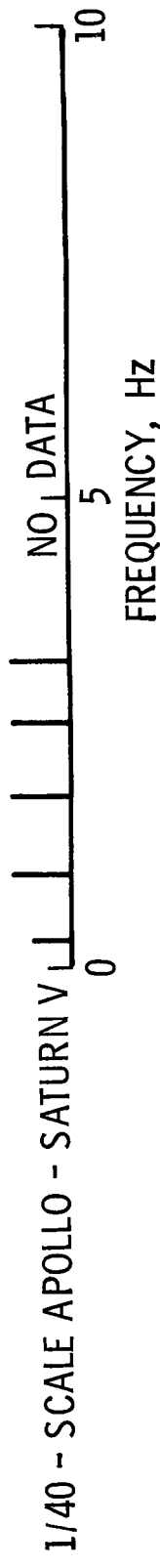


## (Figure 8)

A few selected asymmetric mode shapes from the data shown in figure 7 are given. These are complex modes with the involved interaction of the orbiter, booster, and delta wings. At 2.34 Hz the booster and the orbiter are responding out of the pitch and yaw planes with a first fuselage bending type mode. At a plane intersecting the rear of the orbiter and near mid-booster as indicated by the section arrows, the displacements of the bodies are in opposite directions. At the same time, the orbiter wing tips have a large displacement in a direction opposite to that of the lower level motions of the booster wing tips. At 3.68 Hz, the orbiter is not responding while the booster is vibrating in a bending type mode with the response plane nearly in the yaw direction. The booster wing tips, at this frequency, are moving in opposite directions. At 6.11 Hz, the booster is responding in a second bending-type response near the yaw plane while the orbiter is responding in a first bending-type mode almost in the pitch direction. The booster wing tips are responding in opposite directions. These are examples of some complex asymmetric responses similar to those that can be expected to occur on the full-scale structure.

## SOME ASYMMETRIC MODES OF SPACE - SHUTTLE MODEL

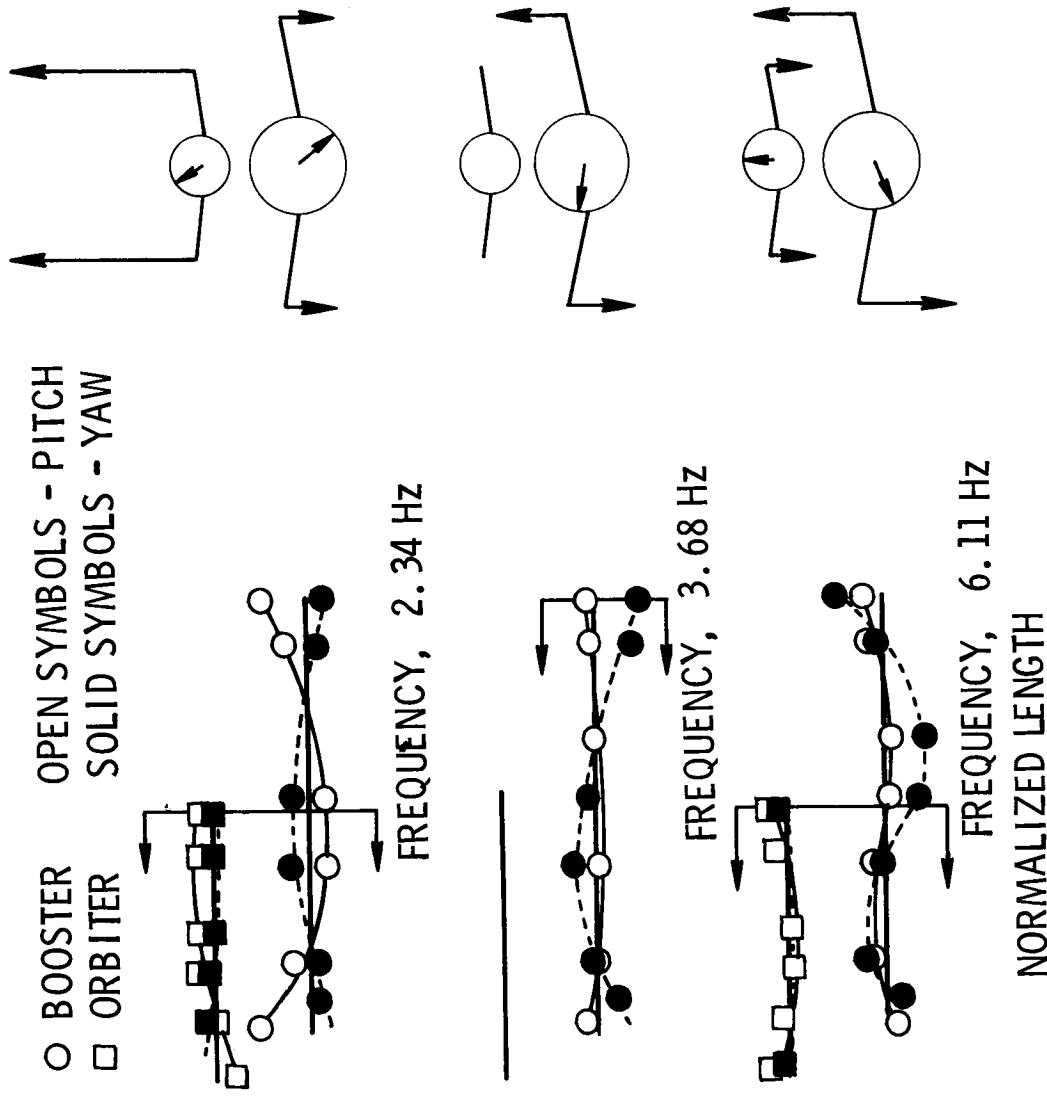


Figure 8

(Figure 9)

A computer program has been designed to predict uncertainty in structural modal characteristics based on uncertainty in structural physical properties. The program, entitled VIDAP (Vibration Data Accuracy Program), can handle both stiffness and mass uncertainty and can work with an arbitrary stiffness matrix or one which involves beam or plate elements. The program and the supporting theory have the following features:

- (a) A linear statistical model which can accurately predict uncertainties of selected frequencies and modes based on the uncertainty in properties of individual elements
- (b) The program never handles matrices of dimension larger than the total degrees of freedom of the system. The program can handle problems of up to 300 degrees of freedom
- (c) The computation speed of the program is less than that required for computation of eigenvectors and eigenvalues
- (d) The program stands alone from any structural dynamics program, requiring for input only the eigenvalues and eigenvectors, the mass and stiffness matrices, and certain element properties
- (e) The input procedure is of such a form that the user need not have any knowledge of statistics

A description of the program, including theory, user's manual, and examples is given in reference 1.

## STRUCTURAL MODES ACCURACY PROGRAM

- PROGRAM USERS MANUAL AVAILABLE
- PROVIDE CAPABILITY TO PREDICT UNCERTAINTIES IN CALCULATING MODAL CHARACTERISTICS RESULTING FROM UNCERTAINTIES IN DEFINING STRUCTURAL PHYSICAL PROPERTIES
- PROVIDE DATA TOLERANCES FOR CONTROL SYSTEM DESIGN AND FOR VEHICLE STABILITY ANALYSIS
- PROVIDE "MOST PROBABLE" MATHEMATICAL MODEL AND REDUCE JUDGMENT ERRORS

Figure 9

(Figure 10)

Structural dynamic analysis of the space shuttle vehicle requires finite-element methods with more detail than on any previous launch vehicle. Improvement in computer program techniques is needed to enable efficient and accurate analysis of complex structures. A computer routine has been developed for analysis of structures too large to solve by direct methods. The substructure method involves three basic steps: (1) calculation of substructure generalized functions and the corresponding sub-structure mass and stiffness matrices, (2) substructure synthesis, in which the system mass and stiffness matrices are formed on the basis of substructure mass and stiffness matrices, interconnection descriptions, etc., and (3) calculation of modes and frequencies of the system.

Two digital programs were developed for implementing the solution procedure. Step (1) is carried out with the Substructure Function Generator program, namely, the Lockheed-developed Structural Network Analysis Program SNAP and its dynamic analysis counterpart, SMAP/Dynamics, which are general-purpose programs for performing static and dynamic analyses of structures consisting of various types of finite elements (beams, triangular and quadrilateral membrane, plate, and shell elements). Steps (2) and (3) are combined in a computer program called the Substructure Synthesis Program. Communication between the Function Generator and Synthesis programs involves substructure data files created by the Function Generator program and read as input by the Synthesis program.

Each substructure data file contains descriptions of a specific act of generalized functions. Provisions are included in the synthesis program to use any specified subset of these functions as generalized coordinates in the system analysis. Accordingly, the effects on overall system modes and frequencies of different classes of substructure generalized functions can be studied without recreating substructure data files.

## ADVANCED SUBSTRUCTURING TECHNIQUES

OBJECTIVE: TO DEVELOP AN ACCURATE AND EFFICIENT TECHNIQUE FOR STRUCTURAL MODES ANALYSIS OF STRUCTURES TOO LARGE TO SOLVE BY DIRECT METHODS.

- SUBSTRUCTURE REPRESENTED BY GENERALIZED DISPLACEMENT FUNCTIONS
- SUBSTRUCTURE MODELED AS ASSEMBLAGE OF BEAM AND SHELL ELEMENTS
- COMPUTER PROGRAM IS OPERATIONAL

Figure 10

## SPACE SHUTTLE LAUNCH CONFIGURATION EXAMPLE

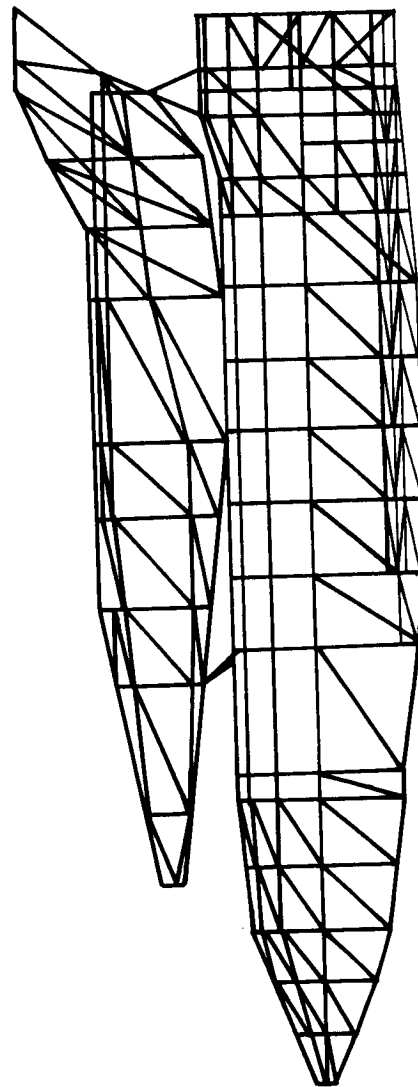
(Figure 11)

A space shuttle launch configuration is illustrated. Each vehicle was used as a substructure in the system model. Two system joints interconnected the two substructures. The forward joint lies on the symmetry plane, and the aft joint lies off the symmetry plane. A half-model on one side of the symmetry plane was used to obtain the symmetric modes of the system. The use of 2 substructures, three modes each, and a total of 15 functions provided the first 5 symmetric modes to an accuracy of 13 percent. The fact that the first mode computed by the substructure program is slightly lower than that computed by the SNAP/Dynamics program is attributed to some small differences in the basic finite-element nets employed in the two analyses.

## REFERENCE

1. Collins, Jon D.; Kennedy, Bruce; and Hart, Gary C.: Bending Vibrational Data Accuracy Study. Tech. Rep. No. 70-1066 (NAS 8-25458), J. H. Wiggins Co., Sept. 1970.

## SPACE-SHUTTLE LAUNCH CONFIGURATION



- 2 SUBSTRUCTURES, BOOSTER AND ORBITER - 3 SYMMETRIC MODES EACH
- 6 FUNCTIONS DEFINE MOTION OF AFT JUNCTURE
- 3 FUNCTIONS DEFINE MOTION OF FORWARD JUNCTURE

COMPARISON OF FREQUENCIES, Hz

MODE	SNAP/DYNAMICS	SUBSTRUCTURE	% DIFFERENCE
1	2. 3329	2. 3179	0. 65
2	2. 6488	2. 6994	1. 91
3	3. 8209	4. 1891	9. 63
4	4. 2454	4. 4330	4. 41
5	6. 2128	6. 9777	12. 31

Figure 11

## SPACE SHUTTLE TPS PANEL VIBRATION STUDIES

By Huey D. Carden, Barbara J. Durling, and William C. Walton, Jr.  
NASA Langley Research Center, Hampton, Virginia.

### INTRODUCTION

As reported at the first Space Shuttle Conference we are working to establish analytical and experimental procedures to predict basic vibration characteristics, such as natural vibration modes and damping of thermal protection system (TPS) panels (ref. 1). The vibration characteristics of the panel systems in thermal environments will be important as inputs to flutter and fatigue investigations.

We are currently following four main lines of effort: (1) experimental studies of the vibration modes and damping of typical TPS panel configurations at room temperature, (2) development of a facility to measure vibration characteristics of panels at elevated temperatures, (3) application and extension of the NASITRAN computer program to compute vibration modes of panels prestressed by static pressure and thermal loads, (4) investigation of impulse testing as an alternative to measuring natural modes to characterize panels for vibrations.

The purpose of this paper is to report preliminary results from the studies of vibrations of panels at room temperature. Two representative metal panels have been investigated. The NASITRAN computer program has been applied to compute vibration modes of both panels. One of the panels has been fabricated and a vibration survey has been made to determine the natural vibration modes. This paper will discuss the objectives and approaches in the analytical modeling, considerations related to computer time to compute the modes, and results and problems arising in an effort to correlate experimentally and analytically determined modes.

PANEL CONFIGURATIONS  
(Figure 1)

The two panel configurations presently being considered are illustrated in figure 1. Both panels are of the refurbishable metal heat-shield category with a corrugated skin.

Channel-stiffened René 41 panel: The panel at the left in figure 1 (designated channel-stiffened panel) represents one of the many designs evaluated in reference 3 for a hypersonic cruise vehicle wing and utilized in reference 3 to study a tin-aluminum-molybdenum coating for heat-shield usage. For the purposes of the present study two of these panels were fabricated from 0.254 mm René 41 sheet. Each corrugation had a nominal pitch and depth of 38.1 mm and 4.8 mm, respectively, and the flats were 6.4 mm wide. Hat-section channel stiffeners and support clips (clips not shown) were formed from 0.43 mm René 41 sheet. The panels were 240 mm wide and 457 mm long. All parts were joined by spot-welding. It is important to realize that the panels as fabricated exhibited substantial imperfections. In particular the depth of the corrugations deviated by 5 to 10 percent from nominal.

Clip-supported TD NiCr panel: The panel at the right in figure 1 (designated clip-supported panel) represents a design presently being considered here at Langley Research Center to investigate materials for space shuttle heat-shield applications. The panel is not yet available for vibration tests but fabrication is expected to begin shortly. This panel will be fabricated from 0.635 mm TD NiCr sheet. The corrugations will have a pitch and depth of 91.3 mm and 9.15 mm, respectively, and the flats are 23.0 mm wide. The twelve clip supports will also be formed from 0.635 mm TD NiCr sheet and are 17.5 mm wide, 76.0 mm long, and have a 6.1 mm by 60.5 mm slot cut out of the leg of the clip. The clips are joined to dimpled sections of the panel with machine screws.

## PANEL CONFIGURATIONS

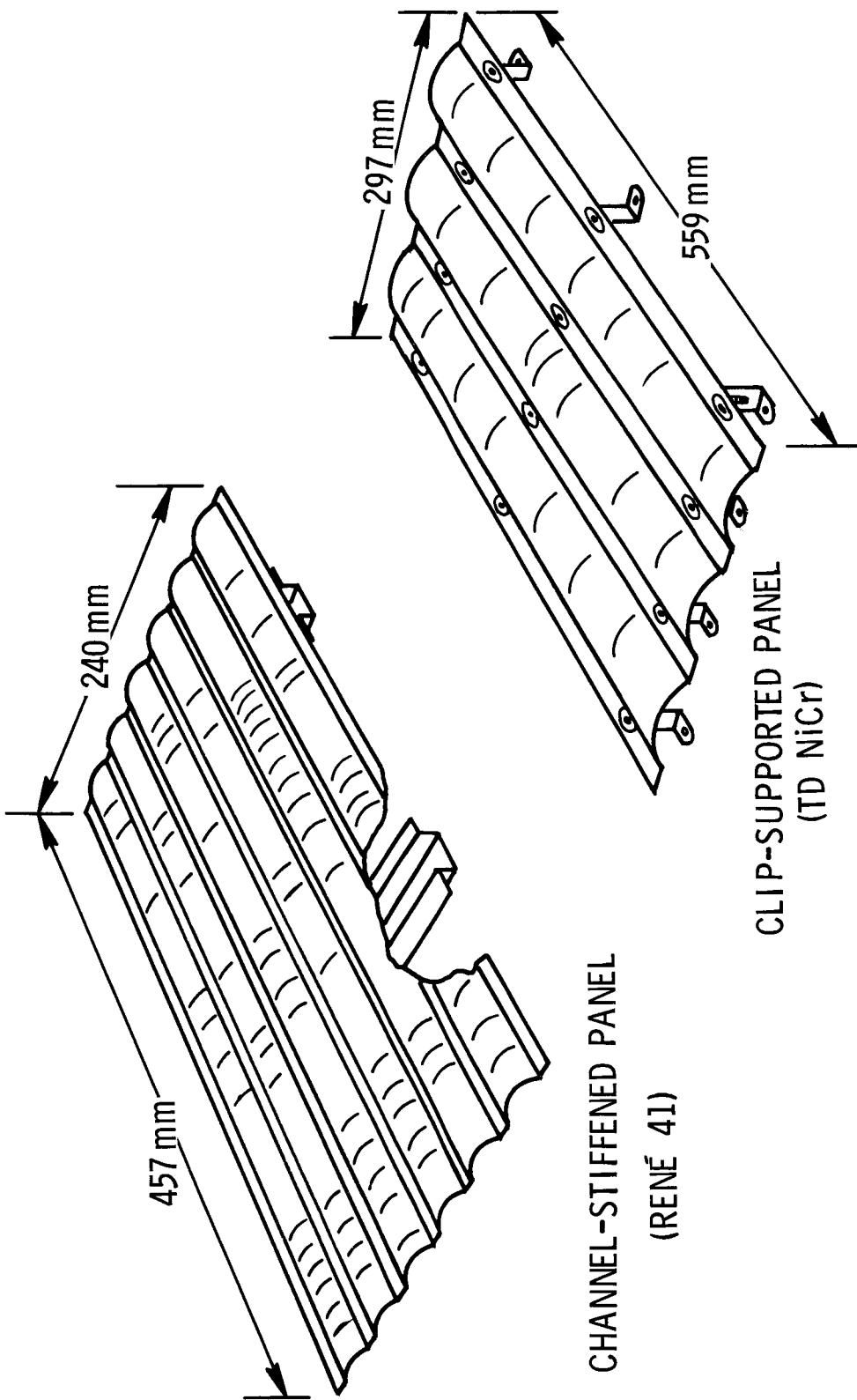


Figure 1

## EXPERIMENTAL SETUP FOR PANEL VIBRATIONS

(Figure 2)

The vibration test setup for simulated free-body conditions is shown in figure 2. The panel was supported as shown on soft elastic bands. Excitation was provided by a small electromagnetic shaker. A noncontacting inductance-type probe was used to measure out-of-plane deflections. The probe was mounted on a mobile unit which permitted a survey of displacements over the entire panel surface to be made. The displacement was automatically plotted using an X-Y plotter. For tests of the clip-supported panel the setup was basically the same. The panel was attached through its support clips to a massive overhead frame.

## EXPERIMENTAL SET-UP FOR PANEL VIBRATIONS

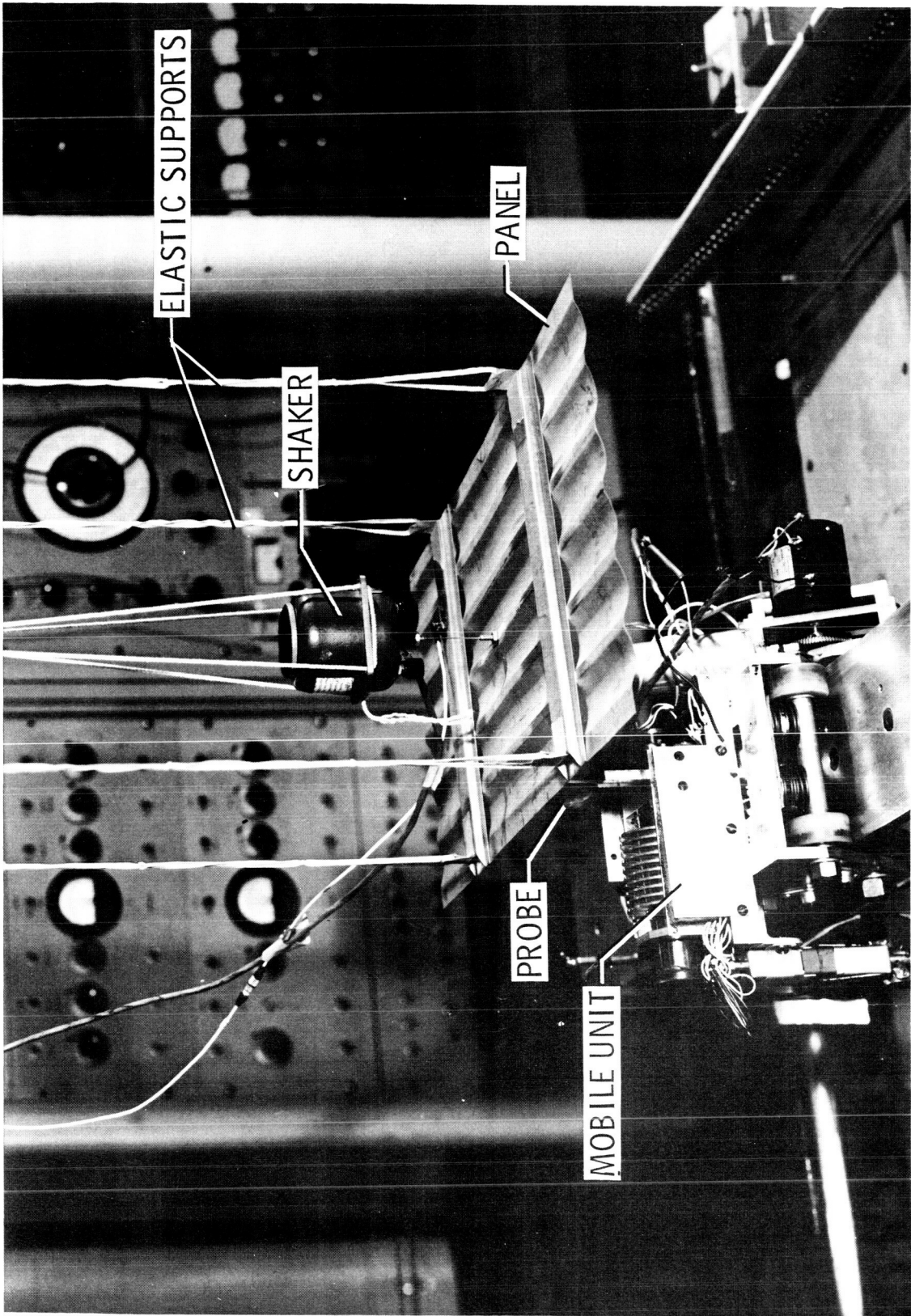


Figure 2

## TYPICAL MEASURED NODAL PATTERNS

## Channel-Stiffened Panel; Free Boundaries

(Figure 3)

Typical measured nodal patterns for the softly supported channel-stiffened panel are shown in figure 3. Modes other than those shown in the figure were detected in the frequency range. A few of the measured nodal patterns are readily associated with classical flat-plate patterns. For example, at 73.3 Hz is a classical first torsional mode and at 114.3 Hz is a classical first bending mode. For the modes at 228.4 Hz and 283.2 Hz the node patterns are somewhat distorted. However, with a little study one may determine that the 228.4 Hz mode is a flat plate second torsion and the one at 283.2 Hz is a second bending. Most of the patterns detected, however, exhibited a complexity which did not allow any clear cut identification or classification. In exciting these modes a number of different shaker locations were tried. It is considered of some interest that the measured nodal patterns were apparently independent of shaker location.

**TYPICAL MEASURED NODAL PATTERNS**  
CHANNEL-STIFFENED PANEL; FREE BOUNDARIES

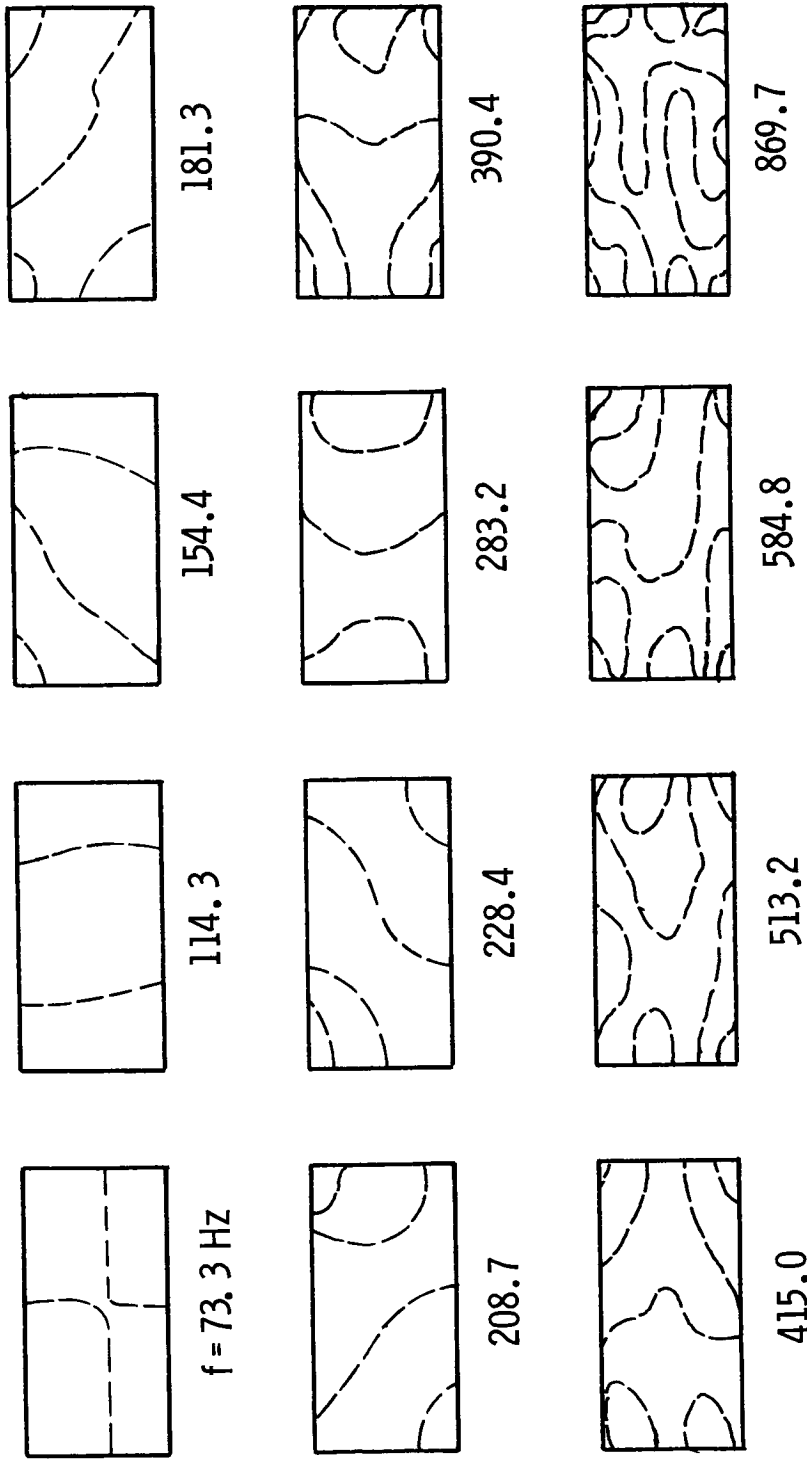


Figure 3

## TYPICAL MEASURED NODAL PATTERNS

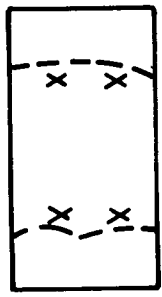
Channel-Stiffened Panel; Clip Supported

(Figure 4)

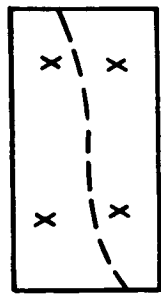
As stated, additional vibration tests were conducted with the channel-stiffened panel supported on four clips. The clips were in turn attached to a rigid massive base. Actually the panel used for these tests was not the same one as used for the free-boundaries tests. The two panels were, however, nominally the same. Typical nodal patterns, measured for this case, are shown in figure 4. The X marks indicate the locations of the clip supports. The clips were welded to the panels on the floor of the channel stiffeners. As was the case for the free-body panel, the nodal patterns measured for the supported panel are comprised of both readily identifiable patterns similar to those associated with flat plate modes and irregular patterns which could not be identified or classified. For this case the patterns are somewhat more regular than in the case of the free-body panel and the measured nodal patterns also appear to be independent of shaker location.

TYPICAL MEASURED NODAL PATTERNS  
CHANNEL-STIFFENED; CLIP SUPPORTED

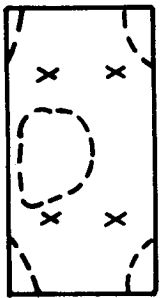
X CLIP LOCATION



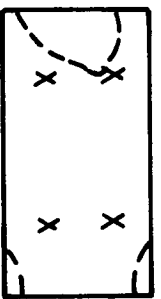
$f = 127.0 \text{ Hz}$



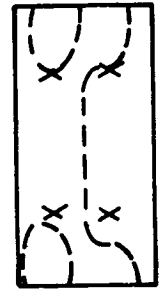
$222.9$



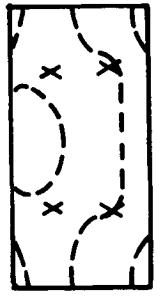
$231.1$



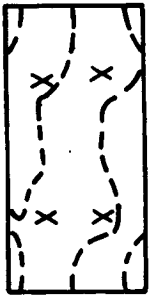
$372.6$



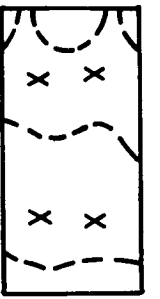
$254.7$



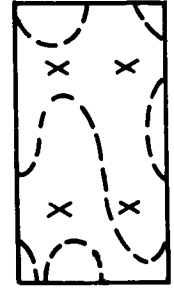
$289.9$



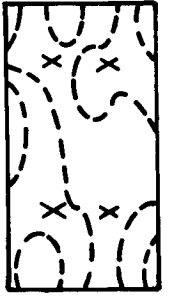
$303.4$



$392.9$



$468.4$



$483.4$

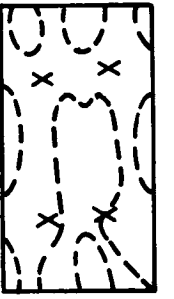


Figure 4

PANEL IDEALIZATION FOR NASTRAN ANALYSIS  
Channel-Stiffened Panel  
(Figure 5)

Figure 5 illustrates the structural idealization involved in applying the NASTRAN computer program to the channel-stiffened panel considered as a free body. Advantage was taken of the four quadrants of symmetry so that only a quarter of the panel had to be modeled. The panel was represented as an assemblage of rectangular flat-plate elements from the NASTRAN element library. A very fine subdivision was made consistent with one of our objectives which is to achieve good stress definition in the computed modes. The subdivision in the end regions and in the channel stiffener illustrates the element size used. The same size elements were used over the entire surface of the panel but were not drawn in the central region. The quarter-panel idealization resulted in a system having about 3500 degrees of freedom. In figuring the computing time required to solve these systems, an important factor is the stiffness matrix semibandwidth which is an indicator of the size of the part of the matrix containing finite numbers. The computing time is roughly proportional to the degrees of freedom times the square of the semibandwidth. For this problem the semibandwidth was about 250. Using the capability of the NASTRAN program to provide advanced estimates of computing time, it was determined that in a direct solution it would require over 9 hours on a CDC 6600 computer to get one mode. This is, of course, prohibitive. Another capability of NASTRAN, the Guyan reduction technique, was used in an attempt to bring down the size of the problem. A reduction from 3500 degrees of freedom to about 250 degrees of freedom was tried. However, the computing time with the standard NASTRAN program was still prohibitive.

Recently, a modified version of NASTRAN has been obtained by the Langley Research Center for evaluation. With the modified version, the Guyan reduction of the problem from 3500 degrees of freedom down to about 250 degrees of freedom has been successfully carried out and 250 eigenvalues and 12 eigenvectors have been computed. A total of 5-1/2 hours elapsed time including approximately 3 hours of CPU (central processing unit) time on a machine with almost 300K core storage was required to obtain the solution. It should be noted that three additional sets of boundary conditions would have to be imposed along the two inner edges of the quarter panel to obtain all possible combinations of modes which can exist for the panel. With the modified NASTRAN program, this would take about 16-1/2 additional hours of elapsed time.

In discussing computing economics it is usual to quote only the CPU time since this is the time for which charges are normally made. However, it is understood that with problems of this size an entire computing machine is occupied excluding all other problems. Therefore, the elapsed time may be a more pertinent time to consider.

PANEL IDEALIZATION FOR NASTRAN ANALYSIS  
CHANNEL-STIFFENED PANEL

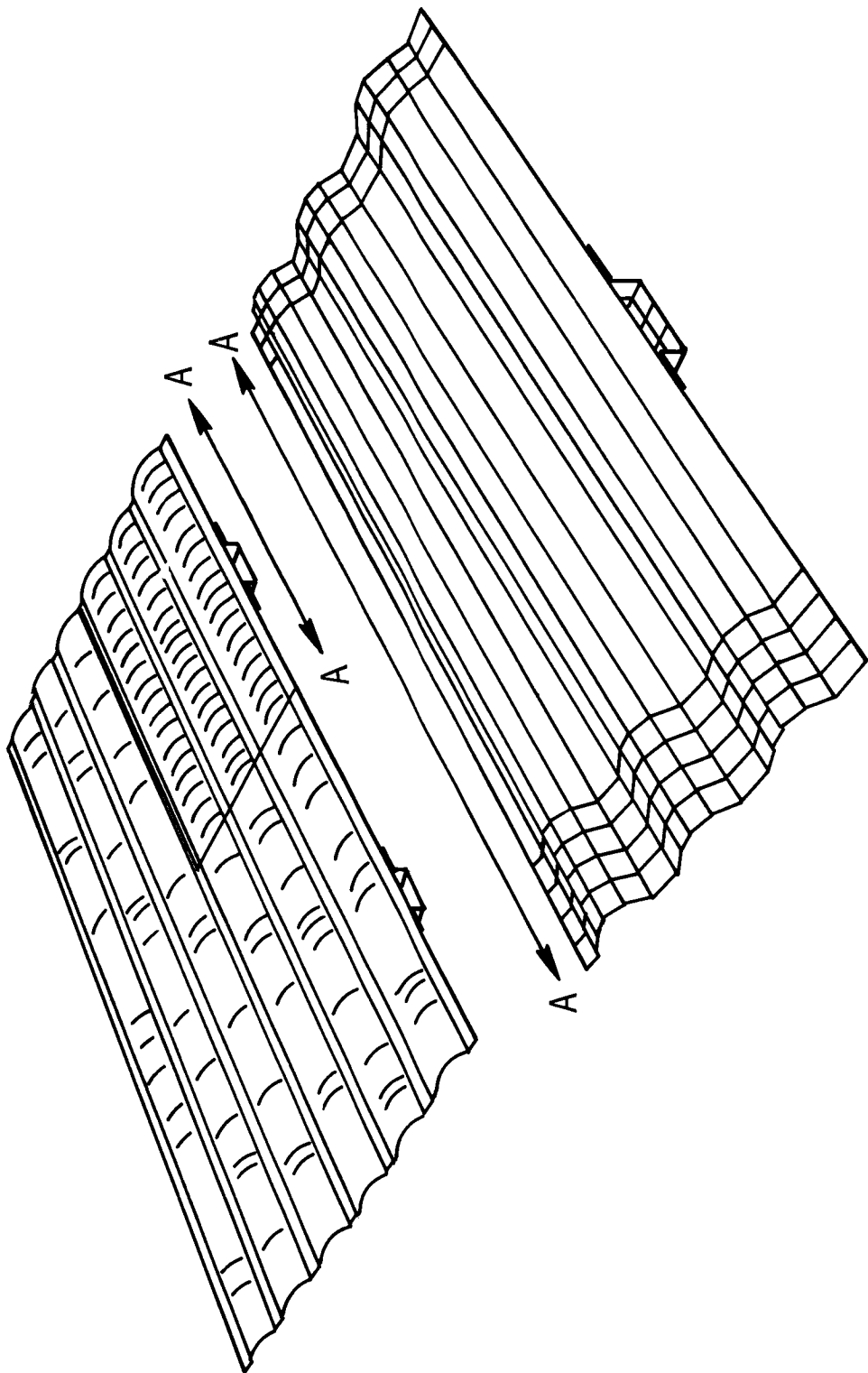


Figure 5

## COMPUTED NODAL PATTERNS USING MODIFIED NASISTRAN

## Channel-Stiffened Panel

(Figure 6)

Presented in figure 6 are 11 nodal patterns and the associated frequencies of the free-body channel-stiffened panel computed with the modified version of NASISTRAN. These nodal patterns represent modes over the entire panel which are symmetric with respect to all four quadrants of symmetry. Employing the three other possible sets of boundary conditions would result in patterns additional to those shown here. A comparison of these modes to the experimental ones for the panel will be made later in the paper.

COMPUTED NODAL PATTERNS USING MODIFIED  
NASTRAN

CHANNEL-STIFFENED PANEL

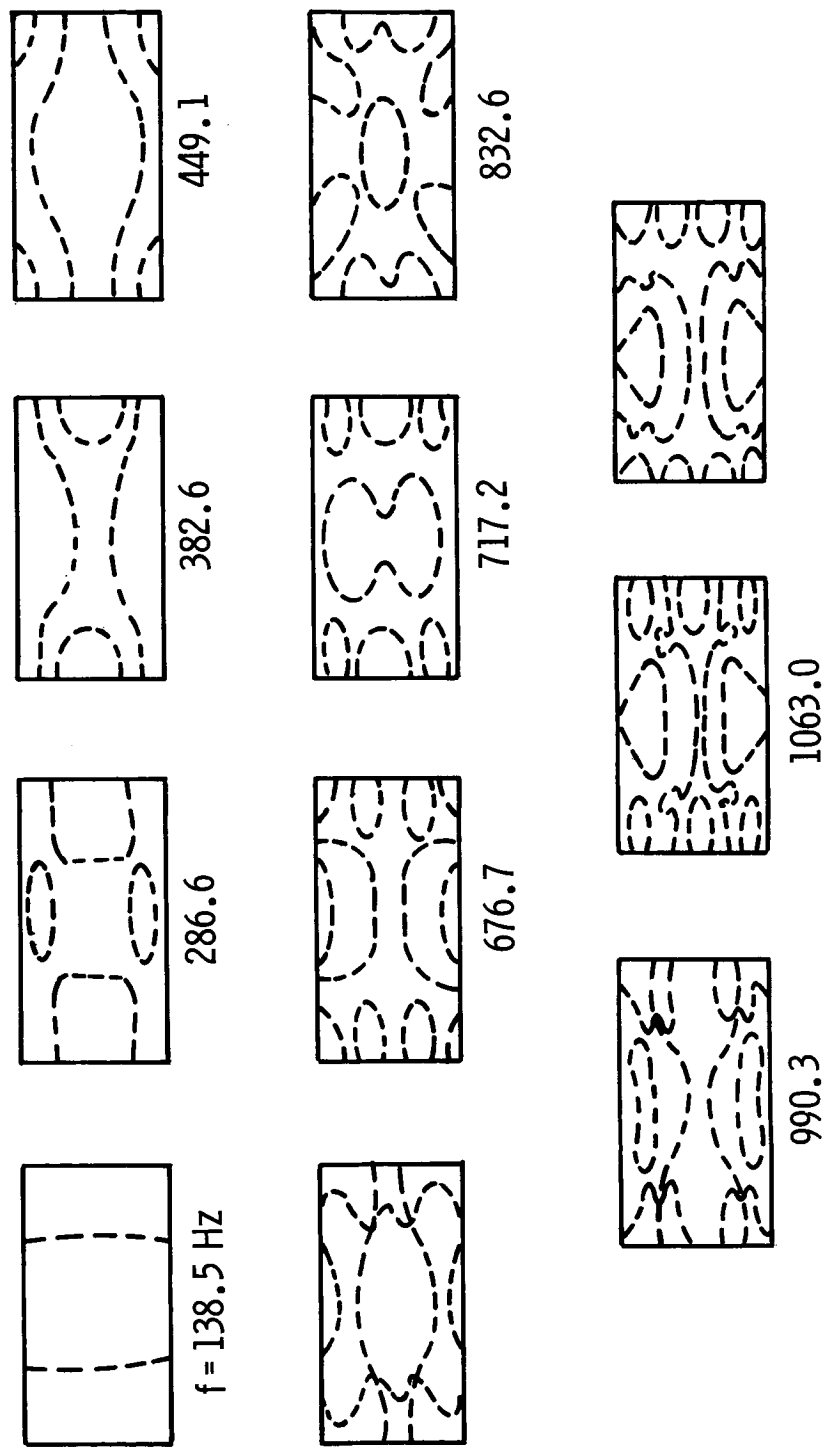


Figure 6

## PANEL IDEALIZATION FOR NASTRAN ANALYSIS

Clip-Supported Panel  
(Figure 7)

As previously stated, in addition to the channel-stiffened panels, we have also been conducting an analytical study of the somewhat simpler panel described as a clip-supported Ti NiCr panel (see fig. 1). Figure 7 illustrates the idealization involved in applying the NASTRAN computer program to the Ti NiCr panel. Since this panel has fewer corrugations, and no adjacent structure is connected by channels as in the channel-stiffened panels, analysis with fewer degrees of freedom and less bandwidth was possible. The standard NASTRAN computer program was used. Once again advantage of symmetry has been taken. However, this time one-half the panel has been modeled to avoid splitting a clip support. A special treatment was tried to compute stress details in the region of the clip supports. A static analysis was first made of a clip support. In this preliminary analysis a very detailed model of the clip was utilized as shown at the right in the figure. This treatment resulted in a system with approximately 1900 degrees of freedom. Static influence coefficients were computed at the four corners which attach to the surrounding panel. The General Element capability of NASTRAN could then be used to input the influence coefficients of the clip supports to represent the supports in the dynamic analysis of the entire panel. Inclusion of the clips as general elements does not increase the degrees of freedom or the stiffness matrix semibandwidth. The coarser mesh used to model the panel surface for the eigenvalue problem resulted in a problem of about 1200 degrees of freedom.

Once computed eigenvectors with element stresses were obtained from the dynamic analysis of the panel, displacements and rotations were input as enforced displacements at the four corners of the clip and the static analysis was rerun to obtain interior displacements and stresses of the clip itself.

A total computing time of approximately 45 minutes was required to obtain the influence coefficients of the clip supports and the displacements and stresses in the clip for the enforced-displacements-input case. Approximately 40 minutes of computing time was required with the standard NASTRAN computer program to obtain two eigenvectors and the associated model stresses in all panel elements for this  $1200 \times 1200$  eigenvalue problem.

PANEL IDEALIZATION FOR NASTRAN ANALYSIS  
CLIP-SUPPORTED PANEL

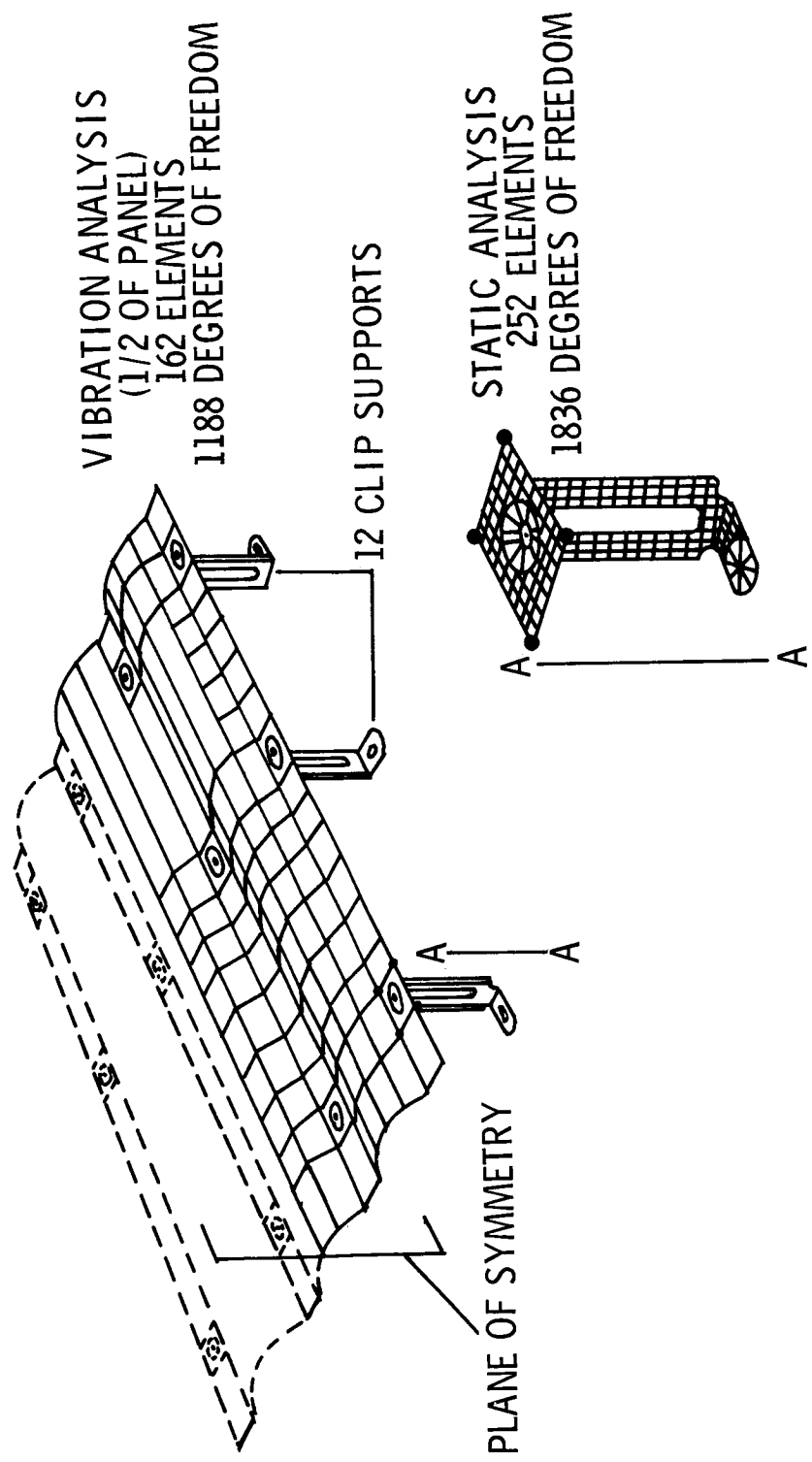


Figure 7

## COMPUTED MODAL DEFLECTIONS

Clip-Supported Panel;  $f = 210.3 \text{ Hz}$   
(Figures 8 and 9)

Presented in figure 8 are modal displacements of the clip-supported panel along the two edges of a flat near the middle of the panel. In figure 9 are deflections for the same mode but running across the panel at the middle. In figure 8, this particular flat includes the general elements of three clip supports. The deflections are also shown for the interior of the center clip support. This is the first symmetric mode of the panel and it has a computed frequency of 210.3 Hz. The somewhat surprising results indicate that the corners of the element to which the clip support is attached are deflecting appreciably more than the area immediately adjacent to the dimple in the center of the element. Since the presence of the dimple greatly increases the local stiffness of the panel element, these displacements appear reasonable. It should be noted that since slopes as well as displacements were enforced at corners of the general element, the mode shape in the elements next to the general element should probably have a dip between its grid points. However, the distribution of displacement between grid points is presently not available as an output from NASTRAN.

In figure 9 the variations in the displacements of the clip element across the panel are not as pronounced as they were in the lengthwise direction. As may be seen in the figure the presence of the clip support has, however, introduced complexities into the shape of the panel mode such that a knowledge of the local disturbances could be required in flutter or fatigue analysis.

COMPUTED MODAL DEFLECTIONS  
CLIP-SUPPORTED PANEL,  $f = 210.3$  Hz

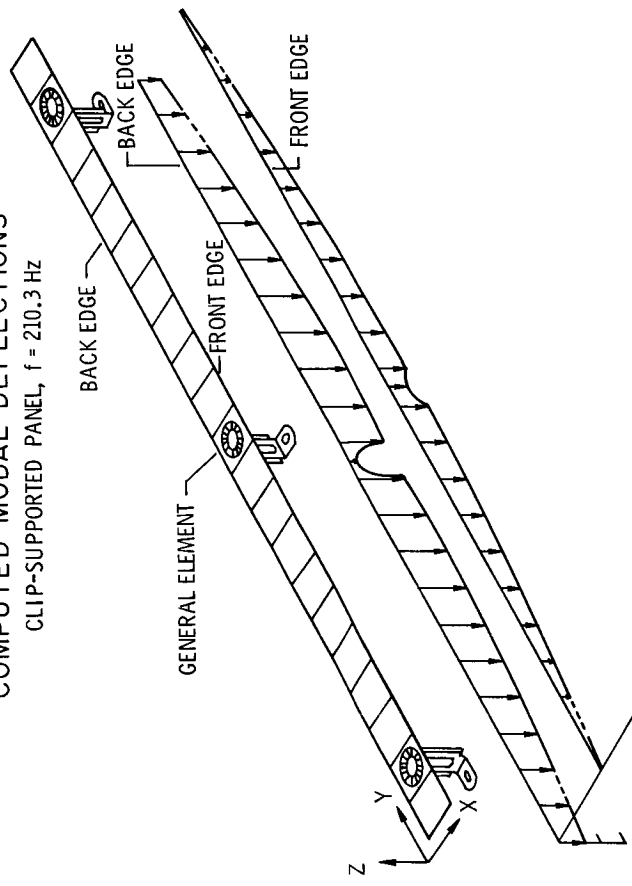


Figure 8

COMPUTED MODAL DEFLECTIONS  
CLIP-SUPPORTED PANEL;  $f = 210.3$  Hz

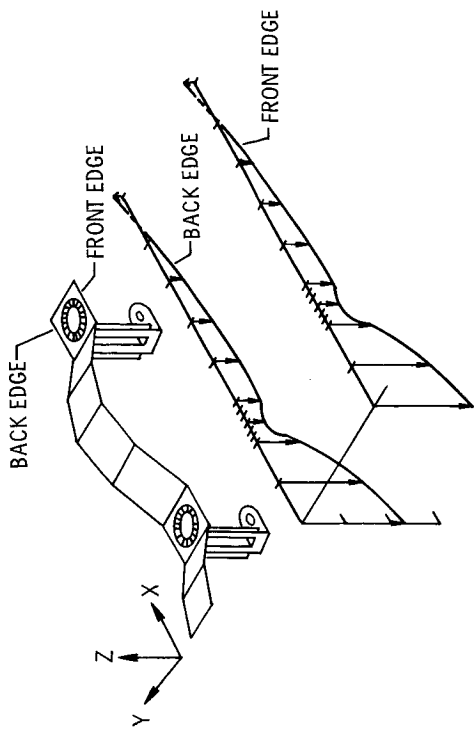


Figure 9

## COMPUTED STRESSES FOR CLIP-SUPPORTED PANEL

$$f = 210.3 \text{ Hz}$$

(Figure 10)

The computed modal stresses in the clip element previously discussed and in the panel elements surrounding the clip area are presented in figure 10 for the 210.3 Hz mode of the panel. The values shown in figure 10 are relative normal Y stresses at the element centers since NASTRAN provides stresses only at the center location. These stresses are presented with a note of caution. The investigation as to the adequacy of NASTRAN elements to represent detailed stress distributions of this sort has just begun. As yet the capability is not available to print out stress distributions within the element itself and this capability is needed to really understand the results.

As indicated in the sketch at the right, several small elements on the panel surface immediately bordering the dimple exhibit the highest values of stress. The occurrence of these relatively high stresses appear to be consistent with the sharp variation of displacement in the region (fig. 8). Likewise, the relatively lower values of stress on the right edge and across the top and bottom edges are consistent with the fairly smooth deflections in these areas (fig. 9). It should be noted that some asymmetry exists in the values of stress in the area around the clip as well as in the clip element itself. The asymmetry should not be present and as yet the source has not been isolated; however, efforts are being made to remedy the discrepancies.

# COMPUTED STRESSES FOR CLIP-SUPPORTED PANEL

$f = 210.3 \text{ Hz}$

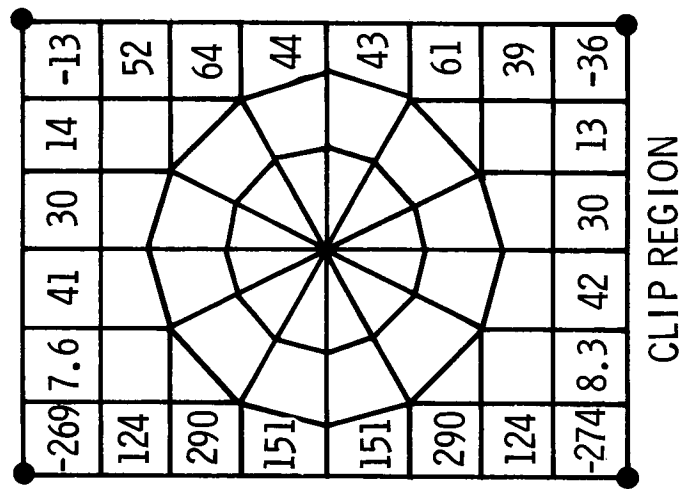
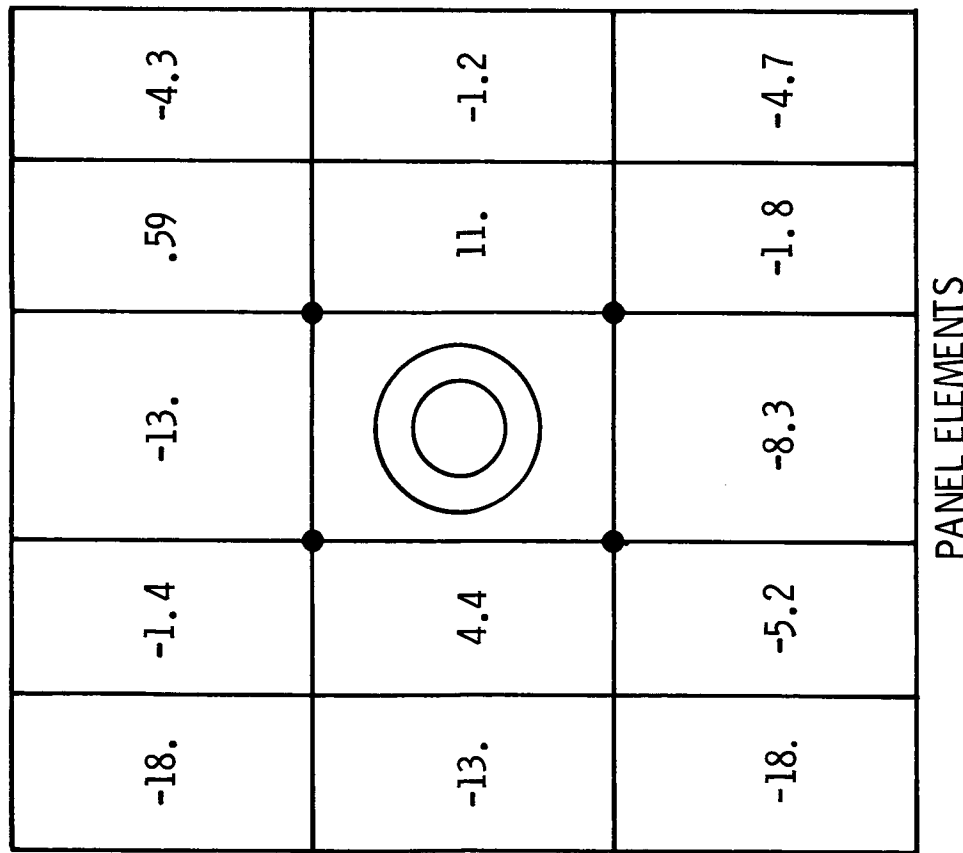


Figure 10

## CORRELATION BETWEEN ANALYTICAL AND EXPERIMENTAL RESULTS

(Figures 3 and 6)

Comments may now be offered on correlations between the experimentally and analytically determined free-body modes for the channel-stiffened panel. As has been indicated, the experimentally determined frequencies and nodal patterns are shown in figure 3 and those determined analytically are shown in figure 6. Each of the two lowest experimental modes has a simple character. Of these the first torsion mode at a measured frequency of 73.3 Hz is excluded from the analytical results because of the symmetry condition imposed. For the first bending mode at a measured frequency of 114.3 Hz the calculated frequency is 138.5 Hz, a substantial discrepancy. A number of the computed frequencies for higher modes are in close proximity to measured frequencies and there are similarities between computed and measured nodal patterns over portions of the panel, tempting one to infer a correlation. However, these similarities are accompanied by such pronounced differences between the measured and calculated nodal patterns one must conclude that a convincing correlation has not been established. Factors which are considered likely to be causing the differences between analysis and experiment are noted as follows:

(1) Imperfections: As discussed in the descriptions of the panel structures, there were substantial variations in the depths of the corrugations. It was determined that the imperfections would cause significant variations of the local bending stiffness. In the NASTRAN analysis the depth of the corrugations was considered to be uniform and equal to the average of the actual depths. The imperfections in the panel are probably more severe than would be the case for a flight article TPS panel. However, there is a need to assess the character of the imperfections which may reasonably be expected and the effects they may have on vibration response.

(2) Inadequate modeling of membrane action: It is generally acknowledged that the flat plate elements in the NASTRAN library do not always provide a good representation of the stretching deformations. Providing a better membrane element is one objective of the continuing NASA effort to improve and extend the NASTRAN program.

## CONCLUDING REMARKS

Both experimental and analytical studies have been conducted of the vibrations of representative TPS panels. In the experimental studies with corrugated panels it has been found that the nodal patterns are very complex and difficult to identify or classify. Furthermore, what would be considered satisfactory correlation between the analytical and experimental results has not been achieved. However, it is encouraging that analyses of panels as complex as the clip-supported panel with acceptable computer run times are possible.

In future studies efforts will be made to obtain more perfect models to use but concurrently imperfections of the panels will be included into the NASTRAN analysis. Such studies are presently underway with nominally flat plates. The effects of prestress due to heat and pressure loadings will also be included in future experiments and analyses.

An additional step to be taken is to critically assess whether the stress variations computed with NASTRAN are reasonably accurate. Finally, channels of communication with the NASTRAN management office will be maintained to encourage the development of elements that are required and to improve the elements now available in NASTRAN.

## REFERENCES

1. Walton, William C., Jr.; and Naumann, Eugene C.: Panel Vibration and Random Loads. Space Transportation System Technology Symposium, NASA TM X-52876, vol. II, 1970, pp. 43-57.
2. Plank, P. P.; Sakata, I. F.; Davis, G. W.; and Richie, C. C.: Hypersonic Cruise Vehicle Wing Structure Evaluation. NASA CR-1568, 1970.
3. Wichorek, Gregory R.; and Stein, Bland A.: Experimental Investigation of Aluminide-Coated Ta-10W for Heat-Shield Applications. NASA TN D-5524, 1969.

APPROXIMATE ANALYSIS AND DYNAMIC TESTS FOR  
A THERMAL PROTECTION SYSTEM PANEL

By I. U. Ojalvo and N. Arcas  
Grumman Aerospace Corporation  
Bethpage, New York

ABSTRACT

A combined analytical and experimental program to determine the transverse dynamic response of TPS panels for the space shuttle is discussed. The panel is idealized as a pinned-pinned/free-free heated plate with corrugation stiffening and local mass and stiffness attachments. Galerkin's procedure is used to generate an algebraic eigenvalue problem from which natural modes and frequencies are calculated. Approximate modal superposition formulas are then presented to predict RMS strain levels to broad-band acoustic excitation. Tests were performed to measure natural frequencies, mode shapes, damping and response to acoustic excitation. Results of the frequency and damping tests appear reasonable. Although difficulties were encountered with mode shape measurements, it is felt that the results obtained can be useful in predicting approximate panel response to combined acoustic, thermal, and quasistatic pressure loading once critical panel loading conditions are specified.

ACKNOWLEDGEMENT

The authors wish to express their appreciation to C. Parente, of the Loads and Dynamics Section, for his assistance with the test phase of this effort.

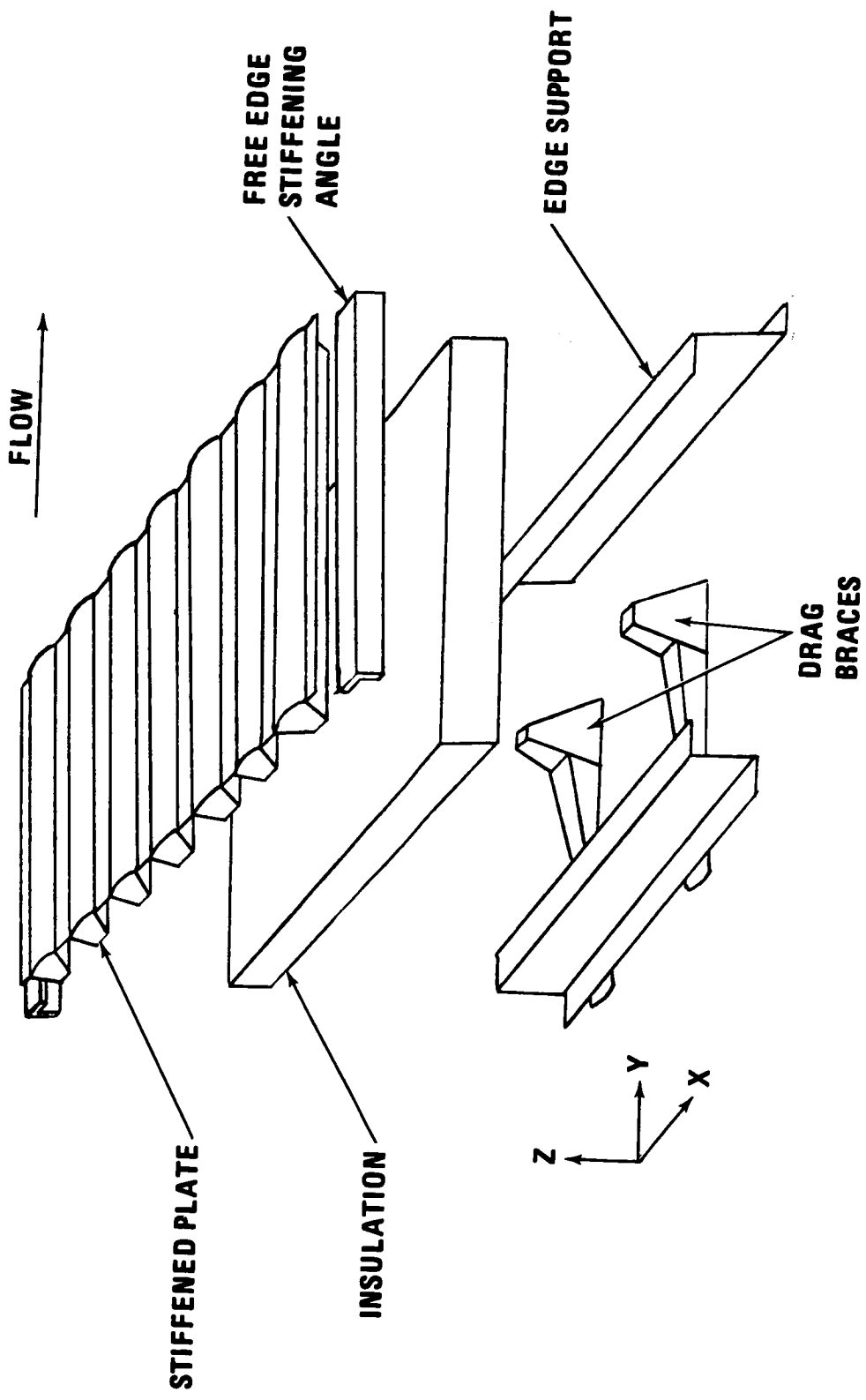
## INTRODUCTION (Slide 1)

Since most shuttle thermal protection system (TPS) panels sized by static elastic loading criteria are likely to be near minimum gage, creep phenomena and dynamic considerations will probably dictate much of their final design characteristics. With regard to dynamic effects, the evolution of reliable light-weight configurations requires that the environment be better defined and applicable analytical procedures be developed. Once critical loads associated with vehicle launch, ascent, and re-entry are believed to be realistically accurate, the weight penalty associated with TPS overdesign may be minimized through detailed and precise analyses. All this will certainly require extensive analytical and experimental work throughout the shuttle development program.

However, what is currently required at Grumman is an engineering tool for preliminary evaluation of the many panel designs being considered. To be useful, this tool would have to combine reasonable accuracy with versatility and convenience of use. The present work reports on an analysis procedure which was developed with this need in mind. It employs Fung's<sup>(1)</sup> corrugated plate theory and Galerkin's method, together with simplifying modal techniques, to predict panel response to acoustic loading and the effects of in-plane loading resulting from differential thermal expansion. The structural idealization employed also provides for both discrete support and mass attachments at arbitrary points over the panel as well as additional stringer stiffening along and normal to the plate's corrugations. Slide 1 shows the structural elements of a typical design which the present analysis was designed to accommodate.

To validate the many assumptions associated with the analysis, a series of tests which were conducted to measure panel frequencies, mode shapes, damping, and response to random acoustic excitation are described. Preliminary results of these experiments are compared with analytically based predictions, and recommendations for further studies are offered.

## STRUCTURAL ELEMENTS



CORRUGATED PLATE THEORY  
(Slide 2)

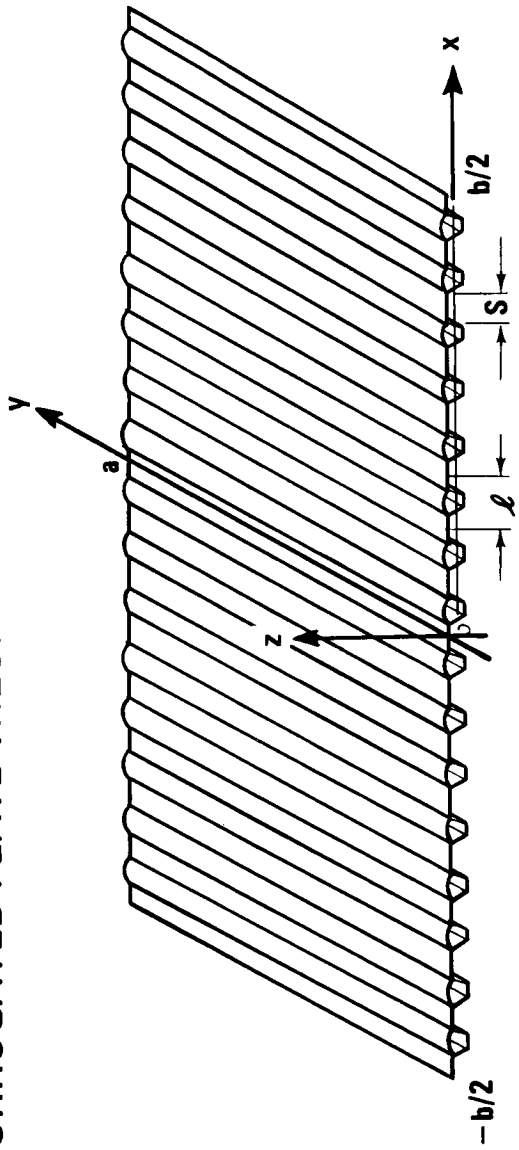
The approximate partial differential equation, derived by Fung (1), governing bending deflections ( $w$ ) of a uniformly corrugated plate is shown in Slide 2, with EI and GJ being beam stiffness properties for a single corrugation, of pitch  $\lambda$ , directed parallel to the  $y$  axis. The cross-pitch bending stiffness is  $K$  which is taken here to be equal to  $\epsilon D$ , where  $D$  is the usual isotropic plate bending stiffness of the cross-sectional material between corrugations and  $\epsilon$  depends upon the details of a single corrugation cross section.

For purposes of the present analyses, the membrane results  $N_x$  and  $N_y$  are assumed to be thermally induced uniform loads while the normal loading  $P$  combines plate inertia as well as random acoustic and static differential pressure loading effects. In addition, the basic plate equation was augmented to include the effects of local mass ( $M_s$ ) and stiffness ( $K_s$ ) as well as continuous stringer ( $m$ , EI) attachments parallel to the  $x$  and  $y$  axes. This was achieved by adding the following terms to the left-hand side of the governing equation

$$\sum_{s=1}^S (K_s - M_s \ddot{w}) \delta(x - x_s) \delta(y - y_s) + \sum_{r=1}^R (\overline{EI}_r \frac{\partial^4 w}{\partial y^4} - m_r \ddot{w}) \delta(x - x_r) + \sum_{q=1}^Q (\overline{EI}_q \frac{\partial^4 w}{\partial x^4} - M_q \ddot{w}) \delta(y - y_q)$$

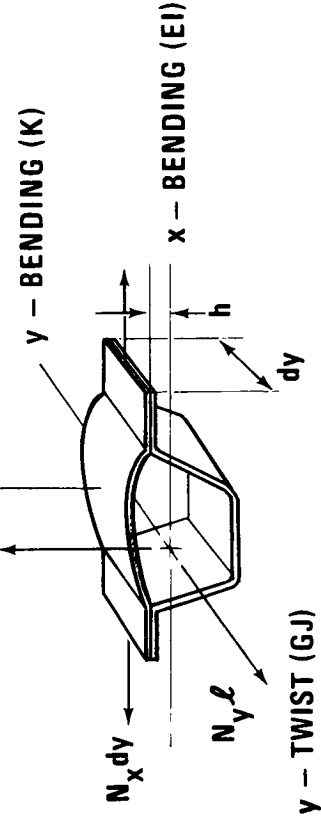
where  $S$ ,  $R$ , and  $Q$  are the number of attachments made at locations  $(x_s, y_s)$ ,  $(x_r)$ , and  $(y_q)$ , respectively, and the  $\delta$ 's are Dirac delta functions.

## CORRUGATED PLATE THEORY



$$\frac{EI}{\ell} \frac{\partial^4 w}{\partial y^4} + K \frac{\partial^4 w}{\partial x^4} + (GJ + D(1-\nu)) \frac{\partial^4 w}{\partial x^2 \partial y^2} - \frac{\partial (N_x \frac{\partial w}{\partial x})}{\partial x} - \frac{\partial (N_y \frac{\partial w}{\partial y})}{\partial y} - h \frac{\partial^2 N_x}{\partial x^2} + h \frac{\partial^2 N_y}{\partial y^2} = P$$

$P\ell dy$



EQUATION SOLUTION  
(Slide 3)

Galerkin's method was used to solve the governing equation through the substitution

$$w = \sum_{i=1}^N w_i \sum_{i=1}^N \beta_i \phi_i (x,y)$$

where each trial function,  $\phi_i$ , was chosen so as to satisfy the geometrical conditions imposed upon  $w$  at the plate's boundaries. After substituting the above series for  $w$ , the resulting equation was alternately multiplied by each of the  $\phi_i$  and integrated over the plate area. This yielded a system of  $N$  second-order ordinary differential equations involving the  $\beta_i$  as functions of time.

Since the rectangular plate tested was symmetrical about an axis contained in the plane of the plate (taken here as the  $y$  axis), simply supported across the corrugations at opposite edges ( $y=0$  and  $a$ ), and free at the remaining edges ( $x=\pm b/2$ ), the trial functions used consisted of an orthogonal symmetric set (about  $x=0$ )

$$\phi_i = \sin \frac{n_i \pi y}{a} \cos \frac{(m_i - 1) \pi x}{b/2}$$

and an orthogonal antisymmetric set

$$\phi_i = \sin \frac{n_i \pi y}{a} \sin \frac{(2m_i - 1) \pi x}{b}$$

For the case of free vibrations, the loading term  $P$  was set equal to the plate inertia. Thus,

$$P = \omega^2 \left( \rho w - I_x \frac{\partial^2 w}{\partial x^2} - I_y \frac{\partial^2 w}{\partial y^2} \right)$$

where  $\rho$  is the plate mass per unit area,  $I_x$  is the mass moment of inertia of the panel per unit surface area about the  $x$ -axis, and  $I_y$  is that about the  $y$  axis which passes through the shear center of each corrugation. This resulted in the symmetric algebraic eigenvalue matrix equation shown in Slide 3 where the elements of each matrix are given in the Appendix.

### EQUATION SOLUTION (Cont)

Solution of the previous equation gives rise to the  $N$  natural frequencies  $\omega_k$  and mode shapes  $\beta_i^k$ , which can then be used to uncouple the governing equations and thus permit the convenient solution of forced modal solutions  $w_k$  where

$$w_k = \sum_{i=1}^N \beta_i^k \phi_i(x,y)$$

and

$$w = \sum_{k=1}^N \xi_k(t) w_k(x,y)$$

The mean square modal response  $\xi_k^2$  to a uniform pressure loading on the plate can then be approximated by that caused by a flat power spectrum  $S_p$  and is (2)

$$\frac{2}{\xi_k} = \frac{\pi}{4\omega_k^3 \zeta_k} \left( \frac{\int w_k dA}{\int \rho_s w_k^2 dA} \right)^2 S_p$$

where  $\zeta_k$  is the modal damping and  $S_p$  is the power spectral density at  $\omega_k$ .

As is common for lightly damped systems with widely separated frequencies, the cumulative cross spectrum density effects are ignored (2) giving

$$\bar{w}^2 = \sum_{k=1}^N \frac{2}{\zeta_k} \frac{w_k^2}{w_k}$$

for the approximate mean square response of  $w$ .

## EQUATION SOLUTION (Cont.)

Similarly, the corresponding RMS strain and acceleration levels, respectively, are given by

$$\overline{\epsilon}_y^2 = \sum_{k=1}^N \frac{\epsilon_y^{(k)2}}{y} \quad \text{and} \quad \overline{\ddot{w}}^2 = \sum_{k=1}^N \overline{\ddot{w}_k}^2$$

where

$$\frac{\epsilon_y^{(k)2}}{y} = \frac{2}{\xi_k^2} \left( z \frac{\partial^2 w_k}{\partial y^2} \right)^2 \quad \text{and} \quad \overline{\ddot{w}_k}^2 = \frac{2}{\xi_k^2} \frac{2}{w_k^2} \omega_k^2$$

## EQUATION SOLUTION

- ASSUMED MODES

$$w = \sum_{i=1}^N w_i$$

- SYMMETRIC

$$w_i = \beta_i \sin \frac{n_i \pi y}{a} \cos \frac{(m_i - 1) 2 \pi x}{b}$$

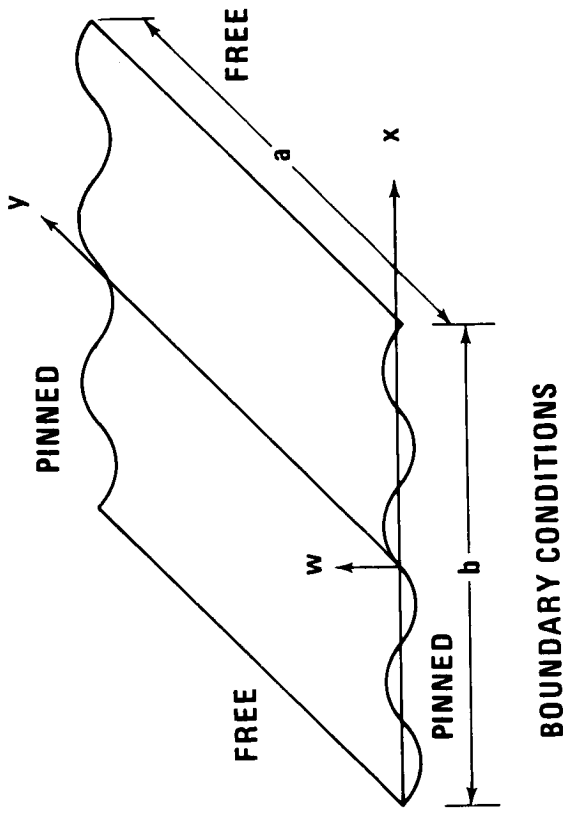
- ANTI-SYMMETRIC

$$w_i = \beta_i \sin \frac{n_i \pi y}{a} \sin \frac{(2m_i - 1) \pi x}{b}$$

- ALGEBRAIC EIGENVALUE PROBLEM

$$\left( [A_i] + [K_{ij}] + [EI_{ij}] \right) \{ \beta \} = \omega^2 \left( [B_i] + [M_{ij}] + [m_{ij}] \right) \{ \beta \}$$

Slide 3

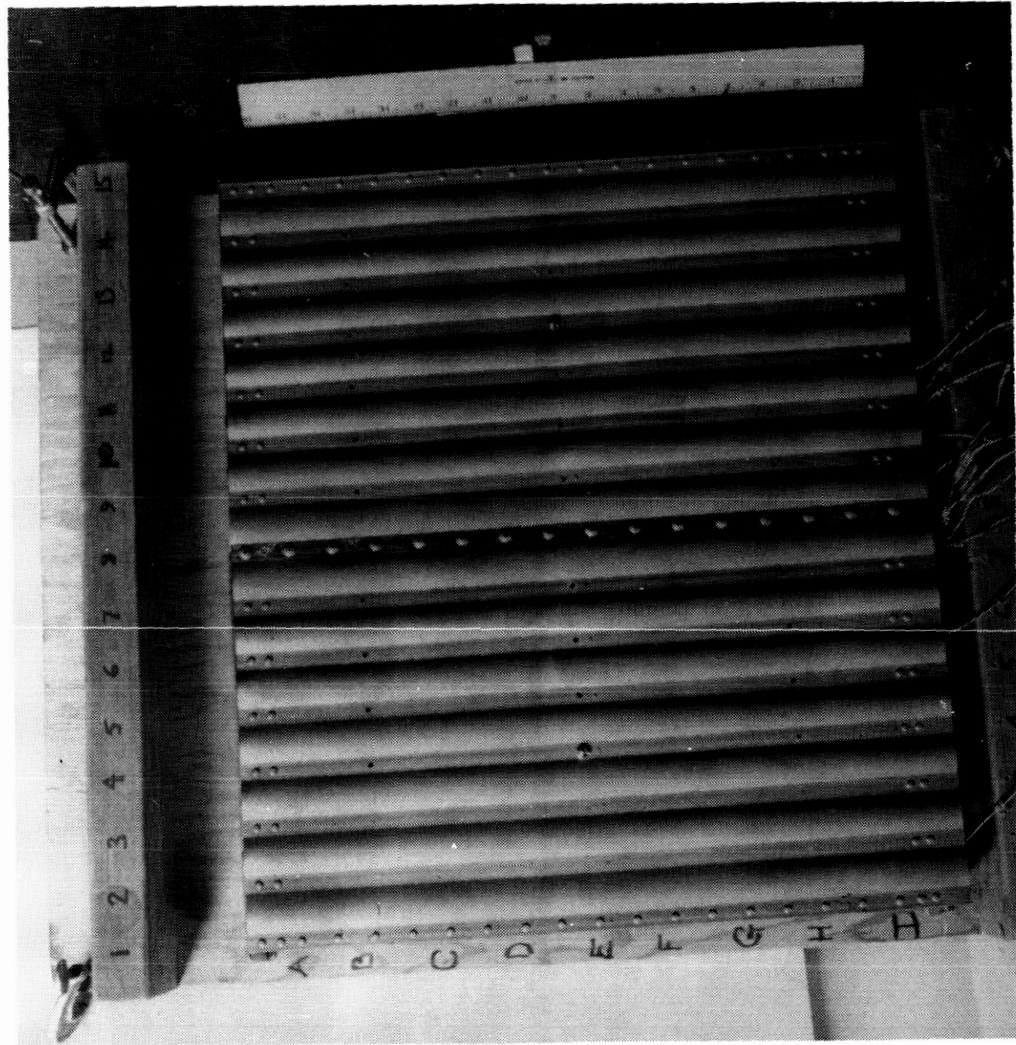


TEST SPECIMEN AND STRAIN GAGE AND ACCELEROMETER LOCATIONS  
(Slides 4 and 5)

Four types of dynamic experiments were performed at room temperature upon a representative segment of a TPS panel; these included frequency sweep, mode survey, exponential decay and random excitation tests. The panel consisted of a 50 x 58 cm (20 x 23 inch) section (Slide 4) of a Haynes-25 corrugation-stiffened, beaded-skin designed to protect primary substructure up to 980°C (1800°F).

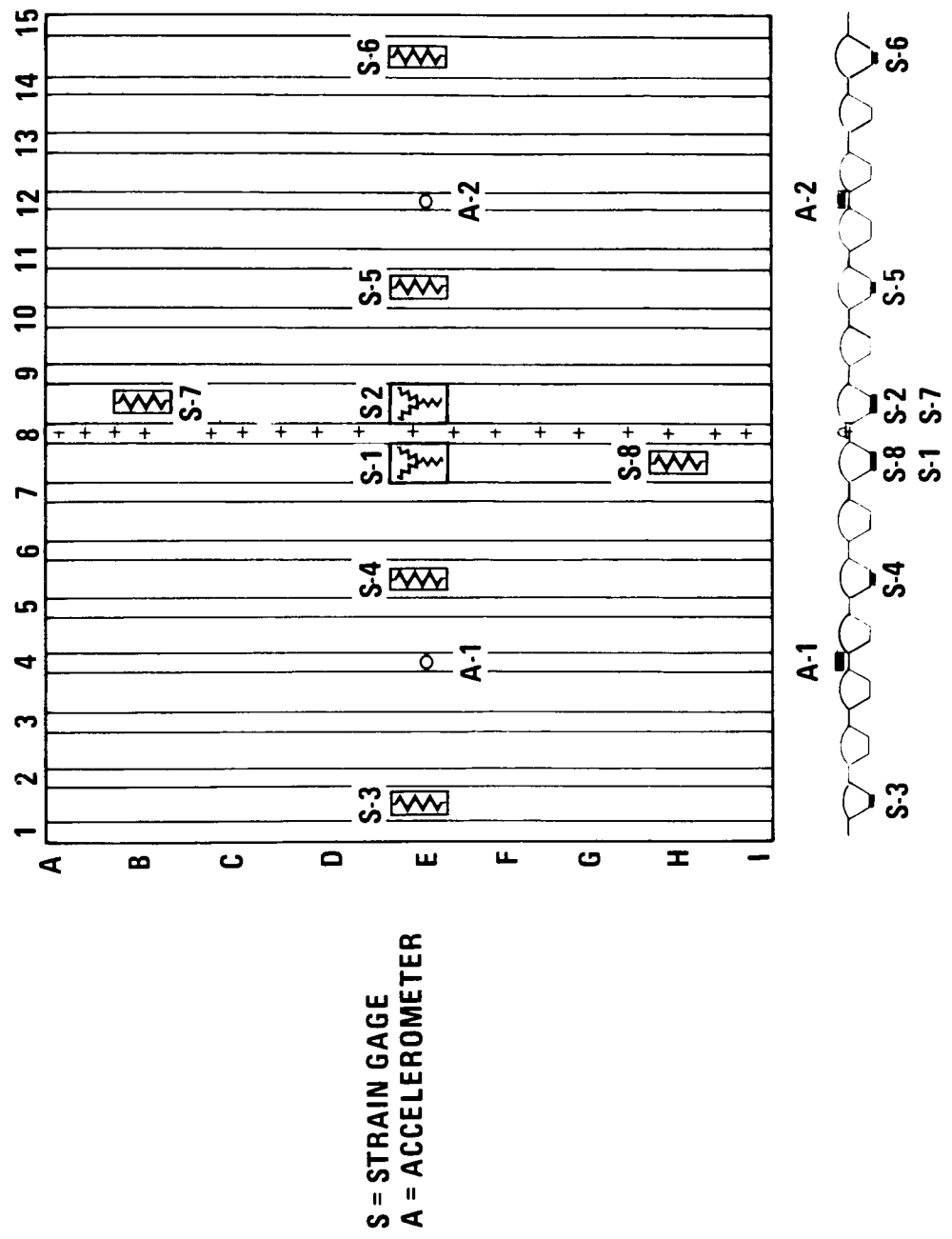
A schematic of the strain gage and accelerometer locations is shown on Slide 5.

TEST SPECIMEN



Slide 4

# STRAIN GAGE AND ACCELEROMETER LOCATIONS



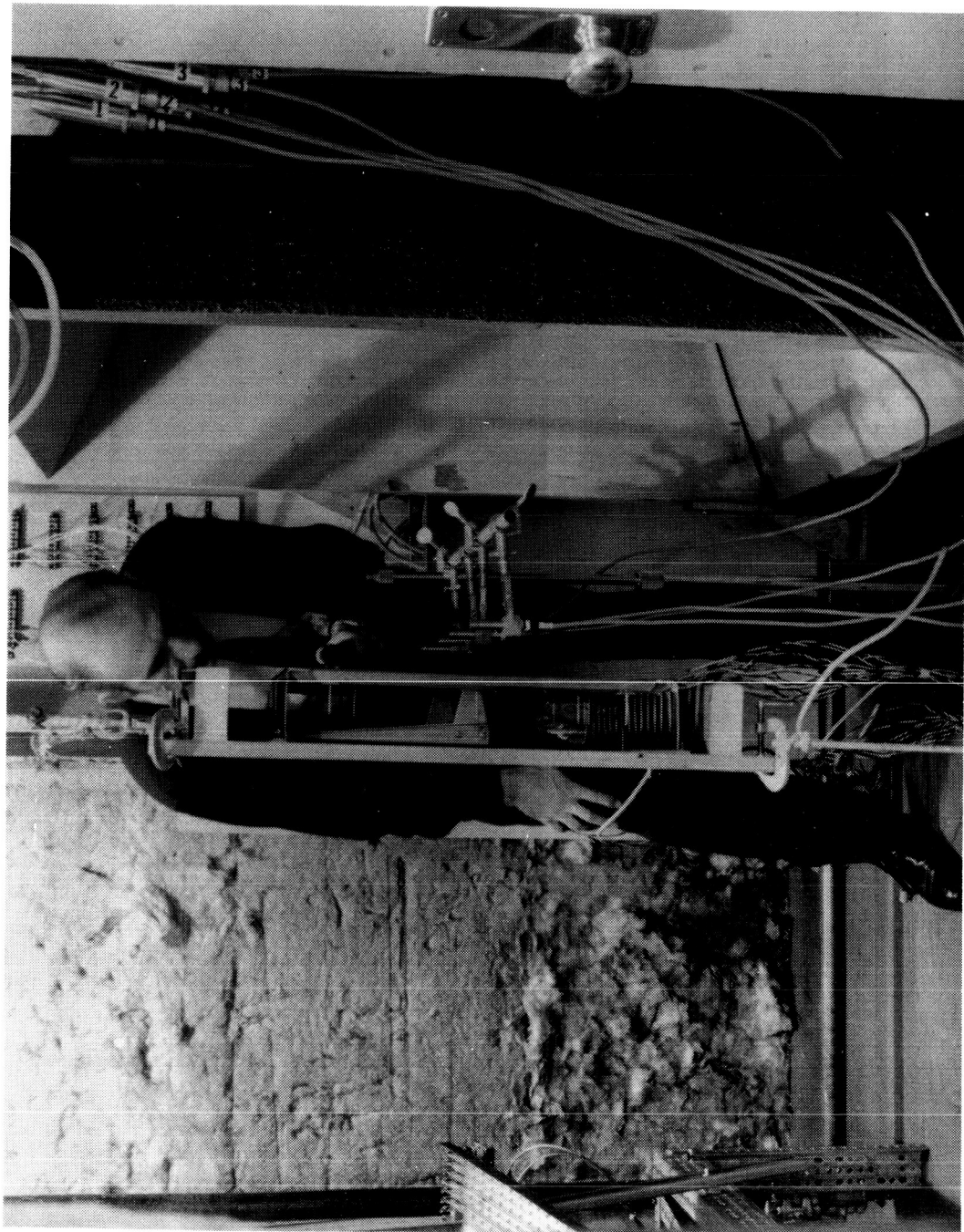
Slide 5

## TEST SETUP IN SONIC CHAMBER

(Slide 6)

The experiments were performed in a sonic fatigue test facility using either low-level acoustic excitation from a speaker or higher level pressures from a horn and air modulator system. To simulate attachment to a rigid substructure, the test article was supported upon a heavily stiffened wood panel which was, in turn, flexibly suspended off shock cords.

## TEST SETUP IN SONIC CHAMBER



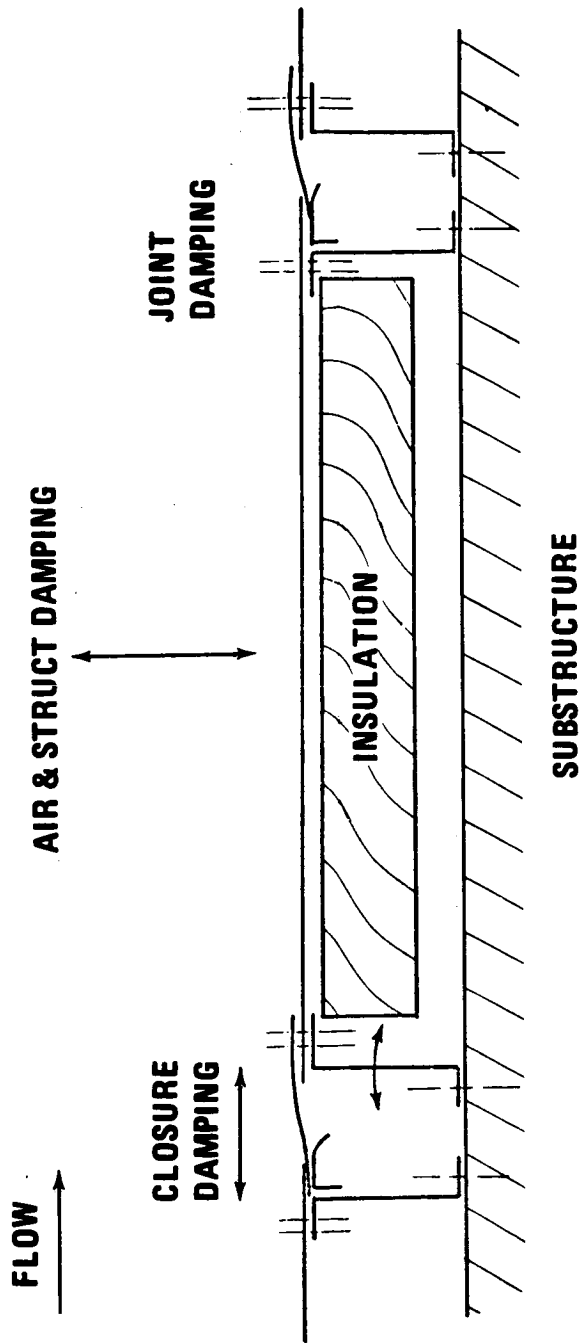
Slide 6

## DAMPING MECHANISMS

(Slide 7)

Tests were conducted both with and without the thermal insulation installed behind the panel and with and without the closure strip, to evaluate damping attributable to each of these items. The thermal insulation blanket consisted of  $48 \text{ kg/m}^3$  ( $3 \text{ lb/ft}^3$ ) density silica fibre (Johns-Manville Microquartz) encapsulated in an Inconel foil envelope with venting holes.

## DAMPING MECHANISMS



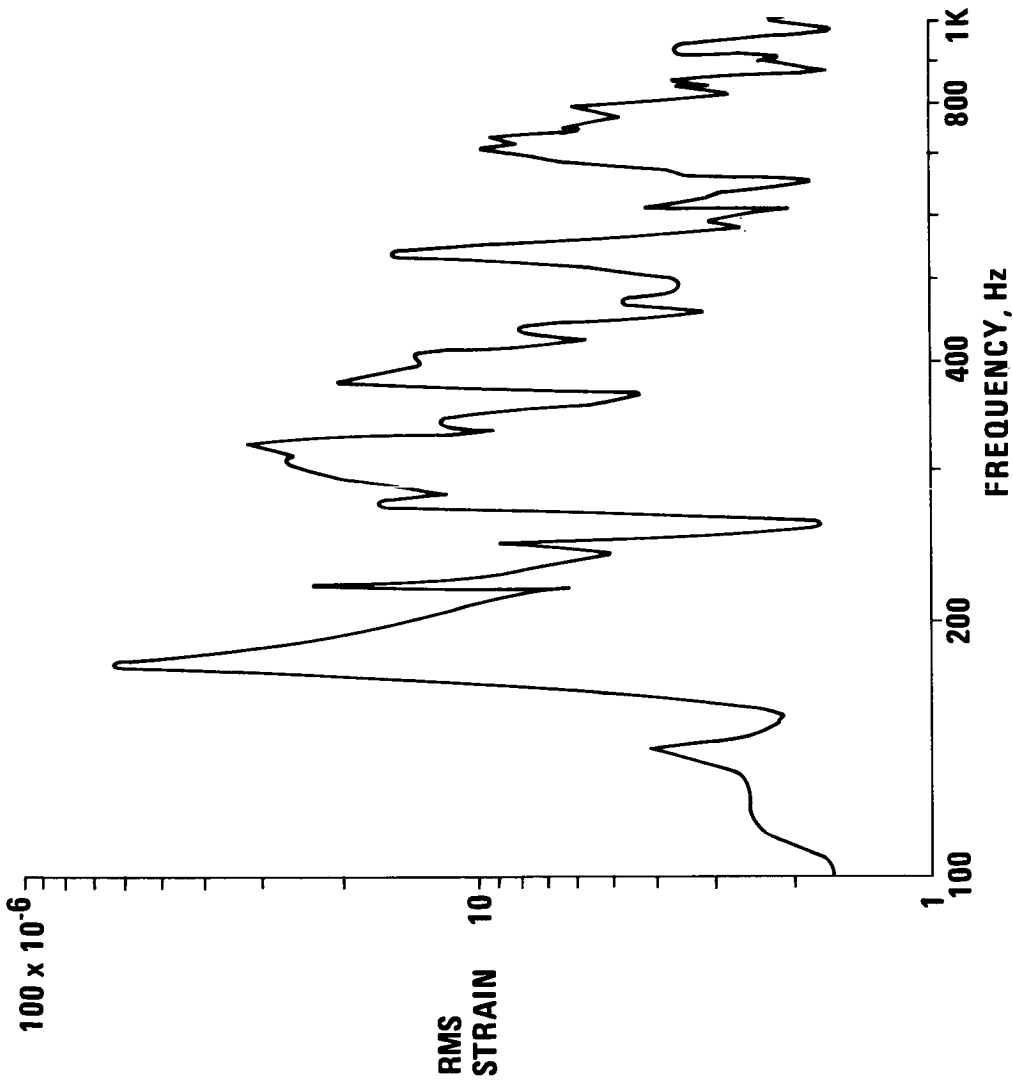
Slide 7

FREQUENCY SWEEP AND MODE SURVEYS  
(Slides 8 and 9)

Sweep tests were used to obtain the frequency response of the specimen when subjected to a constant level sinusoidal pressure. The constant level was maintained using a servo system which averaged sound pressure levels from four microphones over the frequency range swept. Plots of acceleration, strain, and acoustic pressure were obtained over a range of 100 to 1000 Hz. Slides 8 and 9 show typical X-Y recorder plots for a 130-dB sound pressure level sweep.

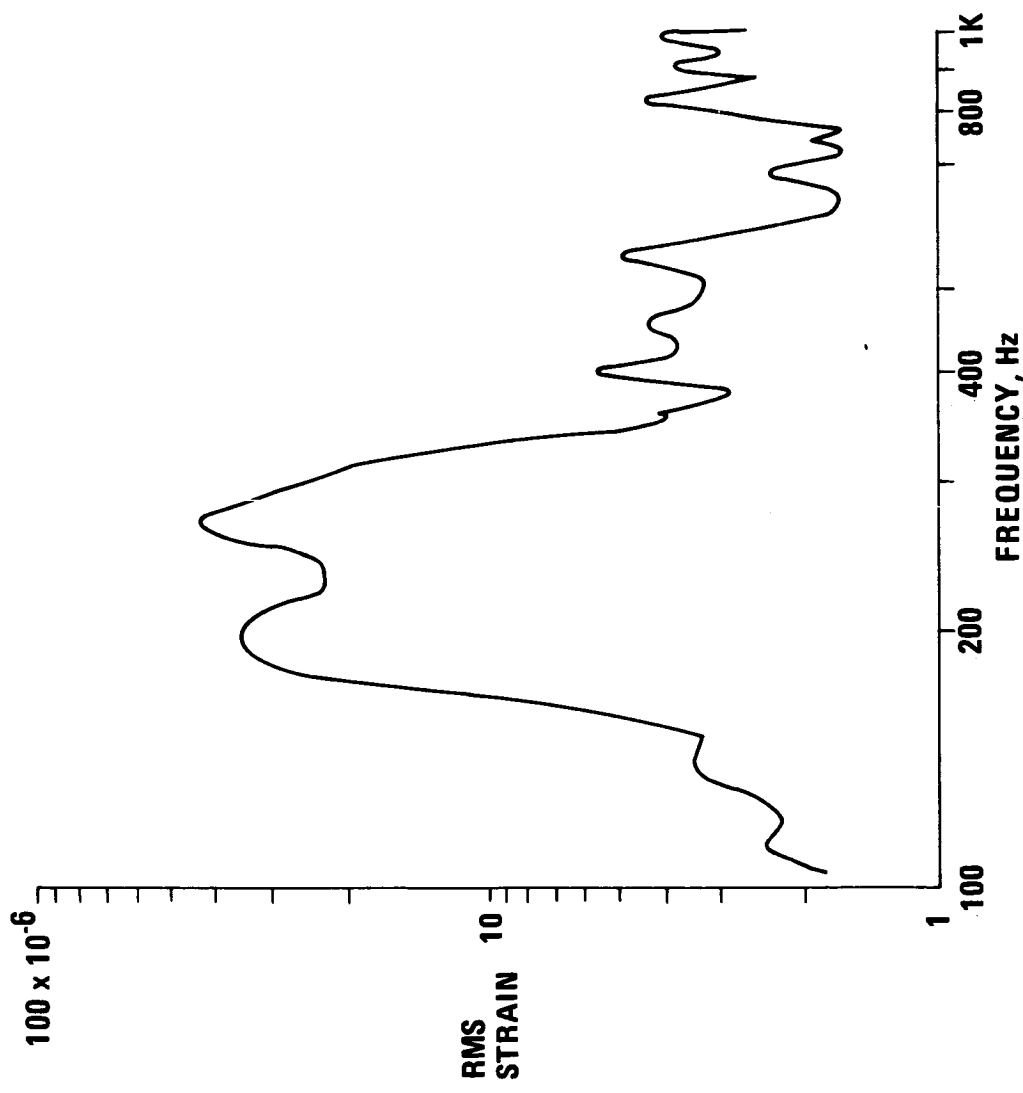
For the mode surveys, acceleration levels at various grid-points on the panel were measured for dominant response frequencies using a hand-held B & K accelerometer probe. A phase meter and oscilloscope were used to obtain relative phase angles between the probe and panel-mounted reference accelerometer.

FREQUENCY SWEEP RESPONSE FOR STRAIN GAGE 2B –  
NO INSULATION – 130 dB SPL REF



Slide 8

FREQUENCY SWEEP RESPONSE FOR STRAIN GAGE 2B –  
INSULATION INSTALLED – 130 dB SPL REF



## DAMPING TESTS

(Slides 10 and 11)

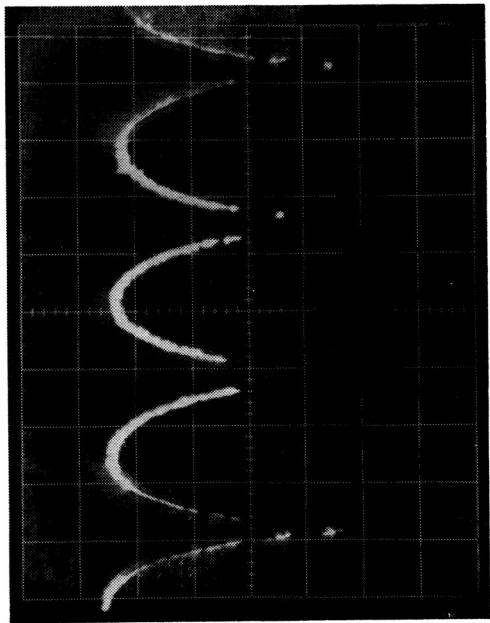
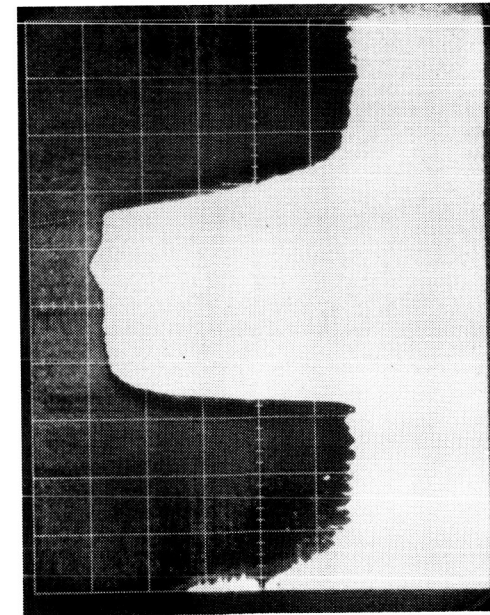
To obtain panel damping, a tone-burst generator, together with an oscillator and speaker, was used to excite the panel in different single dominant modes. The excitation was suddenly removed and the resulting decays of strain gages and accelerometers were recorded on a storage oscilloscope. Photographs (Slide 10) of the damped response were obtained and used to evaluate modal damping. Slide 11 shows a spectral analysis of the recorded output of a typical decay. It indicates that the damping measured is primarily attributable to the mode excited.

## RANDOM TESTS

This test consisted of exciting the panel with random noise using a horn and electro-pneumatic transducers. Accelerometer, strain gage, and microphone outputs were stored on tape using a seven-channel recorder. The tape data was later processed to obtain spectral density plots of the panel excitation and response. Block diagrams for the instrumentation setup for this phase of the program as well as for the frequency sweep, mode survey, and tone burst tests are shown in the Appendix.

## EXPONENTIAL DECAY

OSCILLOSCOPE PHOTOGRAPHS OF STRAIN GAGE 1-B  
RESPONSE TO 181 Hz TONE BURST FOR THE CASE  
OF NO INSULATION



ABSCISSA SCALE: 1 DIV = 0.2 SEC

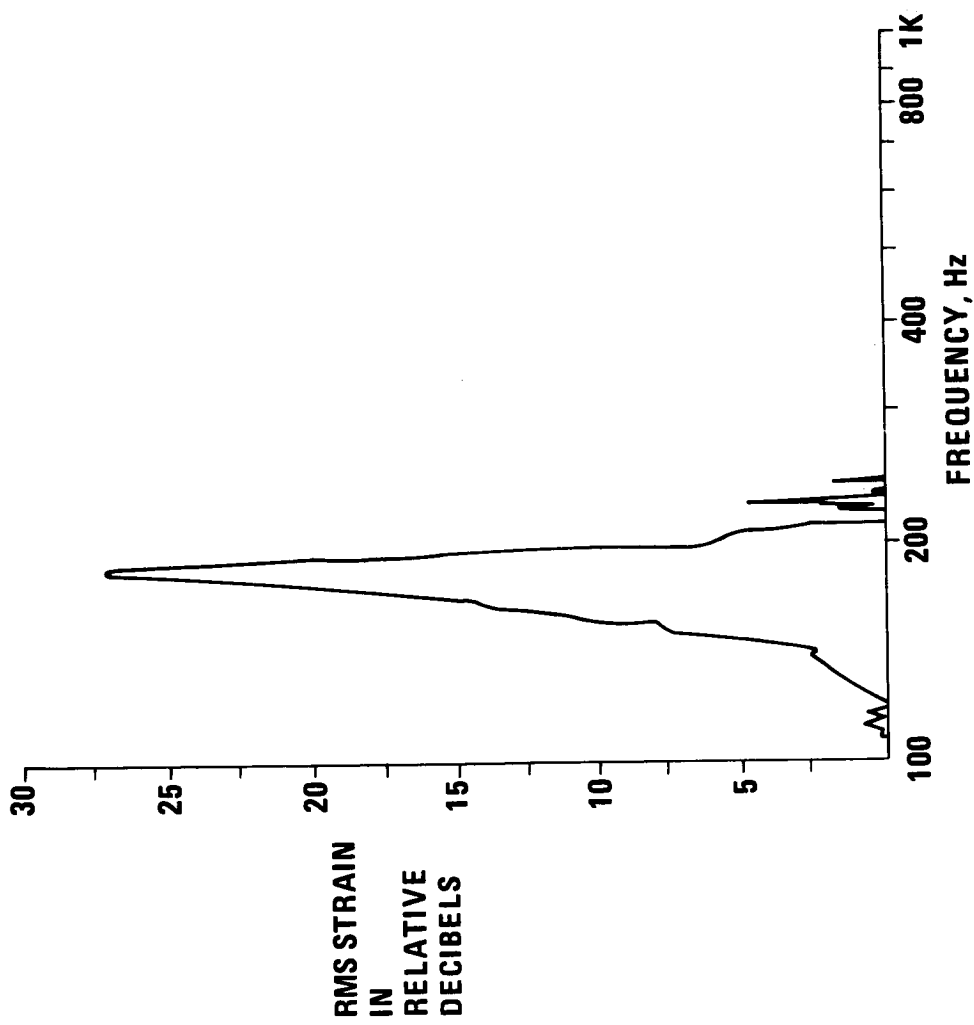
ORDINATE SCALE: 2 DIV = 10 dB

RECTIFIED RESPONSE

ABSCISSA SCALE: 1 DIV = 0.001 SEC

Slide 10

SPECTRAL ANALYSIS OF 179 Hz DECAY FOR STRAIN GAGE 2B  
(TONE BURST EXCITATION AT 179 Hz)



Slide 11

#### POWER SPECTRAL DENSITY ANALYSIS SYSTEM

Power Spectral Density Plots were obtained by using a Hewlett Packard Type 5452A Fourier Analyzer. The analyzer acquired 60 samples of data from the random excitation test, each sample being 0.5 second in duration. A spectral analysis using a 2 Hz bandwidth filter was conducted of each sample, and the results of all 60 spectra were averaged; total sample length was 30 seconds. Limitations on the amount of data recorded necessitated the use of a 25-second tape loop to play back the data. This shortened the length of the time sample somewhat but did not sacrifice good statistical accuracy.

The ratio of the strain spectral density to pressure spectral density was also obtained using the Fourier Analyzer. This calculation yields the square of the magnitude of the transfer function with the acoustic pressure representing the input and the strain representing the output. The acoustic pressure utilized was based upon an average of four microphone measurements taken over the panel surface. This information was stored in the computer. Spectral analyses were performed on strain gage measurements. Output/input ratios were computed and the result was plotted on an X-Y recorder. Results of this data agreed very closely, as to frequency and amplitude, with the frequency sweep results.

FREQUENCY COMPARISONS  
(Slide 12)

The initial program objectives, which included experimental validation of the analysis and measuring panel damping have, thus far, only been partially successful. For example, although the predicted and measured frequencies appear reasonably close (Slide 12), attempts at measuring mode shapes to substantiate the frequency pairing listed have failed to date. Possible reasons for this difficulty may be attributed to multiple or nonsymmetrical mode excitation or unrecognized lack of symmetry in the test specimen. These beliefs are based upon the observation that even though the panel appears symmetrical about the x,z and y,z planes, the measured responses were not.

## FREQUENCY COMPARISONS

TPS PANEL FREQUENCIES, Hz		WITH INSULATION	
TEST	ANALYSIS	ANALYSIS	TEST
NO INSULATION			
179	180	166	145
222	207	194	192
265	—	298	270
325	347	397	400
380	—	422	450
440	454	562	550
470	470	694	680
540	—	758	750
620	635	784	—
710	—	840	830
800	807	864, 883	—
860	890	907	910
915	917	1004	980
1010	1013, 1021	1022	1010

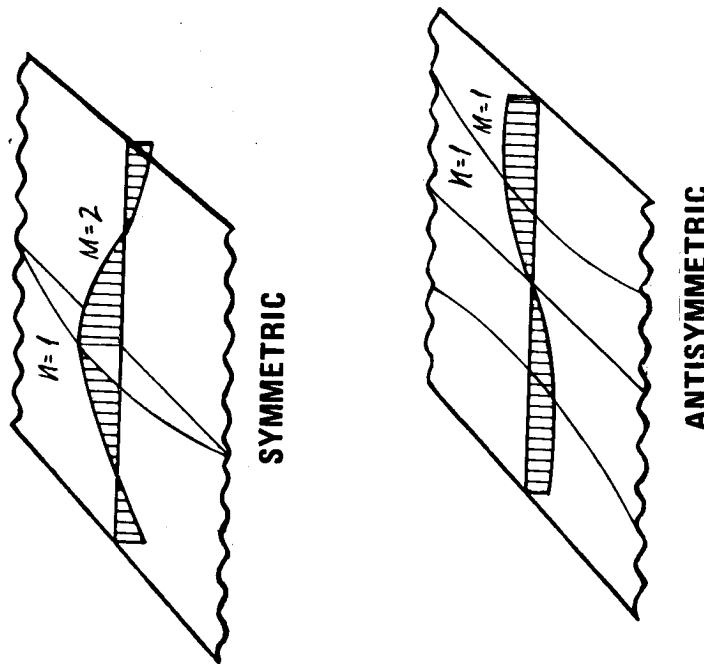
## COMPUTED PANEL FREQUENCIES (UNHEATED AND HEATED)

(Slide 13)

A comparison of analytically computed frequencies for both an unheated and heated case is shown in Slide 13. Note that for the panel design treated, the significant reduction in panel frequencies is almost entirely attributable to the loss in material properties since the panel net compression load in the direction of the corrugations ( $N_y$ ) was only 315 Newtons/m (1.8 lb/in.) and the ratio of hot to cold elastic moduli is 0.40.

## COMPUTED FREQUENCIES, Hz

S	A	70° F	1800° F	70° F	1800° F
174	109			202	127
309	195			407	257
466	295			558	353
713	451			806	506
767	481			879	557
912	574			1000	
974	612			1000	634



Slide 13

## MEASURED DAMPING RESULTS

(Slide 14)

Slide 14 summarizes the average critical damping ratios obtained from decay tests and half-power bandwidth calculations. The most significant result here was the marked increase in response damping once the silica fibre insulation package was attached to the panel. With regard to closure-strip induced damping (caused by Coulomb friction at the edges moving in the plane of the panel), sweep tests run with and without the strip revealed practically no change in the lower frequency response peaks and only a slight attenuating effect in the higher modes.

## MEASURED DAMPING RESULTS

AVERAGE MODAL DAMPING RATIOS, $\xi_{\text{avg}}$					
NO INSULATION			WITH INSULATION		
FREQ, Hz	METHOD	$\xi_{\text{avg}}$	FREQ, Hz	METHOD	$\xi_{\text{avg}}$
179	TONE BURST DECAY SINE SWEEP – 1/2 PWR RANDOM TEST – 1/2 PWR	0.014 0.019 0.020	145	SINE SWEEP – 1/2 PWR RANDOM TEST – 1/2 PWR	0.059 0.050
222	SINE SWEEP – 1/2 PWR RANDOM TEST – 1/2 PWR	0.014 0.013	192	TONE BURST DECAY SINE SWEEP – 1/2 PWR RANDOM TEST – 1/2 PWR	0.042 0.064 0.044
265	TONE BURST DECAY SINE SWEEP – 1/2 PWR RANDOM TEST – 1/2 PWR	0.008 0.012 0.018	270	TONE BURST DECAY SINE SWEEP – 1/2 PWR	0.067 0.062
325	SINE SWEEP – 1/2 PWR RANDOM TEST – 1/2 PWR	0.021 0.014	400	SINE SWEEP – 1/2 PWR	0.028
380	SINE SWEEP – 1/2 PWR RANDOM TEST – 1/2 PWR	0.018 0.016	550	SINE SWEEP – 1/2 PWR RANDOM TEST – 1/2 PWR	0.029 0.020
540	SINE SWEEP – 1/2 PWR RANDOM TEST – 1/2 PWR	0.018 0.015	680	SINE SWEEP – 1/2 PWR	0.033

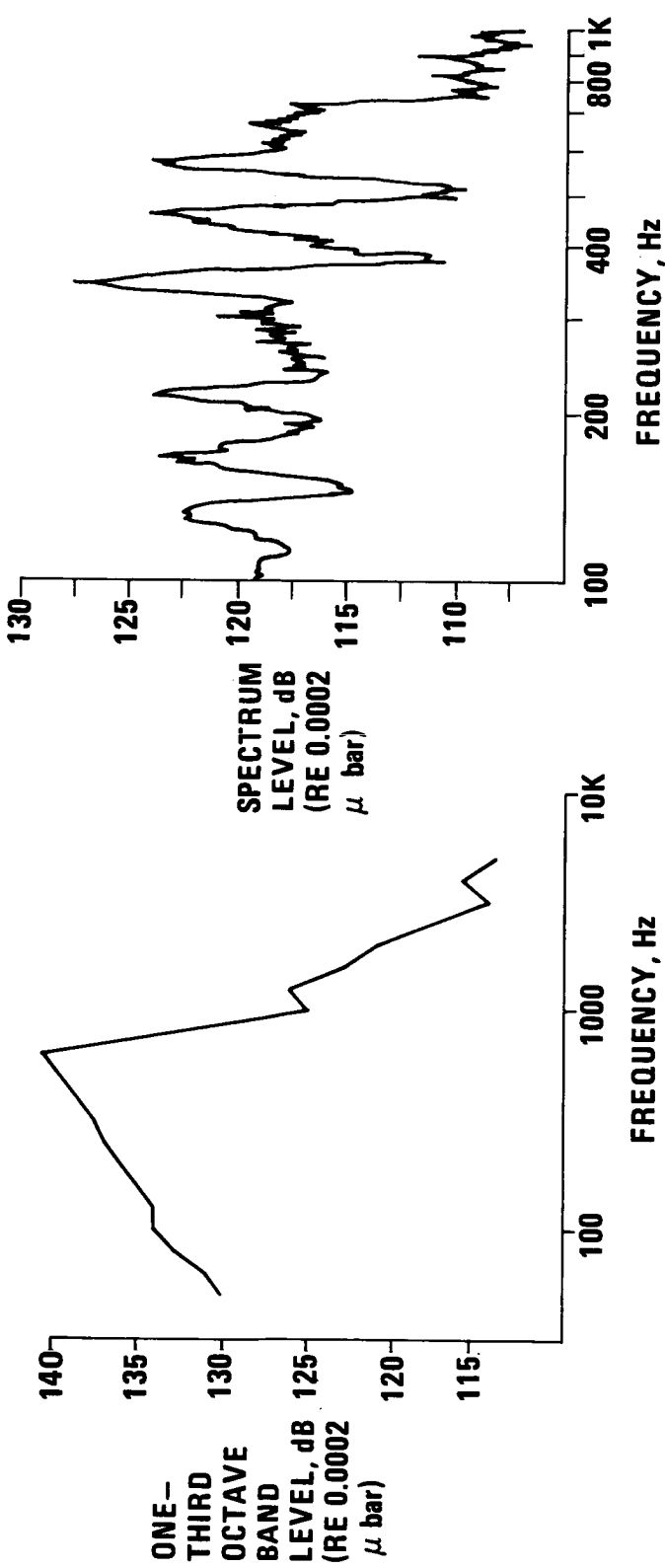
Slide 14

RANDOM TEST EXCITATION SPECTRUM  
(Slides 15 and 16)

The left hand figure of Slide 15 shows the one-third octave band low-level loading spectrum used for the random acoustic tests. However, a two-cycle bandwidth analysis of the same excitation (right hand figure), obtained from averaging four omnidirectional microphone responses located within 8 cm (3 in.) from the panel surface, revealed a pressure distribution that was hardly smooth. Significantly, many of the pressure peaks occur near the panel resonances. This observation, coupled with the fact that the sound level during the sweep tests was exceptionally flat, implies that limitations in the test setup existed. This prevented the application of a smooth random spectrum, unaffected by panel radiation, as is often assumed to result from engine induced noise. The RMS panel stresses for the points measured (Slide 16) were sufficiently low so that they appear safe when linearly scaled up to more realistic launch levels if other effects (such as stress concentration and static pressure differential) are not important.

## RANDOM EXCITATION SPECTRA

ONE-THIRD OCTAVE BAND LEVELS OF THE  
AVERAGE OF 4 MICROPHONES – RANDOM  
EXCITATION TEST



Slide 15

## RMS PANEL STRESS

RANDOM EXCITATION (OVERALL SOUND PRESSURE LEVEL)		3 X RMS STRESS LEVELS - MN/m <sup>2</sup> (PSI)* (SEE SLIDE 5 FOR LOCATIONS)						
		\$1	\$2	\$3	\$4	\$5	\$7	\$8
<b>148 dB MEASURED</b>		38.7 (5,610)	54.2 (7,860)	15.4 (2,241)	24.6 (3,570)	35.8 (5,190)	38.7 (5,610)	29.6 (4,290)
<b>162 dB LINEARLY EXTRAPOLATED</b>		193.4 (28,050)	271.0 (39,300)	77.2 (11,205)	123.1 (17,850)	179.0 (25,950)	193.4 (28,050)	147.9 (21,450)

\*MATERIAL ENDURANCE LIMIT AT ROOM TEMP. = 413.7 MN/m<sup>2</sup> (60,000 PSI)

## CONCLUSIONS AND RECOMMENDATIONS

The effect furnished by adding the insulation blanket to the vibrating panel was to increase the damping substantially over that caused by the other structural, radiation, and seal strip damping mechanisms. In addition, the projected stresses, at anticipated liftoff excitation levels, appear adequately low for the configuration tested.

The analytical procedure presented herein was primarily directed at accommodating recent Grumman TPS designs. Thus, the orthogonal trial functions selected would not be appropriate for panels which are entirely point supported or panels with elastic edge conditions. This is not to say that the existing technique could not be suitably modified. However, the complexities of such modifications would have to be evaluated in light of the convenience in developing and applying the existing formulation. Note, however, that the reasonable correlation with frequency results makes extension of the present approximate idealization appear suitable for flutter stability analyses since the aeroelastic system eigenvalues (like frequency) represent integrated panel parameters.

With regard to additional work, further effort is required to explain the experimentally determined modal deflection patterns. The tone-burst and half-power bandwidth techniques used for measuring panel damping appear convenient for unheated panels. However, difficulties will arise for panels at high temperatures since the capabilities of available instrumentation possess thermal limitations.

## APPENDIX

The following equations define the elements of the matrices introduced in the analysis:

$$A_i = d_i \left[ \frac{EI}{\lambda} \alpha_i^4 + K \gamma_i^4 + \left( \frac{GJ}{\lambda} + D(1-\nu) \right) \alpha_i^2 \gamma_i^2 + N_x \gamma_i^2 + N_y \alpha_i^2 \right]$$

$$B_i = d_i \left[ \rho + I_x \gamma_i^2 + I_y \alpha_i^2 \right]$$

$$K_{ij} = \sum_{s=1}^S K_s \phi_i(x_s, y_s) \phi_j(x_s, y_s)$$

$$M_{ij} = \sum_{s=1}^S M_s \phi_i(x_s, y_s) \phi_j(x_s, y_s)$$

$$\overline{EI}_{ij} = \sum_{r=1}^R (\overline{EI})_r e_{ij} \alpha_i^2 \alpha_j^2 \psi_i(x_r) \psi_j(x_r) + \sum_{q=1}^Q (\overline{EI})_q f_{ij} \gamma_i^2 \gamma_j^2 \chi_i(y_q) \chi_j(y_q)$$

$$\overline{m}_{ij} = \sum_{r=1}^R m_r e_{ij} \psi_i(x_r) \psi_j(x_r) + \sum_{q=1}^Q m_q f_{ij} \chi_i(y_q) \chi_j(y_q)$$

where  $\alpha_i = n_i \pi/a$ ,  $d_i = a b (1 + \delta_{m_i,1})/4$ ,  $e_{ij} = a \delta_{n_i, n_j}/2$ ,  $f_{ij} = b (1 - \delta_{m_i,1}) \delta_{m_i, m_j}/2$

## APPENDIX (cont.)

$$\text{and } \gamma_i = 2(m_i - 1) \pi/b, \quad \psi_i = \cos \gamma_i x, \quad \chi_i = \sin \alpha_i y$$

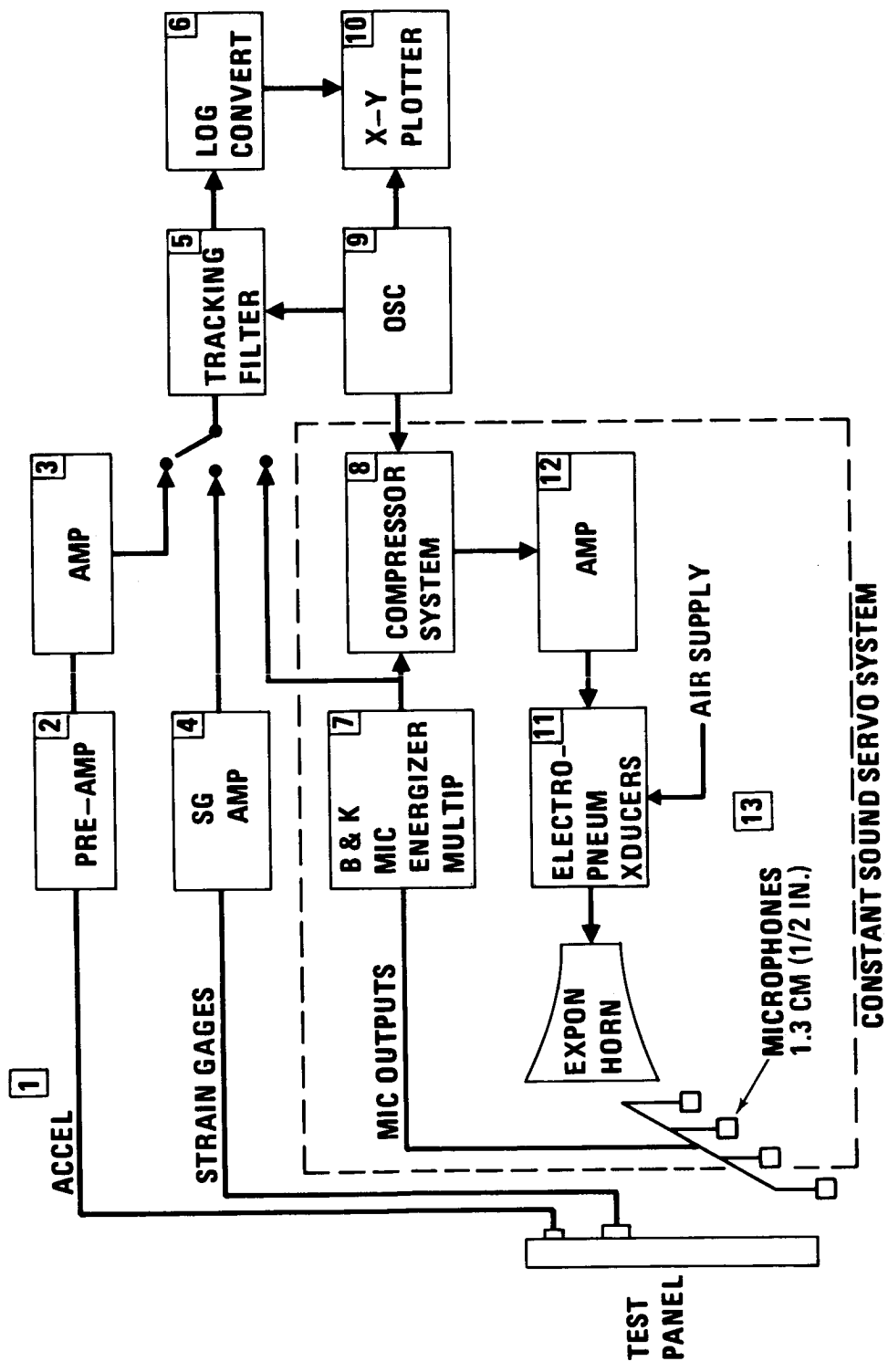
for the symmetric about the y axis panel response, but

$$\gamma_i = (2m_i - 1) \pi/b \quad \text{and} \quad \psi_i = \sin \gamma_i x$$

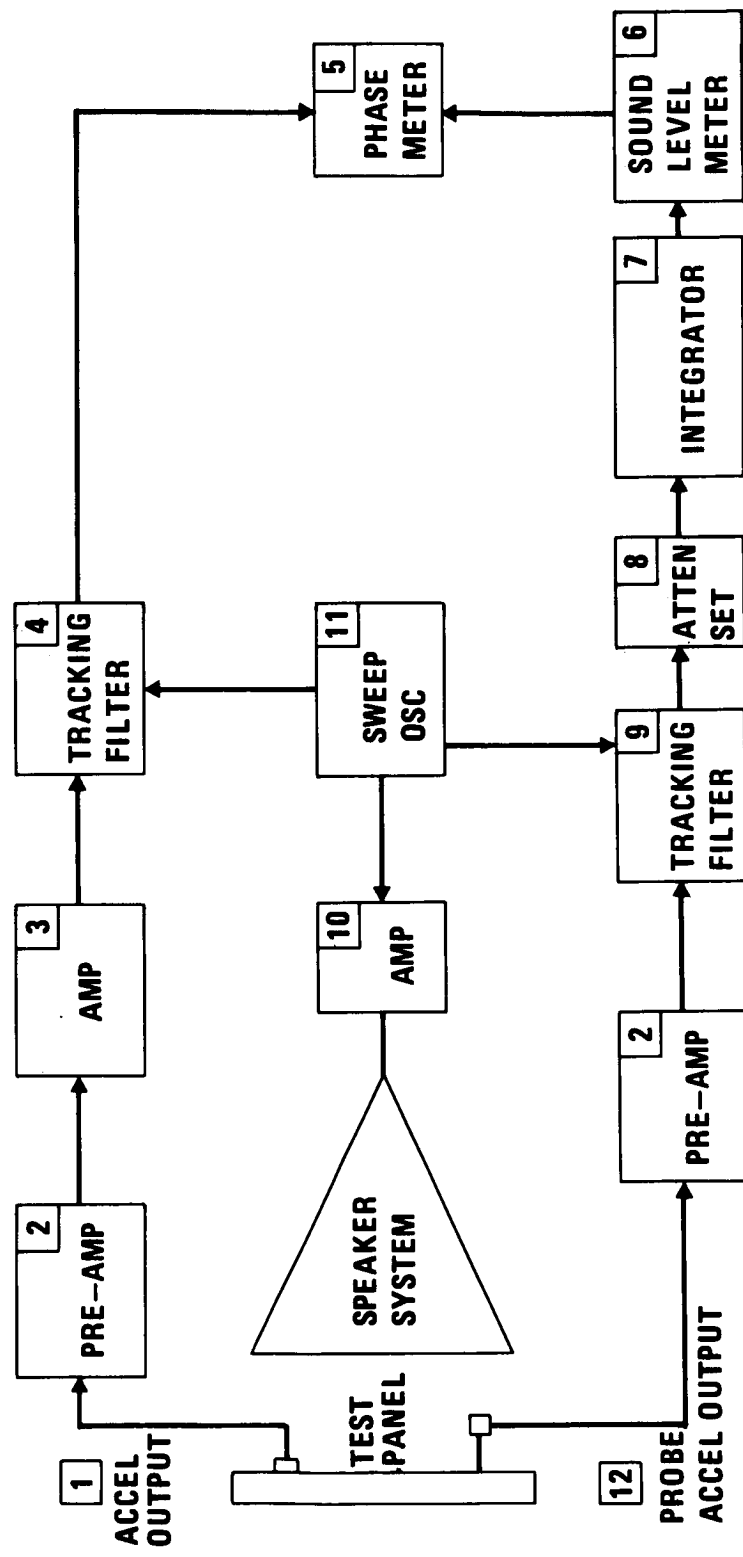
for the antisymmetric about the y axis panel response

Block diagrams of equipment used in performing the frequency sweeps, mode surveys, tone burst, and random excitation tests are shown in slides 17 to 20.

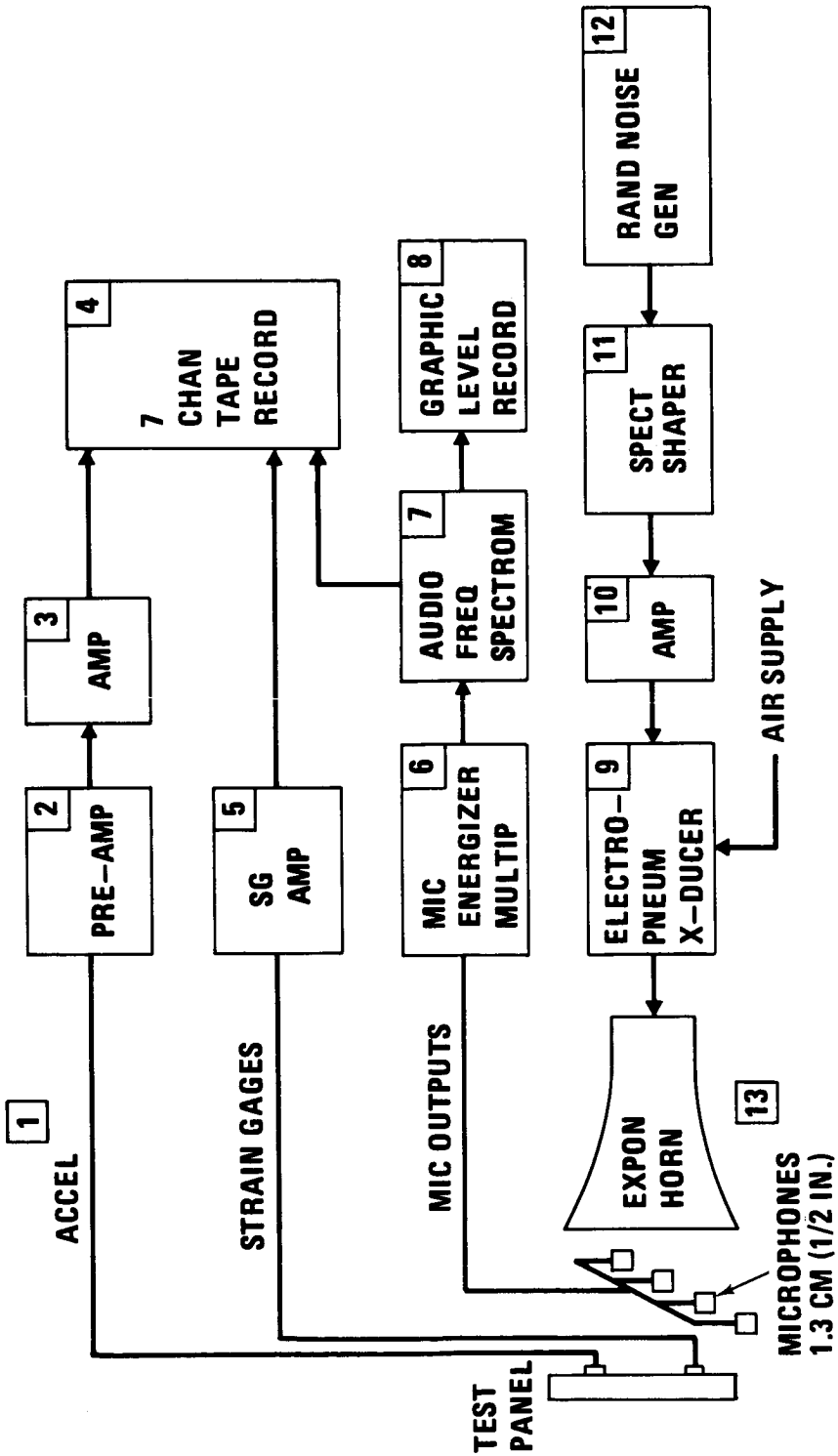
## CONSTANT SOUND LEVEL FREQUENCY SWEEP BLOCK DIAGRAM



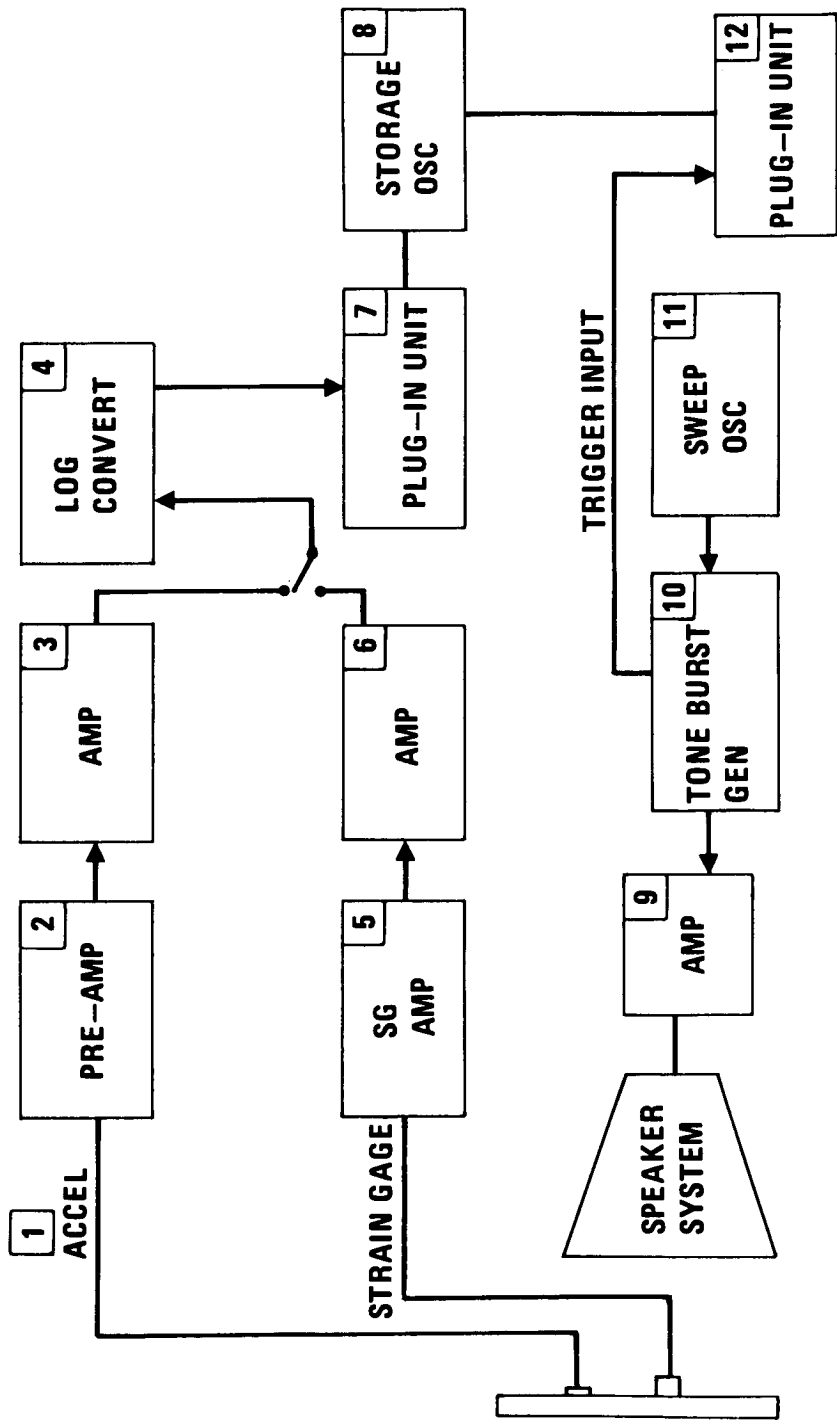
## MODE SURVEY BLOCK DIAGRAM



## RANDOM EXCITATION BLOCK DIAGRAM



## TONE BURST TEST BLOCK DIAGRAM



#### REFERENCES

- (1) Fung, Y. C., "On Corrugation-Stiffened Panels," Graduate Aeronautical Laboratories, California Institute of Technology AFOSR Report 3122, June 1962.
- (2) Harris, C. M. and Crede, C. E., "Shock and Vibration Handbook," Vol. 3, McGraw-Hill Book Co., New York, 1961.

## SPACE SHUTTLE LIQUID DYNAMICS

By Frank M. Bugg  
NASA George C. Marshall Space Flight Center, Marshall Space Flight Center, Ala.

and

Norman S. Land  
NASA Langley Research Center, Hampton, Va.

### INTRODUCTION

Study of the space shuttle orbiter and booster has indicated potential propellant dynamics problem areas which are either new or more severe than the same type problems on earlier space vehicles. Work being done in four of these potential problem areas will be discussed in this paper.

Increased knowledge of the combined propellant dynamics in tanks and feedlines and dynamics of the vehicle, tank walls, pumps, and engines is needed because their combination will be more complex in the shuttle configuration than for the Satlurns. New information is required for description of liquid dynamics in propellant tanks tilted at angles of  $0^{\circ}$  to  $90^{\circ}$  from the total body force vector. Damping of propellant motion must be accomplished while keeping damping device weight to a minimum.

Large amplitude propellant motion, such as might occur during separation or docking, must be defined. A study of propellant feedline dynamics will be discussed first.

## PROPELLANT FEEDLINE DYNAMICS

(Slide 1)

The purpose of this study is to develop the capability to analyze the effects of several factors on the dynamics of propellant feedlines. The effects of steady turbulent flow compared to steady laminar flow are of interest as well as the effect of the mean flow velocity. Changes in the system response due to distributed compliances, such as bubbles of gas or vapor in the flowing propellant or the flexibility of the propellant line, wall should be understood. Determination of the effect of bellows, side branches, large stationary bubbles, and other local compliances is important. The effect of coupled responses between line and structure caused by forced changes of line length or the stiffness of the mounting of line to other structure is also studied.

Other factors of interest are the effect of liquid density and compressibility, effect of line wall mass and radial stiffness, the effect of bends, and the effect of local flexibilities, such as gauges and their lines.

Most of these effects have been treated separately in other studies so that the primary goal here is to include all of these factors in one computer program.

# **PROPELLANT FEEDLINE DYNAMICS**

**THE PURPOSE OF THIS STUDY IS TO DEVELOP A COMPUTER PROGRAM TO  
ANALYSE BOTH THE SEPARATE AND COMBINED EFFECTS ON FEEDLINE  
DYNAMICS OF THE FACTORS BELOW.**

- 1. STEADY, TURBULENT FLOW.**
- 2. DISTRIBUTED COMPLIANCES (BUBBLES, FLEXIBLE WALL).**
- 3. LOCAL COMPLIANCES (BUBBLES, BELLOWs, SIDE BRANCHES).**
- 4. COUPLED RESPONSES BETWEEN LINE AND STRUCTURE  
(MOUNTING STIFFNESS, FORCED LINE LENGTH CHANGES).**

## EFFECT OF BUBBLE LOCATION

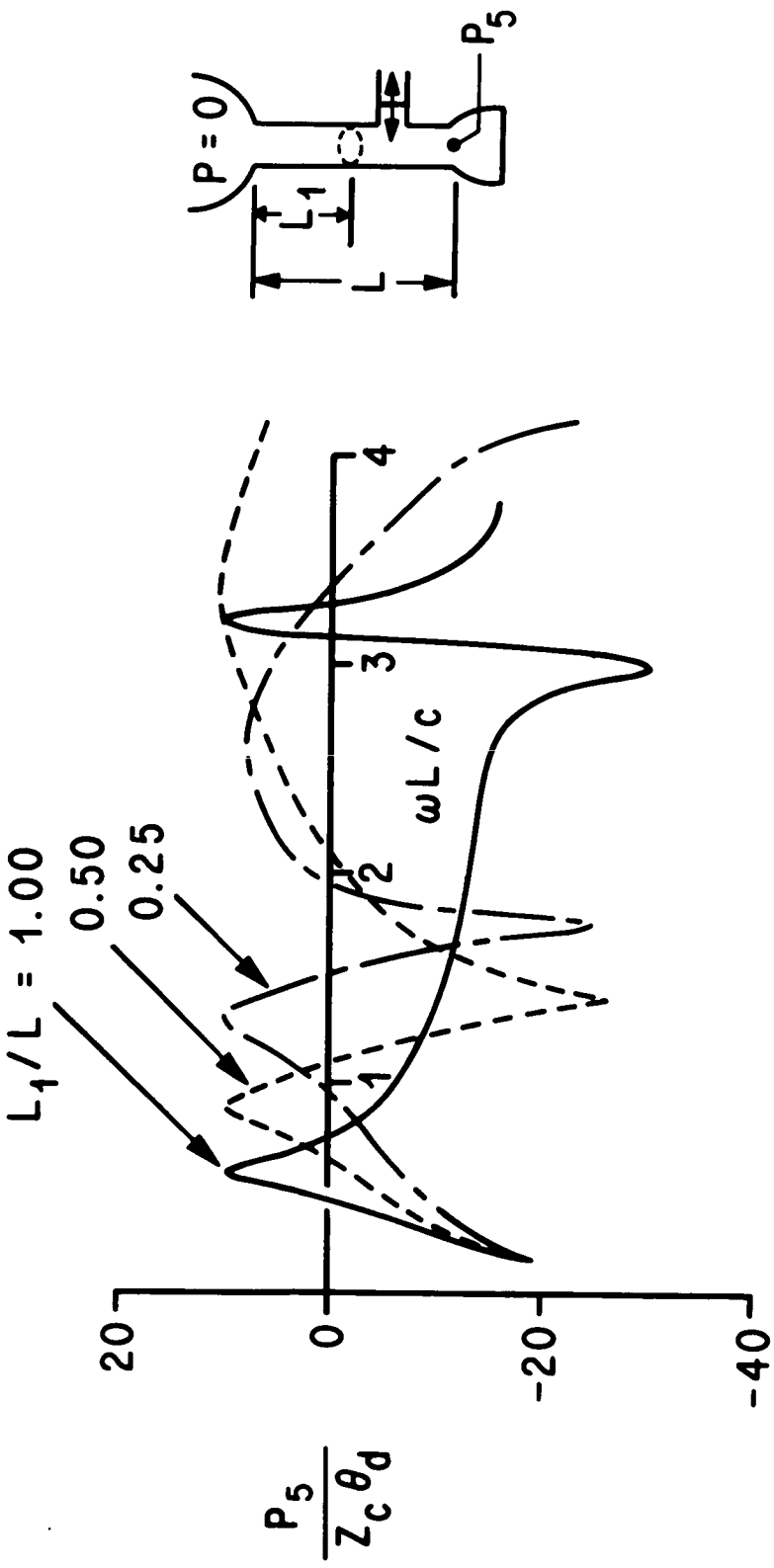
(Slide 2)

The results of an example problem are shown in this slide. The sketch shows the system being considered, a straight feedline of length  $L$  connecting the propellant tank to the pump inlet. A pulser is in the line and a bubble is located distance  $L_1$  from the tank. The pressure  $P$  in the tank is zero, and the pressure at the pump inlet is  $P_5$ . The graph shows a parameter representing pump inlet

pressure  $\frac{P_5}{Z_c \theta_d}$  as a function of pulser frequency parameter, where  $\omega$  is the pulser frequency and  $c$  is the velocity of sound, for three bubble locations.

In addition to the change in frequency of the first resonance, the change in bubble location is seen to affect the shape of the second peak. Curves such as these might be useful for determining bubble location from experimental data.

# EFFECT OF BUBBLE LOCATION

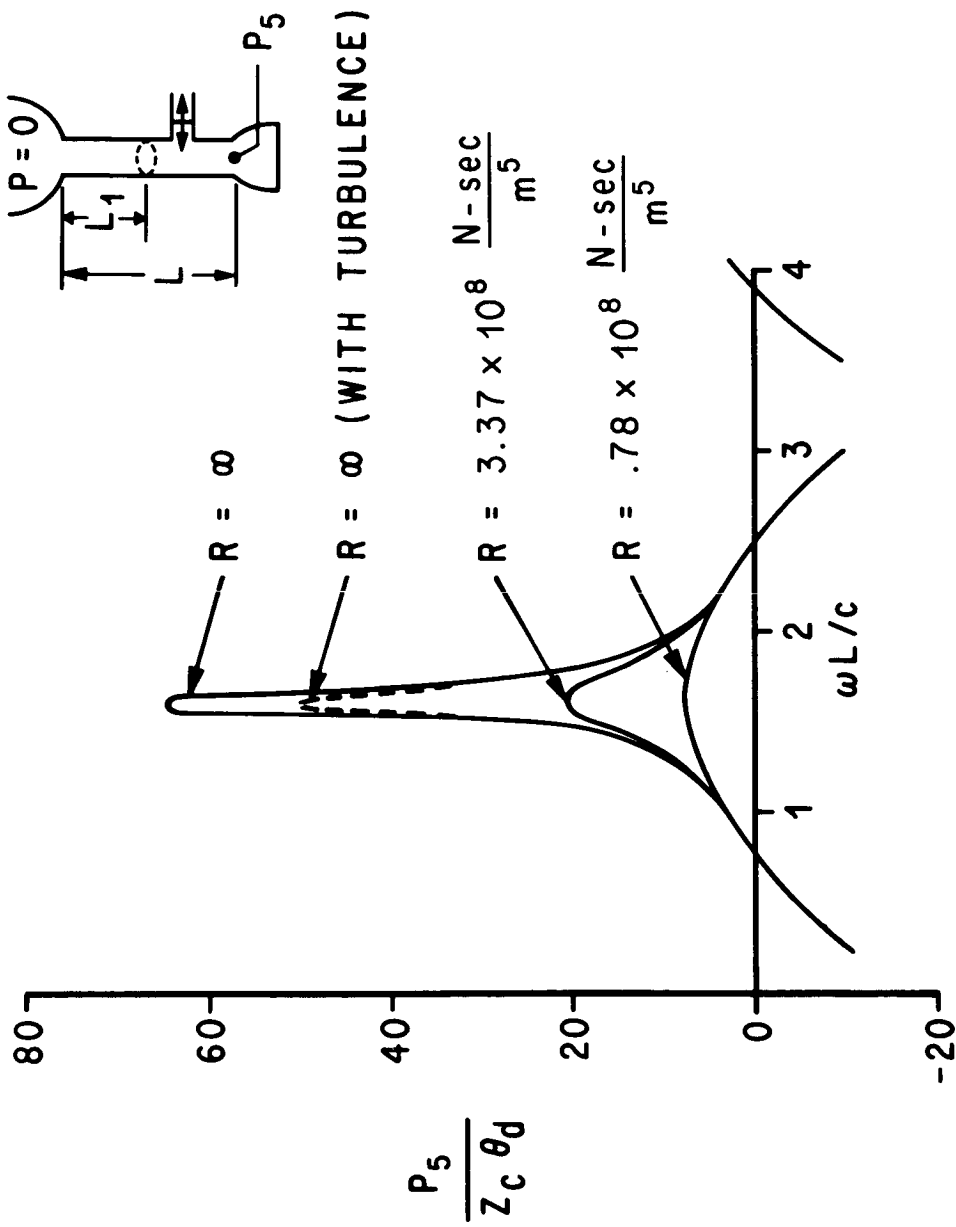


EFFECT OF TURBULENT FLOW

(Slide 3)

The results of another example problem are shown in this slide. The sketch is the same as for the previous slide, but the bubble effects are not considered. The pump inlet pressure versus the pulser frequency is shown for different values of flow resistance  $R$  downstream of the pump inlet and with and without turbulence. For the case of infinite resistance, the effect of turbulence is to reduce the pressure pulse transmitted to the pump inlet by the pulser compared to that transmitted through still liquid. The value  $.78 \times 10^8 \frac{\text{N-sec}}{\text{m}^5}$  was computed to be representative of the resistance of a typical J-2 pump, injector, and engine.

# EFFECT OF TURBULENT FLOW



## RESULTS

(Slide 4)

Other results of this study are summarized here. The line resistance appears negligible compared to the pump inlet resistance for typical systems. The mean flow effect may be neglected so long as the mean flow velocity is small compared to the fluid sonic velocity. A reasonable equation has been found for calculation of sonic velocity in a liquid with distributed bubbles. The damping due to a large bubble appears small compared to the pump inlet damping. The effect of the mass of an elastic propellant line wall is negligible. The effects of forced vibration of the pump end of straight and bent lines have been found.

Thus far in the study no surprising results have been found. The methods of determining the effects mentioned have been incorporated into the total computer program.

## *RESULTS*

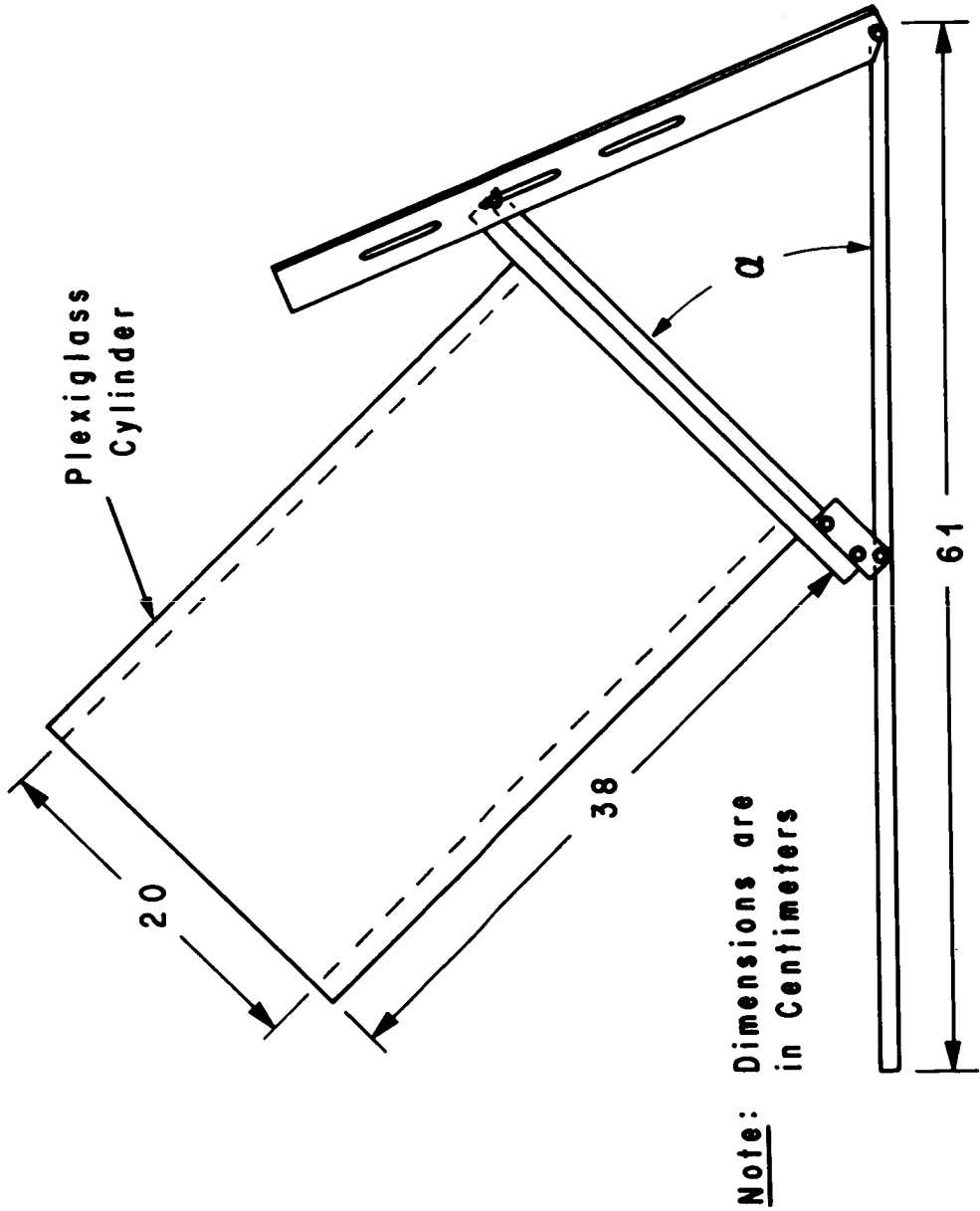
1. DAMPING IN THE LINE IS NEGLIGIBLE COMPARED TO THE PUMP INLET RESISTANCE FOR TYPICAL SYSTEMS.
  2. THE MEAN FLOW EFFECT MAY BE NEGLECTED SO LONG AS THE MEAN FLOW VELOCITY IS MUCH LESS THAN THE FLUID SONIC VELOCITY.
  3. AN EQUATION HAS BEEN INCORPORATED FOR CALCULATION OF SONIC VELOCITY IN A LIQUID WITH DISTRIBUTED BUBBLES.
  4. THE DAMPING DUE TO A LARGE BUBBLE APPEARS SMALL COMPARED TO THE PUMP INLET DAMPING.
  5. THE EFFECT OF WALL MASS IS NEGIGLIBLE.
  6. THE EFFECTS OF VIBRATION OF THE TERMINAL END OF STRAIGHT AND BENT LINES HAVE BEEN FOUND.
- SUMMARY - NO UNEXPECTED EFFECTS HAVE BEEN FOUND. EACH EFFECT HAS BEEN INCORPORATED INTO THE TOTAL COMPUTER PROGRAM.**

## TEST SETUP

(Slide 5)

This is a sketch of the apparatus used in the second study to be discussed, a short experimental investigation of the effect on liquid oscillation frequency of tilting the tank axis relative to the total acceleration vector. Shuttle propellant tanks might be tilted  $10^\circ$  during launch and at much higher angles during high angle of attack fly-back. The apparatus consisted of a plexiglass right circular cylindrical tank, 20 cm in diameter and 38 cm tall, attached to an aluminum frame which held the tank at the desired tilt angle,  $\alpha$ . The test liquid used was water with a wetting agent added. The liquid oscillation was excited by rocking the tank in the direction desired, and the frequency was determined by measuring the time required for 50 cycles of oscillation.

# TEST SET-UP



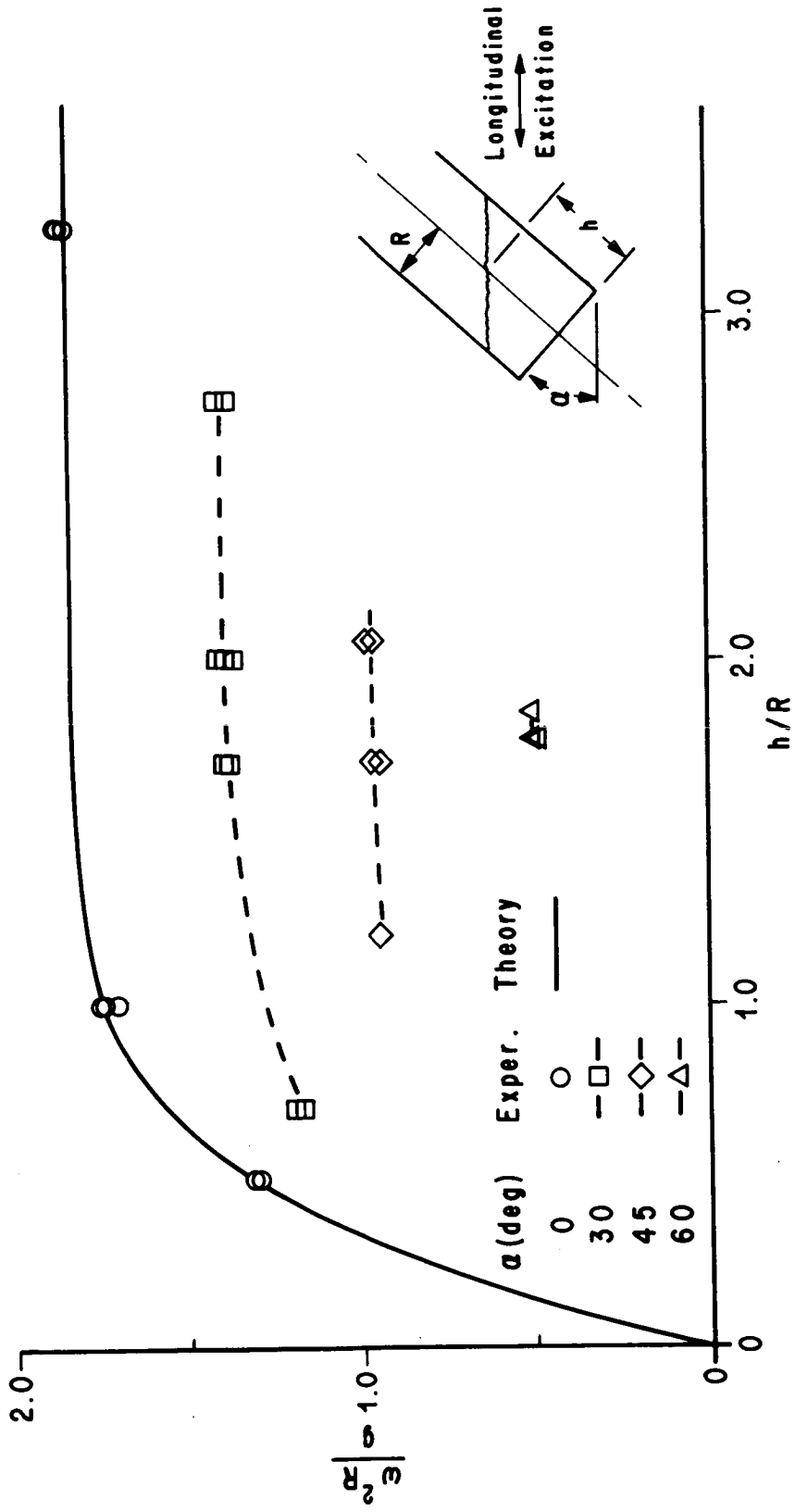
## EFFECT OF LIQUID DEPTH AND TILT ANGLE ON LONGITUDINAL FREQUENCY

(Slide 6)

The longitudinal direction is defined in the sketch and the lateral direction discussed later is  $90^\circ$  from this in a horizontal plane. The frequency parameter, frequency  $\omega$  squared times the tank radius  $R$  divided by the acceleration of gravity  $g$ , is shown as a function of nondimensional liquid depth for four values of tilt angle,  $\alpha$ .

The solid line represents theoretical values for an upright ( $\alpha = 0^\circ$ ) circular cylinder and the experimental values for  $\alpha = 0^\circ$  agree well with the theory. Tilting the tank reduced the frequency so that at  $\alpha = 60^\circ$  the frequency parameter was 27% of the value for an upright cylinder. With the tank tilted, there was very little effect on the frequency of changes in liquid depth as long as the liquid surface did not contact the tank bottom. The appearance of the oscillation was, however, affected by the nearness of the tank bottom. With the surface very near the tank bottom, a geyser of liquid formed at the overhanging tank wall and fell back into the surface once each cycle.

# EFFECT OF LIQUID DEPTH AND TILT ANGLE ON LONGITUDINAL FREQUENCY



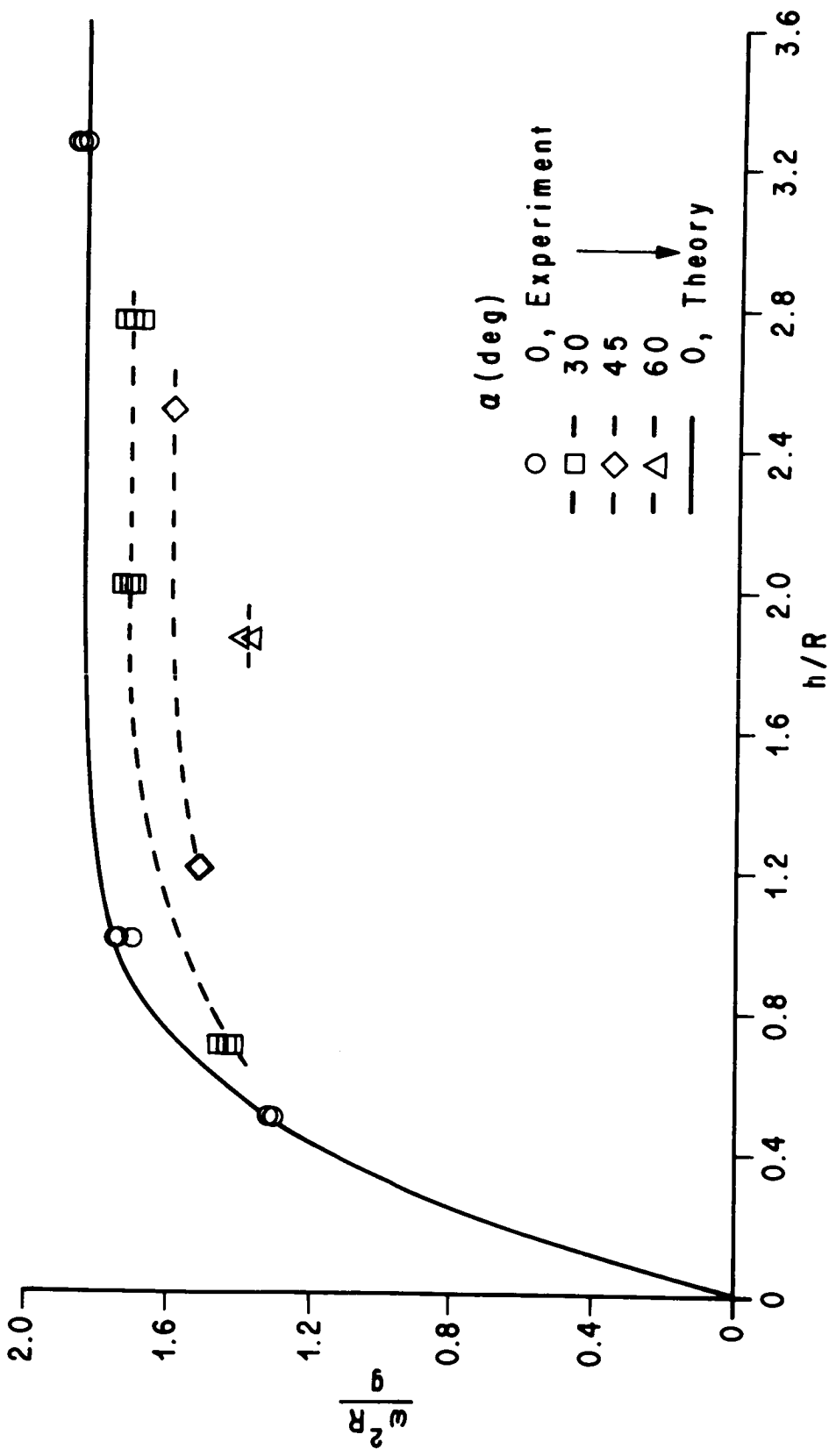
## EFFECT OF LIQUID DEPTH AND TILT ANGLE ON LATERAL FREQUENCY

(Slide 7)

Again the frequency parameter is presented as a function of nondimensional liquid depth for tilt angles of  $0^\circ$ ,  $30^\circ$ ,  $45^\circ$ , and  $60^\circ$ . The lateral oscillation gives a mode which has its node line along the major axis of the elliptical free surface. The effect of tank tilt on frequency parameter is seen to be much less for lateral oscillations than for longitudinal. The value of the frequency parameter at  $\alpha = 60^\circ$  is 75% of that for  $\alpha = 0^\circ$ . The lateral mode did not exhibit any obvious differences in appearance due to liquid depth as did the longitudinal mode. The locus of maximum amplitudes for the lateral mode appeared to be the two cylinder elements one cylinder diameter apart, measured horizontally. Because of this motion along the tilted elements, the lateral mode might contribute forces in both the lateral and longitudinal directions.

Further studies are being made to determine experimentally the forces exerted by these sloshing modes and the damping. Also, frequency is being measured in tilted tanks of different cross-section shapes.

EFFECT OF LIQUID DEPTH AND TILT ANGLE  
ON LATERAL FREQUENCY



## FLEXIBLE RAFFLE MODEL TEST CONCLUSIONS

The third portion of this presentation concerns flexible baffles. Prior studies have indicated that flexible baffles give more damping than rigid baffles of equal size at typical boost slosh amplitudes. Flexible baffles can be constructed lighter than rigid baffles of the same size and should, therefore, be considerably more efficient in terms of damping provided per unit baffle weight. Flexible baffle advantages should be checked in cryogenic liquid and in large scale tanks. As a result of these model tests, an engineering study is now in progress to determine what materials are suitable for fabrication of flexible baffles to be used in cryogenic liquid and to generate design data for use in selecting the proper flexible baffle configuration for particular applications. Another result of this study will be the design of flexible baffle attachment systems.

## FLEXIBLE BAFFLE MATERIAL SELECTION

Some of the materials considered were Mylar, Kapton, Teflon FEP, Kel-F, and aluminum. All of these passed fatigue tests at temperatures lower than that of liquid oxygen. None were flexible at liquid hydrogen temperature.

Mylar showed a tendency to react (a charring of the material) when subjected to the standard liquid oxygen compatibility impact test (98.1 m-N impact in a liquid oxygen environment). The sensitivity of Kapton was found to vary with thickness. Teflon FEP, Kel F, and a few other heavily fluoreinated compounds appear to be the least sensitive to liquid oxygen of the nonmetallic materials considered.

Calculations of baffle thickness required for adequate strength of the baffle edge nearest the tank axis for typical slosh conditions indicated that the plastics are more likely to be flexible enough to improve the damping than the aluminum.

Tests in a 76-cm-diameter tank with liquid nitrogen have shown that flexible baffles of Kapton and Teflon FEP give about 30% more damping than rigid baffles of the same size for a particular set of sloshing conditions.

## FLEXIBLE RAFFLE DESIGN CURVES

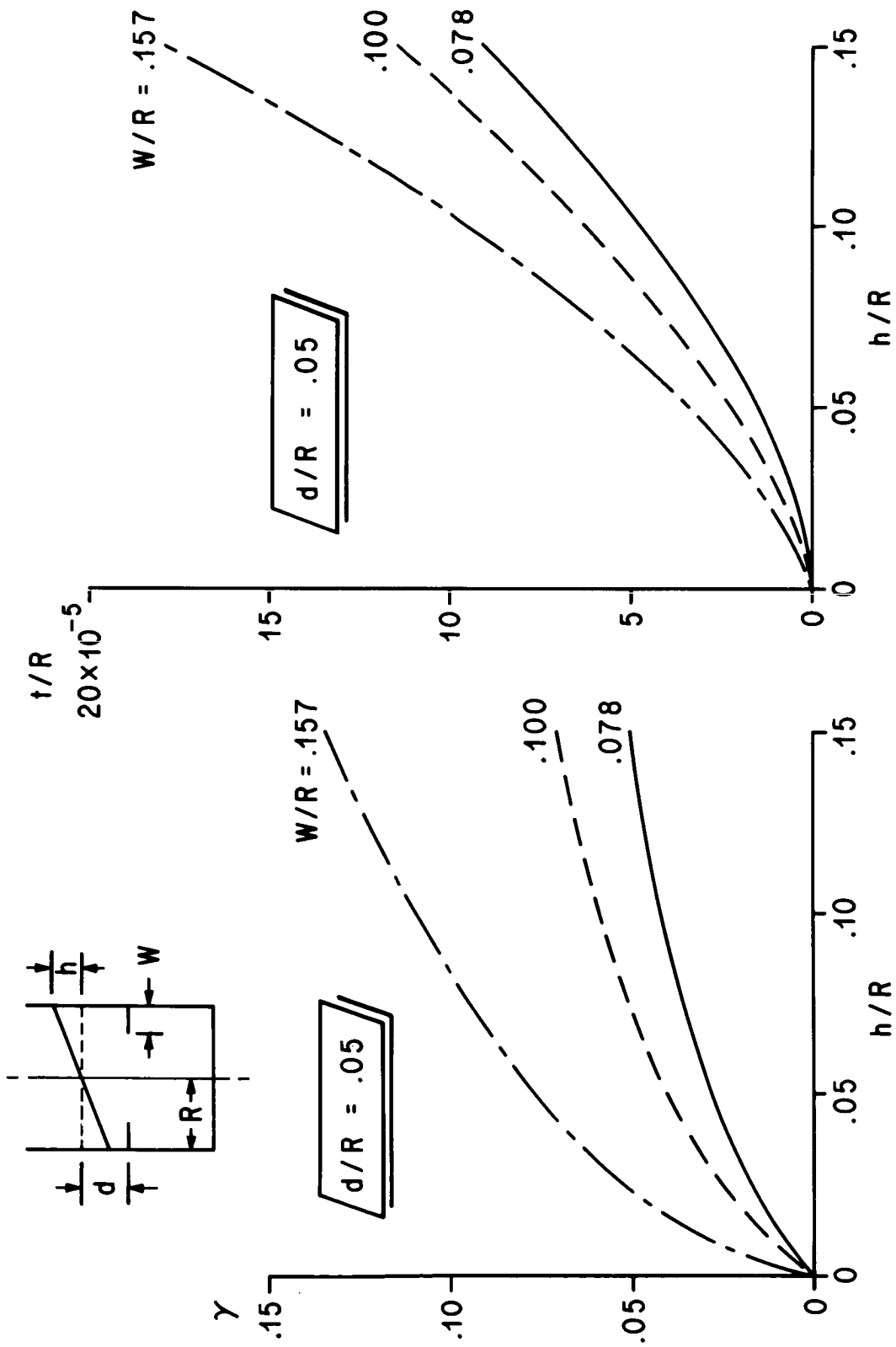
(Slide 8)

These curves are typical of those used to determine baffle width required to give a specified damping and to determine baffle thickness required for adequate strength. The plot at the left shows damping ratio  $\gamma$  as a function of nondimensional sloshing amplitude for three baffle widths  $W$ . Both plots are for a baffle depth  $d$  to tank radius  $R$  ratio equal to .05. The plot at the right gives baffle thickness  $t$  required as a function of amplitude  $h$  and baffle width based on an allowable stress of half the Teflon FEP yield stress.

The damping required and the amplitude expected are normally specified for a particular application. With this information, the baffle width required is chosen from curves such as those at the left and the baffle thickness required is then chosen from curves such as those at the right.

When the present study of flexible baffles has been completed, the results will be used to select a flexible baffle system for testing in a 3.96 m diameter tank with liquid nitrogen as the test liquid.

## FLEXIBLE BAFFLE DESIGN CURVES (TEFLON FEP)



## PROPELLANT DYNAMICS DURING DOCKING

The purpose of this last study is to develop the capability to determine the forces exerted by a propellant on its tank walls for large amplitude, aperiodic propellant flow. This capability is needed for proper analysis of propellant motion in shuttle vehicle tanks at engine cut-off, separation (especially under abort conditions), and docking.

## SIMPLIFIED MARKER AND CELL

The Simplified Marker and Cell computer code, SMAC, developed at Los Alamos Scientific Laboratory was chosen as the basis of the computer program to be developed. This code uses a finite difference technique to solve the equations of liquid motion for incompressible, viscous, two-dimensional, transient flow. The solution utilizes an Eulerian grid mesh with the liquid configuration represented by Marker particles which move with the liquid.

An important addition which was made to the basic program is a method of analyzing the flow along curved boundaries. This is accomplished by an iterative technique of computing the pressure and velocity, treating the boundary as a free surface. A method of including surface tension effects has also been added to the program.

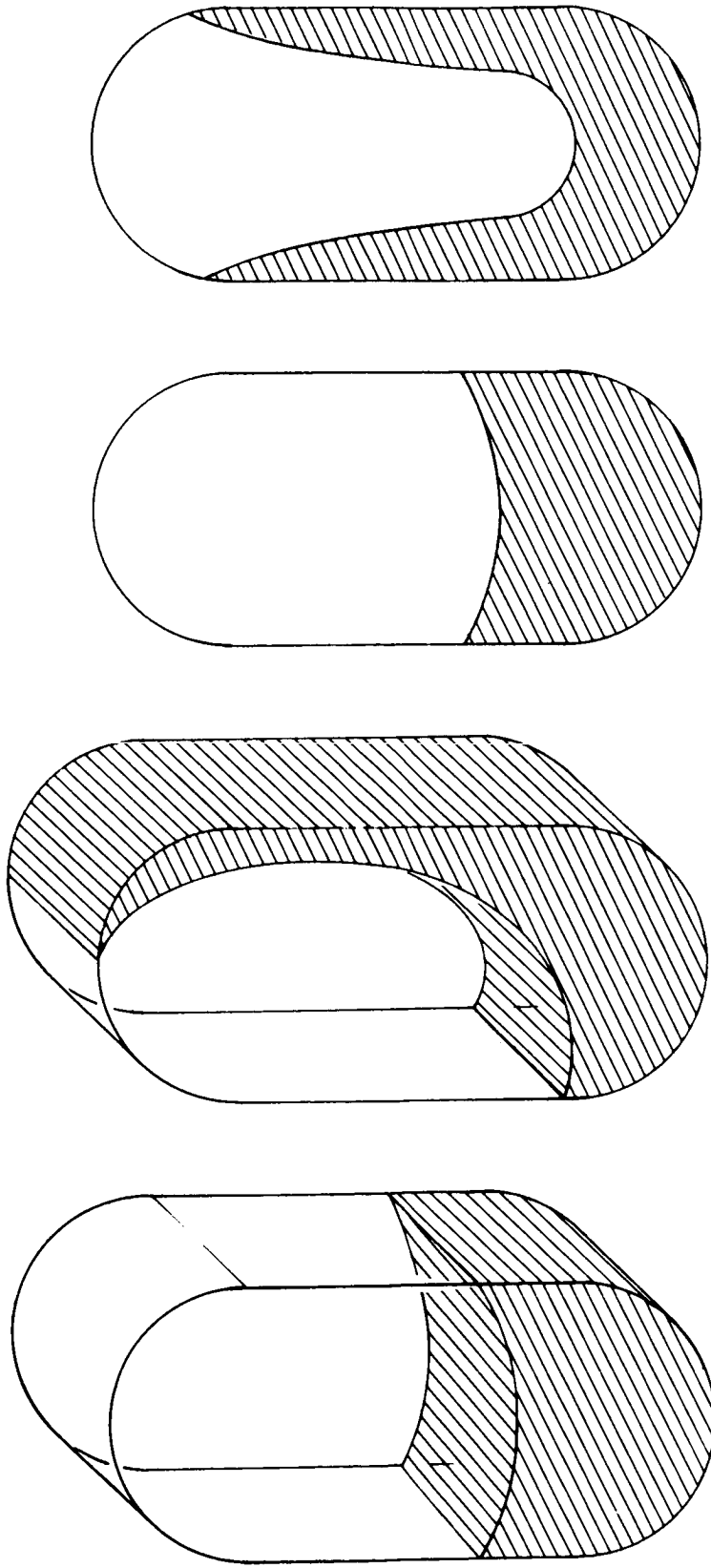
## FLOW TYPES

(Slide 9)

As stated previously, this program computes flow in two dimensions. The slide shows two possible two-dimensional situations, channel-type flow with x-y coordinates at the left and axisymmetric flow with r-z coordinates at the right. Example problems were solved for these two situations.

For the axisymmetric case, the flow was initiated from an equilibrium low gravity interface shape by applying a continuous unsettling acceleration of .1 g along the tank axis. The channel flow problem was begun from the same interface shape, but the .1 g unsettling acceleration was applied at an angle of 6° to the tank axis, with the result that more liquid flowed up one side of the tank than the other.

## FLOW TYPES



TWO DIMENSIONAL

AXISYMMETRIC

## FORCE RESULTS

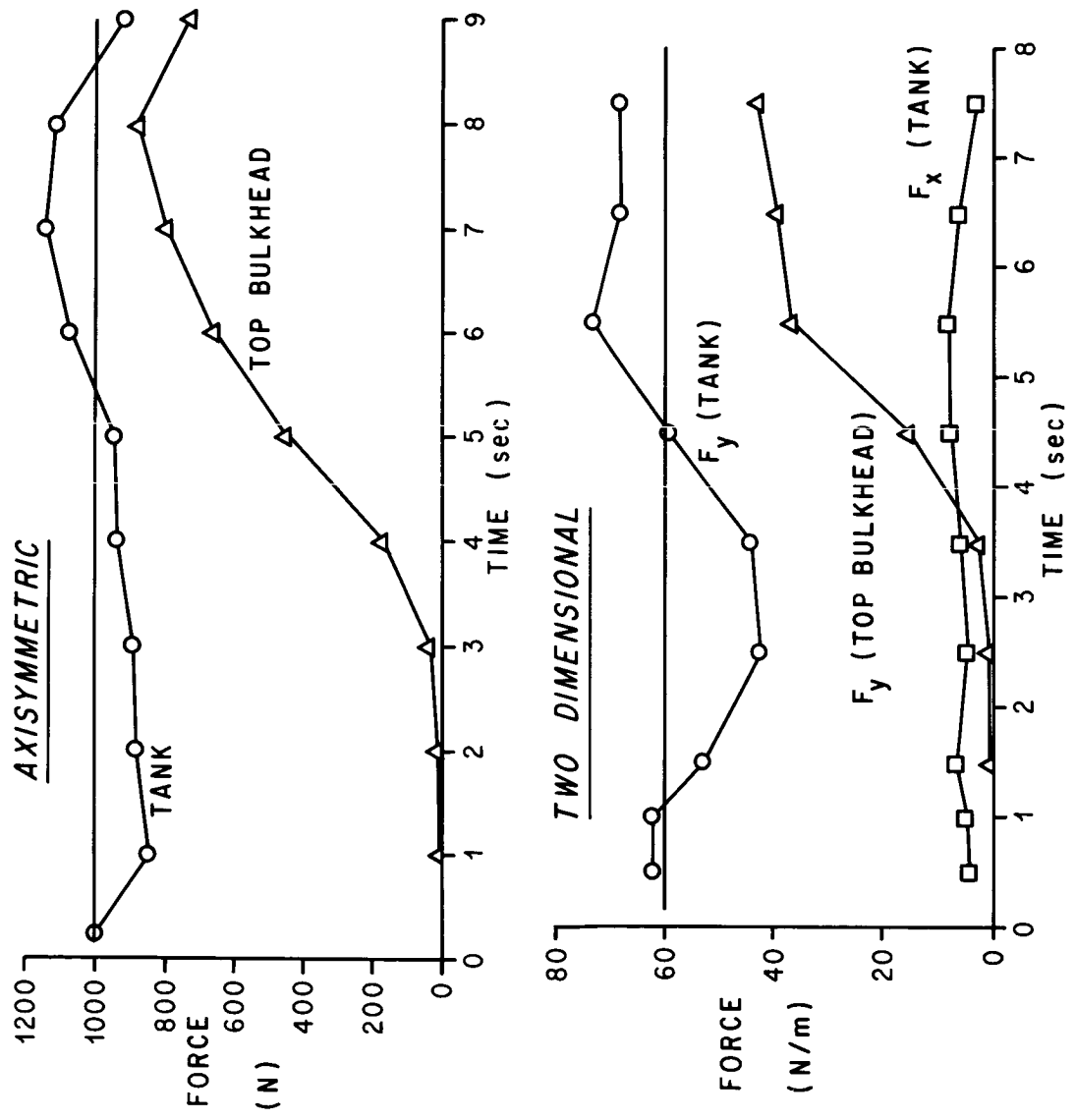
(Slide 10)

This slide shows the forces exerted by the liquid on the tank during the flow shown for the two examples. The upper plot shows force versus time for the axisymmetric tank. One curve shows the total force on the tank, and the other shows the force on the top bulkhead.

The unsettling acceleration is applied at time zero, and a decrease in force exerted by the liquid on the tank is seen as the liquid begins to flow up the tank walls. The gradual increase in force from 1 to 5 seconds is likely due to an increase in drag as the flow up the wall gains velocity. The peak force corresponds to the change in direction of flow at the upper bulkhead and geyser formation.

The lower plot shows similar results for the two-dimensional or channel-flow case, where the unsettling acceleration was at an angle of  $6^{\circ}$  to the vertical. The force is presented per unit of channel length. The force time history in the vertical direction  $F_y$  is similar to that for the axisymmetric case. The side force  $F_x$  reached slightly more than 10 percent of the total vertical force.

## FORCE RESULTS



## SUMMARY

The progress of four studies has been discussed. A computer program has been developed which computes the effects of several factors on propellant dynamics in feedlines. The reduction in sloshing frequency which results when a cylindrical tank is tilted relative to the total acceleration vector has been measured. Flexible baffles have been found to give more damping than rigid baffles of the same size in cryogenic liquid as well as noncryogenic. A computer program has been developed which can be used to determine forces exerted by a propellant on its tank during large amplitude motions.

## SOME LANDING-GEAR CONSIDERATIONS FOR SPACE SHUTTLE VEHICLES

By Brantley R. Hanks and Trafford J. W. Leland  
NASA Langley Research Center, Hampton, Virginia

### INTRODUCTION

Landing of the space shuttle vehicles probably causes less concern to planners than any of the other operational phases - launch, staging, orbit, reentry, flyback, and ground operations. It is generally accepted that the shuttle vehicles will land like aircraft on conventional runways. Since aircraft are currently in operation which have landing weights in the same ranges as the shuttle orbiter and booster, design of landing gear would appear to be a relatively minor problem. However, the importance of landing-gear design should not be underestimated because it is fundamental to the basic concept of the space shuttle, that is, a vehicle which returns safely to ground to be used again. Any shuttle vehicle, no matter how successful otherwise, is a failure if it does not land safely.

Although shuttle vehicles land like aircraft, they are, in fact, hybrid launch vehicle/aircraft and spacecraft/aircraft. There are many differences that affect landing-gear design. Landing-gear weight compared with payload weight is very high; the potential for high temperature exposure of tires is great; landing weight of the booster is large, even for aircraft; increased landing-gear maintenance can be tolerated; design life is shorter; and the cost in both money and notoriety for a landing mishap may be high. Since there are many differences between the shuttle vehicles and conventional aircraft, the possible advantages in new-technology landing gear should be considered in the planning stages.

## LANDING CONDITIONS

(Slide 1)

Landing conditions for space shuttles are much the same as for any aircraft with the exception of abort. A critical factor in landing gear design for normal conditions will probably be braking performance on wet and/or icy runways. In an emergency almost any conceivable landing site may be possible but some, such as short runways, water, or rough surfaces may be considered likely. In abort, whether the landing gear can function at all depends greatly on the amount of excess load on board and the location of the vehicle center of gravity. Ideally, for normal landing, the best possible landing system would be one which is left on the ground, a landing sled or some sort of "superfoam" runway, for example. The perfect emergency landing system would permit landing anywhere, from mountain peak to ocean surface, but would probably constitute the major portion of vehicle weight. Somewhere in between a compromise system which provides reasonable landing flexibility at an acceptable weight penalty must be found. The relative importance of each of these factors must be realistically assessed in making a decision.

# LANDING CONDITIONS

## NORMAL

- DRY RUNWAY
- WET RUNWAY
- ICY RUNWAY

## EMERGENCY

- SHORT RUNWAY
- WATER
- ROUGH SURFACE

## ABORT

- ANY OF ABOVE WITH EXCESS LOAD

Slide 1

## REQUIREMENTS AND CONSTRAINTS

(Slide 2)

The requirements and constraints on shuttle landing gear are, like landing conditions, much the same as for any aircraft. However, they are more severe in several instances. The cost per unit weight for landing gear is much higher for the shuttle. The possibility of high temperature exposure may require refrigeration or additional insulation around the landing-gear storage compartments. Fail-safe deployment and take-off capability are standard requirements but cross-wind landing stability may be a critical factor because of the size and unusual geometry of shuttle vehicles. Any landing-gear system must reasonably satisfy all these requirements and constraints.

## **REQUIREMENTS AND CONSTRAINTS**

**LOW WEIGHT**

**POSSIBLE HIGH-TEMPERATURE EXPOSURE**

**FAIL-SAFE DEPLOYMENT AND OPERATION**

**TAKE-OFF CAPABILITY FOR FERRYING**

**CROSS-WIND STABILITY**

Slide 2

## LANDING-GEAR TYPES

(Slide 3)

There are several different types of landing gear systems which could be used on shuttle vehicles. Conventional pneumatic tire landing gear with servo-controlled antiskid braking is the current most likely candidate. However, for reasons to be discussed later in this paper, some other types may offer certain advantages. Candidates are conventional systems with metal or wire brush wheels replacing pneumatic tires, skids with auxiliary take-off gear for ferrying, either type of wheeled system with skid brakes, and air-cushion landing systems (ACLS).

## LANDING-GEAR TYPES

CONVENTIONAL WHEEL WITH TIRE }  
METAL OR WIRE BRUSH WHEELS }

SKIDS

WHEEL AND TIRE WITH SKID BRAKES

AIR CUSHION WITH SKID BRAKES

Slide 3

## CONVENTIONAL WHEEL AND TIRE

(Slide 4)

A conventional wheel and pneumatic-tire landing gear with a servo-controlled antiskid braking system represents a state-of-the-art approach to shuttle landing gear. This is one of its most attractive features in that it is a proven system and development time and costs should be minimal. Such systems have shown excellent dry runway braking and they are amenable to using gravity-drop emergency deployment. However, there are shortcomings to conventional gear. The rubber compounds usually used in tires tend to revert to their uncured state at about 150°C (300°F). Braking performance on wet runways is much poorer than on dry runways because even the best antiskid system can only give the maximum friction available to it. At landing speeds on a wet runway this available friction is very low as will be shown later. Emergency landing on water, which is probably the single most likely emergency landing site, is not possible. Impact loads on landing are transmitted to the fuselage at "points" which places large moments on the structure. Landing impact loads will be a major factor in longitudinal structural stiffness design. Finally, cross-wind landing stability is solely a function of tire side-force limits unless a rotation capability is designed into the landing gear at a weight and complexity penalty.

Replacing the pneumatic tire on conventional gear with a metal wheel or a wire brush wheel (similar to the brush wheel on a grinding machine) may eliminate the temperature problem and possibly the wet runway braking problem. However, acceptable designs and materials must be developed and more compliance is needed in struts to absorb landing and roll-out loads.

# CONVENTIONAL WHEEL AND TIRE

## ADVANTAGES

- CURRENT TECHNOLOGY
- GOOD DRY RUNWAY PERFORMANCE
- SIMPLE EMERGENCY DEPLOYMENT

## DISADVANTAGES

- TEMPERATURE LIMITS ON TIRES  
(MAY NEED REFRIGERATION)
- POOR WET AND ICY RUNWAY PERFORMANCE
- NO WATER-LANDING CAPABILITY
- POINT LOADS ON STRUCTURE

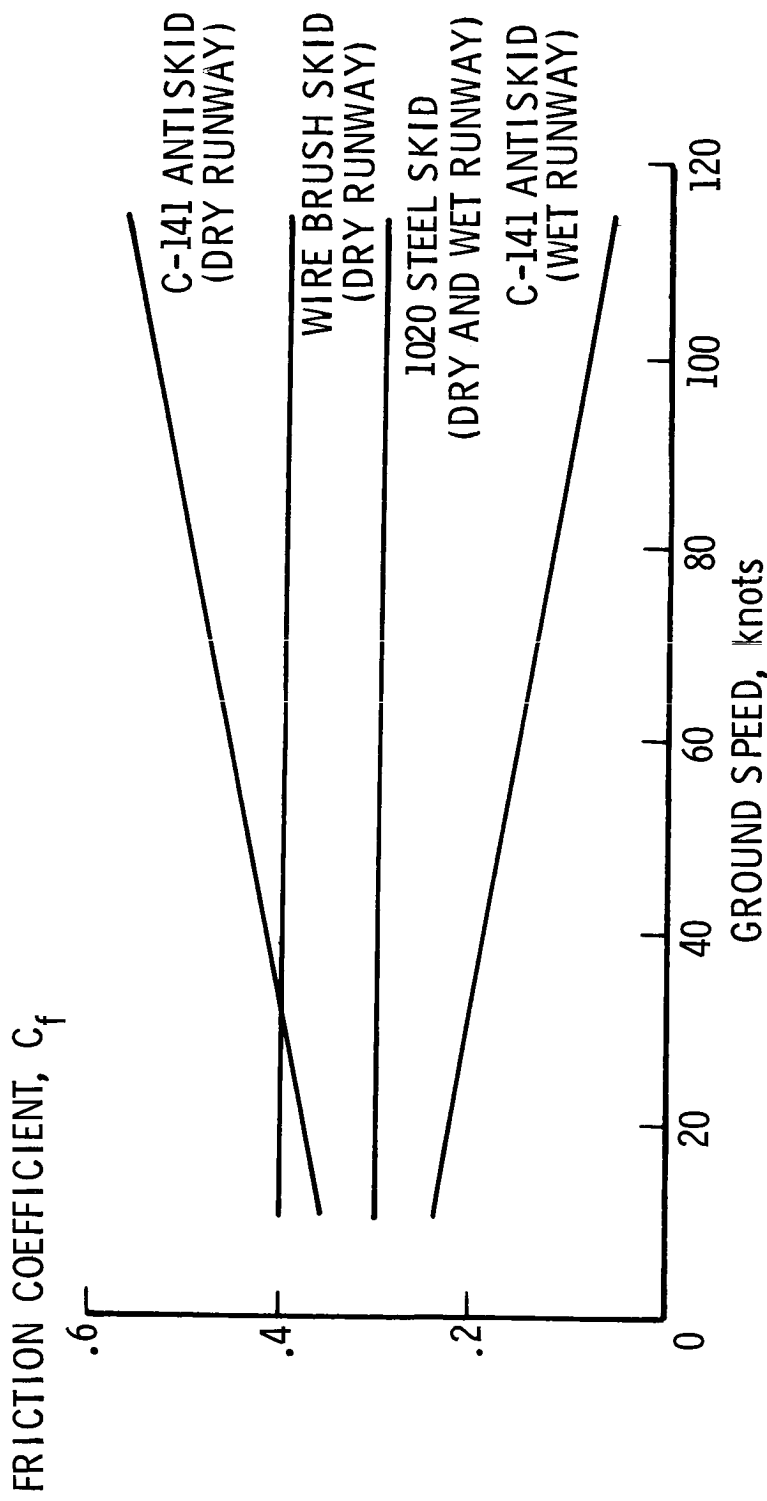
Slide L.

## BRAKING-SYSTEM FRICTION COEFFICIENTS

(Slide 5)

As mentioned earlier, antiskid braking systems do not give very good braking performance on wet runways. Another landing system, a skid system, often mentioned for high-temperature applications does not have this problem. This slide shows a comparison of typical friction coefficients for a C-141A transport aircraft with those for some experimental skids on wet and dry runway surfaces. These coefficients, measured by researchers from Langley Research Center (refs. 1 and 2), will vary with runway surface and aircraft design but are representative of what may be expected. The C-141A gives excellent dry runway braking but its wet runway performance is poor. In fact, the braking distance corresponding to these curves is over twice as long for the wet runway. Brake friction for the 1020 steel skid, however, is unaffected by the wet runway. Although the dry runway performance is not as good as for the antiskid system, the runway needed to assure safe landing can be much shorter since the wet case is the limiting situation. A wire brush skid, made of 5-cm (2-inch) lengths of wire rope welded to a base plate, gives even better performance on a dry runway. No wet or icy runway braking tests have been run on wire brush skids but, intuitively, they would appear to be better than solid skids under these conditions.

## BRAKING-SYSTEM FRICTION COEFFICIENTS



Slide 5

## SKIDS

## (Slide 6)

Skid landing systems for shuttle vehicles have some attractive advantages. They are insensitive to temperature, give good wet runway (and possibly icy runway) braking, and are mechanically simple. Insufficient data on skid performance at various bearing pressures make weight estimates difficult, but savings in insulation and mechanical systems may make them attractive from a weight standpoint. The data shown on the previous slide were for a bearing pressure of 150 kN/m<sup>2</sup> (22 psi), but if 280 kN/m<sup>2</sup> (40 psi) or 410 kN/m<sup>2</sup> (60 psi) could be used, skid area would be reasonable.

The disadvantages of skids for shuttle applications are several. Skids with directional control have not been developed. Take-off for ferrying would require auxiliary wheels, possibly installed after landing and removed for launch. Shock absorbers which are not affected by high temperatures would have to be used and they would need more stroke than in a conventional system where tires take part of the landing impact. Landing on water could conceivably be accomplished by hydroplaning but research would be needed to evaluate this capability. Finally, the ride and structural loads on the runway would be more severe than with conventional gear without some sort of suspension system.

# SKIDS

## ADVANTAGES

- UNAFFECTED BY TEMPERATURE
- GOOD WET RUNWAY PERFORMANCE
- EMERGENCY DEPLOYMENT SIMPLE

## DISADVANTAGES

- NO DIRECTIONAL CONTROL
- FERRYING REQUIRES AUXILIARY TAKE-OFF GEAR
- HIGH-TEMPERATURE AND HIGH-ABSORPTION SHOCKS NEEDED
- WATER LANDING QUESTIONABLE
- ROUGH RIDE ON RUNWAY

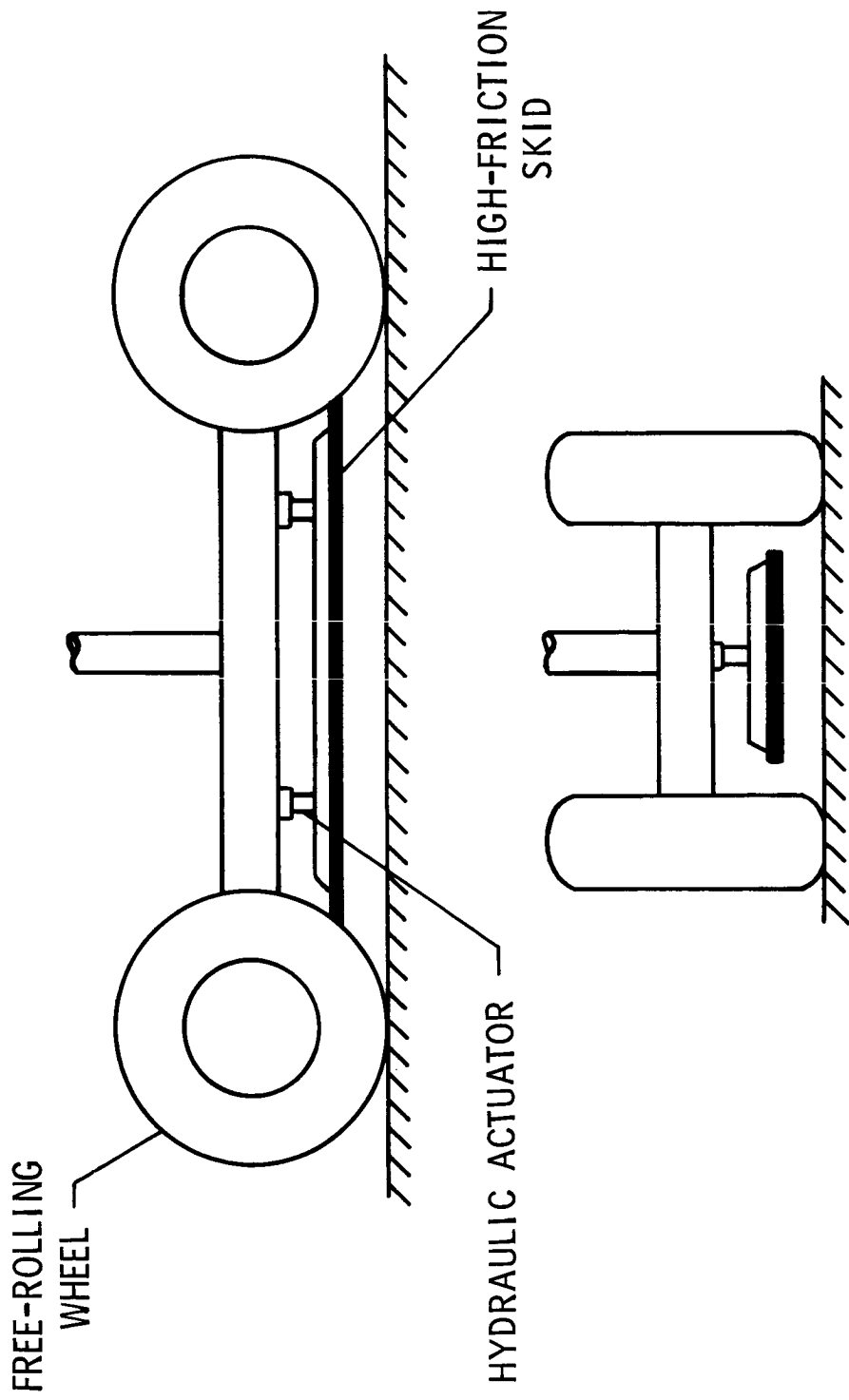
Slide 6

## WHEEL AND SKID SYSTEM - DESCRIPTION

(Slide 7)

An unconventional compromise system which offers some of the advantages of both skids and wheels is shown in this slide. It uses a standard wheel bogey with free-rolling wheels and hydraulically operated skid brakes. The all-weather braking performance and passive operation simplicity of skids are maintained but directional stability, cornering force, ferrying ability, and impact and roll-out cushioning are provided by tires. Since part of the aircraft weight is supported by the tires for directional control during braking, some reduction in skid effectiveness occurs. Probably no more than 15 percent of the aircraft weight would be needed on the tires. A skid having a high friction coefficient (coefficients approaching 0.6 have been obtained experimentally) could easily compensate for this loss.

## WHEEL AND SKID SYSTEM



Slide 7

## WHEEL AND SKID SYSTEM – ADVANTAGES AND DISADVANTAGES

(Slide 8)

The good all-weather runway braking performance of the wheel and skid system while maintaining directional stability and cornering force is its most obvious advantage. However, some less obvious advantages should be explored in a comprehensive study of this system. For example, elimination of the braking function from tires may allow the use of higher temperature materials and/or lighter weight construction. Emergency deployment is the same as with conventional systems.

The wheel and skid combination shares some of the disadvantages of the separate systems. The tires will be temperature limited although the limits may be raised somewhat and the fuselage will be loaded at points. Water landing by hydroplaning is possible but questionable. Cross-wind landing requires either full skid deployment to take side loads off the tires, if the vehicle is angled into the effective wind direction, or unloading of the brakes to put more weight (and, hence, side friction force) on the tires if the vehicle heads directly down the runway. One of the biggest disadvantages is that it is a new-technology system and would require much development research on both skids and the system itself.

# WHEEL AND SKID LANDING GEAR

## ADVANTAGES

- GOOD WET RUNWAY PERFORMANCE MAINTAINING CORNERING CAPABILITY
- BRAKING ELIMINATED FROM TIRE DESIGN (POSSIBLE TEMPERATURE AND WEAR ADVANTAGES)
- EMERGENCY DEPLOYMENT SIMPLE

## DISADVANTAGES

- TEMPERATURE LIMITS ON TIRES
- NEW TECHNOLOGY REQUIRED
- POINT LOADS ON STRUCTURE
- NO WATER LANDING

Slide 8

## SHUTTLE AIR-CUSHION LANDING SYSTEM

(Slide 9)

One candidate landing-gear system for shuttle applications, the air-cushion landing system (ACLS), is very unconventional. The figure shows an artist's conception of an ACLS on a delta-winged booster. It is essentially a ground effects machine attached to the bottom of the fuselage. This system was developed by Bell Aerospace Company (ref. 3) and has been flight tested on a small lightweight airplane.

# SHUTTLE AIR-CUSHION LANDING SYSTEM



Slide 9

## AIR-CUSHION LANDING SYSTEM - OPERATION

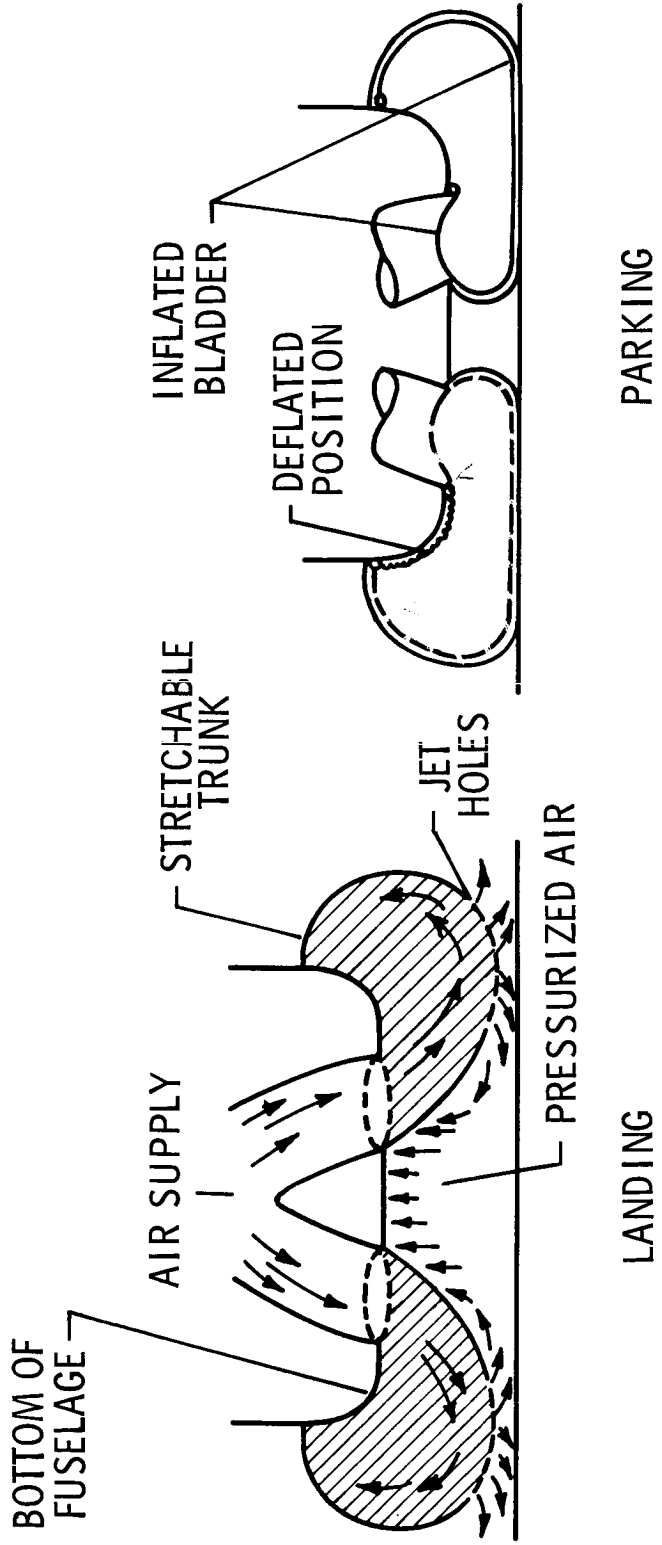
(Slide 10)

The ACLS operating principle is shown in the upper left sketch. A large flexible trunk is attached to the fuselage in an elongated toroid shape. Air is supplied to this trunk by an onboard supply and escapes through small holes in the bottom of the trunk. The escaping air has two functions: it lubricates the cushion to provide vertical support and prevent scuffing; and it pressurizes the air trapped inside the toroid. A combination peripheral jet/plenum type air cushion is the result. The pressurized trunk provides energy absorption during landing impact. Inflation pressures in the trunk can be relatively low, about 14 to 28 kN/m<sup>2</sup> (2 to 4 psi), and the footprint pressure is about one-half that.

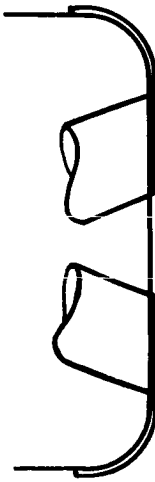
Parking or flotation is accomplished with the use of the inflatable bladder arrangement shown in the upper right sketch. This bladder simply seals the jet holes and air supply holes and retracts against the fuselage when not in use.

During flight the ACLS trunk, which is made of a stretchable material, also retracts against the fuselage as shown in the bottom sketch. The trunk can be covered with doors, if needed, or simply be left exposed if conditions permit.

## AIR-CUSHION LANDING SYSTEM



PARKING



IN FLIGHT

Slide 10

## AIR CUSHION - WATER LANDING

(Slide 11)

Since the ACIS is a ground-effects-type device, it has some of the features of the ground effects machine. One of the more interesting, shown here, is water landing. This capability has been demonstrated with the small demonstration plane as has water take-off, water-to-land transition, and rough-field landing and take-off. The only limiting factor for both water and rough-field landing is wave length and height relative to the air-cushion length and trunk depth. The ACIS also has a large cross-wind landing capability as the vehicle can simply head into the resultant wind at an angle to the landing direction.

# WATER LANDING WITH AIR CUSHION



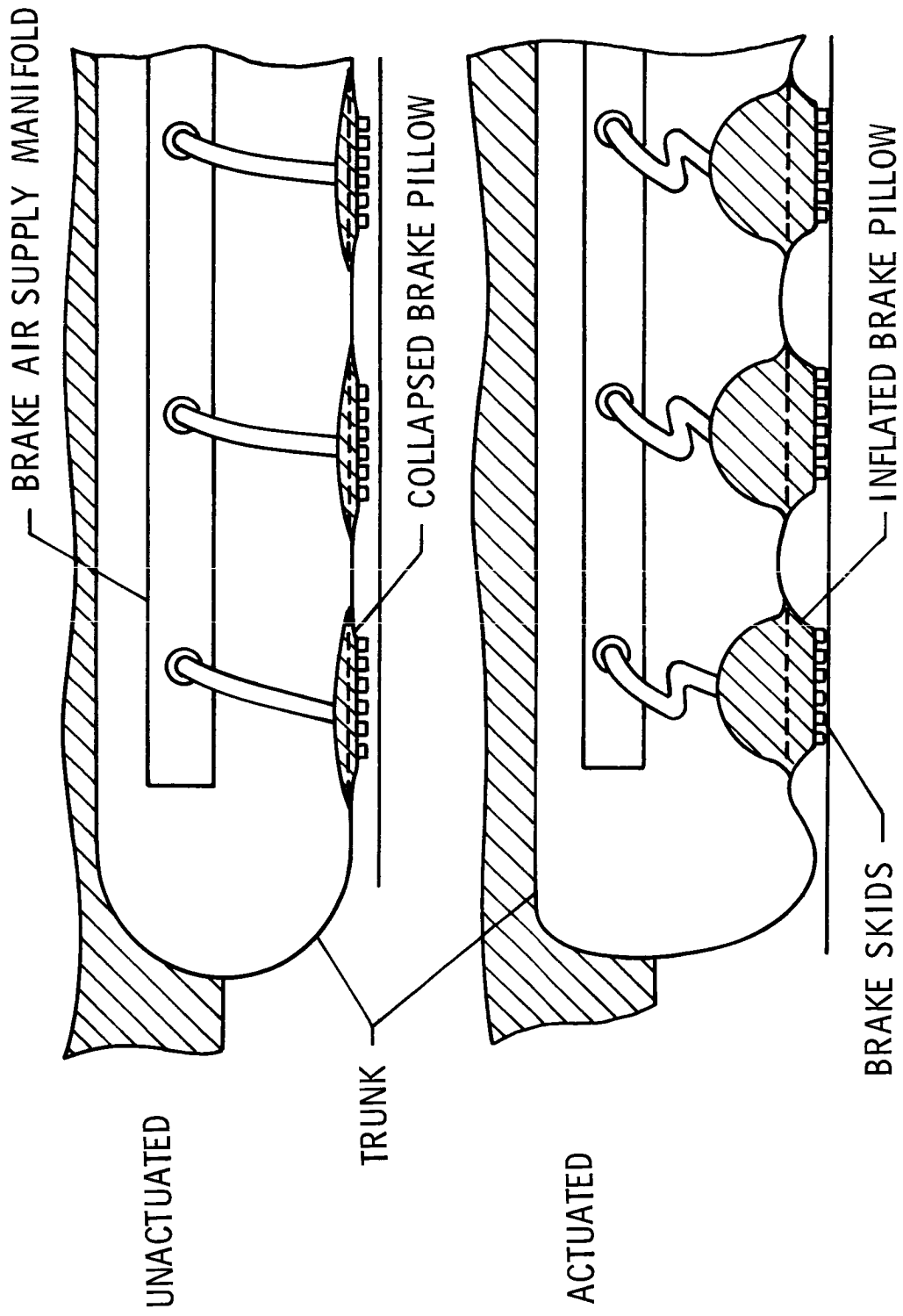
Slide 11

AIR-CUSHION LANDING SYSTEM - BRAKING

(Slide 12)

Braking of the ACLS is by inflatable skids as shown here. The skids, collapsed during take-off and flight as shown in the upper sketch, are pressurized during braking by their own air supply system to pressures higher than trunk pressure as shown in the lower sketch. The vehicle is steered by applying differential braking pressure to each side of the ACLS trunk.

## BRAKING SYSTEM



Slide 12

## TYPICAL SHUTTLE AIR-CUSHION CHARACTERISTICS

(Slide 13)

A feasibility study of the ACIS applied to space shuttle booster and orbiter vehicles was conducted (ref. 4). The ACIS was shown to be both feasible and practical for shuttle applications. This slide shows the dimensions and operating pressures of two of the configurations studied, one for a booster and one for an orbiter. The booster ACIS is rectangular, and dimensions are for the system with the lowest footprint pressure (hence the largest system) studied. Only one orbiter configuration was studied, a triangular one. The study showed that materials are currently available which could be exposed to temperatures up to about  $315^{\circ}$  C ( $600^{\circ}$  F) for as much as 100 hours and to about  $425^{\circ}$  C ( $800^{\circ}$  F) for short periods of time and still function properly. Landing impact studies showed that landings at about 3 m/sec (10 ft/sec) would produce a total impact acceleration of about 1.5 g at the vehicle center of gravity. Trunk compression during landing was about 50 percent, which leaves additional stroke available to compensate for pilot error. Booster braking distances were computed for landing speeds of 120 knots and friction coefficients of 0.35 and 0.70. The distances calculated were about 600 m (1950 ft) and 330 m (1100 ft), respectively. The all-weather braking capability of skids would be maintained.

## TYPICAL SHUTTLE AIR-CUSHION LANDING SYSTEM

	LENGTH, m	WIDTH, m	DEPTH, m	GROUND PRESSURE kN/m <sup>2</sup>
BOOSTER	44	11	4	4.35
ORBITER	17	*8	3	8.70

\* TRIANGULAR CONFIGURATION

### FEATURES

300° C TEMPERATURE CAPABILITY

1.5 g IMPACT ACCELERATION AT 3 m/sec SINK RATE

Slide 13

## WEIGHT COMPARISON - AIR-CUSHION SYSTEM AND CONVENTIONAL GEAR

(Slide 14)

One phase of the feasibility study was a weight comparison of the ACLS with conventional gear. This slide shows the ACLS weights computed, with adjustments made to conform to latest shuttle vehicle weight estimates, compared with conventional landing-gear weight estimates by Phase B contractors. With the ACLS, a total weight savings of 20 kN (4600 lb) for the booster and 11 kN (2500 lb) for the orbiter can potentially be realized. Based on a 1-to-6 payload weight savings for booster weight savings and a 1-to-1 savings for the orbiter, the total comes to about 5 percent of a 290 kN (65000 lb) payload. These weights include an air supply fan, motor, fuel, and thermal protection for the ACLS. Weight savings in fuselage structure were not computed, but distribution of the landing loads along the structure may yield considerable savings. These estimates are subject to the configurations studied and may be conservative or optimistic for any given configuration. The orbiter ACLS weight includes doors for thermal protection but the booster ACLS uses a protective layer. Doors may have to be added if later temperature estimates and materials studies show them necessary.

## WEIGHT COMPARISONS

### AIR CUSHIONS WITH CONVENTIONAL GEAR

LANDING WEIGHT, kN	CONVENTIONAL GEAR WEIGHT, kN	ACLS * WEIGHT, kN	SAVINGS, kN
BOOSTER	1957	83	62
ORBITER	934	47	36

\* INCLUDES FAN, MOTOR, AND THERMAL PROTECTION

$$\text{PAYLOAD SAVINGS} = -\frac{21}{6} + 11 = 14.5 \text{ kN} = 5\%$$

Slide 14

## AIR-CUSHION LANDING SYSTEM – ADVANTAGES AND DISADVANTAGES

(Slide 15)

The potential advantages of the ACLS for shuttle vehicles are many. The potential weight savings may be a critical plus factor. The additional safety value of skid braking, water and rough-surface landing capability, and cross-wind landing capability cannot be minimized. The higher temperature exposure capability and distributed landing loads are important from a structural weight standpoint.

Primary disadvantages of the ACLS are that it requires considerable power (up to 2980 kW or 4000 hp) and it is a totally new concept which has never been applied to large aircraft. Emergency deployment can be accomplished by dynamic pressure during flight and initial touchdown but the most feasible solution at low speed would be to partially inflate the parking bladder at high speed and land on it with the skids to protect it. Finally, since the ACLS is a powered system and uses skids, it would require more maintenance than conventional systems.

# AIR-CUSHION LANDING SYSTEM

## ADVANTAGES

- POTENTIAL WEIGHT SAVINGS
- SAME WET-AND DRY-RUNWAY PERFORMANCE
- WATER AND ROUGH SURFACE CAPABILITY
- INHERENT CROSS-WIND LANDING CAPABILITY
- TEMPERATURE LIMITS ON MATERIALS HIGHER THAN WITH TIRES
- DISTRIBUTED STRUCTURAL LOADS

## DISADVANTAGES

- REQUIRES POWER DURING LANDING
- NEW TECHNOLOGY
- EMERGENCY DEPLOYMENT AT LOW DYNAMIC PRESSURE
- MAINTENANCE

Slide 15

## SUMMARY AND RECOMMENDATIONS

(Slide 16)

An overview of all the systems available for shuttle landing gear shows that the optimum system has not been found. Several new-technology systems may offer attractive advantages for shuttle applications in both operating and weight-saving considerations. With the stakes being rather high in this new breed of flight vehicle, it is inadvisable to ignore landing gear in conceptual design studies. An in-depth comparison study of landing-gear systems should be conducted before final commitments are made. Furthermore, the impact of landing-gear design on total system design including structural design, ground operations, and flight profiles should be assessed.

## SUMMARY AND RECOMMENDATIONS

NEW TECHNOLOGY SYSTEMS MAY OFFER ATTRACTIVE OPERATING ADVANTAGES

WEIGHT SAVINGS MAY BE REALIZED WITH SOME NEW TECHNOLOGY SYSTEMS

IN-DEPTH COMPARISON STUDY OF LANDING-GEAR SYSTEMS IS DESIRABLE

IMPACT OF LANDING-GEAR DESIGN ON TOTAL-SYSTEM DESIGN SHOULD BE ASSESSED

Slide 16

## REFERENCES

1. Yager, Thomas J.; Phillips, W. Pelham; Horne, Walter B.; and Sparks, Howard C.: A Comparison of Aircraft and Ground Vehicle Stopping Performance on Dry, Wet, Flooded, Slush-, Snow-, and Ice-Covered Runways. NASA TN D-6098, 1970.
2. Dreher, Robert C.; and Batterson, Sidney A.: Coefficients of Friction and Wear Characteristics for Skids Made of Various Metals on Concrete, Asphalt, and Lakebed Surfaces. NASA TN D-999, 1962.
3. Earl, T. Desmond; and Cooper, Richard H.: Air Cushion Landing Gear for Aircraft. AFFDL-TR-68-124, U.S. Air Force, Jan. 1969.
4. Ryken, John M.: A Study of Air Cushion Landing Systems for Space Shuttle Vehicles. Contract No. NAS1-9992, Bell Aerosp. Co., Div. of Textron, Inc., Dec. 1970. (Also available as NASA CR-111803.)

RECENT STUDIES OF EFFECTS OF GROUND WINDS ON SPACE SHUTTLE VEHICLES

By Robert W. Hess, Wilmer H. Reed III, and Jerome T. Foughner, Jr.  
NASA Langley Research Center, Hampton, Virginia

SUMMARY

Ground-wind load studies were conducted with models of space-shuttle configurations to assess the importance of aerodynamic instabilities on erected space-shuttle vehicles. Regions of instability for stop-sign flutter and galloping instability are identified and their significance for the full-scale vehicle is examined. Aerodynamic drag coefficients were measured for two booster configurations with and without an orbiter, and the effect of Reynolds number on galloping instability was explored for one configuration.

## SPACE SHUTTLE GROUND-WIND LOAD CONSIDERATIONS

(Figure 1)

At a previous space shuttle technology conference in Cleveland, Ohio, some factors which should be considered in designing shuttle vehicles to withstand the effects of ground winds while erected on the launch pad were identified and discussed (ref. 1). These factors are listed in figure 1. The ground wind environment, which may be defined in terms of steady wind profiles and turbulence spectra, creates both static and dynamic loads on the vehicle. The dynamic loads arise from various sources, including vortices alternately shed from the structure, fluctuation in the wind itself, and various forms of aerodynamic instability denoted here as "stop-sign flutter" and "galloping." These loads, in turn, create problems related to structural strength, deflection, fatigue life, and other factors.

The purpose of this paper is to present results from some studies made since the Cleveland conference which represent a follow-on to those reported in reference 1. Specifically, these studies concern stop-sign flutter, static aerodynamic loads, and galloping instability.

## SPACE SHUTTLE GROUND-WIND LOAD CONSIDERATIONS

- GROUND-WIND ENVIRONMENT
  - STEADY WIND PROFILES
  - TURBULENCE SPECTRA
- VEHICLE LOADS AND RESPONSE
  - STATIC LOADS
  - DYNAMIC LOADS
  - VORTEX SHEDDING
  - TURBULENCE
  - GALLOPING
  - STOP-SIGN FLUTTER
- PROBLEM AREAS
  - STRENGTH
  - DEFLECTION
  - FATIGUE
  - GROUND HANDLING
  - GUIDANCE ALIGNMENT

Figure 1

## STOP-SIGN FLUTTER NOTATION

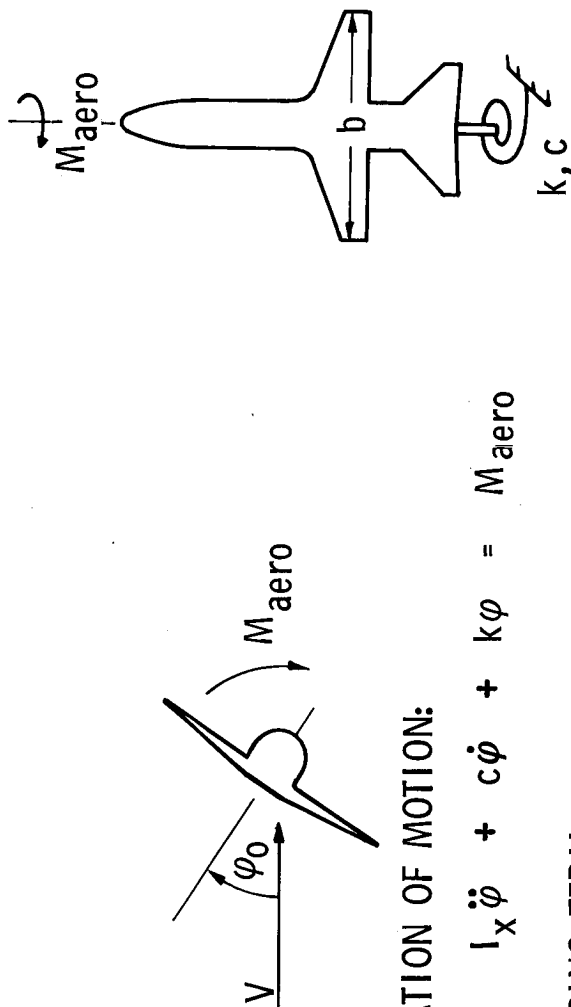
(Figure 2)

Stop-sign flutter is a stall flutter phenomenon which could arise on erected space shuttle vehicles having large lifting surfaces exposed to the wind. The motions envisioned are torsional oscillations ( $\phi$ ) about the vehicle longitudinal axis associated with flexibility of the vehicle structure and/or its hold-down structure. An idealized representation of the vehicle is shown in figure 2, wherein the system is defined by the equation of motion of a lumped-parameter, single-degree-of-freedom oscillator.

In this equation  $I_x$ ,  $c$ , and  $k$  are vehicle structural parameters representing the moment of inertia of the vehicle about its longitudinal axis, the structural damping, and torsional stiffness, respectively. The term  $M_{aero}$  on the right side of the equation is the aerodynamic moment, which is a function of the mean wind azimuth angle  $\Phi_0$ , the angular rotation of the vehicle  $\phi$ , and its time derivatives.

With regard to stop-sign flutter, the significant term is the net damping (structural plus aerodynamic) of the system which is expressed in the nondimensional form given by the second equation in figure 2. In this equation  $\xi_\phi$  is the critical damping ratio of the structure;  $V/f_\phi b$  is a velocity ratio in terms of the natural torsional frequency  $f_\phi$  (hertz), wing span  $b$ , and wind speed  $V$ ;  $\rho S/b/M$  is a mass ratio parameter involving air density  $\rho$ , total planform area  $S$ , wing span  $b$ , and structural mass  $M$ ;  $r_\phi$  is the radius of gyration of the vehicle about the roll axis; and  $C_{l_p}$  is the aerodynamic roll damping coefficient in conventional aircraft stability motion (ref. 2). Stop-sign flutter occurs whenever negative aerodynamic damping exceeds the positive structural damping.

## STOP-SIGN FLUTTER NOTATION



$$\begin{cases} < 0 & \text{UNSTABLE} \\ > 0 & \text{STABLE} \end{cases}$$

Figure 2

## SPACE SHUTTLE STOP-SIGN-FLUTTER MODEL

(Figure 3)

To determine the susceptibility of space shuttle configurations to stop-sign flutter, aerodynamic roll damping derivatives  $C_{Lp}$  were measured for a straight-wing and a delta-wing space shuttle configuration. (A further description of these models may be found in ref. 1.) The straight wing model is shown in figure 3 mounted in the test section of the Langley high-speed 7- by 10-foot tunnel. The model is mounted on an oscillating sting mechanism previously developed for measuring aircraft roll derivatives by a forced-oscillation technique (ref. 2). In the present application the sting is mounted on a sidewall turntable so that the model's roll axis is perpendicular to the flow direction. The model was oscillated in roll through an amplitude of  $\pm 2.5^\circ$  at frequencies ranging from 2 to 8 hertz, and at wind speeds ranging from 20 to 44 meters per second (65 to 145 feet per second). The mean wind azimuth angle was varied from  $-10^\circ$  to  $190^\circ$ . Results from the study are summarized in figure 4.

SPACE SHUTTLE STOP-SIGN-FLUTTER MODEL



Figure 3

## STOP-SIGN FLUTTER BOUNDARIES

(Figure 4)

This figure shows stop-sign flutter boundaries determined for a straight-wing and a delta-wing space shuttle configuration. The boundaries are plotted in terms of the reduced velocity ratio  $V/f_{\Phi}^b$

$$\text{and the nondimensional damping-inertia parameter } \xi_{\Phi} \left( \frac{M}{\rho S b} \right) \left( \frac{r_{\Phi}}{b} \right)^2 \text{ previously described in figure 2.}$$

Although negative aerodynamic damping was observed on each configuration at several wind-azimuth angles, only the boundaries for the most critical azimuth angle in each case are shown. These critical wind azimuth angles, which are indicated by the sketches in the figure, are the angles associated with the minimum wind speeds required for stop-sign flutter.

Note that the delta wing configuration is slightly more susceptible to stop-sign flutter than the straight wing configuration. The really significant finding shown in this figure, however, is that stop-sign flutter boundaries are well removed from the region representative of space shuttle boosters on the launch pad at the maximum design wind condition, 37 m/sec (72 knots). As indicated in the figure, this region lies in a reduced velocity range which is less than one-fifth that required for flutter. Thus, these preliminary results indicate that stop-sign flutter is not likely to be a problem for vehicles in a cantilever mounted condition. However, it should be remembered that during erection the vehicle roll frequency could be drastically reduced, thus bringing stop-sign flutter into the realm of possibility.

## STOP - SIGN FLUTTER BOUNDARIES

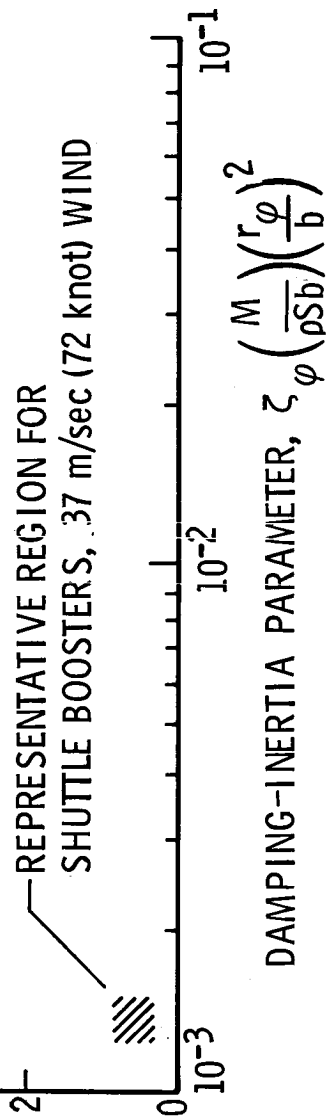
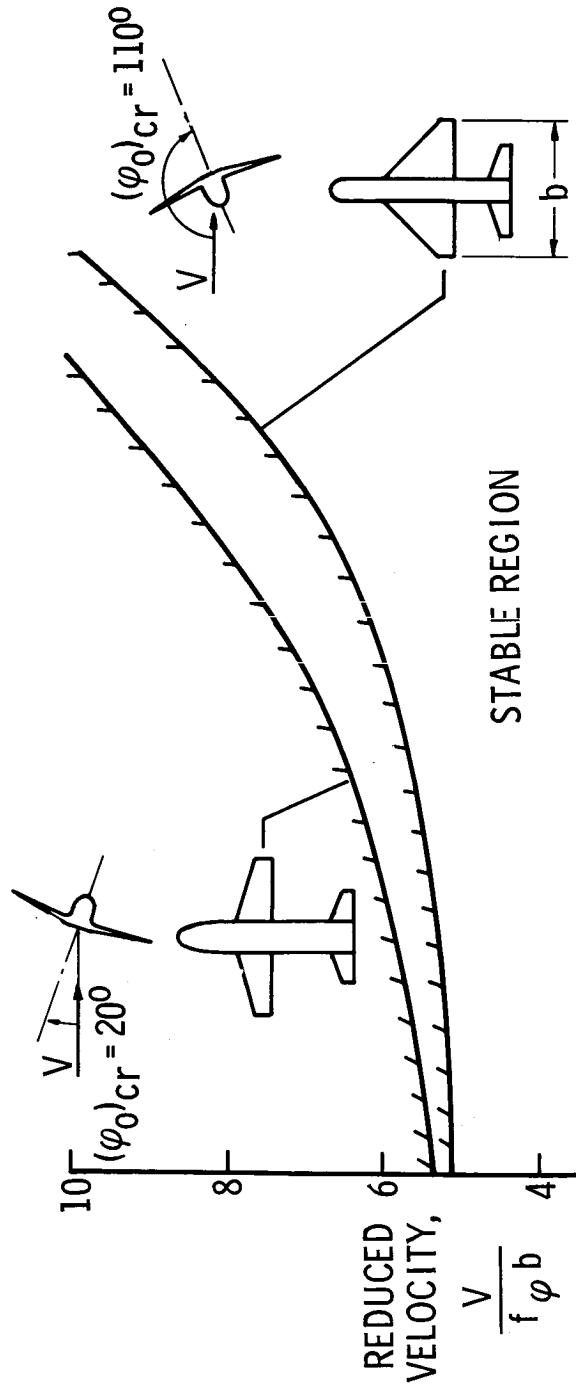


Figure 4

## GALLOPING STABILITY NOTATION

(Figure 5)

In contrast to stop-sign flutter and vortex shedding, which are unsteady aerodynamic phenomena, galloping instability is basically associated with static aerodynamic phenomena. The remaining sections of this paper are concerned with the measurement of static aerodynamic coefficients on various space shuttle configurations and the use of these coefficients in determining sensitivity to galloping instability.

As discussed in reference 1, space shuttle configurations with noncircular cross sections can have aerodynamic characteristics such that for certain wind directions the air forces due to vehicle motion in the cross-stream direction tend to enhance, rather than retard, the motion. At a wind speed where such air forces exceed the structural damping forces, galloping instability occurs and the amplitude of motion will then grow until limited by aerodynamic or structural nonlinearities.

A preliminary assessment of galloping instability can be made by using static aerodynamic coefficients if the erected vehicle is represented as a rigid body supported by springs, as shown schematically in figure 5. The springs allow the vehicle to translate horizontally in a direction normal to the mean wind, and the change in wind direction due to body motion ( $\alpha = \dot{y}/V$ ) is therefore constant along the body. By use of the equation of motion in figure 5 we can deduce galloping stability from static aerodynamic forces (L and D) measured on a stationary model. This idealized representation of the vehicle vibration mode is admittedly a very crude one, but it can provide useful insight regarding galloping instability trends. A nondimensional form of the net damping (structure plus aerodynamic) is shown by the second equation in the figure.

Note the similarities between the damping term given here for translational motion and that given in figure 2 for rotational motion. In comparing the aerodynamic coefficients for the two cases, we see that  $C_{lp}$  is to stop-sign flutter what  $(C_L + C_D)$  is to galloping. The latter term is the basis of the well-known Den Hartog galloping stability criterion (ref. 3) which states that the necessary condition for galloping is that the negative slope of the lift-coefficient curve must exceed the drag coefficient.

## GALLOPING STABILITY NOTATION

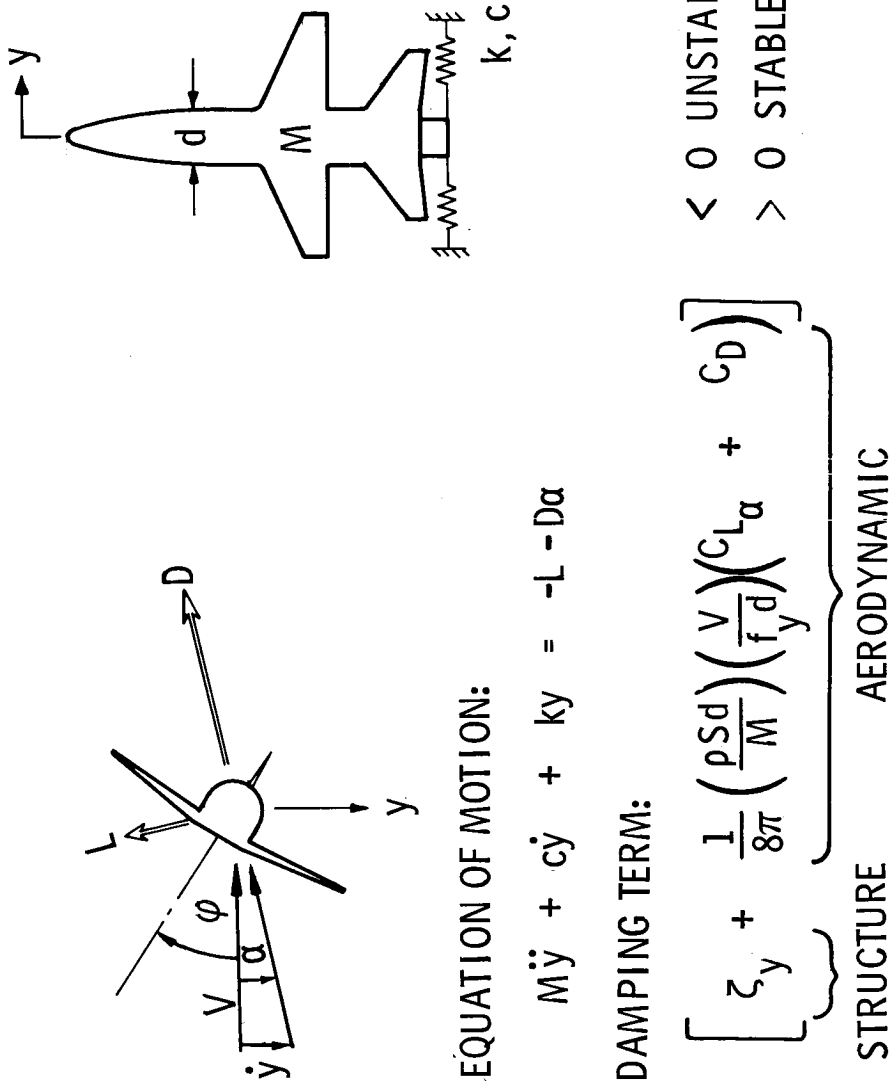


Figure 5

## SPACE SHUTTLE GROUND-WIND LOAD STUDY

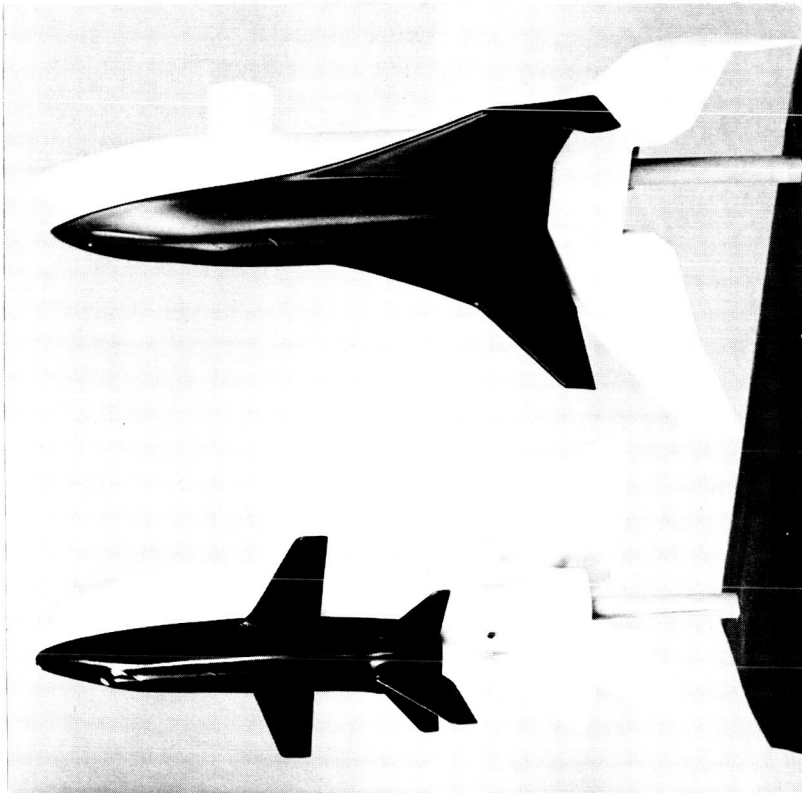
(Figure 6)

This figure shows 1/300-scale models of space shuttle configurations on which static force measurements were obtained. The models were mounted on a turntable balance which measured the two components of horizontal force parallel and normal to the wind. These studies were conducted in a 0.51-by 0.75-meter (20- by 30-inch) open-throat tunnel at wind velocities up to 40 m/sec (130 ft/sec). This tunnel can be characterized as having smooth flow.

As the model was continuously rotated to vary the wind azimuth angle  $\phi$  from  $-10^\circ$  to  $190^\circ$ , the lift and drag forces were plotted against  $\phi$  by means of an x-y plotter.

# SPACE SHUTTLE GROUND-WIND LOAD STUDY

## SPACE SHUTTLE MODELS



## MODEL IN TUNNEL



Figure 6

## STATIC AERODYNAMIC COEFFICIENTS FOR SPACE SHUTTLE

(Figure 7)

The static lift and drag coefficients for four configurations are given in figures 7(a) and 7(b) as functions of wind azimuth angle. The coefficients are for the booster alone and the booster and orbiter combined. The reference areas used in these coefficients are the projected planform areas of the booster and coupled booster-orbiter, respectively. Figure 7(a) is for the delta-wing booster alone, as shown by the dashed line, and for the combination of delta-wing booster and straight-wing orbiter, shown as a solid line. Figure 7(b) gives the results for the booster with wing-tip fins as the dashed curve, and the combination of this booster and the delta-wing orbiter is shown as a solid curve.

In comparing the booster-alone configurations, substantial differences in the lift and drag characteristics can be seen. Both lift and drag are higher for the delta-wing booster than for the tip-fin booster. As was mentioned in the discussion of figure 5, the criterion for galloping instability depends on the magnitude of the negative lift-curve slope. From these curves one would judge that the delta booster is the most susceptible to galloping instability because of the steepness of the negative lift-curve slope near an azimuth of  $5^{\circ}$ . Also, it should be noted that mounting the orbiter on the booster has a stabilizing effect in both cases, particularly for the tip-fin booster.

# STATIC AERODYNAMIC COEFFICIENTS FOR SPACE SHUTTLE

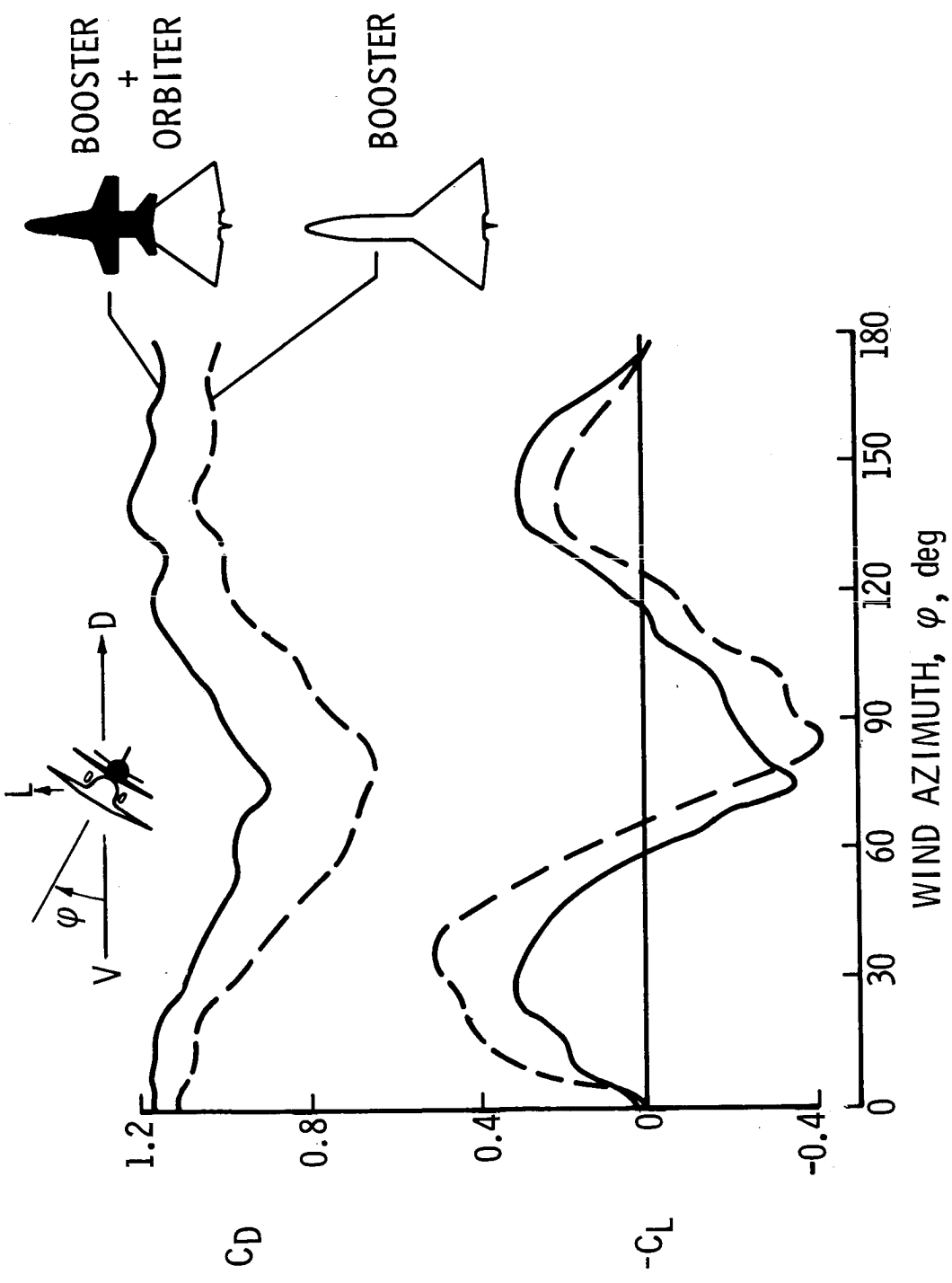


Figure 7(a)

# STATIC AERODYNAMIC COEFFICIENTS FOR SPACE SHUTTLE

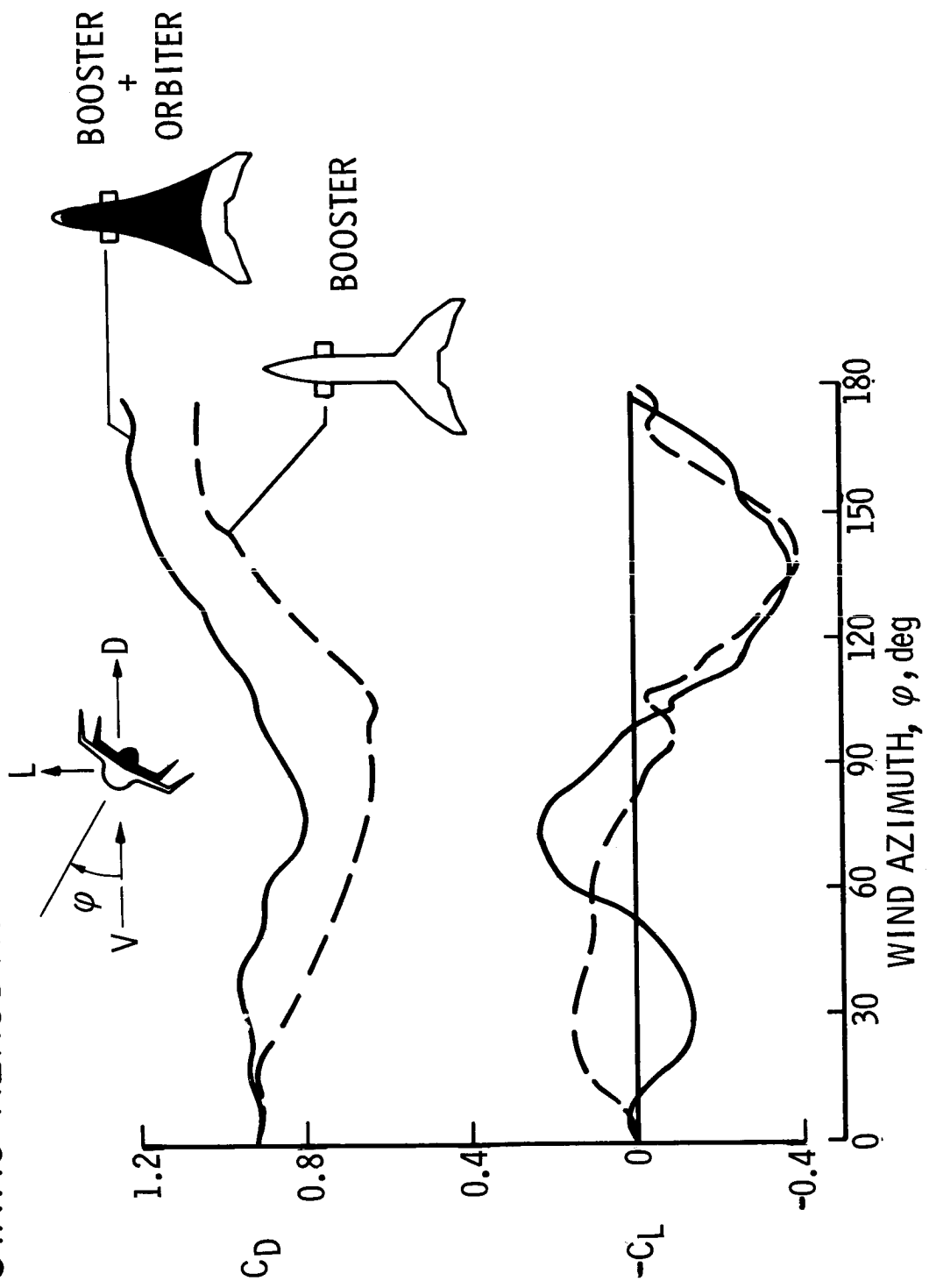


Figure 7(b)

GALLOPING INSTABILITY CHARACTERISTICS OF SPACE SHUTTLE CONFIGURATION -

DELTA-WING BOOSTER

(Figure 8(a))

This figure shows the region of negative aerodynamic damping for the delta-wing booster, for wind azimuth directions near  $\varphi = 0$ . The ordinate on the left side of the plot is the negative aerodynamic damping coefficient  $-(C_{L\alpha} + C_D)$ . The ordinate on the right is the structural damping that would be required to prevent galloping instability for the most critical condition; that is, for an empty-fuel weight condition at the design maximum wind speed of 40 m/sec (130 ft/sec).

The next figure shows how the galloping instability of this booster would be affected by the addition of an orbiter.

GALLOPING INSTABILITY CHARACTERISTICS  
OF SPACE SHUTTLE CONFIGURATION

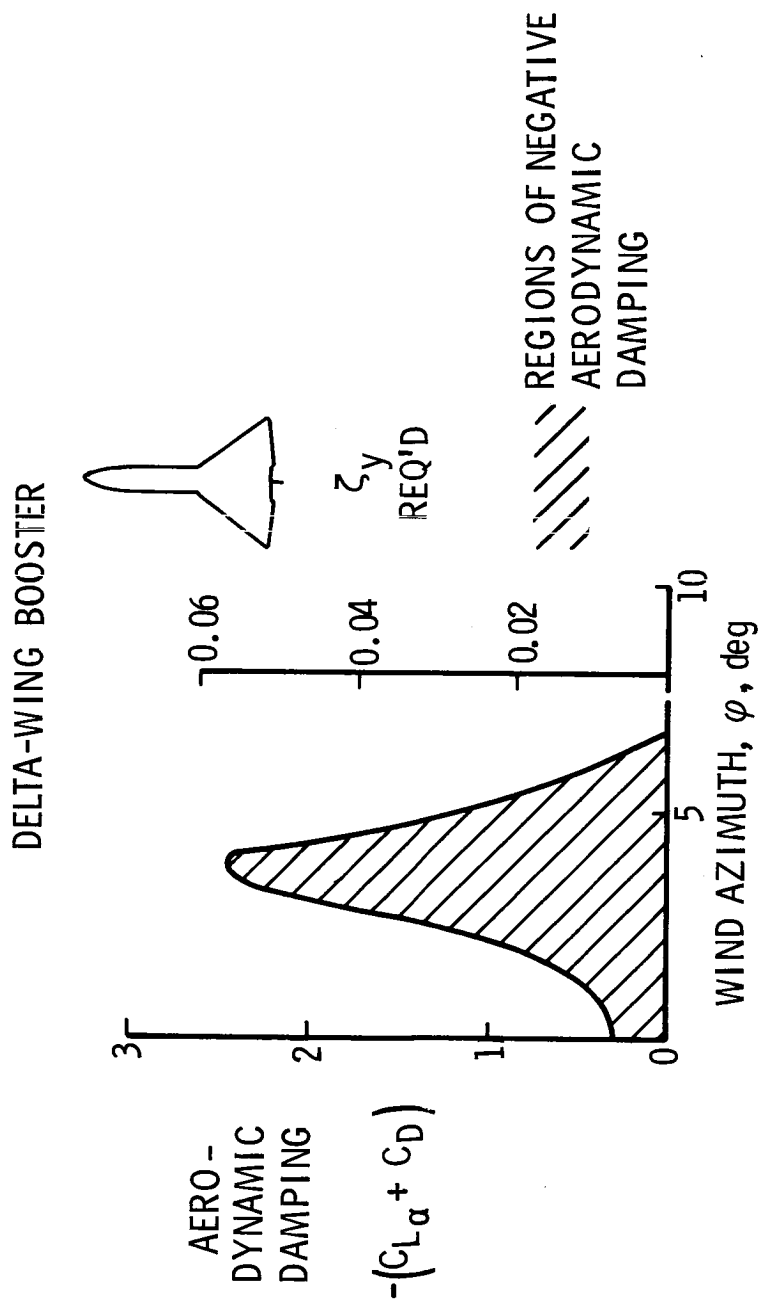


Figure 8(a)

GALLOPING INSTABILITY CHARACTERISTICS OF SPACE SHUTTLE CONFIGURATION –  
DELTA-WING BOOSTER/STRAIGHT-WING ORBITER

(Figure 8(b))

This figure indicates that mounting the orbiter on the booster has a significant stabilizing influence on galloping instability. In comparing these results with those shown in the previous figure for the booster alone we see that for the combination the maximum negative aerodynamic damping is reduced by a factor of 4 (note ordinate scale change) and that the range of critical wind azimuth angles is also reduced. Furthermore, the levels of structural damping required to prevent galloping appear to be less than the inherent structural damping expected in typical launch vehicle structures.

GALLOPING INSTABILITY CHARACTERISTICS OF  
 SPACE SHUTTLE CONFIGURATION  
 DELTA-WING BOOSTER / STRAIGHT-WING ORBITER

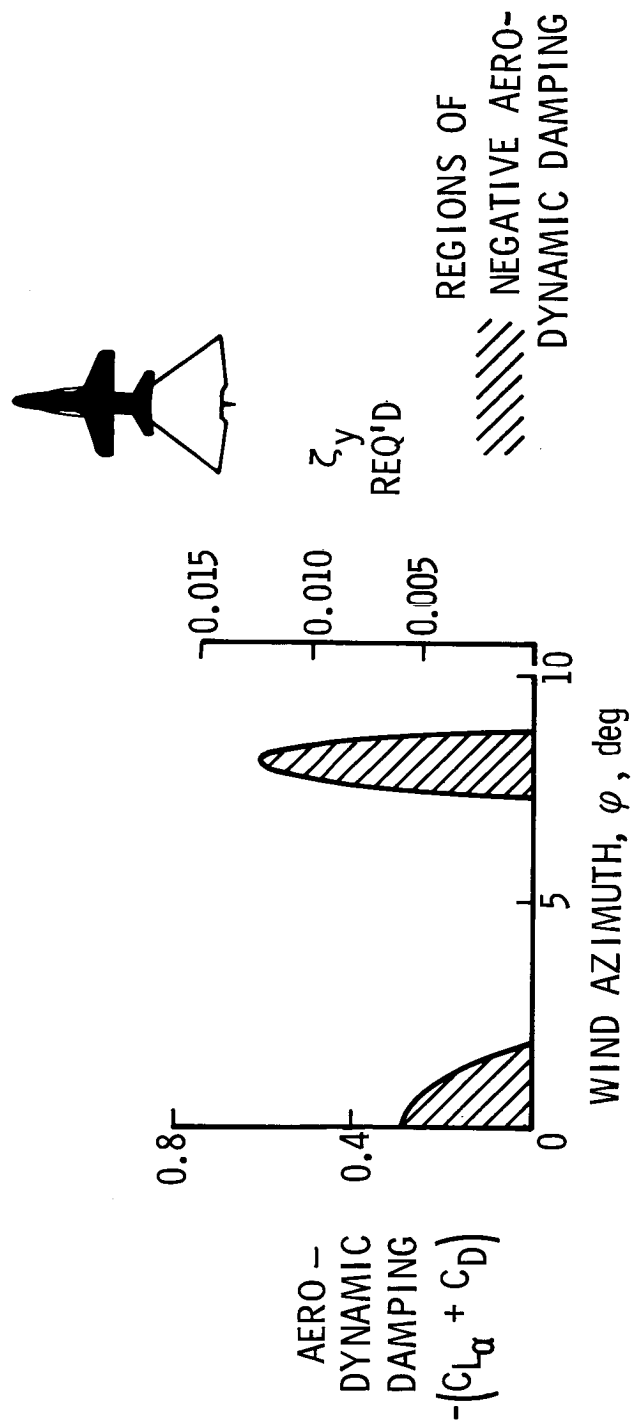


Figure 8(b)

## EFFECT OF REYNOLDS NUMBER

(Figure 9)

The static aerodynamic data thus far presented in this paper have been for small models and at low Reynolds numbers (less than 100 000). Legitimate questions can therefore be raised regarding the use of such low Reynolds number data in predicting drag loads and galloping stability of full-scale shuttle vehicles. Polhamus addressed a similar question in studies related to aircraft directional stability and spinning (ref. 4). These studies showed that the aerodynamic side force on noncircular two-dimensional cylinders frequently exhibits a change in sign with change in Reynolds number. Thus, from the standpoint of galloping, such a body might be stable at one Reynolds number and unstable at another.

To gain some insight into Reynolds number effects for body shapes representative of space shuttle vehicles, a study was conducted in the Langley low-turbulence pressure tunnel on a 1/88-scale straight-wing orbiter model, at pressures up to  $1 \text{ MN/m}^2$  (10 atmospheres). This configuration is the same as the 1/300-scale straight-wing orbiter configuration shown in figure 6. The model was attached, through a strain-gage balance, to a sting which entered the top side of the fuselage so that the model center line was perpendicular to the wind direction. The model could be rotated about its longitudinal axis to simulate a range of wind azimuth angles  $\phi$  from  $-40$  to  $+20^\circ$ . Two fuselage cross-sectional shapes were studied. One had sharp corners on the underside (hard chine) and the other had the corners rounded to a radius of approximately 0.08 of the body width (soft chine).

Results from this study are presented in figure 9 together with data from the smaller scale model of the same configuration. The figure shows the variation of drag coefficient  $C_D$  and the aerodynamic damping coefficient  $-(C_{L\alpha} + C_D)$  over a Reynolds number range of  $0.04 \times 10^6$  to  $4.0 \times 10^6$ . Also shown is a wind velocity scale for the full-scale vehicle.

Some conclusions to be drawn from this figure are that drag is relatively insensitive to Reynolds number for both the soft- and the hard-chine bodies. Aerodynamic damping, on the other hand, undergoes large variations with Reynolds number — particularly for the soft-chine model, which changes from a maximum stable damping to a maximum unstable damping in going from a Reynolds number of  $1.2 \times 10^6$  to  $2.2 \times 10^6$ . The hard-chine model is less sensitive to Reynolds number, presumably because sharp corners tend to fix the point of flow separation. Thus it appears that galloping stability predictions presented in figure 8 may be drastically altered by Reynolds number effects. These and other considerations serve to emphasize the need for subsequent space shuttle ground-wind load studies in a high Reynolds number facility, such as are planned in the Langley transonic dynamics tunnel with Freon as a test medium. In addition to these studies in smooth-flow wind tunnels, similar studies are planned in which the wind shear and turbulence spectra of atmospheric ground winds will be simulated in a wind tunnel by use of techniques such as those described in reference 5.

EFFECT OF REYNOLDS NUMBER ON SPACE SHUTTLE  
GALLOPING STABILITY COEFFICIENTS

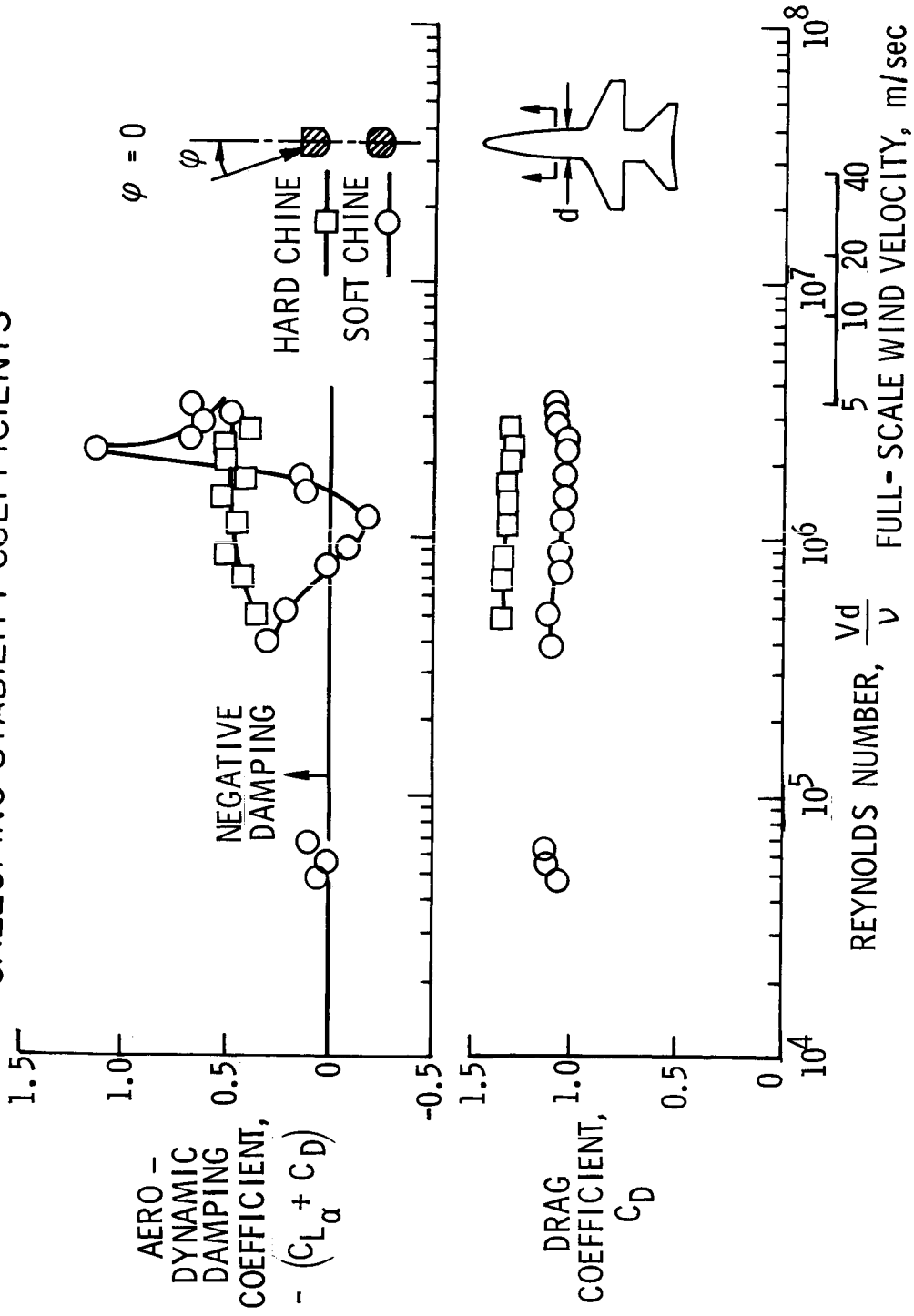


Figure 9

## CONCLUDING REMARKS

Results of wind-tunnel tests indicate that stop-sign flutter is not a cause for concern except perhaps during erection of the vehicle on the launch pad. On the other hand, galloping instability may be a real problem. Because of the sensitivity to Reynolds number effects, the extent of the problem will have to be determined by studies at high Reynolds numbers.

The next phase of ground-wind-load model studies will be conducted in the Langley transonic dynamics tunnel in Freon. Lightweight rigid models of space shuttle configurations will be attached to a flexible mount system to simulate fundamental bending modes of the vehicle. It is expected that these tests will result in clarification of the extent of the ground wind loads problem of proposed space shuttle configurations.

The development of an analysis to calculate the response of space shuttle configurations to loads from wind shear and turbulence is also underway.

## REFERENCES

1. Reed, Wilmer H., III: Ground-Wind-Load Considerations for Space Shuttle Vehicles. Space Transportation System Technology Symposium, NASA TM X-52876, Vol. II, 1970, pp. 143-160.
2. Boyden, Richmond P.: Theoretical and Experimental Studies of the Effects of Leading-Edge Vortex Flow on the Roll Damping of Slender Wings. AIAA Paper No. 70-540, May 1970.
3. Den Hartog, J. P.: Mechanical Vibrations. Fourth ed., McGraw-Hill Book Co., Inc., 1956.
4. Polhamus, Edward C.: Effect of Flow Incidence and Reynolds Number on Low-Speed Aerodynamic Characteristics of Several Noncircular Cylinders With Applications to Directional Stability and Spinning. NASA TR R-29, 1959. (Supersedes NACA TN 4176.)
5. Templin, R. J.: Wind Tunnel Simulation of Ground Wind Shear and Turbulence Spectra With Possible Application to Space Shuttle Launch Problems. Space Transportation System Technology Symposium, NASA TM X-52876, Vol. II, 1970, pp. 161-175.

EFFECTS OF SPACE SHUTTLE CONFIGURATION ON WING BUFFET AND FLUTTER

PART I - LAUNCH VEHICLE WING WITH TIP FIN

By Robert C. Goetz  
NASA Langley Research Center, Hampton, Virginia

SUMMARY

Several emerging configuration features of the space shuttle vehicle are examined in an effort to determine their influence on wing aeroelastic behavior. Configuration features discussed include wings with intersecting surfaces, wings in proximity to one another, and thick wings at high angles of attack. Some recent experimental results are presented that are applicable to these configuration features.

These results indicate that large tip fins proposed for launch vehicle wings have a detrimental effect on the wing flutter characteristics over the subsonic and transonic speed range; that aerodynamic interference effects of wings in proximity affect their transonic flutter behavior, and that a continuing investigation to determine the exact effects for specific configurations is needed; that thick delta wings with tip fins will experience buffet during launch, and that maximum buffeting associated with a current design was encountered between angles of attack from about  $25^{\circ}$  to  $30^{\circ}$ . The full-scale maximum buffet intensities were higher than those associated with more conventional wing configurations.

## INTRODUCTION

(Figure 1)

Last year at the Space Transportation System Technology Symposium held at the NASA Lewis Research Center, the technical areas of wing buffet and flutter were surveyed to determine whether the present state of the art of these fields was sufficient to encompass envisioned space shuttle vehicles and their proposed missions. (See ref. 1.) While the mission was rather well defined, a large number of vehicle configurations for the mission were still being studied. Consequently, the emphases of the presentations at that time were devoted more to the problems associated with particular flight conditions. Since the phenomena of wing buffet and flutter are also highly configuration dependent and since specific vehicle designs are now emerging, the emphasis of this paper will be on configuration effects pertaining to wing buffet and flutter.

An effort has been undertaken to determine the buffet and flutter susceptibility of some unique wing configuration features that are evolving for the space shuttle vehicle. Several of these configuration features are illustrated in figure 1. The launch vehicle configuration shown has intersecting surfaces, that is, wing tip fins. In the launch configuration, the orbiter vehicle wing is located so as to have an aerodynamic interfering effect on the launch vehicle wing. During reentry and the transition maneuver, the relatively thick wings of each vehicle will be, individually, at high angles of attack. The purpose of this paper is to present highlights of some recent experimental results obtained at the NASA Langley Research Center that are applicable to these unique space shuttle wing configurations.

SOME SPACE SHUTTLE CONFIGURATION EFFECTS  
ON WING BUFFET AND FLUTTER

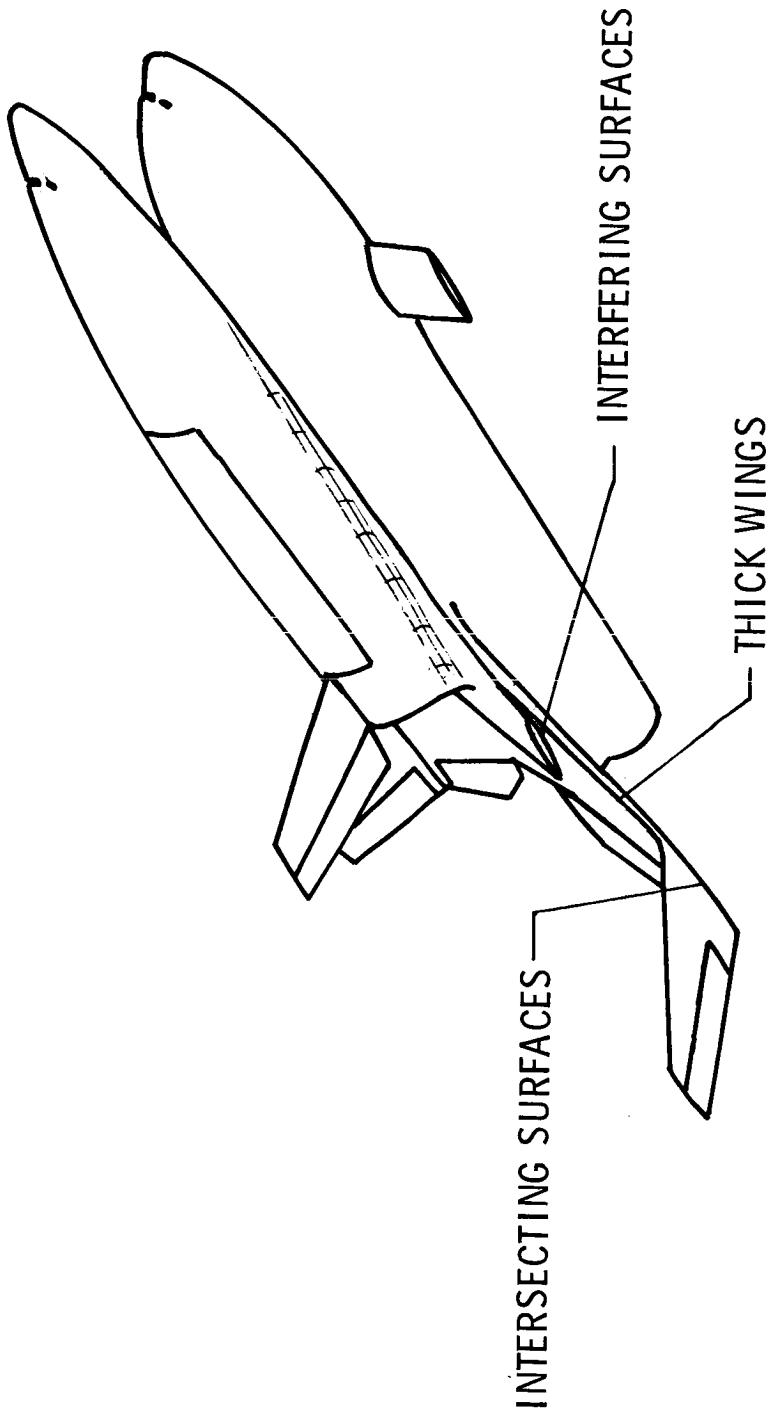


Figure 1

## FLUTTER MODELS OF A SPACE SHUTTLE LAUNCH VEHICLE WING WITH TIP FINS

(Figure 2)

First, a program was conducted to determine the effect of a large tip fin on the flutter characteristics of a 0.01-scale model of a proposed space shuttle launch vehicle wing. Several model configurations were tested, and two of these semispan models mounted on a sting in the Langley transonic blowdown tunnel are shown in figure 2. These two model configurations were tested at zero angle of attack in an effort to isolate the aerodynamic influence of the large tip fin on the wing flutter behavior. The model shown on the left has leading- and trailing-edge sweep of  $40^{\circ}$  and  $20^{\circ}$ , respectively. The fin span is about 0.9 of the wing span. The fin has  $60^{\circ}$  of dihedral and is at zero angle of attack with respect to the flow, that is, has no toe-in. Both the wing and the fin have 10-percent-thick NACA 64-series airfoil sections. The wing model shown on the right is an identical model with the fin removed and replaced with a ballast, which simulates the mass and torsional inertia of the fin. Flutter data have been obtained for both models over the Mach number range from about 0.5 to 1.3.

**FLUTTER MODELS OF SPACE SHUTTLE LAUNCH  
VEHICLE WING**

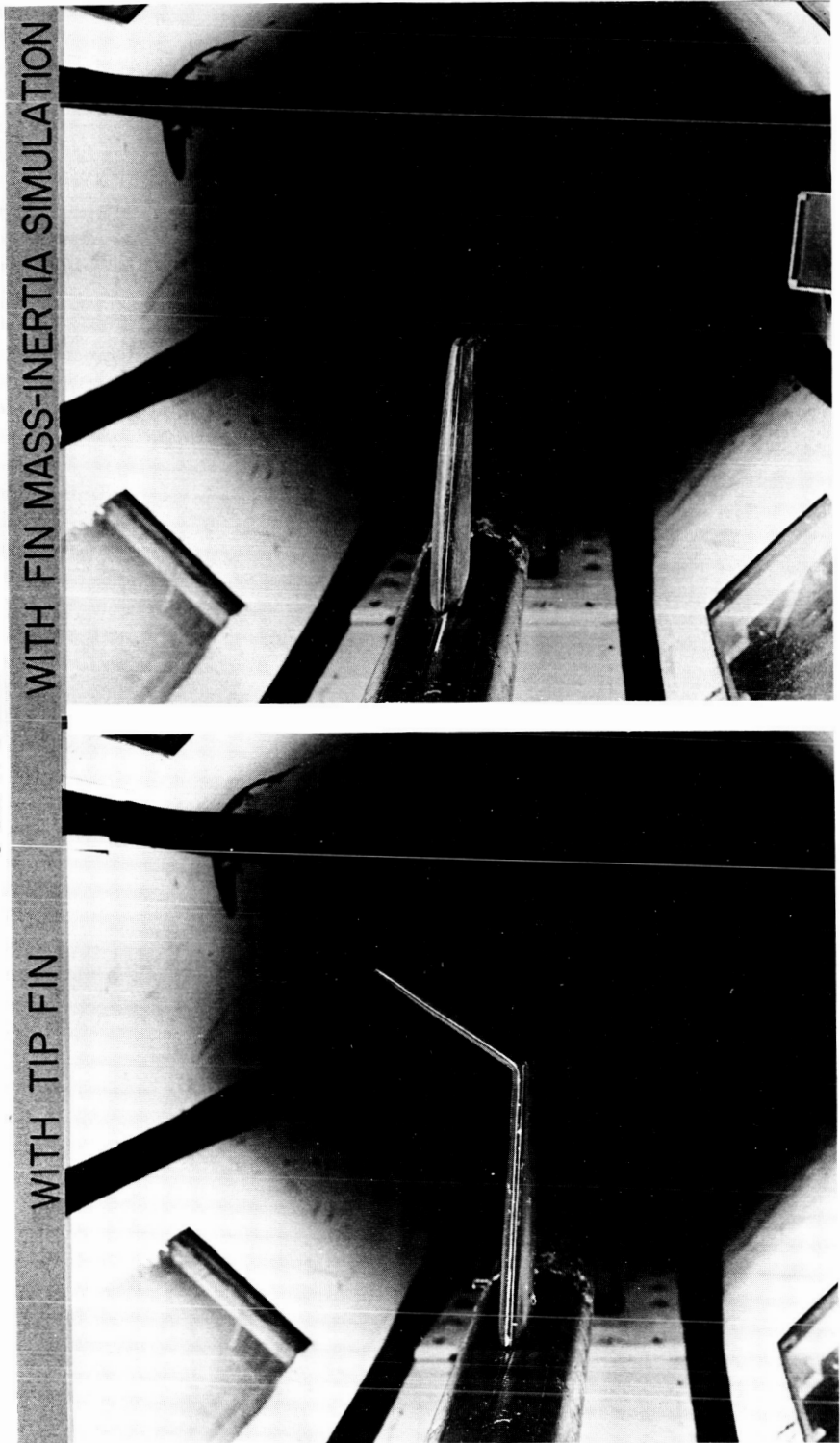


Figure 2

## EFFECT OF WING TIP FIN ON WING FLUTTER CHARACTERISTICS

(Figure 3)

Some results of this flutter program illustrating the effect the tip fin has on the flutter behavior of the wing are shown in figure 3. The results are presented in terms of the Mach number  $M$  and the flutter-velocity-index parameter  $\frac{V}{b\omega_r \sqrt{\mu}}$ . This parameter is proportional to the flutter velocity  $V$  which is nondimensionalized by the product of a reference semichord  $b$ , a reference circular frequency  $\omega_r$ , and the mass ratio  $\mu$ .

The solid curve represents the flutter boundary for the wing with tip fin, and the dashed curve represents the flutter boundary for the wing alone. A comparison of these boundaries reveals two predominate effects associated with the fin on the wing flutter behavior. First, the Mach number at which the minimum flutter speed is encountered shifts to a lower value. For example, for the wing alone, the minimum flutter speed occurs at a Mach number of about 1.05 to 1.10, and for the wing with tip fin, the minimum flutter speed occurs at a Mach number of about 0.95. Secondly, the flutter speed is reduced over the Mach number range up to  $M = 1.15$ . For the lower range of subsonic Mach numbers, this reduction is about 27 percent, and at transonic speeds, the value of minimum flutter velocity is reduced about 45 percent. Supersonically, the two boundaries seem to be coalescing. Consequently, it can be concluded that the tip fin has a detrimental effect on the flutter behavior of this proposed wing configuration of the space shuttle launch vehicle over the subsonic and transonic Mach number range.

## EFFECT OF WING TIP FIN ON WING FLUTTER CHARACTERISTICS

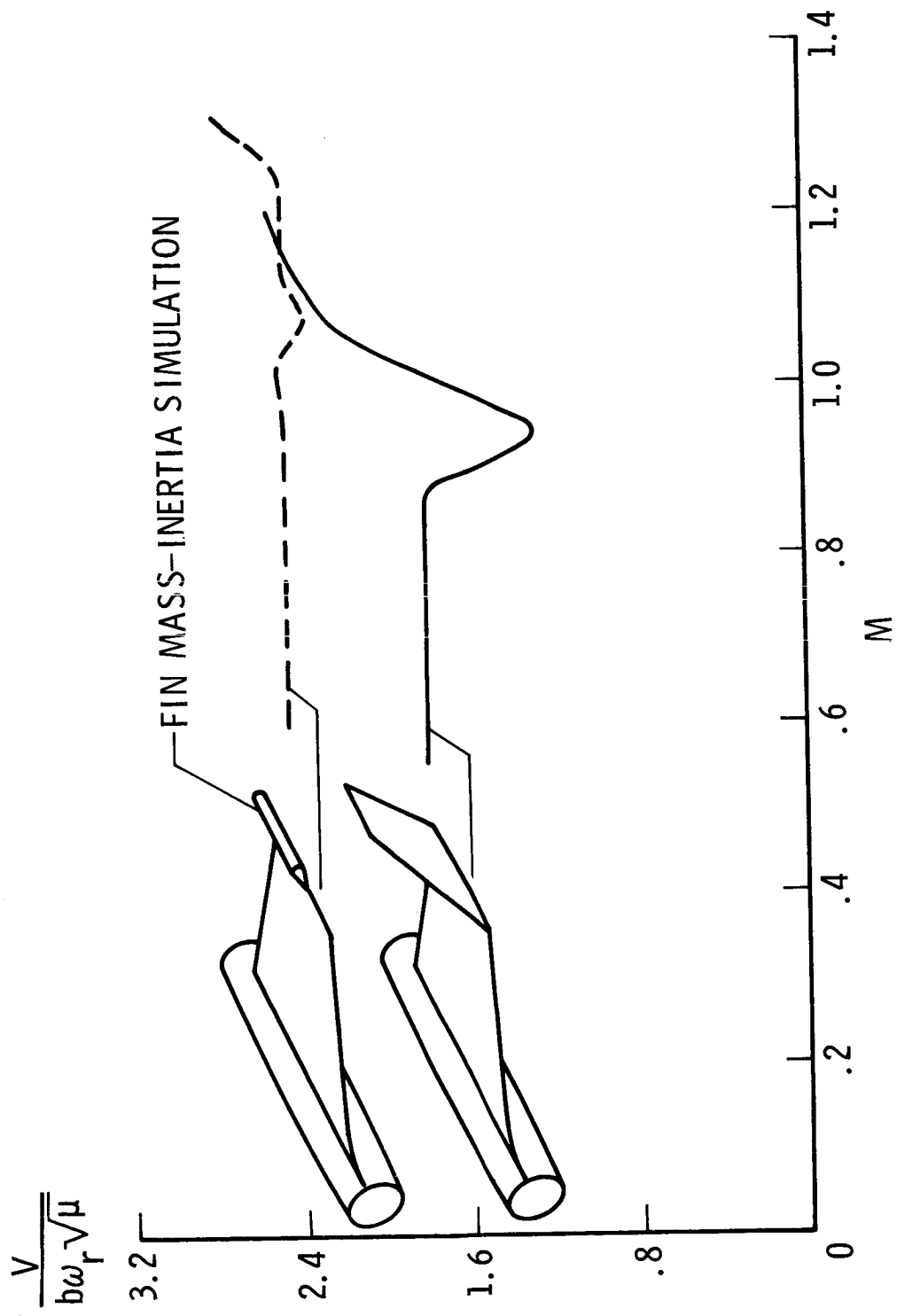


Figure 3

## INTERFERING-SURFACE FLUTTER MODEL

(Figure 4)

The semispan launch vehicle wing model with tip fin that was used for establishing the preliminary flutter trends previously described was also used in combination with other wing configurations to investigate aerodynamic interference effects on the launch vehicle wing flutter trends. One such combination is shown in figure 4. The interfering model is a low aspect ratio, clipped delta wing which simulated the planform of a high cross-range orbiter vehicle configuration. It has an aspect ratio of about 1, leading- and trailing-edge sweep of about  $70^{\circ}$  and  $20^{\circ}$ , respectively, and a taper ratio of about  $1/3$ . This model of the orbiter vehicle wing is a relatively rigid, constant-thickness plate with sharp leading and trailing edges and did not, therefore, simulate wing profile.

Flutter data have been obtained in the Langley transonic blowdown tunnel for the one relative arrangement shown in the figure. More specifically, the biplanar separation distance  $h$  between the two models is about 0.20 of the root chord of the fin  $c_f$ , and the coplanar separation placed the trailing-edge tip of the model of the orbiter vehicle wing directly over the leading edge of the model of the launch vehicle wing at about its  $3/4$  span.

INTERFERING-SURFACE FLUTTER MODEL



Figure 4

## (Figure 5)

Some results of the flutter investigation of two wings in proximity to one another are shown in figure 5. Flutter boundaries are again presented as variations of the flutter-velocity-index parameter with Mach number. The solid curve represents the boundary for the launch vehicle wing with tip fin, and the dashed curve, as defined by the circular symbols, represents the boundary for the same wing in combination with the interfering orbiter vehicle wing. Interference effects on the flutter characteristics of the launch vehicle wing are seen by comparing the two boundaries. The minimum flutter speed shifts to a slightly lower Mach number and the flutter speed is increased over most of the Mach number range investigated. These results were expected based on previous experimental interference flutter studies of straight wings. (See ref. 2.) However, these previous studies also indicated that relative flexibilities of the two wings, as well as wing profile of the interfering wing, are important variables affecting flutter boundaries. Consequently, as these detailed design parameters become available, they will be incorporated into configurations investigated in our continuing interference flutter program.

TRANSONIC FLUTTER OF WINGS IN PROXIMITY

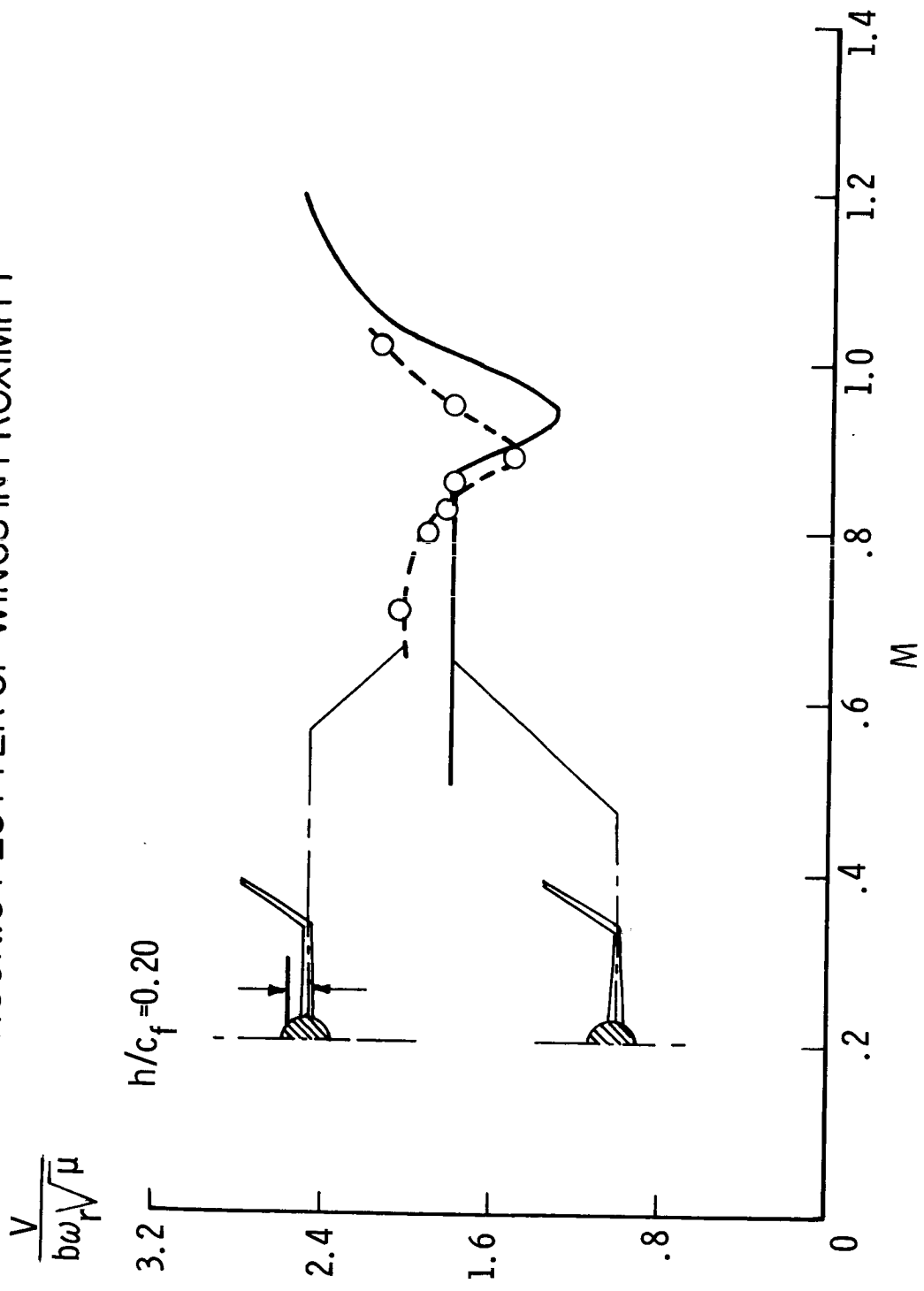


Figure 5

## STALL-FLUTTER AND BUFFET MODEL

### (Figure 6)

Previous experience (refs. 3 to 5) has shown that stall flutter and buffeting of wings at angles of attack are highly configuration sensitive. Buffet boundaries depend almost entirely on the aerodynamics of the configuration, whereas stall-flutter boundaries may also be altered by changes of structural parameters as well. At present, there are no analytical methods available for predicting either of these two phenomena. Such predictions must be based on experimental information, generally obtained from wind-tunnel tests of scaled models. An exploratory wind-tunnel investigation was conducted of some early wing concepts for the space shuttle vehicle. (See ref. 2.) A more recent study was conducted to determine the buffet and stall flutter susceptibility of the concept of the launch vehicle wing with tip fins. The 0.05-scale semispan wing model used in the study is shown in figure 6. The model is shown mounted on a fairing to the side wall of the Langley transonic dynamics tunnel. The model had about a 0.9-meter (3-foot) root chord, as an indication of its overall size. The general testing procedure included the establishment of flow at a given Mach number and dynamic pressure with the model at zero angle of attack as shown on the left of the figure. The model was then rotated through the angle-of-attack range at a constant rate to  $90^\circ$ , as shown on the right of the figure. Response of the model was studied in terms of bending-moment response. Although this quantity may not represent the critical design-load condition, bending moments do provide a measure of buffet onset and a relative measure of buffet intensities. Strain gages used to record bending moments were located at the wing root and just outboard of the wing-fin junction.



Figure 6

## BUFFET BOUNDARIES

(Figure 7)

Some results from this program are shown in figure 7. No stall flutter was encountered over the angle-of-attack  $\alpha$  range from  $0^\circ$  to  $90^\circ$  and over the Mach number range from about 0.5 to 1.1. However, buffet was encountered as expected and the resulting buffet boundaries are presented as functions of angle of attack and Mach number. The buffet boundary for the launch vehicle wing with tip fin is shown by the solid curve in this figure; and wing buffeting at very low angles of attack including zero is indicated. This boundary implies that the launch vehicle wing will buffet during launch from high subsonic speeds to a Mach number slightly over 1.0. The angles of attack at which the configuration experienced maximum relative buffet intensities are indicated by the circular symbols in the figure. Over the Mach number range of the investigation, these angles were consistently between about  $25^\circ$  and  $30^\circ$ .

## BUFFET BOUNDARIES

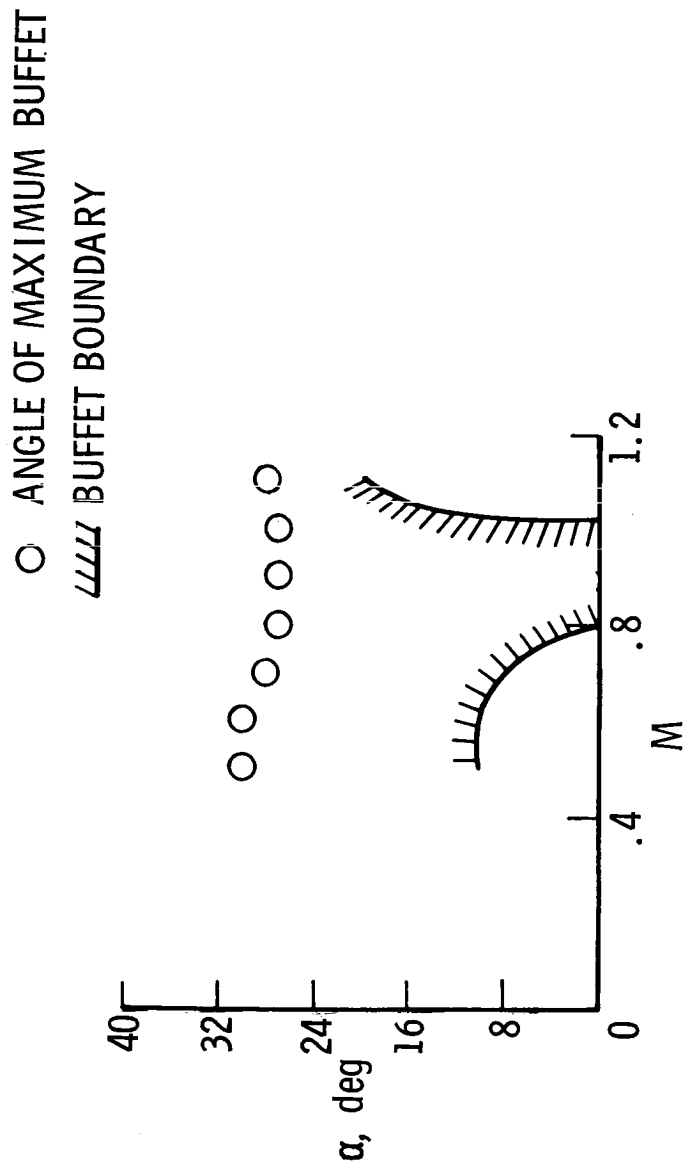


Figure 7

## PREDICTED FULL-SCALE MAXIMUM BUFFET INTENSITIES

(Figure 8)

The severity of the maximum buffet intensities associated with the angles of attack between  $25^\circ$  and  $30^\circ$  is shown in figure 8. The results on the left of the figure show the ratio of maximum predicted full-scale bending-moment fluctuations  $\bar{M}_{\text{dyn}}$  to static bending moments  $\bar{M}_{\text{static}}$  as a function of Mach number. The highest value of this ratio occurs at a Mach number of about 0.8, where the fluctuating bending-moment intensities are about 25 percent of the static bending moment measured at the wing root. However, a similar evaluation of the fin response, shown on the right of the figure, indicates fluctuating bending-moment intensities of about 55 percent of the static bending moments measured at the fin root. The point to be amplified from these results is that these buffet intensities are higher than those normally associated with more conventional wing configurations.

It should be kept in mind that these buffet intensities are only first approximations. However, they dictate that additional experimental investigations using elastically scaled models of similar wing configurations with intersecting tip fins be conducted in order to avoid large weight penalties in the wing structure due to dynamic loads.

PREDICTED FULL-SCALE MAXIMUM BUFFET INTENSITIES

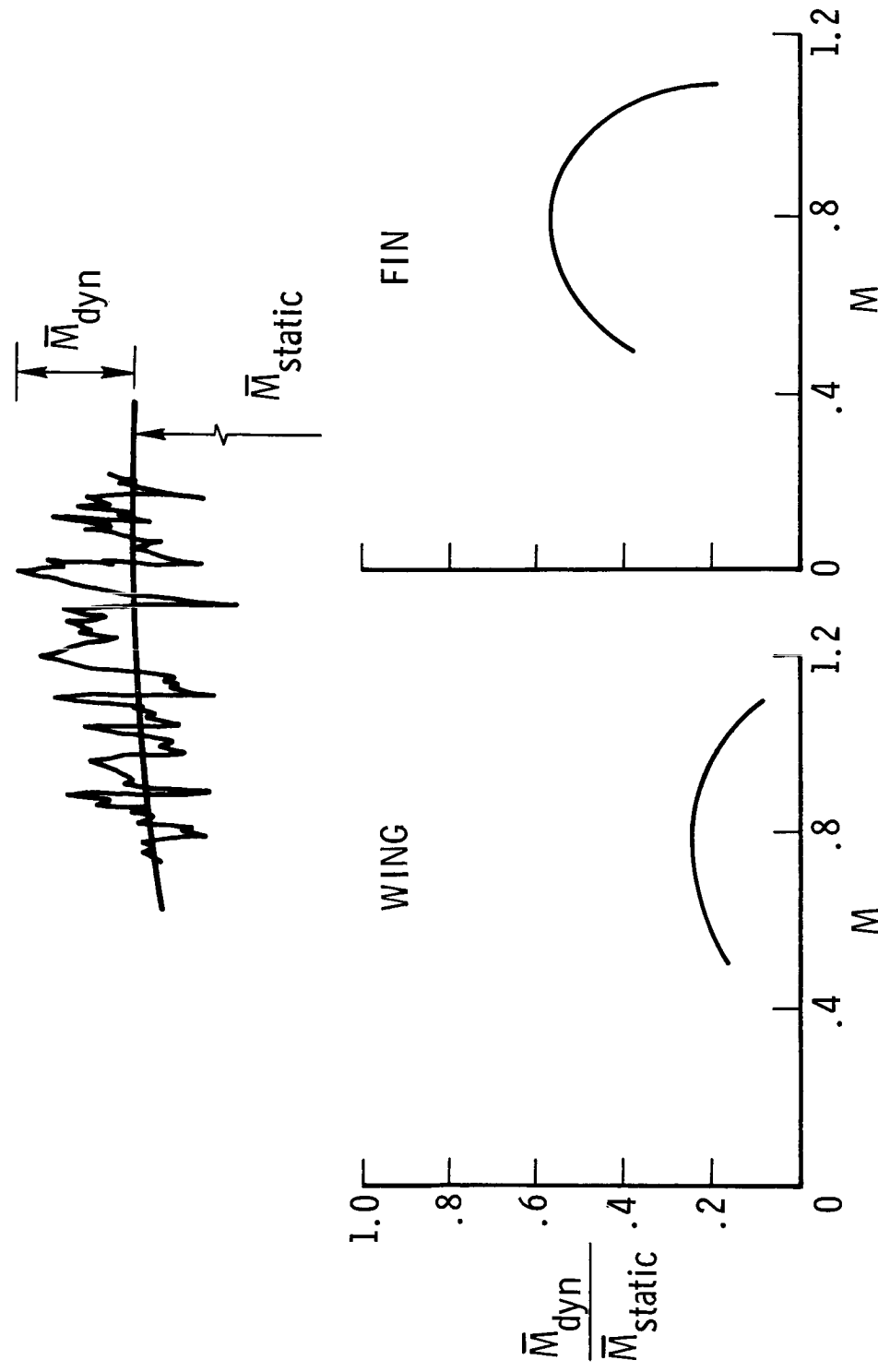


Figure 8

## CONCLUDING REMARKS

Flutter and buffet of wings are so configuration sensitive that the most critical research will be needed after final configuration selection. However, some important research is needed in the interim as unique space shuttle wing configurations evolve. The purpose of this interim research is threefold. First, experimental subsonic and supersonic flutter data for new configurations must be provided. These data can be compared with existing nonplanar flutter theories in order to access the range of applicability of these relatively new theories. Second, preliminary design information, such as experimental transonic flutter trends, stall flutter at angle of attack, and buffet data, is needed since no analytical prediction methods for these phenomena are presently available. And finally, wing-flutter and buffet technology must be available so that no unexpected problem areas are encountered because of configuration uniqueness. These problem areas would require costly modifications or payload penalties late in the development stage of the program. Avoidance of these problems would help to insure vehicle reliability.

#### REFERENCES

1. Anon.: Space Transportation System Technology Symposium. NASA TM X-52876, Vol. II, 1970.
2. Goetz, Robert C.: Lifting and Control Surface Flutter. Space Transportation System Technology Symposium, NASA TM X-52876, Vol. II, 1970, pp. 177-198.
3. Rainey, A. Gerald: Preliminary Study of Some Factors Which Affect the Stall-Flutter Characteristics of Thin Wings. NACA TN 3622, 1956. (Supersedes NACA RM 152D08.)
4. Wyss, John A.; and Manfort, James C.: Effects of Airfoil Profile on the Two-Dimensional Flutter Derivatives for Wings Oscillating in Pitch at High Subsonic Speeds. NACA RM A54C24, 1954.
5. Rainey, A. Gerald: Some Observations on Stall Flutter and Buffeting. NACA RM 153E15, 1953.

By Larry L. Erickson, Bruno J. Gambucci,  
and Phillip R. Wilcox

NASA Ames Research Center  
Moffett Field, Calif.

#### SUMMARY

Transonic flutter and buffet results are presented for two elastic models of a proposed space-shuttle straight wing. The models were tested at Mach numbers from 0.6 to 1.1 at various dynamic pressures and at angles of attack up to 18°. Zero degree angle of attack flutter occurred in a narrow Mach number range centered at about Mach 0.85. Stall flutter was not observed although several instances of low torsional damping were noted. At conditions of maximum buffet intensity, model peak dynamic bending moments ranged up to 80% of the corresponding static bending moments.

#### INTRODUCTION

Some straight-wing versions of the proposed space shuttle vehicle have thick, high aspect ratio wings normally associated with flight speeds below the transonic range. The space shuttle must operate through the transonic range where, unfortunately, the aeroelastic behavior cannot be reliably predicted by analytic means.

The present wind-tunnel investigation was undertaken to obtain information on flutter and buffet phenomena associated with transonic flight of the straight wings proposed by the Manned Spacecraft Center. This paper describes the experimental results obtained for two semi-span wall-mounted models. Both models were of identical construction except for a difference in skin thickness. The stronger model was used to investigate buffet and stall flutter at angles of attack up to 18°. The second model was used to investigate zero-degree angle of attack flutter. Tests were conducted in the NASA-Ames 11- by 11-Foot Transonic Wind Tunnel. Results are given in both SI and U. S. Customary Units; measurements were made in U. S. Customary Units.

## WIND TUNNEL AND TEST CONDITIONS

Tests were conducted in the NASA-Ames 11- by 11- Foot Transonic Wind Tunnel. This facility is a slotted-throat, variable-pressure tunnel with an operating range of  $51 \leq p_t \leq 220$  kN/m<sup>2</sup> ( $15 \leq p_t \leq 65$  in.-Hg), where  $p_t$  is the total (stagnation) pressure. The tunnel was operated by varying Mach number while  $p_t$  was held constant.

The stronger wing (model 1) was tested at Mach numbers from 0.6 to 1.05, for angles of attack from zero to 18°, with  $p_t$  held fixed at 51 kN/m<sup>2</sup> (15 in.-Hg). The variation in free-stream dynamic pressure with Mach number at  $p_t = 51$  kN/m<sup>2</sup> (15 in.-Hg) is given by the bottom curve in figure 1. Along this curve the Reynolds number per meter (foot) varies from  $5.9 \times 10^6$  ( $1.8 \times 10^6$ ), at  $M = 0.6$ , to  $7.5 \times 10^6$  ( $2.3 \times 10^6$ ) at  $M = 1.05$ . (The mean aerodynamic chord for both models was 0.473 meters (1.55 feet).)

Wing model 2 was tested at zero degrees angle of attack over the complete pressure range of the tunnel at Mach numbers from 0.6 to 1.1. Flutter occurred only at  $M = 0.85$ , at which the free-stream velocity was approximately 280 m/sec (920 ft/sec). The variation in free-stream dynamic pressure with total pressure, for the 0.85 Mach number, is given by the top curve of figure 1. Along this curve the Reynolds number per meter (foot) varies from  $6.6 \times 10^6$  ( $2 \times 10^6$ ), at  $p_t = 51$  kN/m<sup>2</sup> (15 in.-Hg), to  $29 \times 10^6$  ( $8.8 \times 10^6$ ) at  $p_t = 220$  kN/m<sup>2</sup> (65 in.-Hg).

## DATA ACQUISITION AND REDUCTION

The wing motion was continuously monitored by oscilloscope displays of wing-root strain-gage signals and by a television display from a camera mounted above the wing tip. Five-hundred-frame-per-second motion pictures of the wing motion were taken at several test conditions.

The strain-gage signals due to the fluctuating airloads were recorded on magnetic tape while the flow was held at fixed total pressure and Mach number and the model was held at a fixed angle of attack. These time histories of the model response were taken over a 135 second period for each test condition.

Statistical properties of the recorded strain-gage signals (rms values, peak values, autocorrelation functions) were obtained over a 120 second period. Predominant frequency components were determined from spectral densities, autocorrelations, and oscillograph traces of the recorded time histories. Damping levels were obtained from the envelopes of the autocorrelation functions (reference 1).

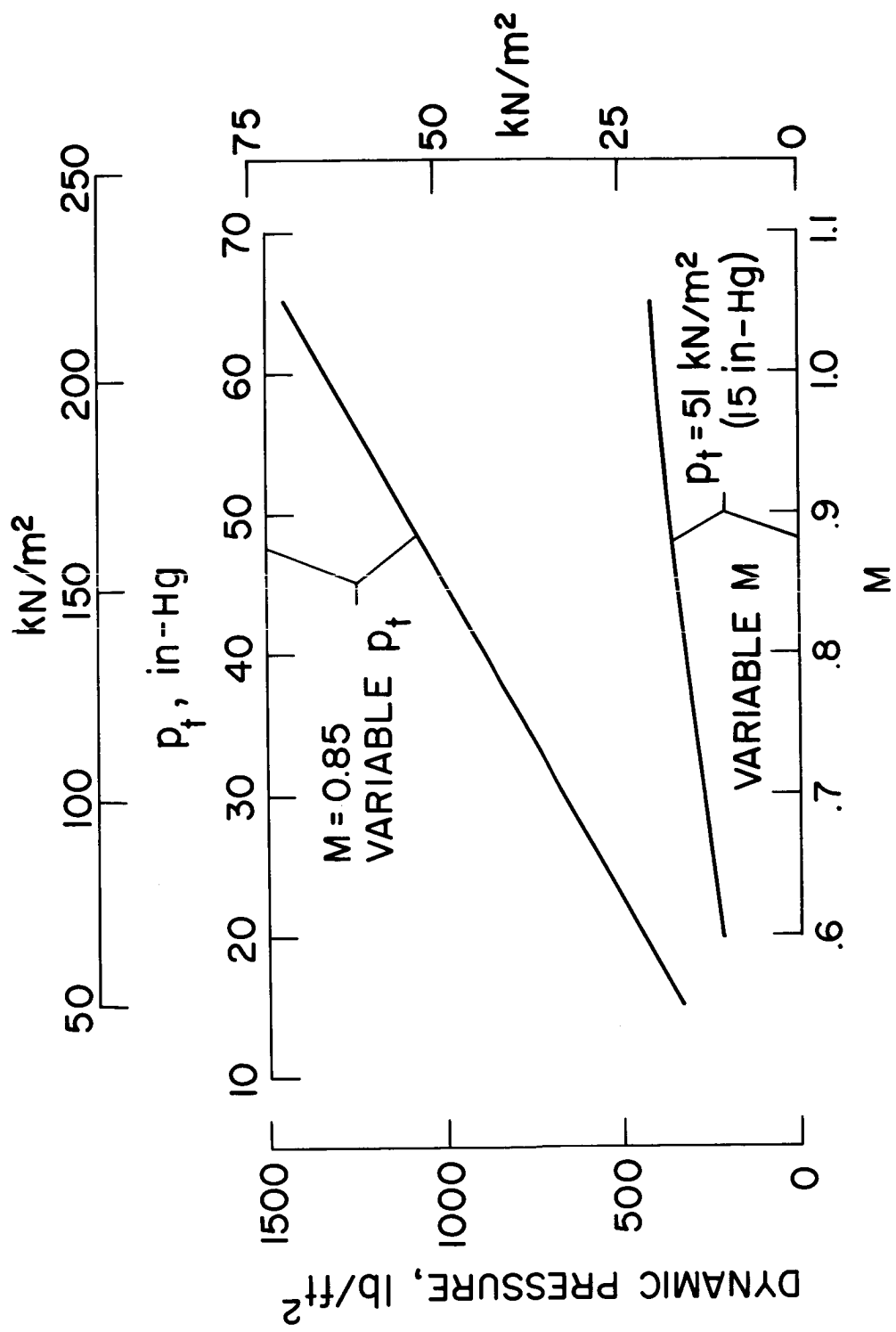


Figure 1

## MODEL GEOMETRY AND CONSTRUCTION

Based on a full-scale (prototype) wing span of 22.9 meters (900 inches), the elastic models have a scale factor of  $\lambda = L_m/L_p = 2/15$ . The model characteristics are described below.

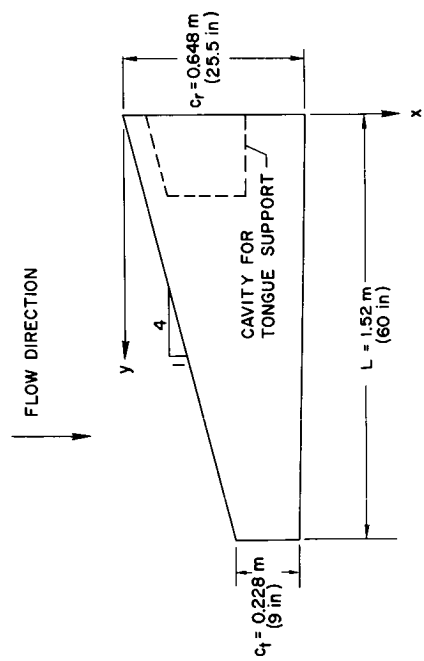
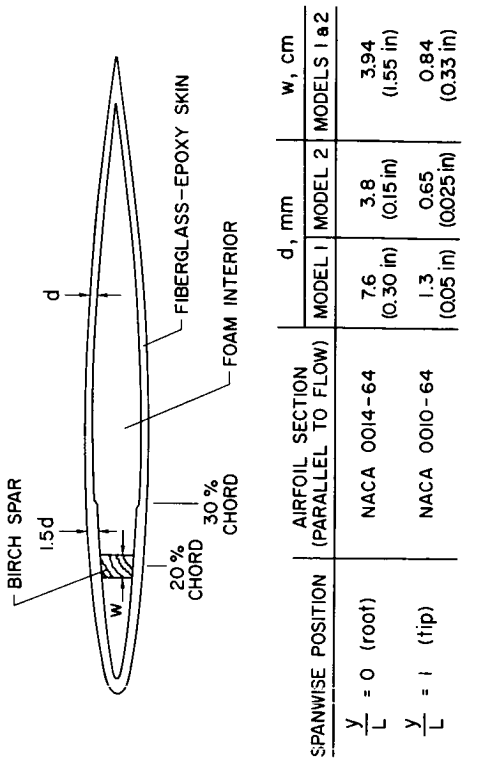
Figure 2a shows the wing-planform geometry. Planform parameters are:

$$\begin{aligned}
 \text{Aspect Ratio} &= \frac{(2L)^2}{S} = 6.96 \\
 \text{Taper Ratio} &= c_t/c_r = 0.353 \\
 \text{Semispan Wing Area} &= \frac{S}{2} = 0.666m^2 \text{ (1035 in.}^2\text{)} \\
 \text{Leading Edge Sweep} &\approx 14^\circ
 \end{aligned}$$

The root chord,  $c_r$ , is at the centerline of the full wing span ( $y = 0$ ).

Wing-construction details are illustrated in figure 2b. The airfoil sections (parallel to the flow) are NACA 00XX-64 profiles with maximum thickness ratios varying from 14% at the wing root ( $y = 0$ ) to 10% at the wing tip ( $y = L$ ). The load carrying structure consists of a fiberglass-epoxy skin (laid over a lightweight foam interior), and a birch spar at the 20% chord position. The spar, and a skin-thickness change at 30% chord, were incorporated to adjust the chordwise positions of the section elastic axis and center of gravity. Spar and skin-thickness dimensions along the span vary linearly between the root and tip values given in the figure. Models 1 and 2 are identical except for the difference in skin thickness dimensions.

Except where noted, testing was performed with boundary-layer trips located 5.7 cm (2-1/4 inches) from the leading edge. These trips ran the length of the wings and consisted of 3.2 mm (1/8 inch) wide strips of 0.25 mm (0.010-inch) diameter glass spheres. There were approximately 40 (100) spheres per cm (inch) of trip length.



(a)

(b)

Figure 2

## SECTION PROPERTIES

The spanwise variation of the section bending stiffness (EI) and the bending-to-torsion stiffness ratio (EI/GK) for both models and the full-scale wing<sup>1</sup> are shown in figure 3 (for sections parallel to the flow). The values of EI and GK for the models were computed from the wing-cross-section geometry and by using  $E = 14 \text{ GN/m}^2$  ( $2.0 \times 10^6 \text{ lb/in}^2$ ) for the fiberglass skin and the birch spar, and  $G = 3.6 \text{ GN/m}^2$  ( $0.53 \times 10^6 \text{ lb/in}^2$ ) for the fiberglass. (The torsional rigidity of the spar was neglected.) The tongue EI was an order of magnitude larger than the root EI of the models.

The wing-root bending stiffnesses were chosen on the basis of static scale relations, tunnel operating range, and model strength. For static spanwise bending deflections of the model and prototype to be geometrically similar, the model test dynamic pressure ( $q_m$ ) is related to the full-scale flight dynamic pressure ( $q_p$ ) by

$$q_m = q_p \frac{(EI)_m}{(EI)_p} \frac{1}{\lambda^4}$$

For the values of EI at  $\bar{y} = y/L = 0.2$  given in figure 3 the above relation becomes  $q_m \approx 2.4 q_p$  for model 1 and  $q_m \approx 1.5 q_p$  for model 2. On this basis model 2 most closely scales the prototype stiffness and was used to investigate zero-degree angle of attack flutter. Model 1 was used to investigate buffet and stall flutter at angles of attack because of its greater strength.

Additional section properties of the model and prototype are given in table I. The model section properties in the table were computed from the chordwise distribution of mass and bending stiffness ( $c$  = chord length).

Table I

	Models	Prototype
	1	2
Distance from leading edge to elastic axis	0.39c 0.43c	0.37c 0.41c
to center of gravity		
Radius of gyration about elastic axis	0.30c	0.29c

<sup>1</sup>The full-scale values of the wing properties stated herein are preliminary estimates obtained from the Manned Spacecraft Center.

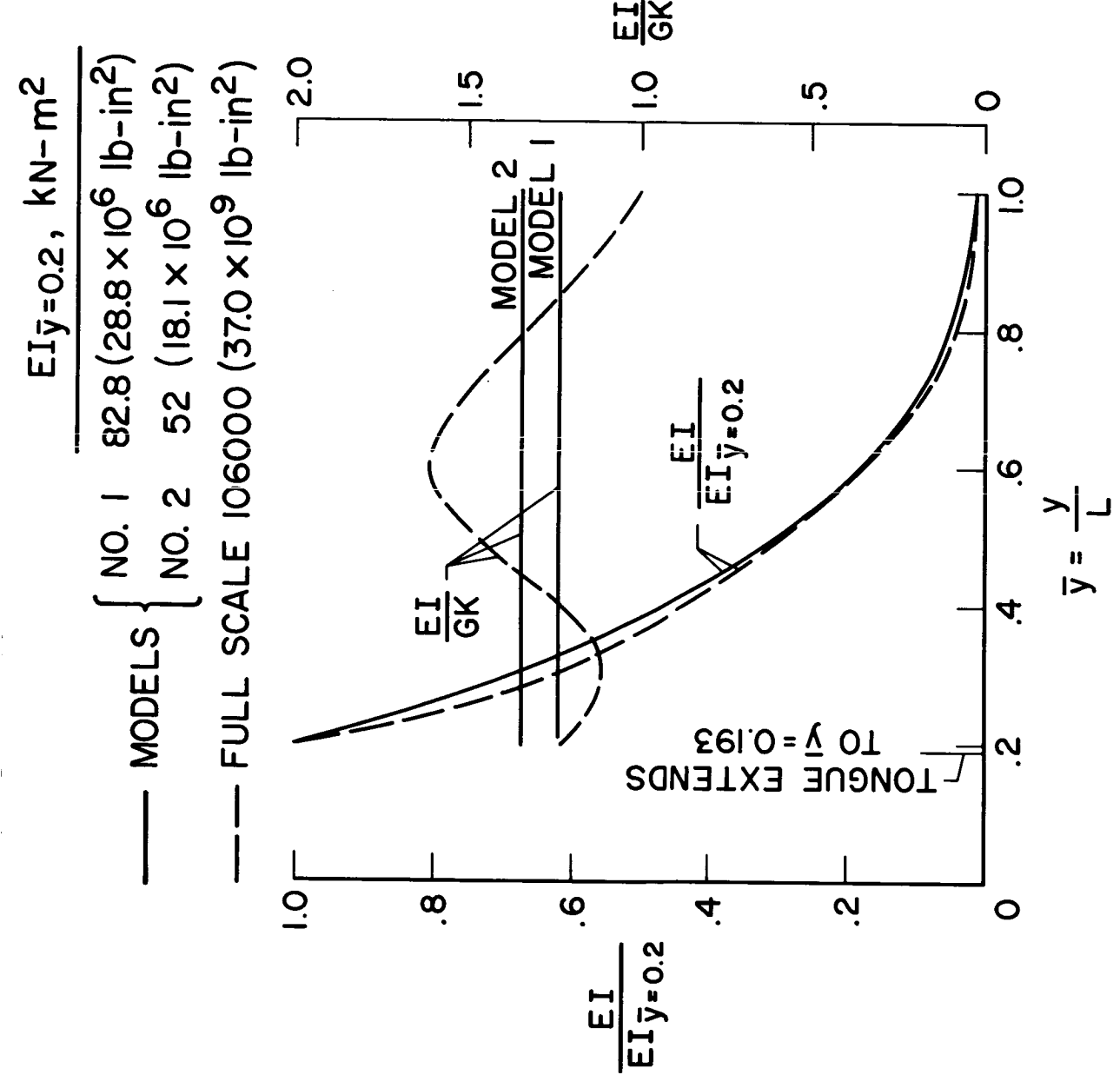


Figure 3

#### STATIC DEFLECTION CURVES

By use of the stiffnesses given in figure 3, spanwise deflections due to a tip load, and spanwise angles of twist due to a tip torque were computed on the basis of simple beam theory. These bending and twisting displacements are shown in figures 4a and 4b, respectively. Also shown are measured deflections and angles of twist. The bending deflections were measured at 40% chord positions and the tip load was at 40% chord. Angles of twist were measured in planes approximately perpendicular to the 40% chord line.

The fairly good agreement between the measured and computed displacements indicates that the model stiffness properties given in figure 3 are reasonably accurate.

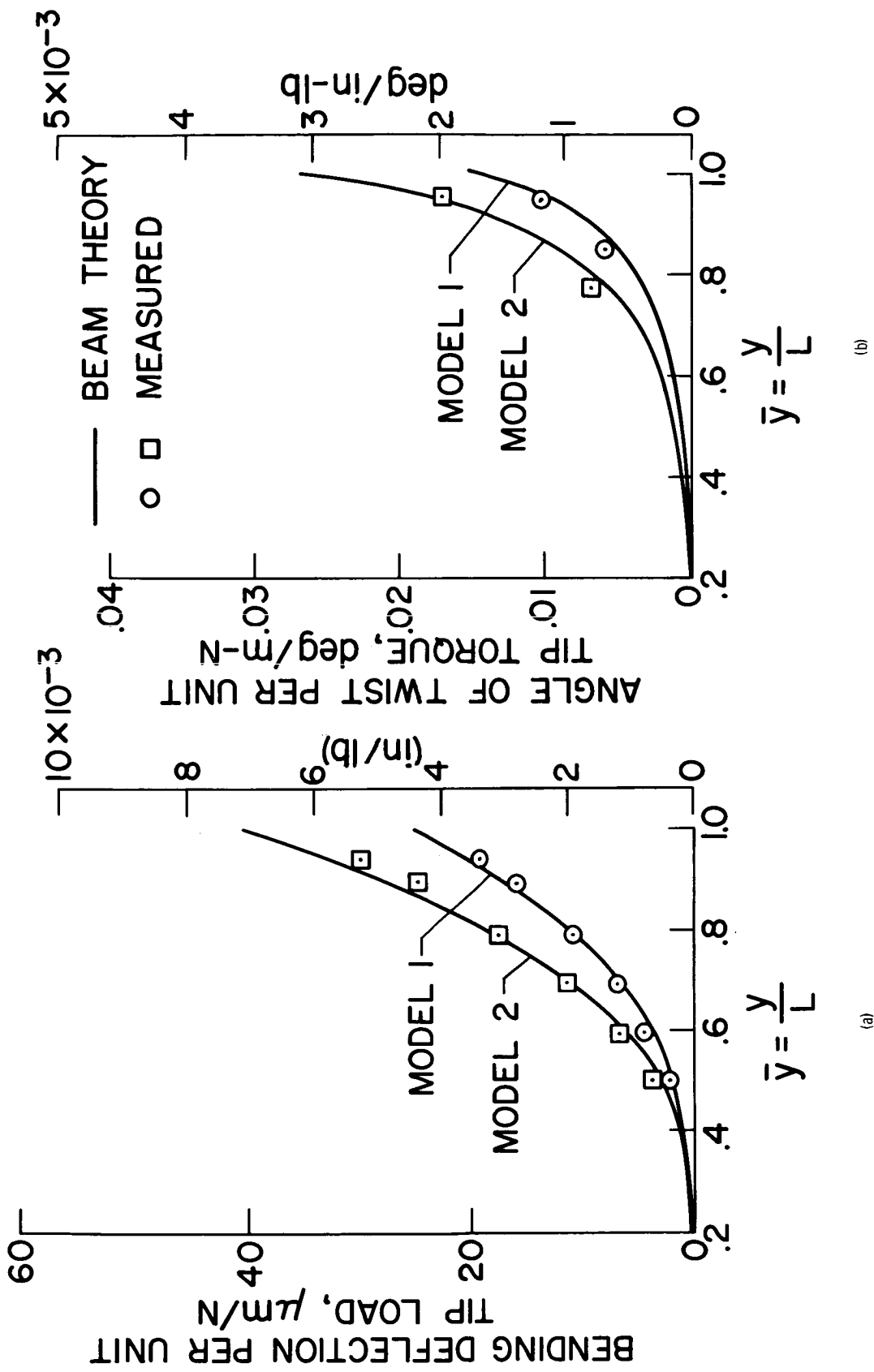


Figure 4

## MASS RATIOS, FREQUENCIES, AND DAMPING RATIOS

The mass ratios<sup>2</sup> of the portion of the model wings extending from  $\bar{y} = 0.2$  to  $\bar{y} = 1.0$  are

$$\mu_1 = 53.5/\rho_\infty, ((1040 \times 10^{-4}) / \rho_\infty)$$

$$\mu_2 = 31.2/\rho_\infty, ((608 \times 10^{-4}) / \rho_\infty)$$

for models 1 and 2, respectively, where  $\rho_\infty$  is the free-stream density in  $\text{kg/m}^2$  (slugs/ft<sup>3</sup>). These mass ratios are shown in figure 5.

Measured still-air frequencies and damping ratios are given in table II.

		Strongback Installation		Wind-Tunnel Installation	
		Model 1	Model 2	Model 1	Model 2
Frequencies (Hz)	1st Bending	39	36.5	38	35.5
	2nd Bending	100	102		
	1st Torsion	140	143		
Damping Ratios (% of critical)	1st Bending	0.3%	0.5%	0.8%	0.8%
	2nd Bending	0.5%	0.5%		
	1st Torsion	0.8%	0.8%		

Predicted first bending and first torsional frequencies for the full-scale wing are 6.98 and 19.3 Hz, respectively.

$$2\mu = \frac{\int m_w dy}{\rho_\infty \frac{\pi}{4} \int c^2 dy}$$

where  $m_w$  is the wing mass per unit length.

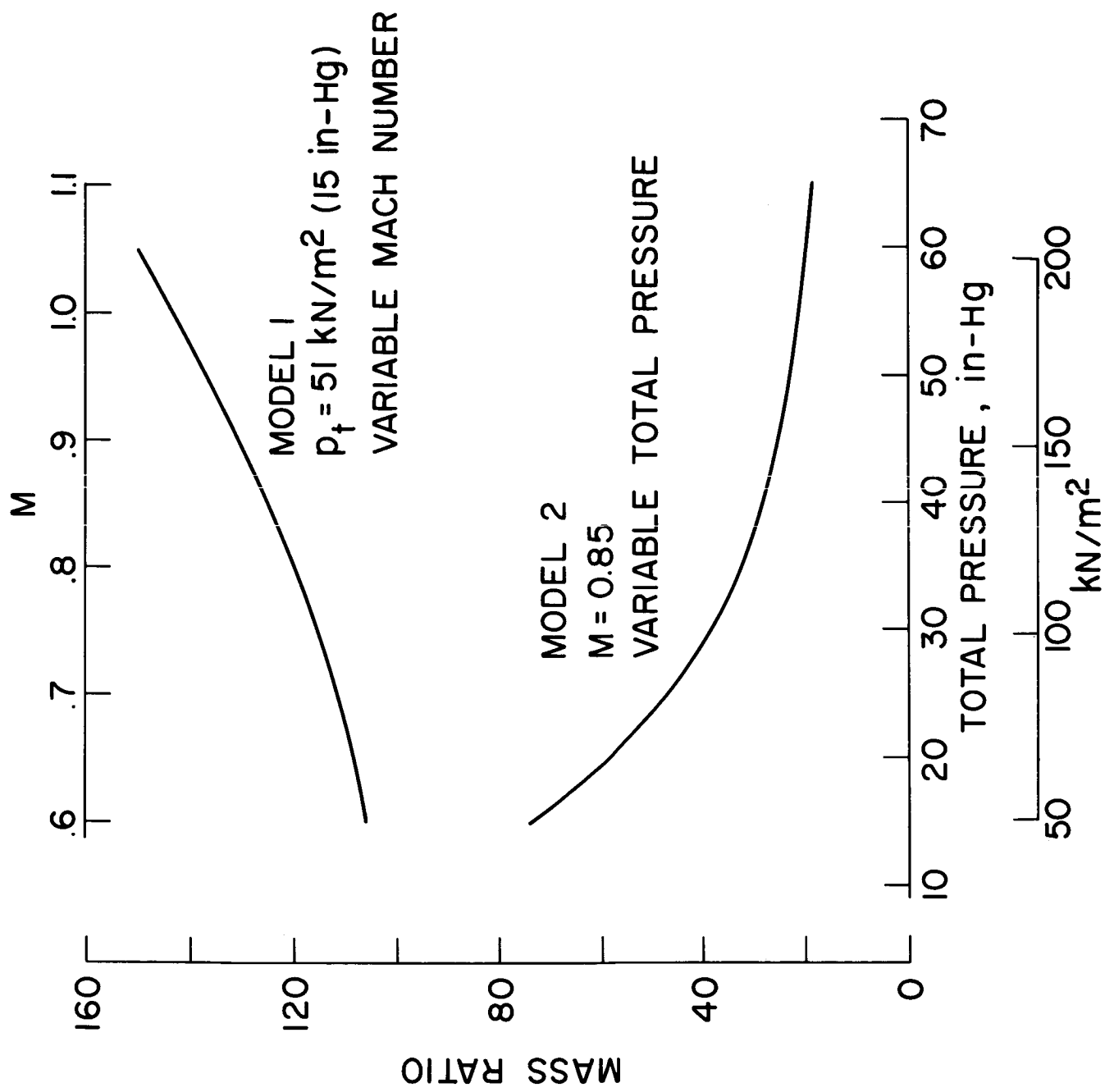


Figure 5

FLUTTER AT  $\alpha = 0^\circ$ 

Wing model 2 was tested at total pressures ( $P_t$ ) ranging from  $51 \text{ kN/m}^2$  (15 in.-Hg) to  $220 \text{ kN/m}^2$  (65 in.-Hg). The Mach number was varied from 0.6 to 1.1 with the wing at zero degrees angles of attack.

## Response Levels - Effect of Mach Number

Figure 6a shows the effect of Mach number on the rms<sup>3</sup> signal level,  $\sigma_B$ , of the "bending" gage for  $P_t = 84 \text{ kN/m}^2$  (25 in.-Hg). The signal levels have been divided by  $q_\infty$  and normalized by the "signal to  $q_\infty$ " ratio at  $M = 0.6$ . For Mach numbers below 0.82 and above 0.92 there was no visually detectable wing motion as observed from the television display. In the range  $0.82 < M < 0.92$  the wing motion became noticeable. As indicated by figure 6a the response was particularly large in the narrow Mach number range between 0.84 and 0.86. (The rms signal level from the "torsion" gage behaved in the same manner.)

<sup>3</sup>All rms values referred to herein are the rms values of the fluctuating part of the strain-gage signals. The d.c. outputs due to static loads were filtered electronically (i.e.,  $\sigma_B$  is the standard deviation of the bending-gage signal).

EFFECT OF MACH NUMBER ON WING ROOT BENDING  
MOMENT

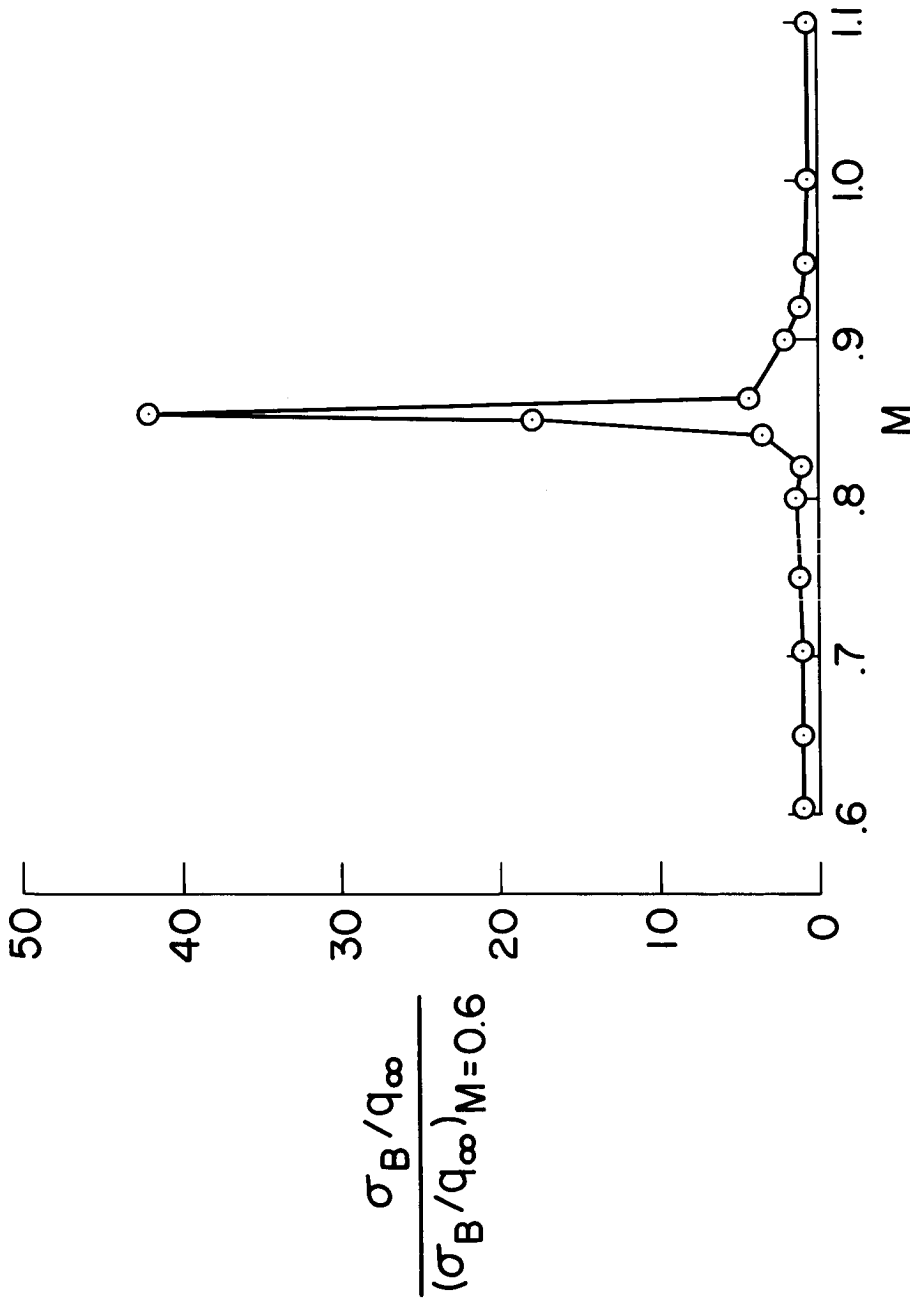


Figure 6(a)

### Change in Response Levels with Total Pressure

The general character of the response shown in figure 6a was the same for each total pressure. However, the actual magnitude of the response was affected by changes in pressure as indicated in figure 6b. The bending and torsion responses at  $M = 0.6$  and  $M = 1.0$  increase in an approximately linear fashion with increasing pressure (torsion response not plotted). This behavior suggests that the aerodynamic loading (e.g., turbulent boundary layer pressure fluctuations) acts like an external forcing function at these Mach numbers. However, at  $M \approx 0.85$  a different phenomenon is evidently present since, for the pressure range considered, the bending response tends to decrease with increasing pressure.

The  $M \approx 0.85$  points in figure 6b were obtained by adjusting the Mach number at each total pressure until the wing response appeared to be a maximum. The scatter of these points is probably due to the sharpness of the response peaks (see figure 6a). Due to operating limitations of the tunnel no data could be obtained at pressures less than  $51 \text{ kN/m}^2$  ( $15 \text{ in.}-\text{Hg}$ ). Because of this limitation the minimum pressure required to sustain the flutter could not be determined.

Since Reynolds number as well as dynamic pressure increases with increasing total pressure (see discussion of figure 1) the model was also tested without boundary-layer trips. In this "smooth" condition the  $M \approx 0.85$  response levels for  $P_t \leq 203 \text{ kN/m}^2$  ( $60 \text{ in.}-\text{Hg}$ ) were much smaller than those shown in figure 6b. But, at  $P_t = 220 \text{ kN/m}^2$  ( $65 \text{ in.}-\text{Hg}$ ) (Reynolds number  $\approx 13.6 \times 10^6$  based on the mean aerodynamic chord<sup>4</sup>) the rms strain-gage outputs increased to the same order of magnitude levels shown in figure 6b at  $P_t = 51 \text{ kN/m}^2$  ( $15 \text{ in.}-\text{Hg}$ ). Whether further increases in  $P_t$  would have caused a decrease in response level similar to that shown in figure 6b could not be determined due to tunnel operating limitations.

<sup>4</sup>During launch, the Reynolds number per meter (foot) is expected to be on the order of  $10 \times 10^6$  ( $3 \times 10^6$ ) at  $M = 0.85$ .

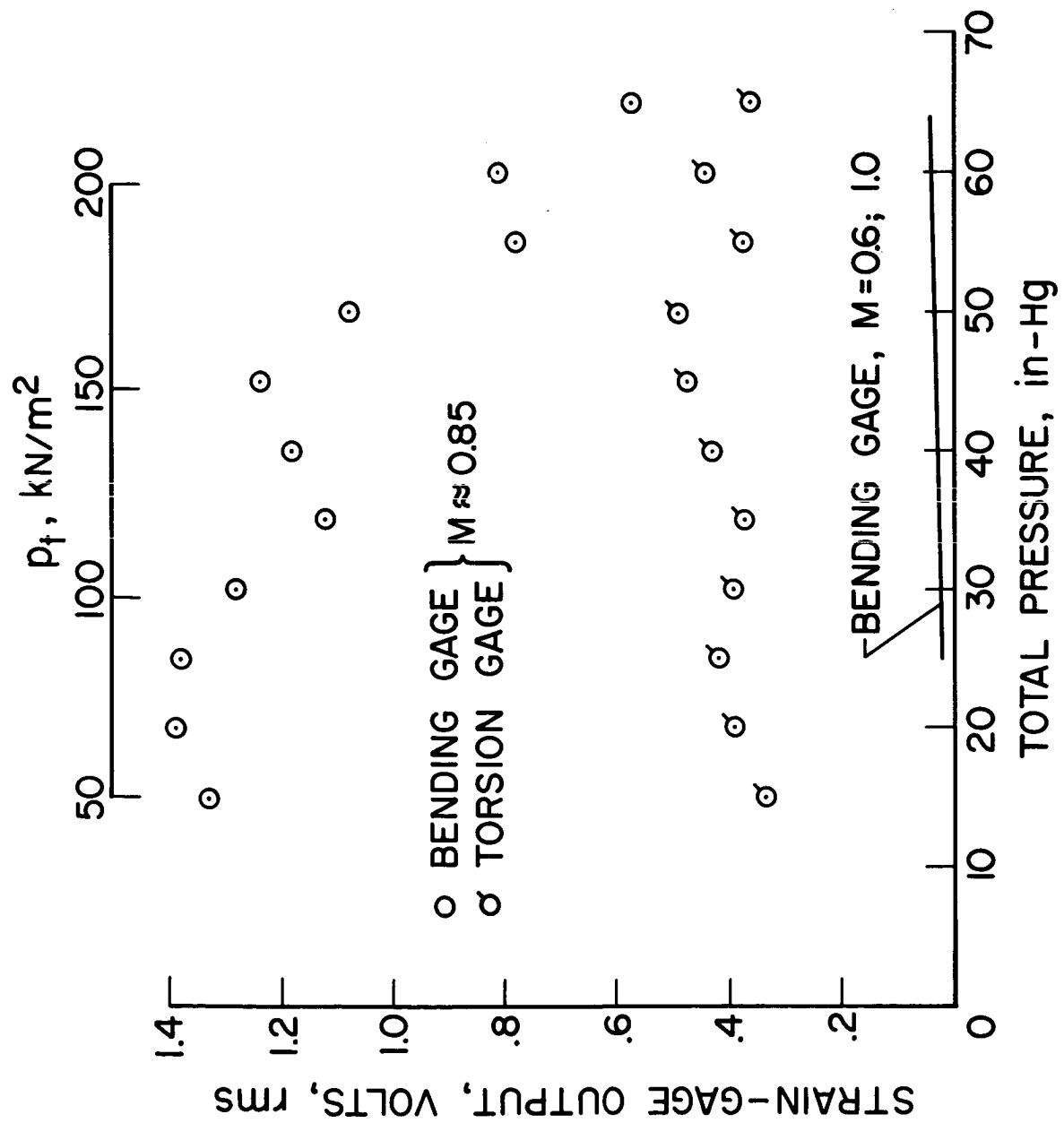


Figure 6(b)

### Time Histories

A section of a typical oscillograph trace for  $M \approx 0.85$  is shown in figure 7. The trace shows:

1. The predominant frequency component in both the bending and torsion-gage signals is about 38 Hz, a value just slightly greater than the still-air bending frequency.
2. The bending and torsion signals are very nearly in-phase.
3. The motion is amplitude limited, suggesting the presence of nonlinear forces.

The  $M \approx 0.85$  strain-gage signal levels of figure 6b correspond to the linear range of the model load-deflection curves. Thus, the wing elasticity is evidently not the cause of the nonlinear behavior indicated by item 3 above.

### Damping Levels

The net damping levels (aerodynamic plus structural) associated with the 38 Hz frequency are shown in figure 8 where  $\zeta$ , the ratio of damping to critical damping, is plotted against Mach number. These damping ratios were obtained by passing the bending-gage signals through a 55 Hz low-pass filter and computing the autocorrelation of the resulting signal. The net damping ratio is seen to be less than the wind-off value for the first bending mode ( $\zeta = 0.008$ ,  $f = 35.5$  Hz) in the narrow Mach number range centered about  $M \approx 0.85$ . This indicates that the large response levels at  $M \approx 0.85$  are due to negative aerodynamic damping. Therefore, they more closely correspond to a flutter condition (dynamic instability) than to a severe buffeting input. The nature of this instability (high response and low damping in a very narrow Mach number range) is similar to the instabilities observed on several configurations of axisymmetric hammerhead launch vehicle models (reference 2). The instability of the hammerhead configurations was attributed to fluctuations between separated and attached flow.

EFFECT OF MACH NUMBER ON DAMPING

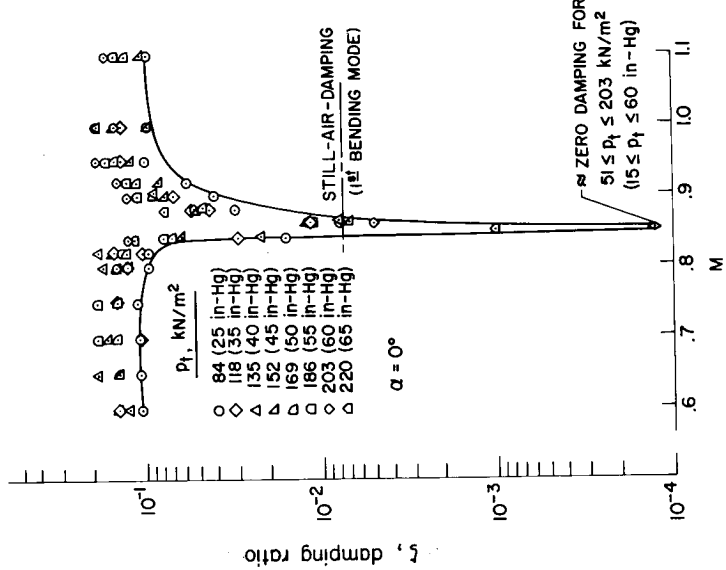
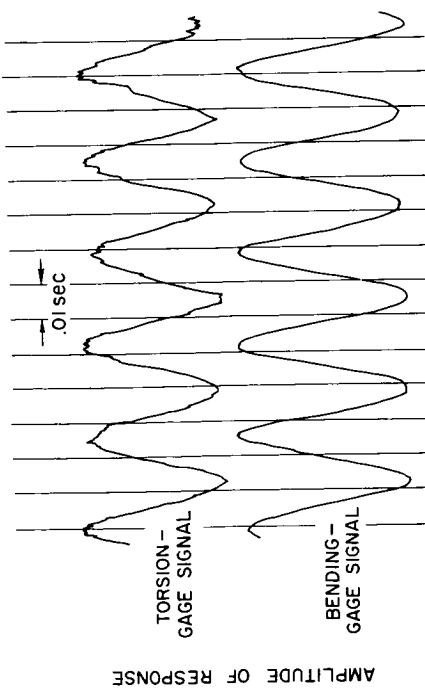


Figure 8

Figure 7

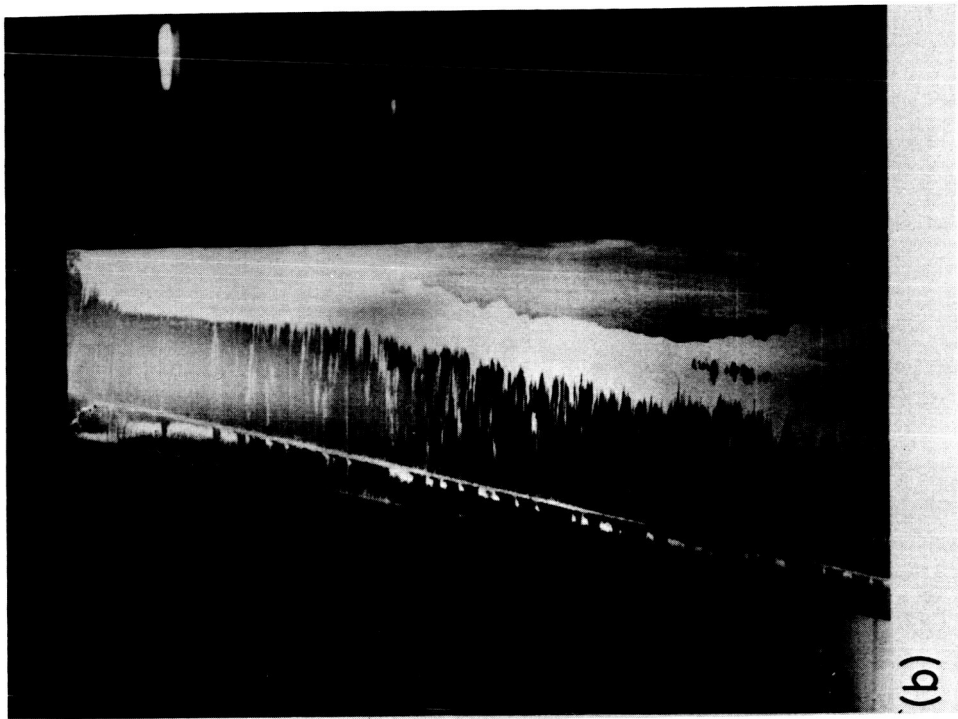
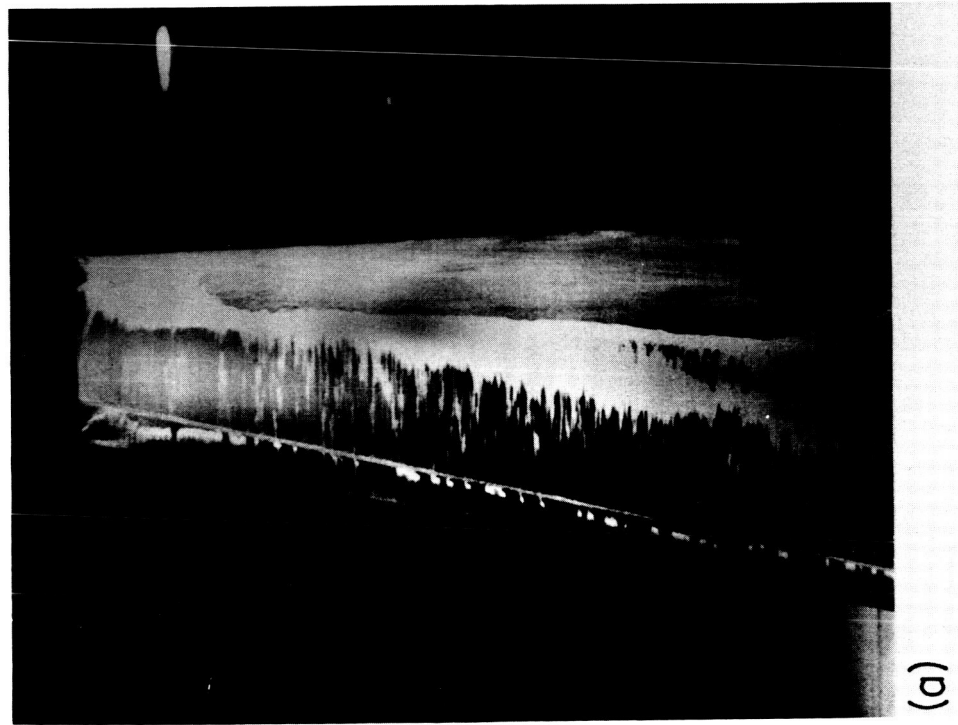


AMPLITUDE OF RESPONSE

### Oil-Flow Patterns

No information on the flow dynamics at the wing surface was obtained during the test, but several photographs of oil flow patterns were taken. Two of these photographs are shown in figure 9. The wing was initially covered with a white, highly viscous oil smeared uniformly along the wing in the spanwise direction. Figure 9a shows the oil-flow pattern shortly after a test condition of  $M \approx 0.85$  had been reached. The large area of undisturbed oil along the aft portion of the model is an indication of shock induced separated flow over that region. After this photo was taken the Mach number was being lowered to 0.84 when the oil suddenly started to flow into the previously undisturbed region and established the pattern shown in figure 9b. The character of the flow is, thus, notably different for  $M \approx 0.84$  and  $M \approx 0.85$  and is presumably responsible for the large difference in wing response levels at these two Mach numbers.

Figure 9



## Wing Motion

The flutter motion of the wing was established by high-speed motion pictures. One cycle of this motion at quarter-cycle intervals is illustrated in figure 10. The downward displacement and nose up attitude shown at the one-quarter-cycle position ( $t = P/4$ ) could be produced by a wing exhibiting negative lift coefficients and positive pitching-moment coefficients at positive angles of attack. Such a pitching moment would be unstable while the lift force would contribute to negative aerodynamic damping. (The induced angle of attack produced by a downward bending velocity would be accompanied by a downward lift force tending to increase the velocity.)

This observation is of interest because force coefficients such as postulated above have been observed, statically, on airfoil sections similar to the one used for the model (reference 3). The force coefficients presented in reference 3 were obtained from chordwise pressure distributions over an inboard section of a wing having an NACA 0015 airfoil section (symmetric, 15% thick at 30% chord). At Mach numbers from about 0.85 to 0.90 the pressure distributions were strongly influenced by shock positions on the upper and lower wing surfaces. This caused: (1) nonlinear lift curves which were slightly negative at small positive angles of attack and (2) nonlinear pitching-moment coefficients,  $c_m$ , which were large and positive ( $c_m = +0.1$ ) at small positive angles of attack. That this type of force behavior occurred only in a narrow, high subsonic Mach number range suggests that the flutter behavior described above may be due, in part, to similar force characteristics.

Figure 10 also shows the variation in the rms bending-to-torsion signal levels ( $\sigma_B/\sigma_T$ ) at  $M \approx 0.85$  as a function of total pressure. This plot indicates that the flutter values of the bending-to-torsion displacement ratio,  $h/\theta$ , decrease in an approximately linear fashion with increasing pressure. Such a result could be used for comparison with approximate analytic flutter predictions.

The motion pictures taken at  $M \approx 0.85$  indicate that the maximum double-amplitude wing-tip displacements were  $2\theta \approx 6^\circ$  and  $2h \approx 10$  cm (4 inches),  $h$  being measured at the 50% chord position.

## WING MOTION AT FLUTTER

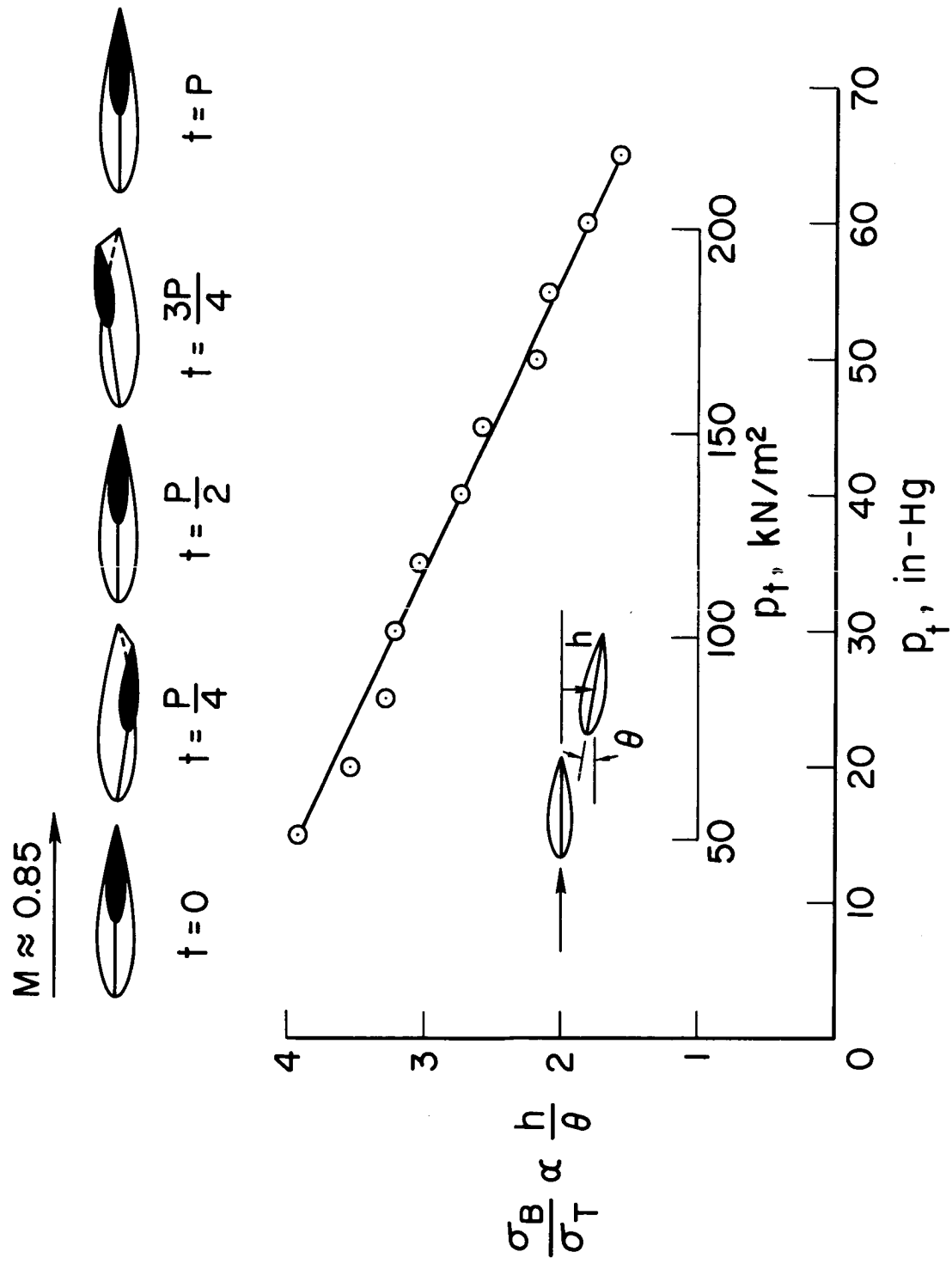


Figure 10

#### BUFFET AND STALL FLUTTER

Wing model 1 was tested at a total pressure of  $51 \text{ kN/m}^2$  (15 in.-Hg). The angle of attack was varied from zero to  $18^\circ$  at Mach numbers from 0.6 to 1.05.

#### Buffet Boundary

Figure 11 shows relative changes in the wing-root bending-moment fluctuations on model 1, for several Mach numbers, as the angle of attack is varied from zero to  $18^\circ$ . (The quantity  $\sigma_B$  is the standard deviation of the wing-root bending-gage signal.) The relatively large response at  $\alpha = 0.4^\circ$ ,  $M = 0.85$ , is associated with low damping ( $\approx 1\%$  of critical). For  $M \leq 0.8$  and  $M > 0.9$  the 1st bending-mode damping at  $\alpha = 0^\circ$  varies between 3 and 4 percent.

On the basis of figures 6a and 11 (and curves similar to those of figure 11 for other Mach numbers), a buffet region can be estimated, the somewhat arbitrarily selected boundary of which is shown in figure 12. Also shown in this figure are the Mach number and angle-of-attack combinations where the maximum buffet intensity occurs (for  $\alpha \leq 18^\circ$ ). Additional information concerning these points of maximum buffet intensity will be shown.

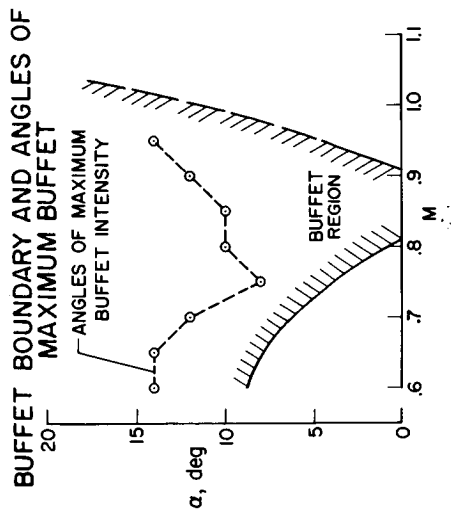


Figure 12

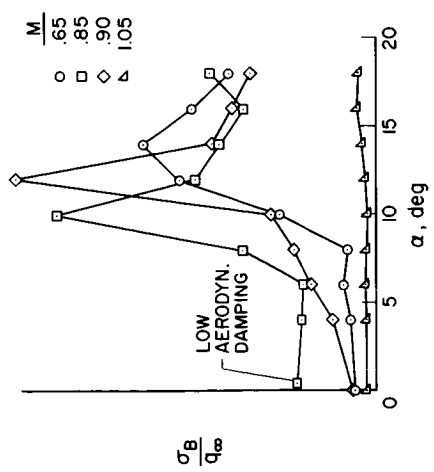


Figure 11

### Peak Buffet Loads

Figure 13 presents the ratio of the peak dynamic bending moment to the static bending moment for the conditions of maximum buffet intensity. The peak value for each case was obtained from oscilloscope records representing 120 seconds of the time history ( $\approx 4500$  cycles at the wing 1st bending frequency). The highest level of this ratio is seen to occur at  $M = 0.85$ ,  $\alpha = 10^\circ$ , where the peak dynamic load is 80% of the static load.

Scaling laws for buffet loads depend on both structural and aerodynamic damping (ref. 4). The net 1st bending mode damping levels (structural + aerodynamic) associated with the peak dynamic bending moments are also given in figure 13, as is the still-air damping value. The net damping levels exceed the still-air damping level by factors varying from about 3.5 to 6. At higher pressures the aerodynamic damping would generally become even more predominant. In such cases the dynamic bending moment response (buffet) is proportional to  $\sqrt{q}$  whereas the static moment is proportional to  $q$ . By use of the results of reference 4, the following scaling relation between the prototype and the model is obtained<sup>5</sup>

$$\left( \frac{M_{\text{peak-dyn}}}{M_{\text{static}}} \right)_P^2 = \left( \frac{M_w \omega_1^2}{L q} \right)_P / \left( \frac{M_w \omega_1^2}{L q} \right)_m = \frac{\mu_p}{\mu_m}$$

where  $\omega_1$  = fundamental bending frequency and  $M_w$  is the wing mass ( $M_w = 8.8$  kg (0.6 slugs) for model 1). Since  $\omega_1^2 \propto (1/L^4) (EI/(M_w/L))$  the above ratio can be also expressed as

$$\left( \frac{M_{\text{peak-dyn}}}{M_{\text{static}}} \right)_P^2 = \left( \frac{\frac{EI}{4}}{\frac{EI}{4} L q} \right)_P / \left( \frac{\frac{EI}{4}}{\frac{EI}{4} L q} \right)_m$$

which, for model 1, is equal to  $\frac{q_m}{2.4q_p}$  ( $q_m$  is given by the bottom curve of figure 1).

<sup>5</sup>In addition to the assumption on damping, the above scaling ratios require model and prototype to have similar geometry, and similar reduced frequencies and modal characteristics pertinent to the 1st bending mode.

**RESPONSE AND DAMPING AT ANGLES OF MAXIMUM BUFFET**

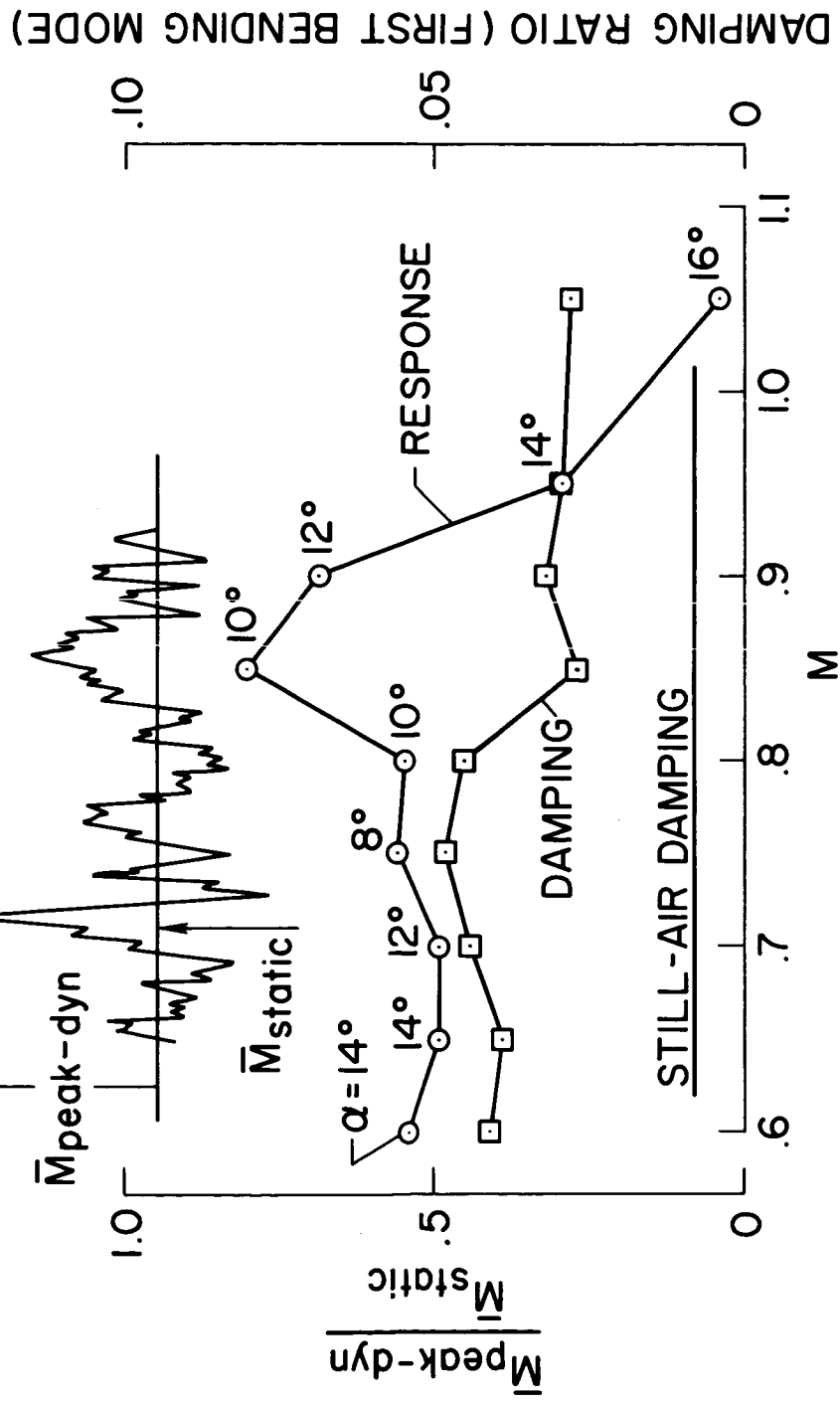


Figure 13

### Stall Flutter

The net damping levels (structural plus aerodynamic) of the 1st torsional frequency are indicated in figure 14 for  $\alpha < 180$  and for  $0.6 \leq M \leq 0.956$ . Values for the velocity coefficient  $V/(b\omega_a)$  are also shown ( $b = \text{semichord}$  at  $3/4$  semispan),  $\omega_a = \text{circular frequency of the 1st torsion mode}$ . The flagged symbols denote the angles at which minimum damping occurs for each Mach number. The actual values of these minimum damping levels are shown in figure 15. Note that the aerodynamic damping approaches zero but does not overcome the structural damping. Thus, the model wing (which has a value of  $b\omega_a/a \approx 0.46$ ,  $a = \text{speed of sound}$ ) does not appear to exhibit stall flutter.

---

<sup>6</sup>The torsional damping ratios were obtained from autocorrelations of the torsion-gage signals. Before computing the autocorrelations, the signals were passed through a bandpass filter having a 30 Hz bandwidth centered at the torsional frequency.

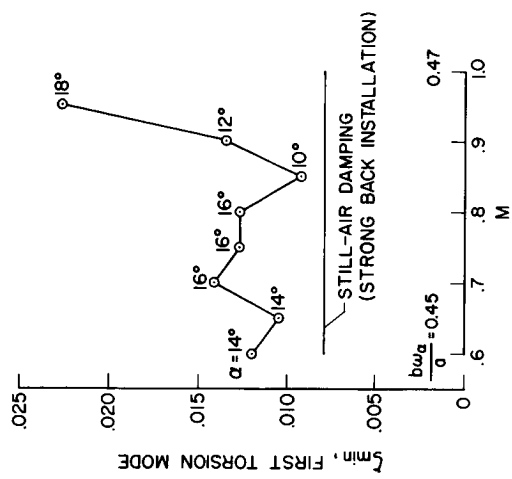


Figure 15

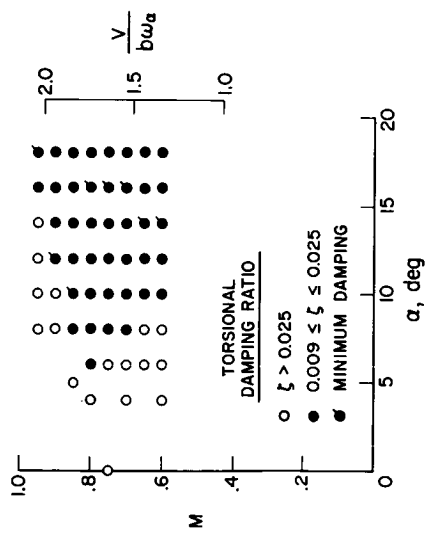


Figure 14

## CONCLUDING REMARKS

Experimental results have been presented for the transonic flutter and buffet behavior for elastic semispan wing models of a straight-wing configuration proposed for the space-shuttle vehicle. The models employed NACA 00XX-64 airfoil sections with maximum thickness ratios varying from 14% at the wing root to 10% at the wing tip. Aspect and taper ratios were 6.96 and 0.353, respectively. The models were tested at Mach numbers from 0.6 to 1.1, at angles of attack from zero to 18°, and at various dynamic pressures in the NASA-Ames 11- by 11-Foot Transonic Wind Tunnel. The following results are noted:

1. Zero-degree-angle-of-attack flutter occurred in a narrow Mach number range centered about  $M = 0.85$ . The flutter motion was of a limit-amplitude type and was comprised of both bending and twisting oscillations which were very nearly in-phase. The flutter frequency was slightly larger than the still-air frequency of the fundamental bending mode. For the pressure range considered, the bending component of the flutter motion was found to decrease with increasing pressure.
2. For the Mach number and angle-of-attack range considered, stall flutter was not observed. However, several instances of low torsional damping were noted. These results were obtained at a value of  $b\omega_a/a \approx 0.46$ .
3. Conditions of maximum buffet intensity occurred at angles of attack from 8° to 14°. For these angles, and for Mach numbers from 0.6 to 0.9, the model experienced peak dynamic bending moments ranging from 50% to 80% of the corresponding static moments.

#### REFERENCES

1. Cole, Henry A., Jr.: On-the-Line Analysis of Random Vibrations. AIAA Paper No. 68-288, AIAA/ASME Structures, Structural Dynamics and Materials Conference, April 1-3, 1968.
2. Robinson, Robert C.; Wilcox, Phillip R.; Gambucci, Bruno J.; and George, Robert E.: Dynamic Response of a Family of Axisymmetric Hammerhead Models to Unsteady Aerodynamic Loading. NASA TN D-4504, 1968.
3. Mellenthin, Jack A.: The Flow about a Section of a Finite-Aspect-Ratio NACA 0015 Airfoil on a Transonic Bump. NACA TN 3036, 1953.
4. Huston, Wilber B.: A Study of the Correlation Between Flight and Wind-Tunnel Buffet Loads. AGARD Rept. 111, April - May 1957.

APPLICATION OF RECENT PANEL FLUTTER  
RESEARCH TO THE SPACE SHUTTLE  
PART I - BOUNDARY LAYER AND HYPERSONIC EFFECTS

By Peter A. Gaspers, Jr.  
NASA Ames Research Center  
Moffett Field, California

INTRODUCTION

Within the past three years it has been established experimentally that the boundary layer has a large stabilizing influence on panel flutter. About a year ago the first theoretical results employing a reasonably rational and complete mathematical model were obtained and are in fairly good agreement with the experiments. In this paper the previously published results, both experimental and theoretical, are reviewed and some very recent and very significant theoretical results for large boundary layer thickness are presented.

In addition, some theoretical results for panel flutter at hypersonic speeds which show nonlinear destabilizing effects will be reviewed.

Finally the significance of these results and their application to the space shuttle will be discussed.

SYMBOLS

a	panel length, m
b	panel width, m
c	speed of sound, m/sec
D	plate stiffness, $\frac{Eh^3}{12(1 - \nu^2)}$
E	modulus of elasticity, N/m <sup>2</sup>
h	plate thickness, m
K	panel in-plane restraint spring constant, N/m <sup>2</sup>
k	stiffness parameter, $\left(\frac{\tau^2 E}{c^2 \rho_s (1 - \nu^2)}\right)^{1/2}$
M	Mach number
N <sub>x</sub>	nondimensional midplane stress
q	dynamic pressure, N/m <sup>2</sup>
q <sub>o</sub>	flutter dynamic pressure for zero boundary layer thickness, N/m <sup>2</sup>
U	free stream velocity, m/sec

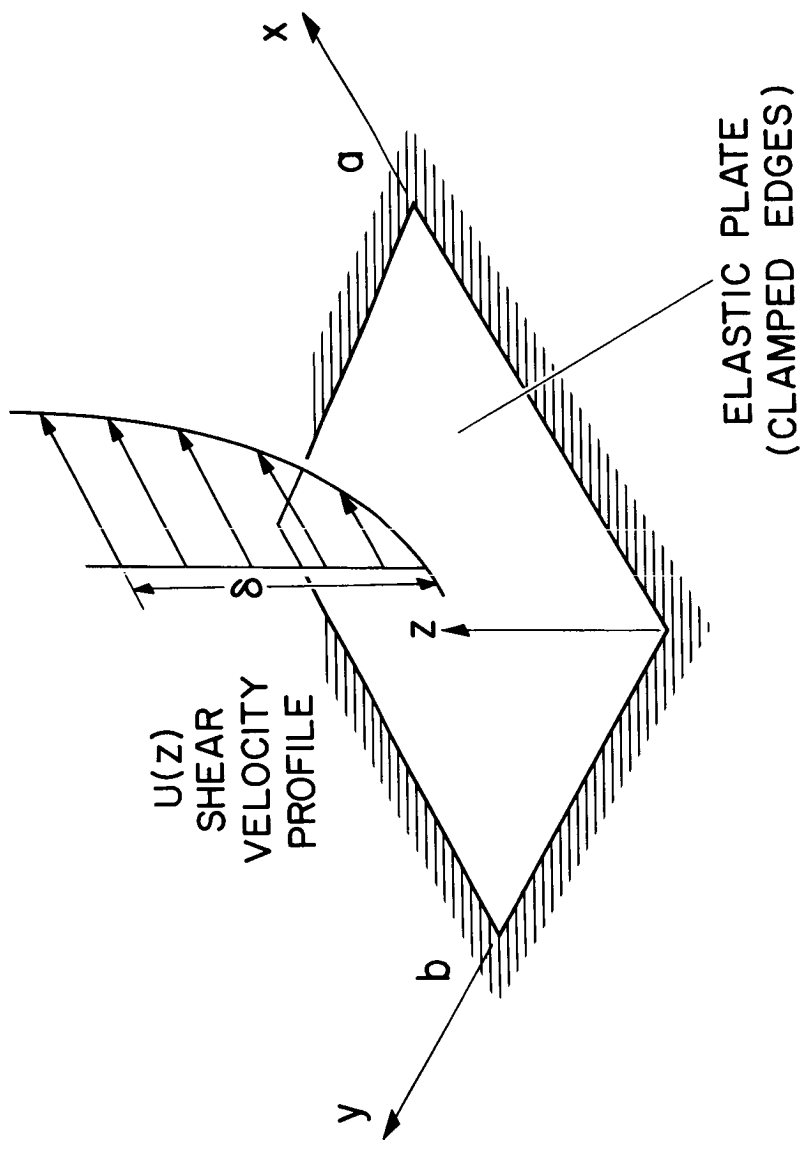
$\alpha$	in-plane restraint parameter, $\frac{K}{K + Eh/a(1 - \nu^2)}$
$\beta$	$(M^2 - 1)^{1/2}$
$\delta$	boundary layer thickness, m
$\gamma$	nondimensional dynamic pressure, $\frac{2qa^3}{\beta D}$
$\gamma^*$	nondimensional dynamic pressure, $\frac{2qa^3}{D}$
$\mu$	mass ratio parameter, $\frac{\rho_\infty a}{\rho_s h}$
$\nu$	Poisson's ratio
$\rho_s$	plate density, kg/m <sup>3</sup>
$\rho_\infty$	free stream density, kg/m <sup>3</sup>
$\tau$	thickness ratio, h/a

PANEL GEOMETRY AND BOUNDARY LAYER PROFILE

(Slide 1)

In the first slide the panel geometry and boundary layer flow are indicated. The elastic isotropic plate, of length  $a$  and width  $b$  with clamped edges, is imbedded in an otherwise infinite rigid plane and exposed on one side to a shear flow which in the theoretical calculations is taken to be steady and 2-dimensional. Although isotropic plates with clamped edges are not typical of space shuttle designs, it is expected that the influence of the boundary layer will be very similar for those designs.

## PANEL GEOMETRY AND BOUNDARY LAYER PROFILE



Slide 1

## EXPERIMENTAL FLUTTER BOUNDARIES

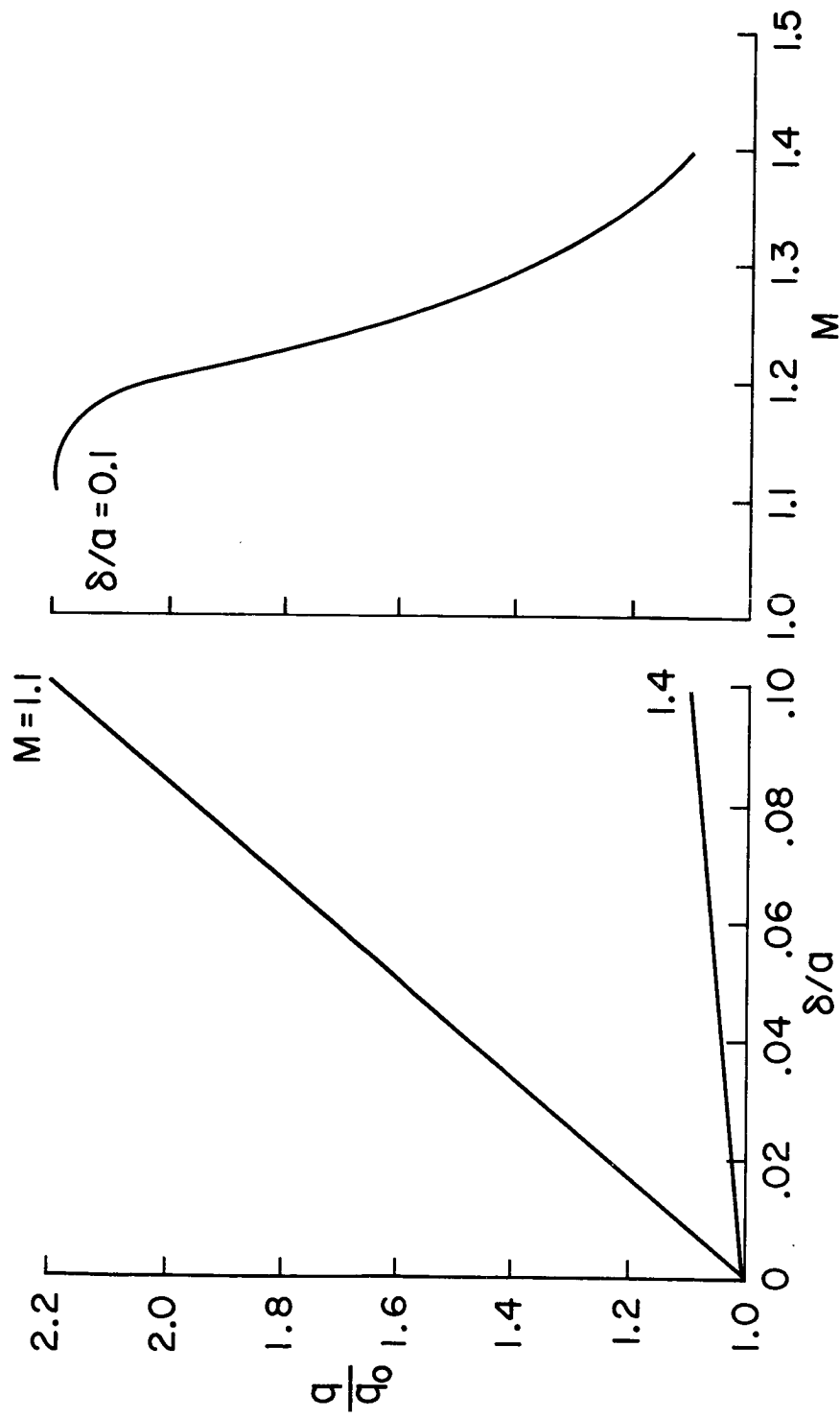
(Slide 2)

In this slide are shown some typical experimental results obtained by Muhlstein, Gaspers, and Riddle (ref. 1). In the lefthand plot the flutter  $q$  normalized with respect to the flutter  $q$  for zero boundary layer thickness is shown as a function of nondimensional boundary layer thickness for a length-to-width ratio of .5 and stiffness parameter of .074. The flutter  $q$  for zero boundary layer thickness was obtained by a linear extrapolation of the experimental results which ranged from  $\delta/a = .025$  to .1. For the range of boundary layer thickness shown, the flutter  $q$  varies linearly with boundary layer thickness for Mach numbers of 1.1 to 1.4. On the righthand plot  $q/q_0$  is shown as a function of Mach number for  $\delta/a = .1$ . The effect of the boundary layer is largest at a Mach number slightly above 1.1 and decreases rapidly as the Mach number increases. It should also be noted that the effect depends fairly strongly on the stiffness parameter  $k$ , being larger for smaller values of  $k$ .

The value of  $\delta/a$  for space shuttle panels will depend on the local boundary layer thickness and panel size. Values as large as .25 to 1.0 may be expected over a large part of the surface and therefore the boundary layer will have a very strong stabilizing influence on the flutter of space shuttle panels.

## EXPERIMENTAL FLUTTER BOUNDARIES

$$a/b = 0.5 \quad k = \left( \frac{\tau^2 E}{c^2 \rho_s (1-\nu^2)} \right)^{1/2} \approx 0.074$$



## COMPARISON OF THEORY WITH EXPERIMENT

## (Slide 3)

In this slide the experimental data are compared with theoretical results obtained by E. H. Dowell of Princeton University (refs. 2 and 3). The aerodynamic loading in the theoretical model results from considering linear 2- or 3-dimensional perturbations of a 2-dimensional steady shear flow. On the left side the nondimensional dynamic pressure is plotted as a function of nondimensional boundary layer thickness for a clamped plate at Mach number 1.2. The theoretical results are in good agreement with experiment and improve as the boundary layer thickness increases. On the right side the nondimensional dynamic pressure is plotted as a function of Mach number for  $a/b = .5$  and boundary layer thicknesses of 0 and .1. The agreement is fairly good but the theoretical results consistently underestimate the effect at the lower Mach numbers and overestimate at the higher Mach numbers. It is possible that the inclusion of cavity effects, internal damping, and a 3-dimensional shear flow to account for boundary layer growth may further improve the agreement.

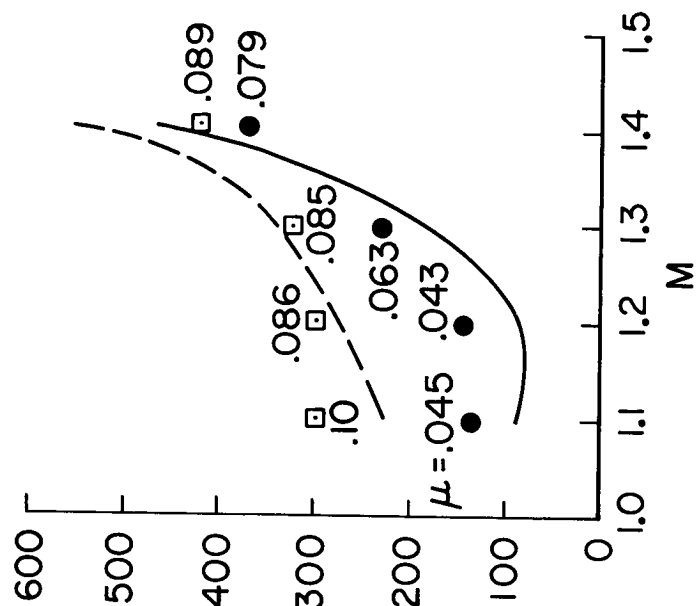
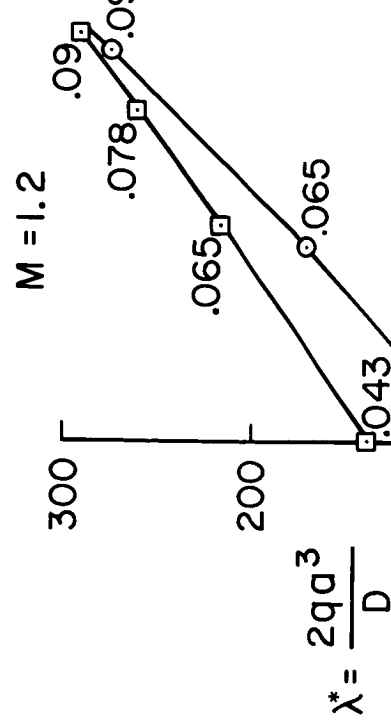
# COMPARISON OF THEORY WITH EXPERIMENT

$a/b = .5$

□ EXPERIMENT  
○ THEORY

CLAMPED PLATE  
 $U = (z/\delta)^{1/7}$

EXP {   □  $\delta/a = .1$   
 •  $\delta/a = 0$   
 THEO {   ---  $\delta/a = .1$   
 —  $\delta/a = 0$



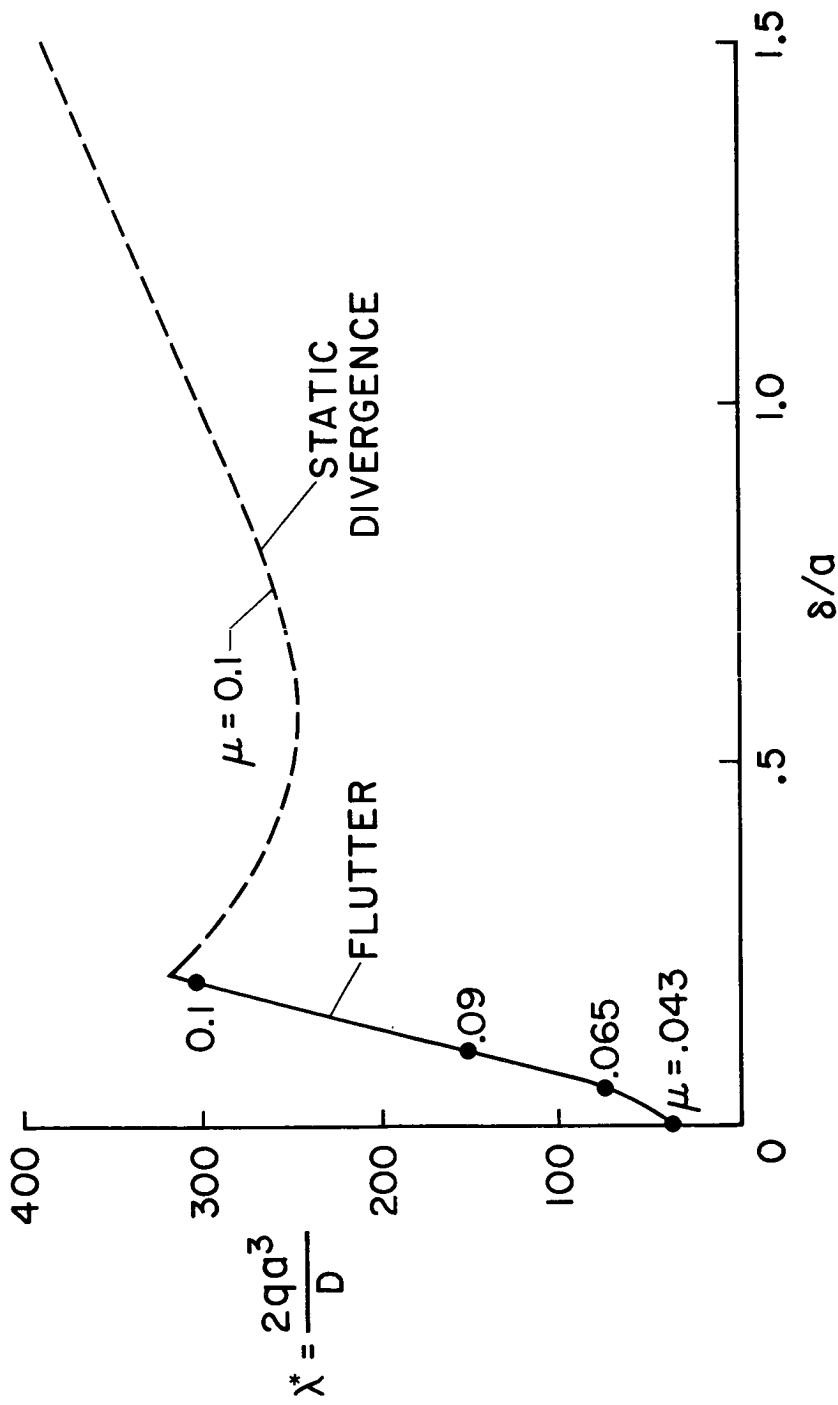
THEORETICAL RESULTS FOR LARGE BOUNDARY LAYER THICKNESS

(Slide 4)

In this slide some very recent unpublished theoretical results of E. H. Dowell are shown. The nondimensional dynamic pressure is again plotted as a function of nondimensional boundary layer thickness but for a much larger range. The results shown are for the 2-dimensional model at a Mach number of 1.2. The flutter dynamic pressure increases rapidly with boundary layer thickness until at a value of  $\delta/a \approx .25$  flutter is completely suppressed and for larger values of  $\delta/a$  only static divergence occurs. It had not been anticipated that such a small value of  $\delta/a$  would completely suppress flutter and it will be of considerable interest to obtain corresponding results for other Mach numbers and for the 3-dimensional case. This result also indicates the need for further experimental results for larger values of  $\delta/a$ .

**THEORETICAL RESULTS FOR LARGE BOUNDARY LAYER THICKNESS**

**M = 1.2    a/b = 0    CLAMPED PLATE**



NOTE : UNPUBLISHED THEORETICAL RESULTS OF E. H. DOWELL,  
PRINCETON UNIVERSITY, NASA GRANT NGR 31-001-197

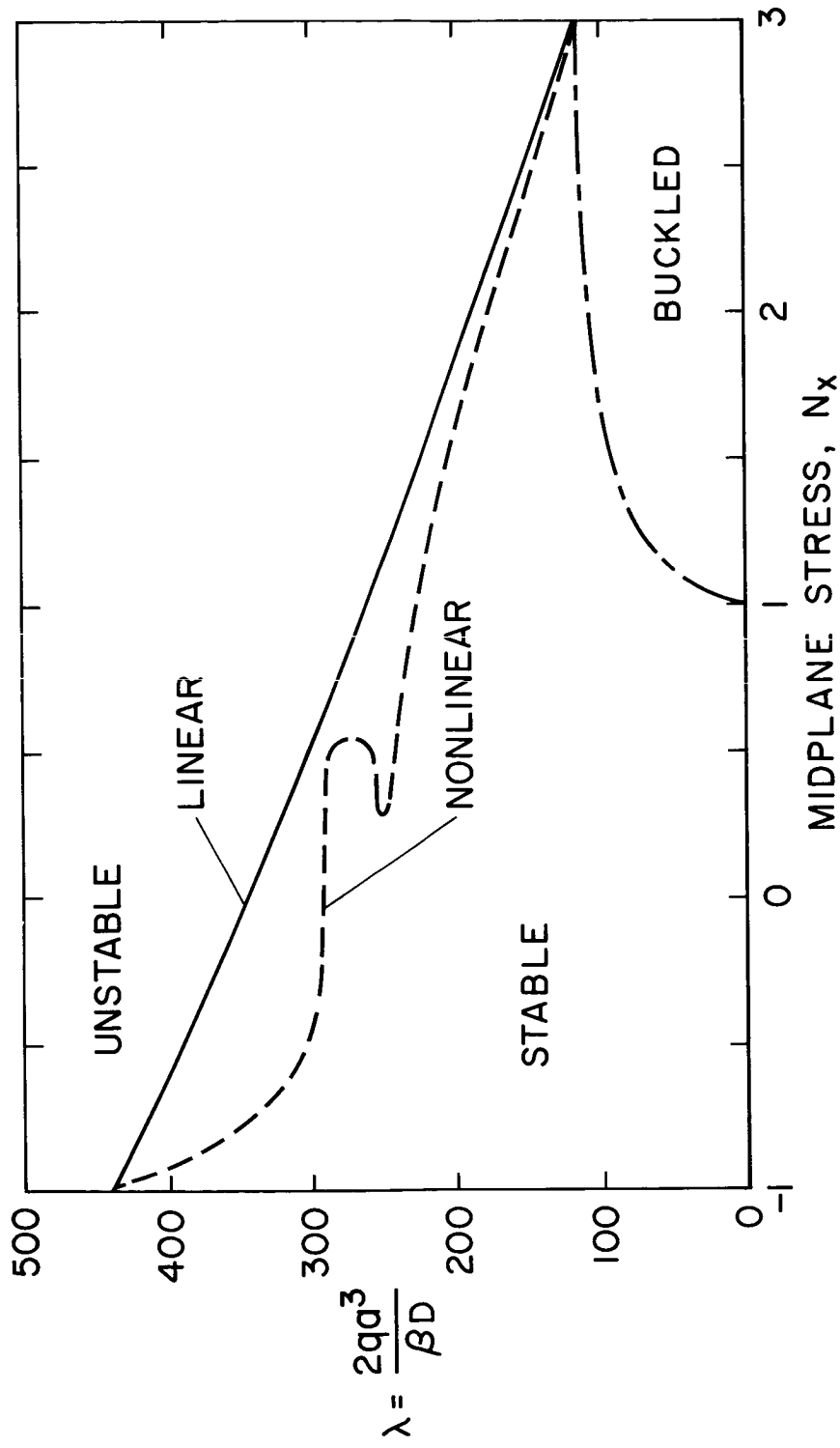
## NONLINEAR HYPERSONIC EFFECTS

(Slide 5)

At hypersonic speeds the aerodynamic loading is appreciably nonlinear and this results in the flutter boundary being dependent on the initial conditions. The results shown are due to S. C. McIntosh of Stanford University (ref. 4). The theoretical model incorporates the large deflection Von Karman plate equations and nonlinear piston theory aerodynamics. In the slide, a nonlinear stability boundary, for the parameters indicated and corresponding to a peak initial deflection of 2.5 to 3 plate thicknesses, is compared with the linear boundary. The maximum decrease in the  $\lambda$  parameter is approximately 20% and occurs at a low tensile midplane stress. At hypersonic speeds a decrease in  $\lambda$  of 20% is not large enough to be of concern for typical space shuttle trajectories and it is not expected that any other reasonable combination of the parameters would result in a significant effect. These results indicate that theoretical results based on linear aerodynamics will be adequate for the design of space shuttle panels.

## NONLINEAR HYPERSONIC EFFECTS

SIX ASSUMED MODES     $\mu/M = 0.01$      $M_h/a = 0.05$      $a = 0.1$   
 PEAK INITIAL DEFLECTION  $\approx 3$  PLATE THICKNESSES



Slide 5

## SUMMARY

The influence of the boundary layer on panel flutter is particularly important for the space shuttle because the stabilizing effect is largest at the low supersonic speeds where it is needed most and, also, because it is a large vehicle the boundary layer thickness will be a significant fraction of the panel chord over much of the surface. In the design of space shuttle panels, consideration should be given to the possibility of minimizing panel weight by sizing panels according to the local boundary layer thickness. It should also be noted that in all panel flutter calculations the local flow variables, rather than free stream, should be used. Based on the theoretical results of Dowell, it appears that it may be possible to size panels so that flutter is completely suppressed for some range of Mach number. Although static divergence could still occur, it would be limited in amplitude by nonlinear inplane forces and would not present a fatigue problem.

## REFERENCES

1. MUHLSTEIN, Lado, Jr.; GASPERS, Peter A., Jr.; and RIDDLE, Dennis W.: An Experimental Study of the Influence of the Turbulent Boundary Layer on Panel Flutter. NASA TN D-4486, 1968.
2. DOWELL, E. H.: Generalized Aerodynamic Forces on a Flexible Plate Undergoing Transient Motion in a Shear Flow with an Application to Panel Flutter. AIAA Paper No. 70-76, January 1970.
3. DOWELL, E. H.; and VENTRES, C. S.: Quarterly Progress Report for NASA Grant NGR 31-001-197. Princeton University, October 1970.
4. EASTEP, F. E.; and MCINTOSH, S. C.: Analysis of Nonlinear Panel Flutter and Response Under Random Excitation or Nonlinear Aerodynamic Loading. Presented at AIAA/ASME 11th Structures, Structural Dynamics and Materials Conference, April 1970.

APPLICATION OF RECENT PANEL FLUTTER  
RESEARCH TO THE SPACE SHUTTLE  
PART II - INFLUENCE OF EDGE CLIPS AND FLOW ANGULARITY

By Herman L. Bohon and Charles P. Shore  
NASA Langley Research Center  
Hampton, Virginia

#### INTRODUCTION

Elevated temperatures encountered during entry of the shuttle orbiter or booster necessitate the use of a thermal protection system (TPS) to shield the primary structure from the deleterious effects of a high-temperature environment. In order to accommodate the thermal growth associated with the high temperature, many TPS designs utilize a corrugated surface structure connected to the primary structure without by flexible clips. These clips must transmit external pressure loads to the primary structure without excess panel deflections or buckling of the clips and must minimize the heat transferred to the primary structure. At the same time the clips must be flexible enough to permit growth in the plane of the panel to alleviate thermal stresses. Use of a corrugated surface structure improves the load-carrying ability of the panel and minimizes the number of supports required. Alignment of the maximum flexural stiffness in the direction of the airstream also improves the resistance to panel flutter.

Reference 1 briefly summarizes the state-of-the-art for supersonic flutter of orthotropic panels mounted on flexible supports. The purpose of the present paper is to examine parameters that are known contributors to aeroelastic problems in light of current TPS designs. In particular, the nature of boundary conditions and flow angularity as they affect panel flutter will be discussed. The data to be presented are not restricted to metallic panels but, in fact, may also apply to panels with external insulation. Emphasis, however, is placed on the orthotropy of the surface structure and the deflectional flexibility of the clips which connect it to the primary structure.

## (Figure 1)

Perhaps the lightest type of heat-shield panel and one that is simple to fabricate consists of a corrugated surface formed from a single flat sheet attached to rows of flexible supports (ref. 2). Such a panel is shown from the back side in the figure; flow occurs over the front surface of the panel only. The corrugated surface improves the load-carrying ability of the panel and minimizes the number of supports. The support clips must be strong enough to carry external loads into the primary structure, but flexible enough to permit thermal growth of the panel in the direction of the corrugations. Expansion in the direction of the supports results in an outward growth of the corrugations between flats. The center support is rotated 90° and is required to carry pressure drag and inertia loads, as well as normal loads, into the primary structure. Panel size is governed by handling requirements or the amount of thermal expansion permissible at the extreme supports. Many current TPS designs utilize uniform support configurations for both the leading and trailing edges; however, designs which have a continuous sheet supported over several rows of supports may have quite different effective spring flexibilities normal to the plane of the panel depending upon which bay of the panel is considered.

Surface structures of this type are being analyzed for flutter at the NASA Langley Research Center (LaRC) both experimentally and analytically. The experimental program is in the fabrication phase and wind-tunnel data are not yet available. The analytical studies presently include a closed-form flutter solution for a single-bay panel supported at the leading and trailing edges with continuous line springs of arbitrary deflectional stiffness. Side edges are free, and the direction of flow over one surface is aligned with the corrugations so that the flow angle  $\Lambda$  is zero. Some results of this study are shown in figure 2.

SPACE - SHUTTLE SURFACE STRUCTURE

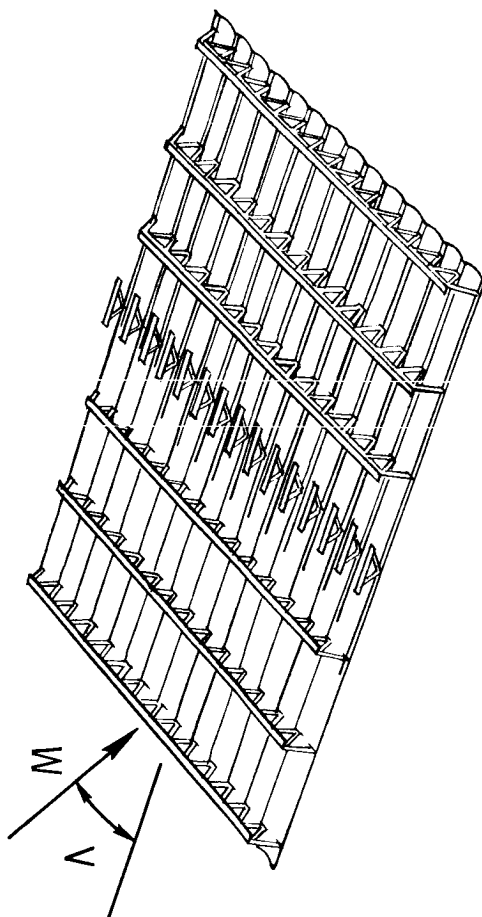


Figure 1

## EFFECTS OF UNEQUAL ELASTIC DEFLECTIONAL EDGE RESTRAINTS ON FLUTTER

(Figure 2)

Some effects of unequal elastic deflectional edge restraints on flutter of panels are shown in this figure, where the dynamic-pressure parameter  $\lambda = \frac{2qa^3}{D_1\sqrt{M^2 - 1}}$  is plotted as a function of spring-

stiffness-parameter ratios  $K_2/K_1$  from 0 to 1.0 and  $K_1/K_2$  from 1.0 to 0. In the ordinate parameter,  $q$  is the dynamic pressure,  $a$  is the panel length,  $D_1$  is the flexural stiffness in the stream direction, and  $M$  is the Mach number. The deflectional spring stiffnesses at the leading and trailing edges are designated as  $k_1$  and  $k_2$ , respectively. These spring stiffnesses are nondimensionalized as shown in the figure. Calculations are made for large streamwise bending stiffness  $D_1$  and essentially zero cross-stream bending stiffness  $D_2$  and twisting stiffness  $D_{12}$ . The flutter boundaries are for constant values of the spring-stiffness parameter  $K_1$  of 100, 10, and 1. The dashed curve, shown for comparison, is the value of  $\lambda$  for infinite spring stiffness or simple supports.

The curves show large reductions in  $\lambda$  as the edge spring stiffness is decreased. If the leading-edge-spring-stiffness parameter is large, for example,  $K_1 = 100$ , the effect of reducing the trailing-edge-spring-stiffness parameter is small as shown for values of  $K_2/K_1 < 1$ . However, if the trailing-edge-spring-stiffness parameter is large, small values of the leading-edge-spring-stiffness parameter, for example,  $K_1 = 1$ , may introduce divergence and result in a large reduction in  $\lambda$  (see results for  $K_1/K_2 < 1$ ).

Current indications are that most TPS supports will have spring stiffness constants greater than  $K_1 = 10$ ; however, in some instances effective spring constants on the order of  $K_1 = 1$  are possible. For example, a panel supported on clips at the corners only is essentially unrestrained along the edges. For such cases, divergence may occur if the weak support is at the trailing edge.

EFFECTS OF UNEQUAL ELASTIC DEFLECTIONAL EDGE RESTRAINTS ON FLUTTER

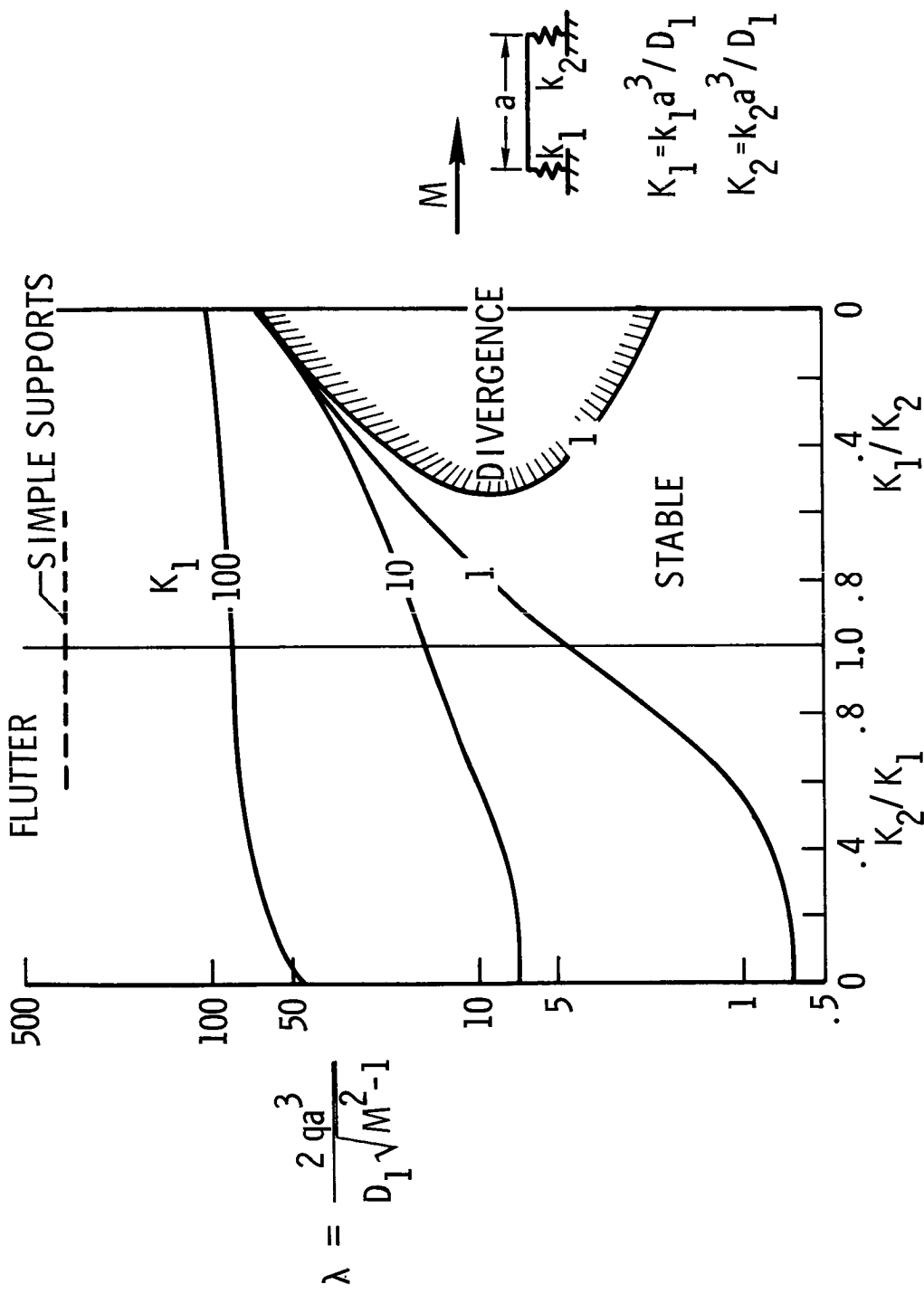


Figure 2

EFFECT OF IN-PLANE LOADING ON VIBRATION CHARACTERISTICS OF PANELS WITH  
UNEQUAL ELASTIC DEFLECTIONAL EDGE RESTRAINT

(Figure 3)

Although the edge supports for most heat-shield configurations are designed to accommodate thermal growth, some in-plane loading may be introduced by the supports or by nonuniform temperature distributions over the panel surface. The effect of this thermal stress on the vibration characteristics of a panel on flexible supports is shown in this figure. The variation of the frequencies for the first two modes is shown as a function of an in-plane load parameter  $k_x = \frac{Nx^2}{\pi^2 D_1}$  (where  $N_x$  is a uniform in-plane load). Calculations are made for  $K_1 = 10$  and values of  $K_2$  of 5, 10, and 20. The frequencies  $\omega$

are nondimensionalized by the fundamental frequency of a simply supported beam  $\omega_0 = \frac{\pi^2}{a^2} \sqrt{D_1/\gamma}$  (where  $\gamma$  is the mass per unit length of the beam). For flutter considerations there are three significant points indicated by these vibration results. First, for zero stress the values of mode 1 and mode 2 frequencies are far below the corresponding beam values of 1 and 4, respectively. Secondly, the static buckling load is much lower than that of a simply supported beam for which  $k_x = 1$ ; thus, permitting deflections at the supports results in reduced frequencies and buckling loads. Thirdly, as  $k_x$  increases, the frequencies come closer together and for equal springs the second mode crosses the first and becomes the lower buckling mode. This behavior can have an adverse effect on flutter as shown in figure 4.

EFFECT OF IN-PLANE LOADING ON VIBRATION CHARACTERISTICS  
OF PANELS WITH UNEQUAL ELASTIC DEFLECTIONAL RESTRAINT

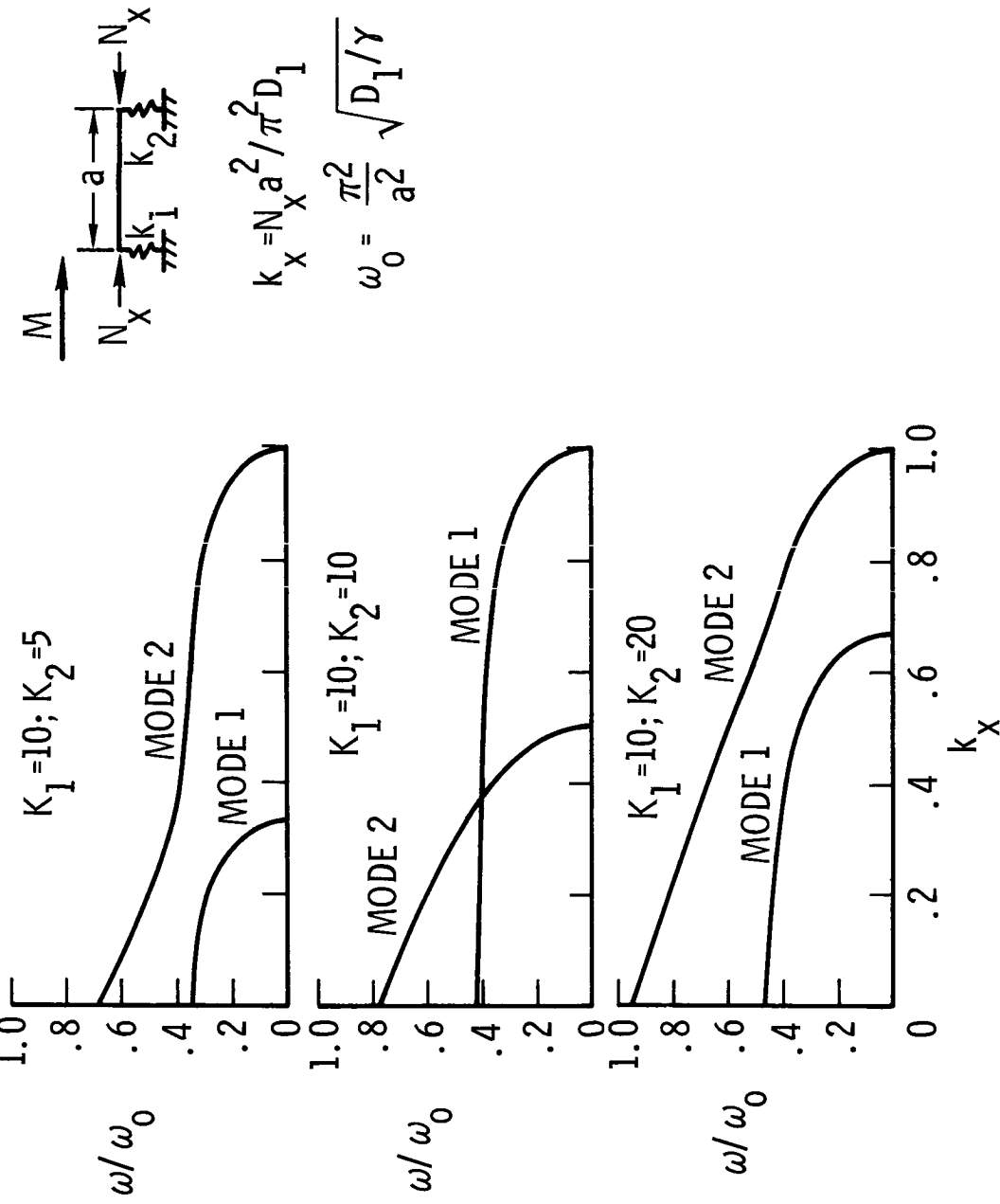


Figure 3

## EFFECT OF IN-PLANE LOADING ON FLUTTER OF PANELS WITH UNEQUAL

ELASTIC DEFLECTIONAL EDGE RESTRAINT;  $K_1 = 10$ 

(Figure 4)

A sample flutter calculation for a stressed panel with  $K_1 = 10$  is shown in this figure. The variation of  $\lambda$  with the ratios of the edge-deflectional-spring-stiffness parameters is shown for values of the in-plane load parameter  $k_x$  of 0 and 0.4.

The dashed curve at the lower left indicates a region of static instability for the spring-panel system. This instability is characterized by a rotation of the panel about the leading edge and occurs at only 40 percent of the well-known Euler buckling load  $k_x = 1$ . In this region, as the dynamic pressure is increased, the panel is gradually blown flat and then remains stable until further increases in  $\lambda$  cause flutter to occur. Along the flutter boundary for  $k_x = 0.4$ , as  $K_2$  increases,  $\lambda$  decreases to a minimum and then increases with further increases in  $K_2$ . This phenomenon is common for panels on classical supports and occurs when the separation of the natural frequencies of the predominant flutter modes becomes small. Usually the inclusion of structural and aerodynamic damping in the theory eliminates the large reduction in  $\lambda$ . The solid symbols show the effect of structural and aerodynamic damping on the flutter of the spring-panel system. For both calculations the structural damping is 1 percent; for the aerodynamic damping associated with a 12-km (40 000-foot) altitude, the anomalous decrease in  $\lambda$  is less severe, whereas for aerodynamic damping at sea level, the decrease is completely eliminated. During shuttle ascent, maximum  $q$  occurs at about 12 km (40 000 feet), where the theory indicates a large effect of in-plane stress. Thus flutter theories for shuttle-type panels may have to include both structural and aerodynamic damping for reliable panel-flutter predictions.

EFFECT OF IN-PLANE LOADING ON FLUTTER OF PANELS  
WITH UNEQUAL ELASTIC DEFLECTIONAL EDGE RESTRAINT;  $K_1 = 10$

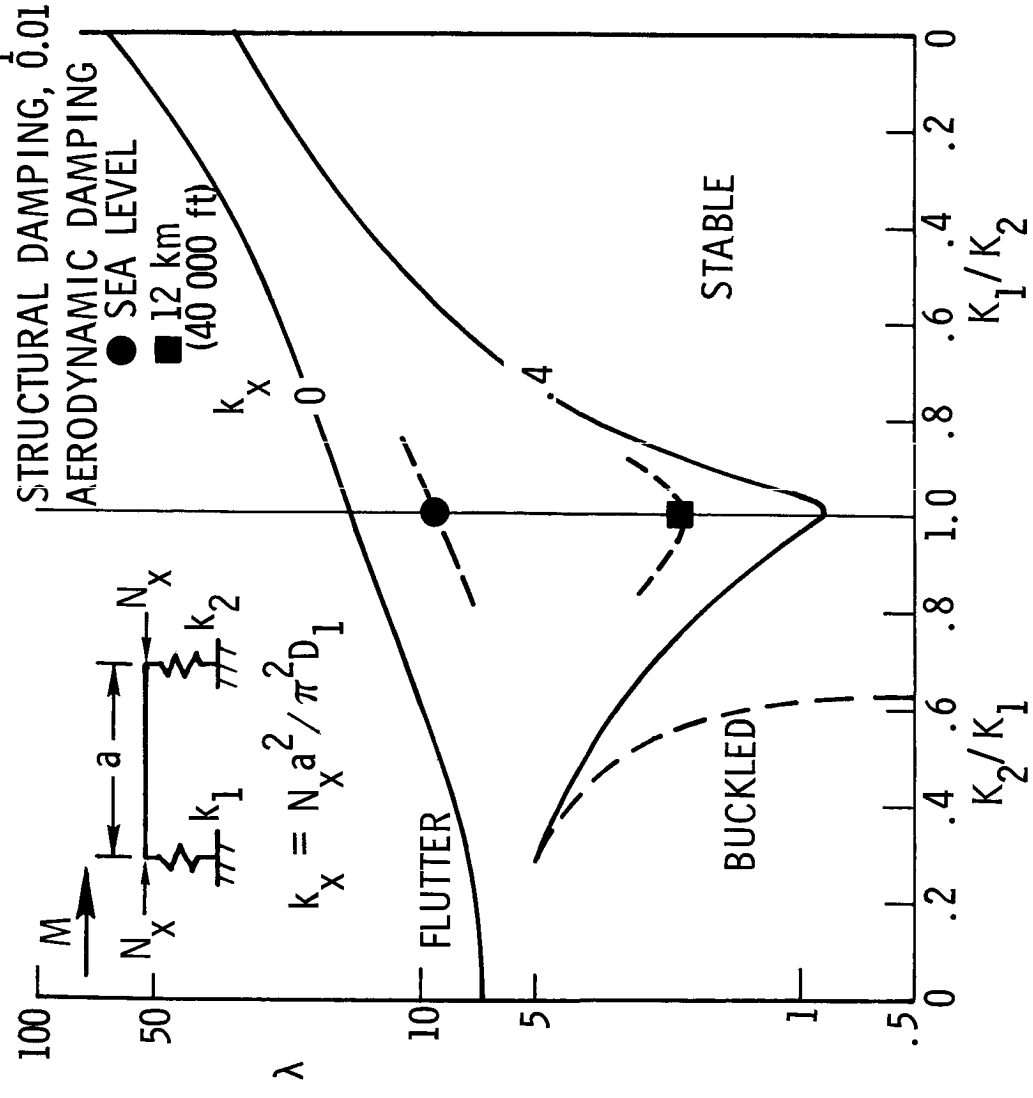


Figure 4

(Figure 5)

Next, attention is directed to the effect of flow angularity on flutter of orthotropic panels. This figure shows some recent results generated from a study at the NASA Ames Research Center (ref. 3). The data are obtained from a modal analysis of a square orthotropic panel that was clamped on all edges and had infinite deflectional stiffness or rigid supports. As many as 50 plate modes were used in some cases to obtain converged results. The ordinate is the ratio of the dynamic-pressure parameter to the value of the parameter for zero flow angle. The curves show the influence of the ratios of panel stiffnesses on flutter. The solid curves are for a constant value of  $D_2/D_1 = 0.001$  and the dashed curves are for  $D_2/D_1 = 0.01$ . The maximum flexural stiffness  $D_1$  is in the stream direction when  $\Lambda = 0^\circ$ . Numbers on the curves are values of the ratio of twisting stiffness  $D_{12}$  to maximum flexural stiffness  $D_1$ . The stiffness ratios of the lower solid curve are representative of an orthotropic panel formed by a single corrugated sheet. This curve shows a very pronounced reduction in dynamic pressure at small flow angles. For example, at a flow angle of  $70^\circ$  the panel retains only 1 percent of its flutter resistance at  $\Lambda = 0^\circ$ . On the other hand, the upper dashed curve is representative of typical orthotropic panels formed by double corrugated sheets. For this case the panel is less sensitive to small flow angles and retains 35 percent of its flutter resistance at  $\Lambda = 90^\circ$ .

Two significant points should be made here. First, in areas of the shuttle vehicle surface where flow angles of  $20^\circ$  to  $30^\circ$  are anticipated, the designer of orthotropic panels may have to use the flutter theory at  $\Lambda = 90^\circ$  for conservative flutter estimates. Secondly, the single corrugated skin is most prone to flutter at small flow angles and should be examined carefully on the basis of mission requirements.

## INFLUENCE OF FLOW ANGULARITY ON FLUTTER

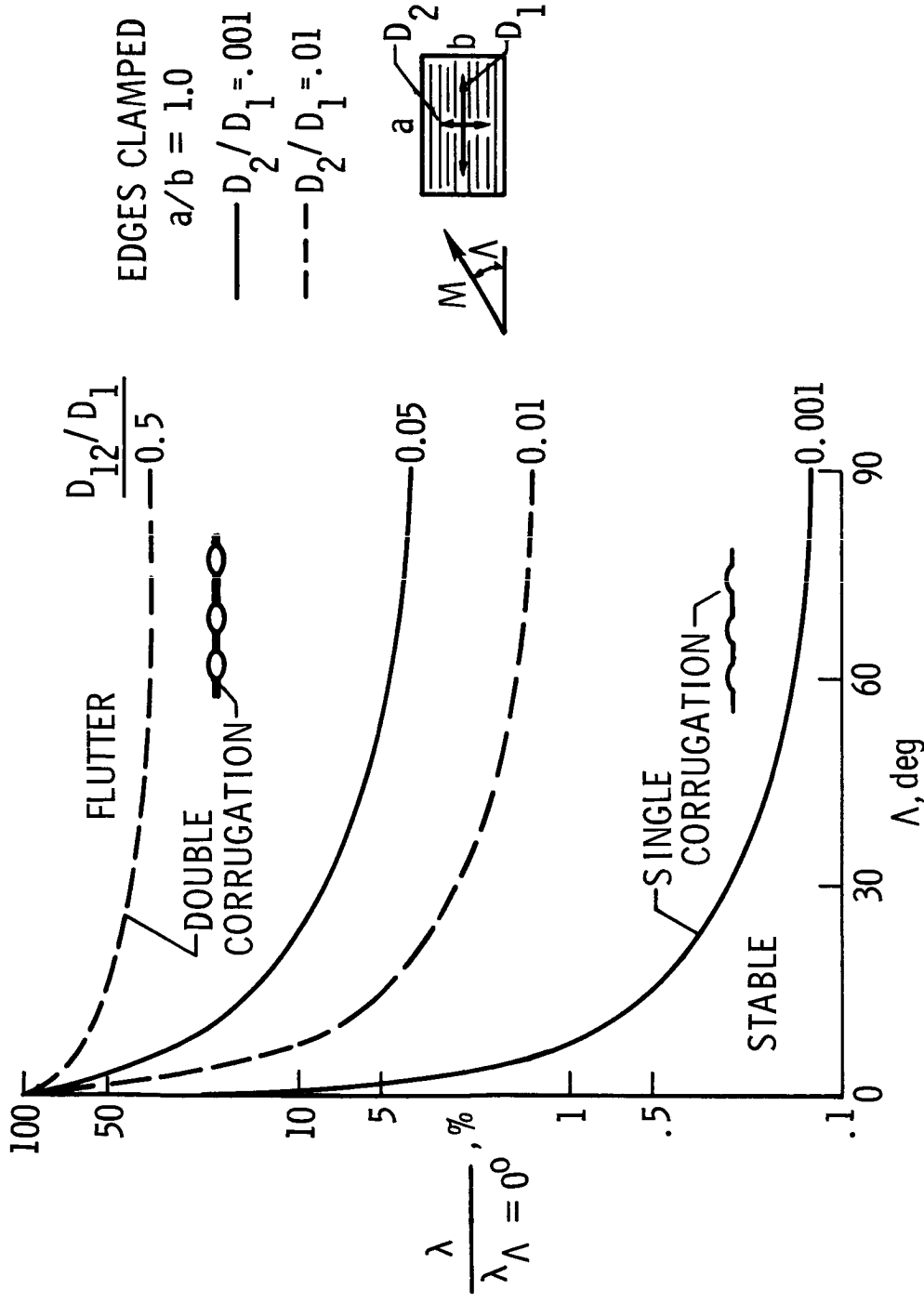


Figure 5

(Figure 6)

Very limited experimental data exist for highly orthotropic panels at flow angles to verify the trends predicted; however, this figure shows a comparison of theory and some limited experimental data obtained from a corrugation-stiffened panel. The ordinate is the ratio of the dynamic-pressure parameter to the value of the parameter for a simply supported panel with  $\Lambda = 0^\circ$ . The panel was 48 cm (19 inches) square and had the panel stiffness ratios shown in the figure. The panel was essentially simply supported (ss) along two edges parallel to the direction of maximum flexural stiffness, and the other two edges were on flexible supports with calculated deflectional-spring-stiffness parameters  $K_1 = K_2 = 60$ . (Note that the symbol  $K$  is used to represent  $K_1$  or  $K_2$ .) The panel was tested in

the Langley 9- by 6-foot thermal structures tunnel, and flutter was obtained at  $15^\circ$  increments for  $\Lambda = 30^\circ$  to  $90^\circ$ . These data points are represented by the square symbols. Tunnel limitations prevented flutter boundary definition at smaller flow angles. The theory corresponding to the panel boundary conditions is represented by the lower dashed curve. Although flutter theory is not available for a panel on flexible supports at arbitrary flow angle, the end points at  $0^\circ$  and  $90^\circ$  are exact (ref. 4) and the curve is faired on the basis of trends in figure 5. The upper curve is the theoretical flutter boundary for the panel with all edges on rigid supports.

The theory indicates a marked reduction in dynamic pressure for flutter as a result of the flexible supports. For example,  $\lambda$  is only 17 percent of the value for  $K = \infty$  (rigid supports) at  $\Lambda = 0^\circ$  and decreases to only 0.6 percent at  $\Lambda = 90^\circ$ . This pronounced reduction is supported by the experimental data over the range of flow angles covered. Thus, the effect of flexible support clips designed to permit thermal growth in the plane of the panel may be to degrade the flutter dynamic pressure seriously unless special provisions are made to insure that the supports are rigid against deflections normal to the panel.

# COMPARISON OF THEORY AND EXPERIMENT

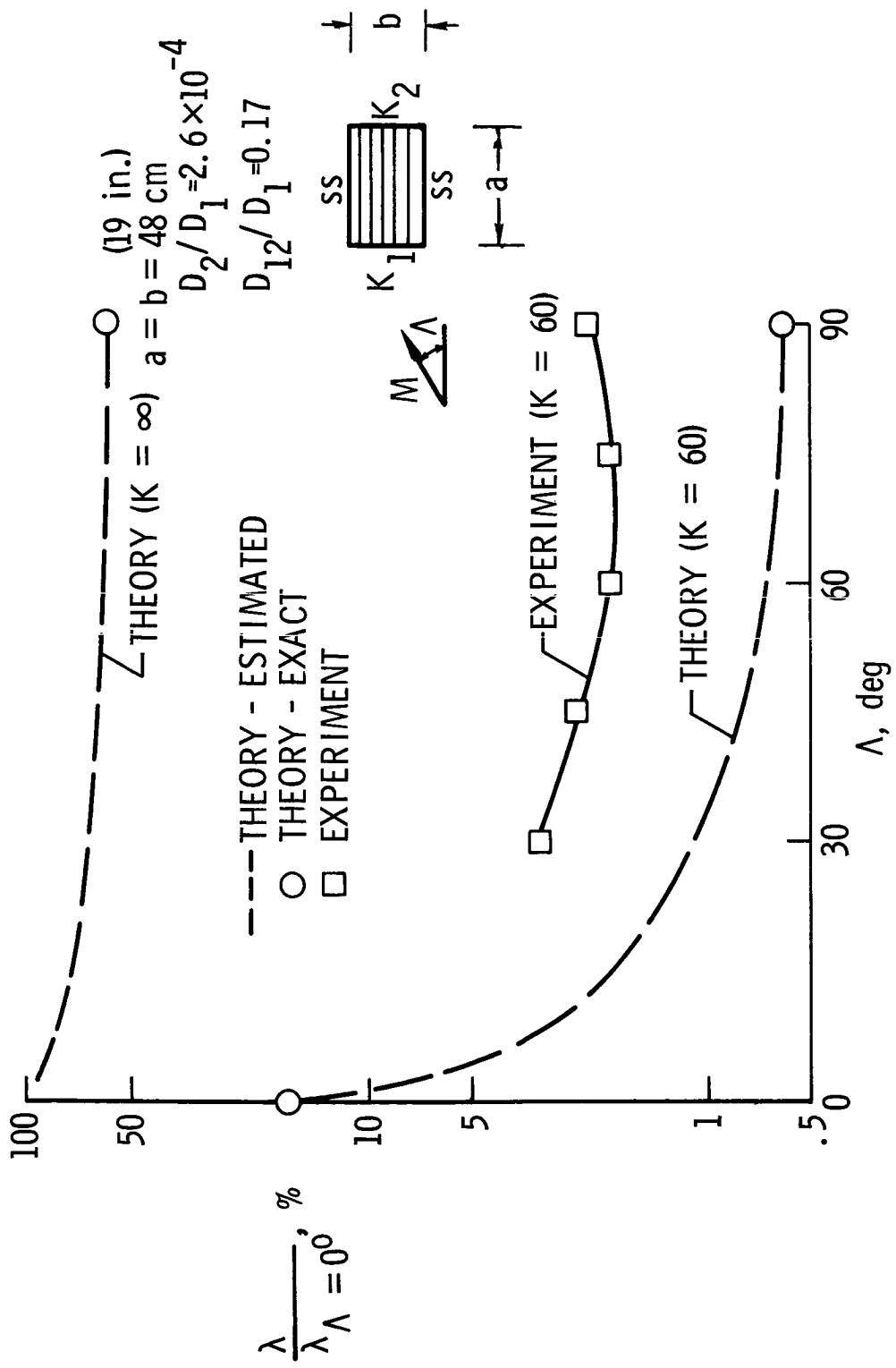


Figure 6

## FLUTTER COMPARISON OF SHUTTLE SURFACE STRUCTURES

(Figure 7)

How significant are the adverse effects of flexible supports and flow angularity to the shuttle mission? This question is best answered by comparison of flutter predictions of actual heat-shield designs with the shuttle trajectory, as shown in this figure. The flutter of panels when presented in terms of the aerodynamic parameter on the ordinate  $q_l / \sqrt{M^2 - 1}$  has been shown (ref. 5) by both theory and experiment to be independent of Mach number from low supersonic speeds to hypersonic speeds. Consequently, panel designs will be flutter-free if the value of the ordinate parameter for flutter exceeds the maximum value encountered by the shuttle in the supersonic and hypersonic speed range. In the ordinate parameter both the dynamic pressure and the Mach number are local values. The range of this aerodynamic parameter for the shuttle is shown by the shaded band; the upper boundary is the maximum value on ascent when the structure is cool, and the lower boundary is the maximum value during entry of the orbiter when the structure is hot.

The values of the ordinate parameter are determined for flutter of two panel designs currently under study at LARC - the single corrugation and the double corrugation. Panel details are shown in the figure. The panel is supported at 36-cm (14-inch) intervals and is 107 cm (42 inches) wide. The short edges of the panel are free. Corrugations are aligned with the stream when  $\Lambda = 0^\circ$ , as indicated in the sketch. The single corrugation is 0.041-cm-thick (0.016-inch) René 41. The double skin has the same corrugation pattern as the single corrugation and is made from two sheets of 0.025-cm-thick (0.01-inch) René 41. Thus the mass of the double corrugated panel is 25 percent greater than that of the single corrugation.

Panel stiffnesses are given in the following table and reflect a large increase in twisting stiffness  $D_{12}$  for the double corrugation:

Symbol	Corrugation shape	$D_1$ , N-m (1b-in.)	$D_2$ , N-m (1b-in.)	$D_{12}$ , N-m (1b-in.)	K
□		900 (8000)	1.2 (11)	0.9 (8)	70
○		2150 (19 000)	2.8 (25)	860 (7600)	30

# FLUTTER COMPARISON OF SHUTTLE SURFACE STRUCTURE

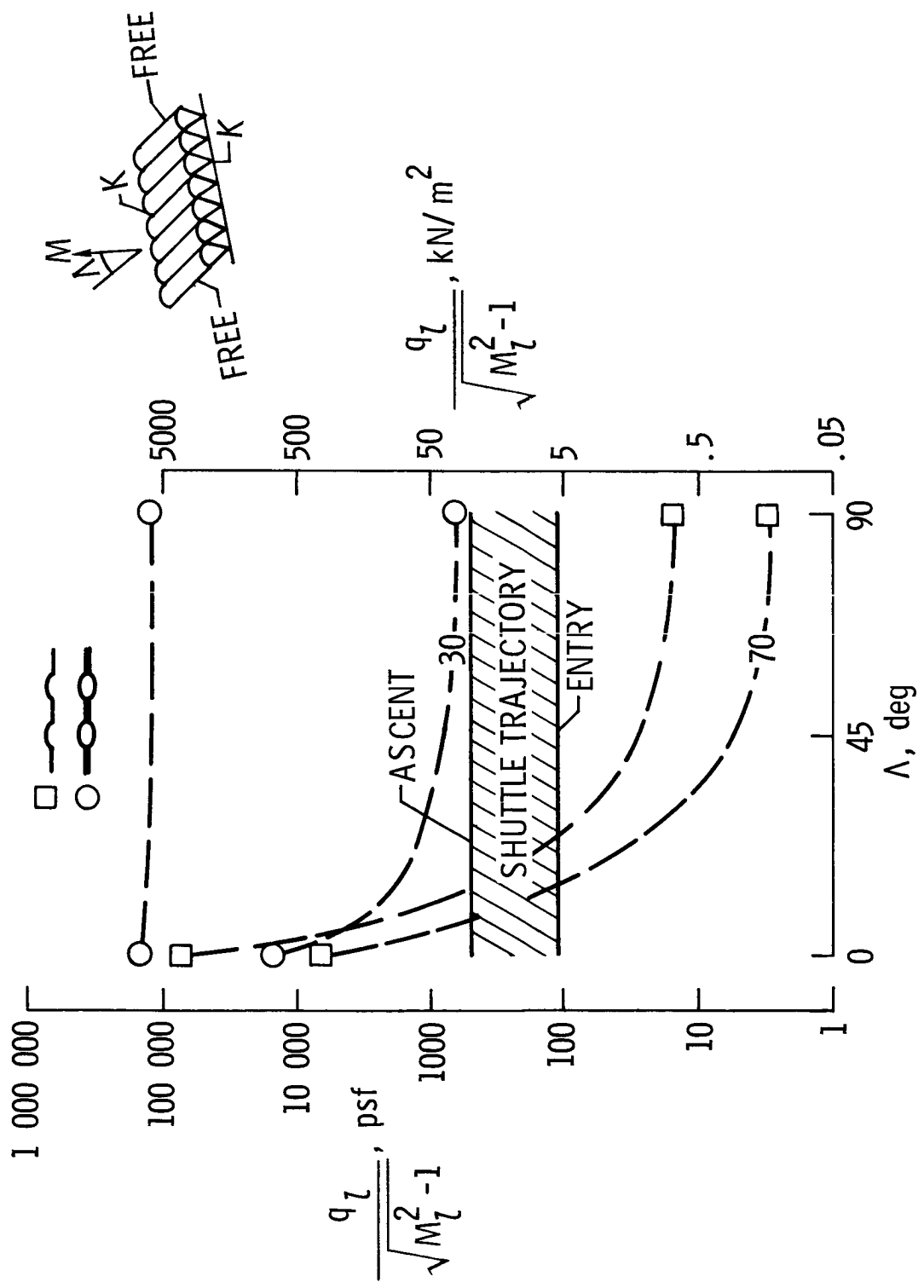


Figure 7

## (Figure 7 - Concluded)

Flutter calculations are made for flow angles of  $0^\circ$  and  $90^\circ$  for two support conditions: (1) the panel rigidly supported along the long edges ( $K = \infty$ ) and (2) the panel flexibly supported on the same edges on equal springs with a constant panel support stiffness of  $1.4 \text{ MN/m}^2$  ( $200 \text{ lb/in}^2$ ) corresponding to the values of  $K$  given in the table. The square symbols are the calculated flutter points for the single corrugation and the circle symbols are for the double corrugation.

Comparison of the flutter calculations with the shuttle trajectory when  $\Delta = 0^\circ$  indicates a large flutter margin for both panels on either rigid or flexible supports. However, the single corrugated panel would encounter flutter at small flow angles even for rigid supports. On the other hand, the flutter region of the double corrugated panel is completely out of the range of the shuttle trajectory. Neither of these panel designs has been optimized for flutter nor has their structural integrity been demonstrated in a hostile environment. However, based on present theories, lightweight designs for space shuttle application are possible provided sufficient attention is given to flutter prevention.

#### CONCLUDING REMARKS

In summary, it is important to note that present flutter theories are based on assumptions that may be somewhat strained when applied to shuttle thermal protection systems. In particular, continuous line supports are assumed, whereas spatial variations of the supports are generally more realistic. Finally, experimental programs are underway to provide data to assess the credibility of the theories and trends presented herein.

## REFERENCES

1. Dixon, Sidney C.; and Shore, Charles P.: State of the Art for Panel Flutter as Applied to Space Shuttle Heat Shields. NASA TM X-52876, Vol. II, 1970, pp. 199-221.
2. Plank, P. P.; Sakata, I. F.; Davis, G. W.; and Richie, C. C.: Hypersonic Cruise Vehicle Wing Structure Evaluation. NASA CR-1568, 1970.
3. Gaspers, Peter A., Jr.; and Redd, Bass: A Theoretical Analysis of the Flutter of Orthotropic Panels Exposed to a High Supersonic Stream of Arbitrary Direction. NASA TN D-3551, 1966.
4. Bohon, Herman L.; and Anderson, Melvin S.: Role of Boundary Conditions on Flutter of Orthotropic Panels. AIAA J., vol. 4, no. 7, July 1966, pp. 1241-1248.
5. Bohon, Herman L.; Anderson, Melvin S.; and Heard, Walter L., Jr.: Flutter Design of Stiffened-Skin Panels for Hypersonic Aircraft. NASA TN D-5555, 1969.

BUFFET RESPONSE OF SPACE SHUTTLE LAUNCH CONFIGURATIONS  
AS DETERMINED BY TESTS OF AN AEROELASTIC MODEL

By Lado Muhlstein, Jr.  
NASA Ames Research Center, Moffett Field, Calif.

INTRODUCTION

A number of launch vehicles used in the past have encountered severe buffet problems. Some of the early launch vehicle failures are believed to be the result of buffet. Thus, the investigation of the buffet response of a proposed launch vehicle should begin early in its development. In the case of the space shuttle vehicle, the proposed configurations consisting of two large winged vehicles mated in parallel are without precedent. Such a configuration has numerous potential sources of buffet.

A series of tests designed to investigate the buffet response of a typical straight wing and a delta wing SSV\* launch configuration have recently been completed at the Ames Research Center. This paper presents the first preliminary results of these tests.

The purpose of these tests was to determine what are some of the potential buffet problems of a typical SSV launch configuration. Because buffet is strongly configuration dependent, these tests were not intended to provide design information and should not be used for that purpose.

It should be emphasized that the results presented in this paper are very preliminary. A much more detailed analysis will be performed and it is expected that the detailed results will be published at a later date.

---

\* SSV - space shuttle vehicle

## CONFIGURATIONS TESTED

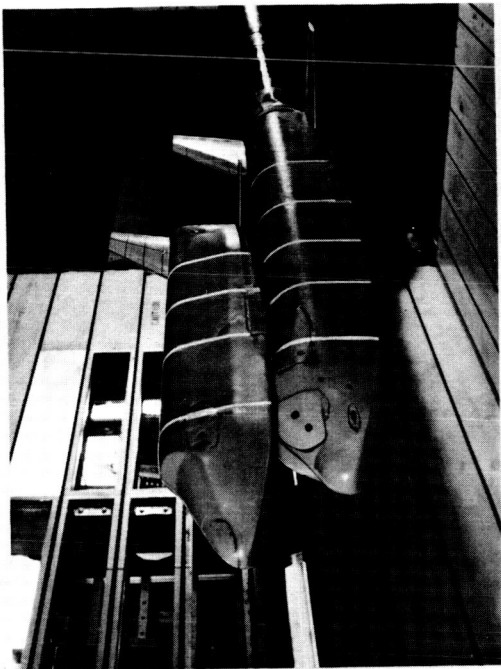
(Figure 1)

A .025 scale elastic model was used to investigate the buffet response of the launch configuration of a space shuttle vehicle. The model tested consisted of a single pair of bodies with removable wings and tail surfaces. The four configurations tested are shown installed in the Ames 11- by 11-foot transonic wind tunnel in Figure 1.

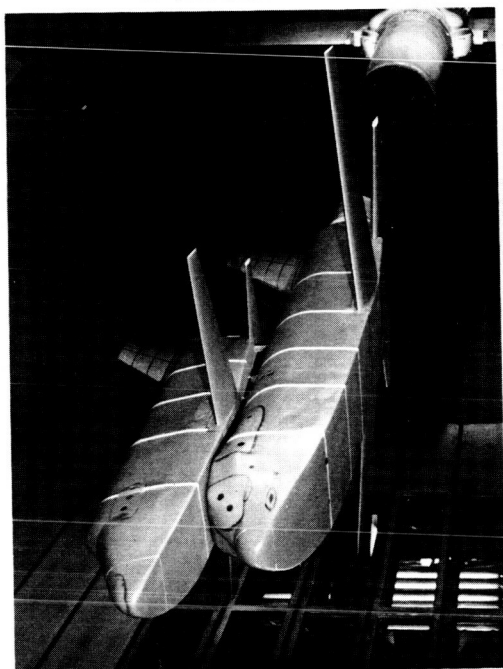
The airfoil section of the straight wings varies from 0010-64 at the tip to 0014-64 on model centerline. The horizontal and vertical tails have a constant 0012-64 section. The wings have a +4° angle of incidence relative to the body axes.

The airfoil section of the delta wings is 0006-64. The leading edge sweep is 70° and the tip rudders are canted upward 50°.

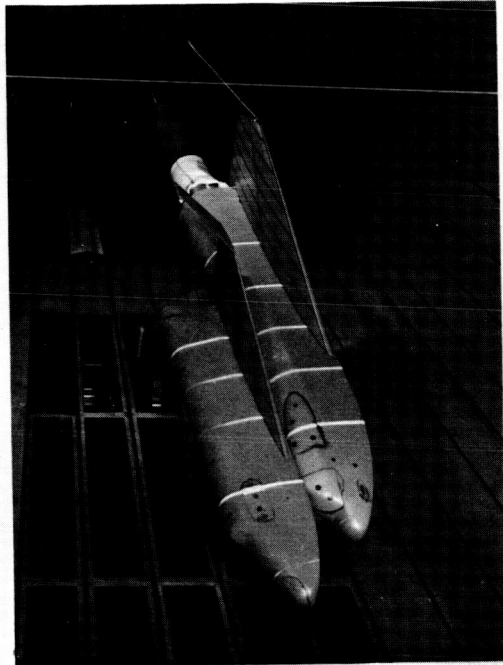
AEROELASTIC MODEL CONFIGURATIONS TESTED



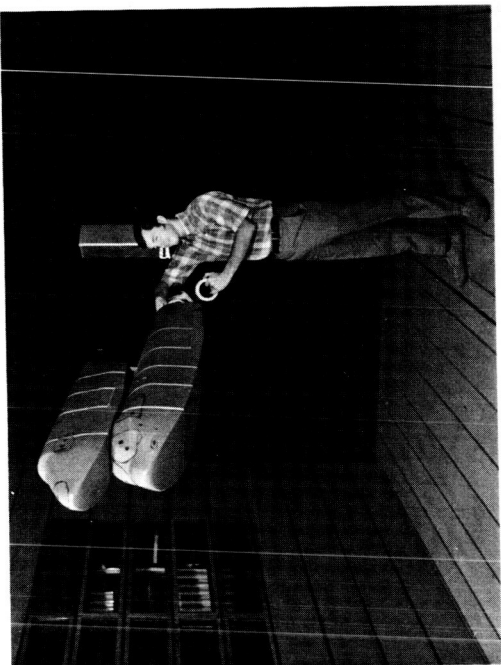
BODIES + TAILS



BODIES + WINGS + TAILS



DELTA WINGS



BODIES ONLY

Figure 1

## DESIGN FEATURES OF SSV AEROELASTIC MODEL

(Figure 2)

Details of the model construction are shown in Figure 2. The scaled stiffness and mass for the orbiter and booster fuselage were simulated over most of the vehicle lengths by aluminum tubes of varying diameter and wall thickness. The additional mass necessary in the area of the liquid oxygen tanks was provided by adding lead cylinders inside of the tube. The bending and torsional frequencies of the straight wings were also scaled.

The horizontal and vertical tail surfaces were not mass and stiffness scaled because of the difficulty of doing so while maintaining the strength necessary to carry the static aerodynamic loads. These surfaces are constructed of thin sheets of magnesium formed into an airfoil section and filled with rigid polyurethane foam.

The delta wings were constructed in the same manner as the horizontal and vertical tails. They were not elastically scaled because the mass and stiffness distribution of a representative delta wing for a space shuttle vehicle was not readily available.

The external contours of the fuselages were formed by rigid polyurethane foam cast over the spines and covered with a layer of glass fiber cloth and polyester resin. To reduce the stiffness contribution of the layer of glass fiber cloth, several shallow circumferential saw cuts were made in the orbiter and booster. The outer portions of these cuts were filled with a silicone rubber for aerodynamic smoothness.

The entire model was attached to a forked sting by a flexure system near the front and rear node points of the vehicles first two bending modes as shown in Figure 2. The flexures used allowed the model to respond in pitch and yaw simultaneously.

SCHMATIC OF SSV AEROELASTIC BUFFET MODEL

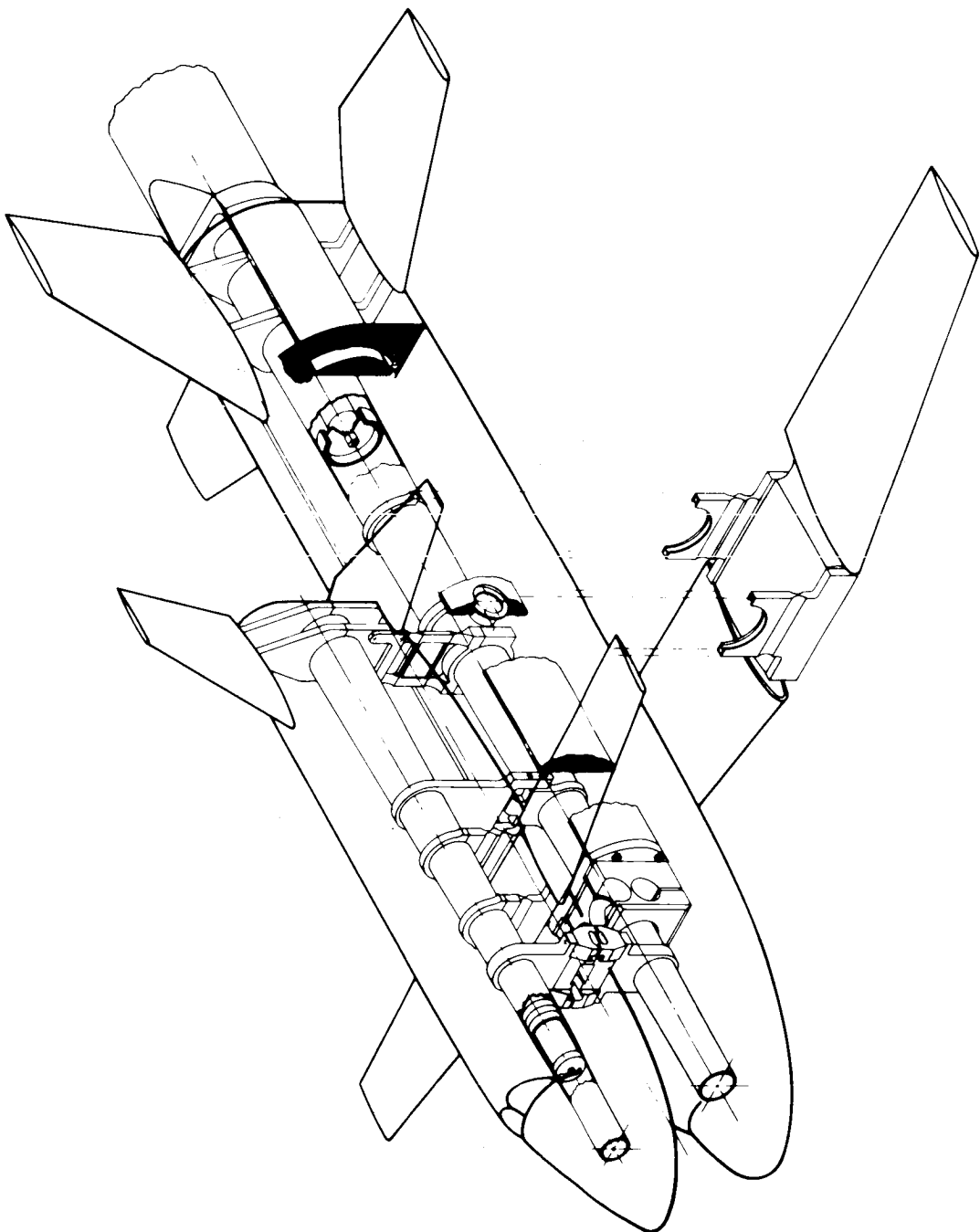


Figure 2

MASS AND STIFFNESS DISTRIBUTION OF SSV AEROELASTIC MODEL

270

(Figure 3)

The mass distribution and stiffness distribution of the model fuselages as built are shown in Figure 3. The design is based on estimated values of mass and stiffness obtained from the Manned Spacecraft Center. The full scale condition used for scaling was the fuel condition existing at maximum dynamic pressure. For the selected trajectory, this occurs at Mach number 1.0. The locations of the flexures connecting the orbiter to the booster and the flexures between the model and support sting are also shown.

All response measurements presented in this paper were taken at the gage locations shown in

Figure 3.

# MASS AND STIFFNESS PROPERTIES OF ORBITER AND BOOSTER BODIES

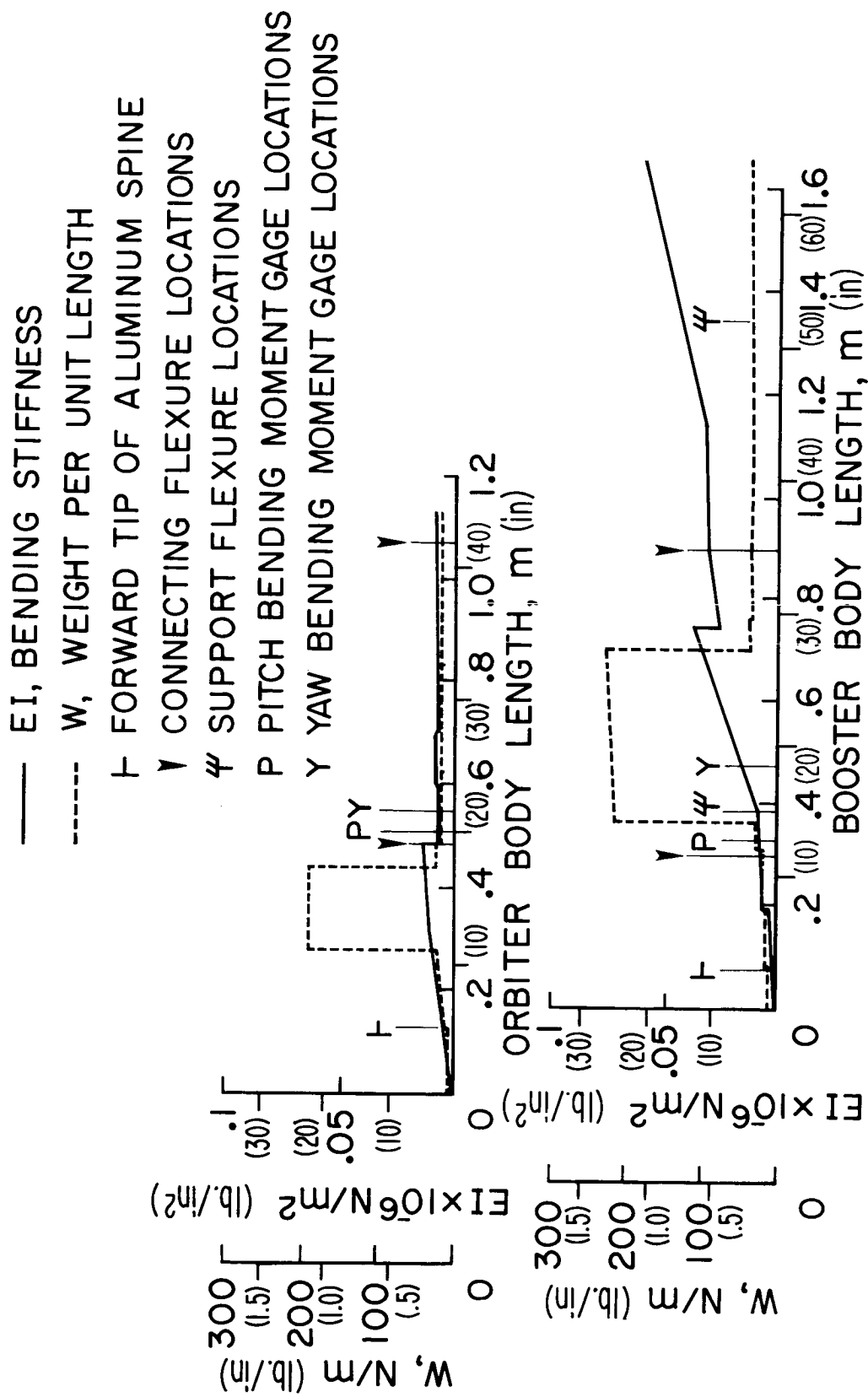


Figure 3

DYNAMIC CHARACTERISTICS OF MODEL

(Figure 4)

The measured resonant frequencies and the corresponding mode shapes for the straight wing configuration are shown in Figure 4. The removal of the wings and tail surfaces increased the body bending frequencies 5 to 8 percent and had negligible effect on the mode shapes.

The delta wings, which are not elastically scaled, significantly increased the body bending frequency because of their large stiffness.

DYNAMIC CHARACTERISTICS OF MODEL WITH STRAIGHT WINGS AND TAILS

MODE SHAPES

FIRST PITCH BENDING MODE, PI



FIRST YAW BENDING MODE, Y1



SECOND PITCH BENDING MODE, P2



SECOND YAW BENDING MODE, Y2



MODE	NATURAL FREQUENCY, Hz	DAMPING RATIO
P1	41.2	0.020
P2	118.0	0.026
Y1	74.8	0.018
Y2	123.2	0.012

Figure 4

## (Figure 5)

The model was instrumented at numerous points to measure forces, bending moments and accelerations. Bending moments and accelerations were measured on the wings, the horizontal tail, the vertical tail and the spine in the pitch and yaw directions for the orbiter and booster. In addition, the normal forces, side forces and axial force were measured on the flexures connecting the orbiter and booster. This paper will deal only with the spine bending moments in the pitch and yaw plane measured on the orbiter and booster at the stations specified in Figure 3.

During the wind tunnel test, the model response was recorded on magnetic tape. Power-spectral density analyses of selected records were performed to verify the resonant frequencies of the modes of interest. Band pass filters were centered on these frequencies to determine the root-mean-square value of the response of the mode of interest. This approach was used to exclude response to strong modes which are not representative of the vehicle in flight.

All response data presented in this paper are root-mean-square value of all modes of interest. A representative PSD\* plot of the orbiter spine bending moment in the pitch plane is shown as

Figure 5. Also shown are the responses of representative filters used.

---

\*PSD - power spectral density

Typical Power-Spectral Density Plot of Orbiter  
Spine Pitch Bending Moment

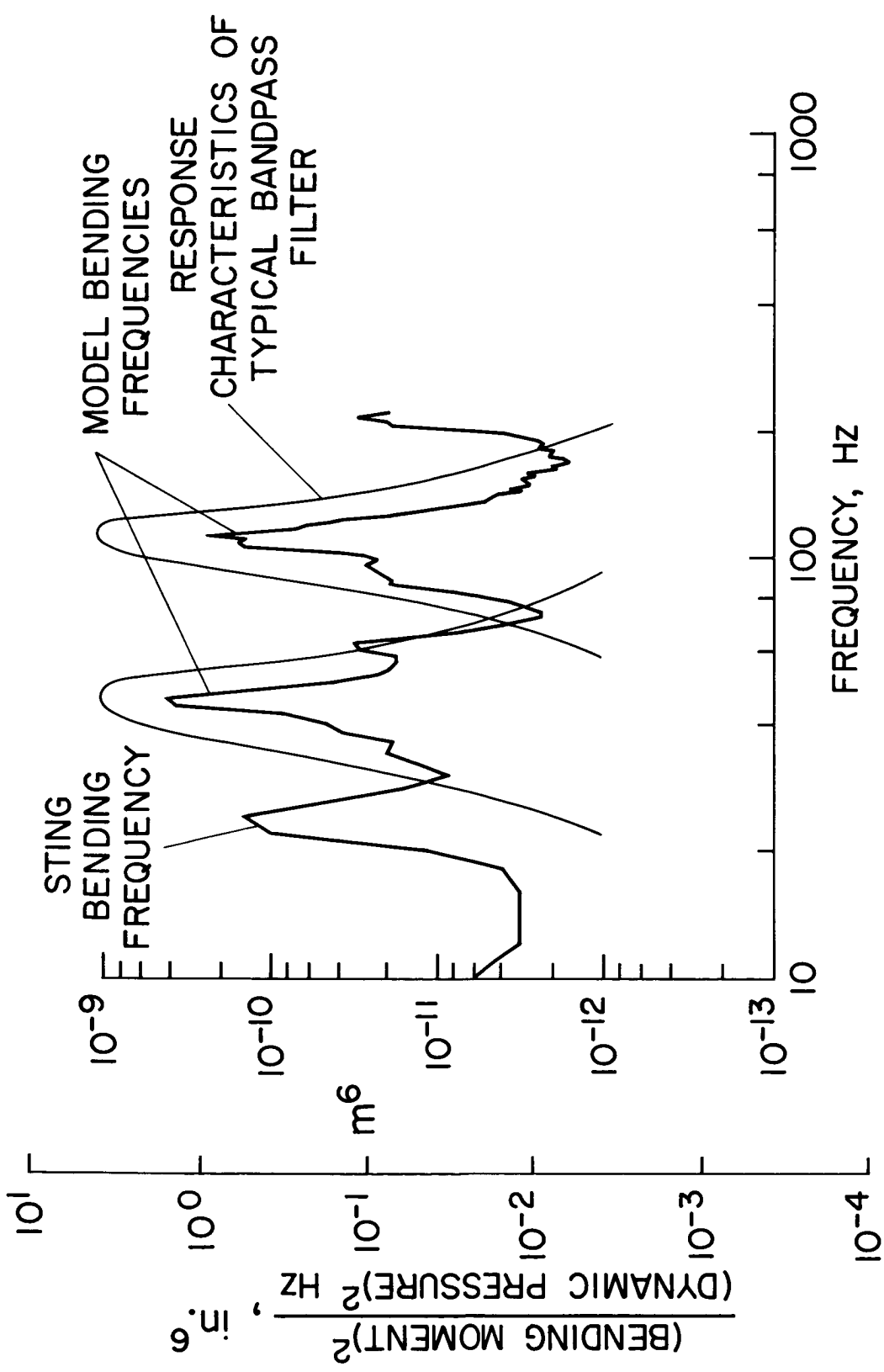


Figure 5

BUFFET RESPONSE IN PITCH PLANE  $M = 0.90$ 

(Figure 6)

The normalized RMS response as a function of angle of attack is shown in Figure 6 for  $M = 0.90$ .

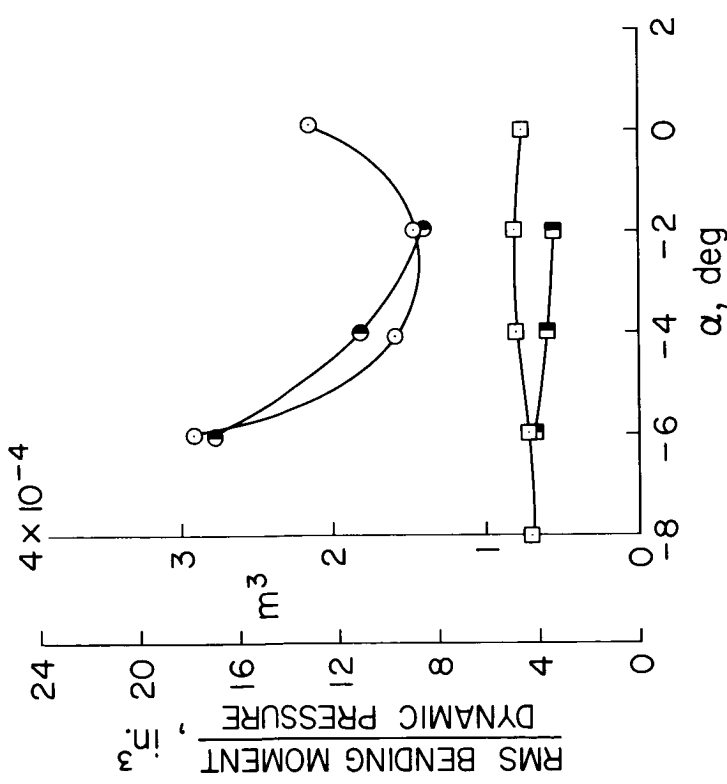
For the bodies only configuration, the response is low and is insensitive to changes of angle of attack and yaw.

For the straight wing configuration, the response is also insensitive to yaw but is significantly larger and is a strong function of angle of attack. Minimum buffet occurs at approximately zero lift. The rapid increase in buffet with increasing lift is typical of thick wings in this Mach number range. This figure is typical of the buffet response at high subsonic Mach numbers. At supersonic Mach numbers, the response is lower and less sensitive to angle of attack.

# BUFFET RESPONSE IN THE PITCH PLANE

$M = 0.90$

ORBITER



BOOSTER

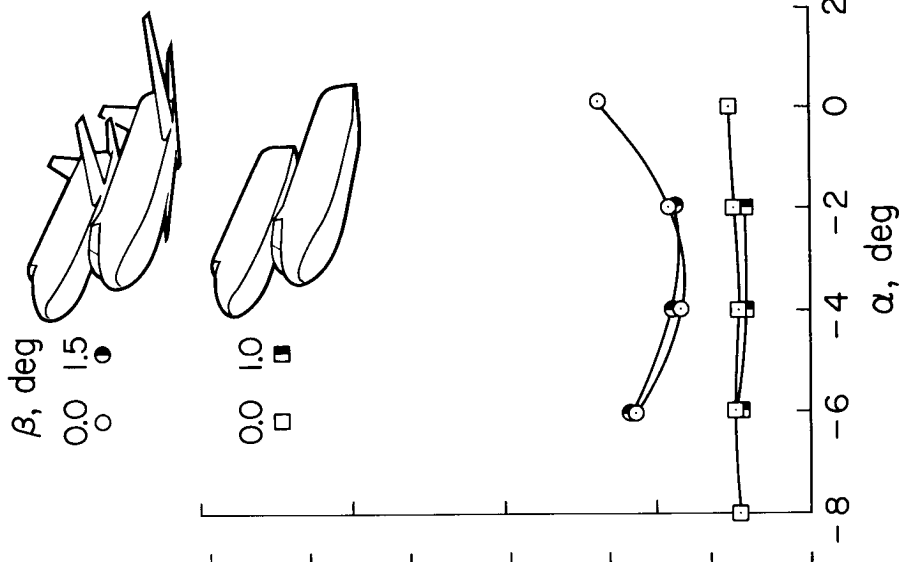


Figure 6

BUFFET RESPONSE IN PITCH PLANE  $M = 0.85$ 

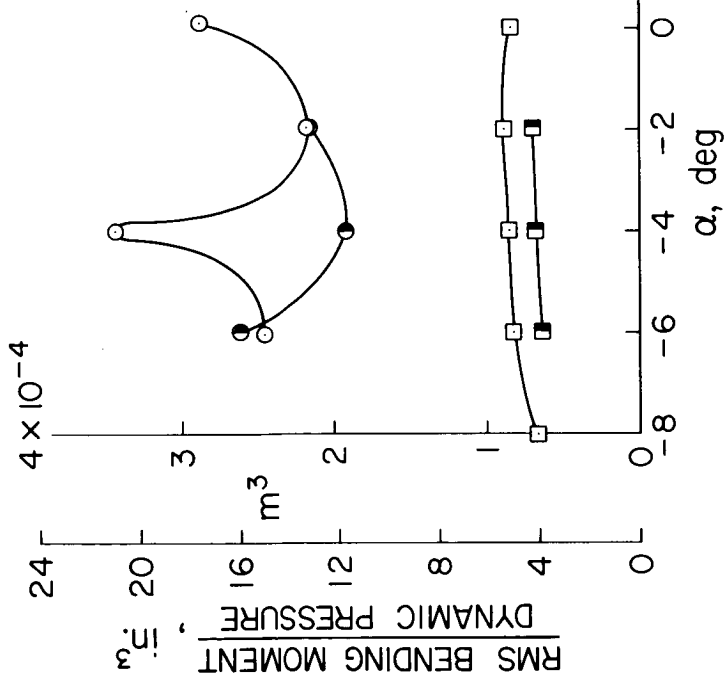
(Figure 7)

The buffet response in the pitch plane for  $M = 0.85$  is shown in Figure 7. The results are similar to those for  $M = 0.90$  except at  $\alpha = -4^\circ$ ,  $\beta = 0.0^\circ$  for the straight wing model. This point is very near a flutter condition for the booster wing and produces significant response of the bodies. The significantly lower response for  $\beta = 1.5^\circ$  does not mean that yaw suppresses this flutter. This difference is probably due to a very slight difference in Mach number. However, a small change in angle of attack does suppress the flutter. The extreme Mach number sensitivity of this flutter is discussed by Larry L. Erickson in paper no. 7-II of this volume.

# BUFFET RESPONSE IN THE PITCH PLANE

$M = 0.85$

ORBITER



BOOSTER

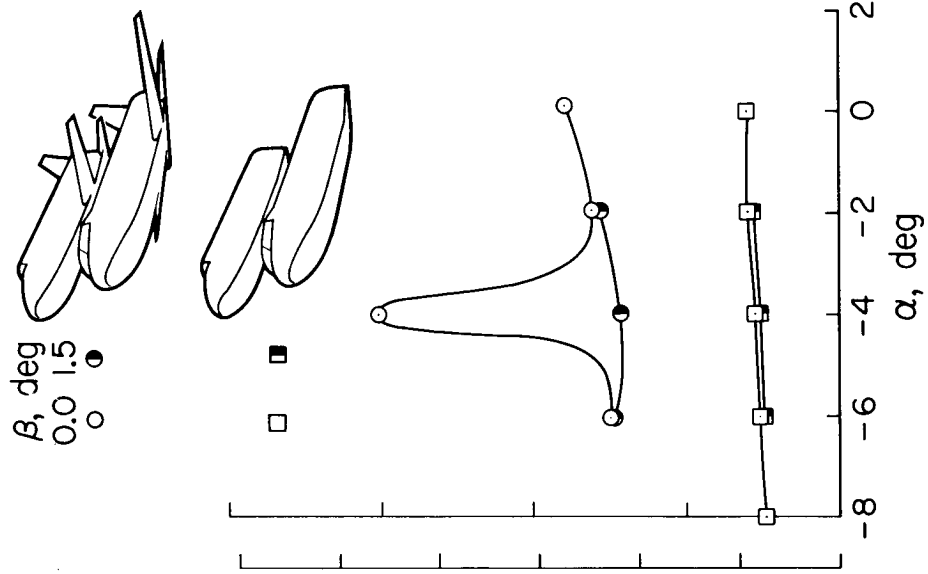


Figure 7

## BUFFET RESPONSE IN YAW PLANE

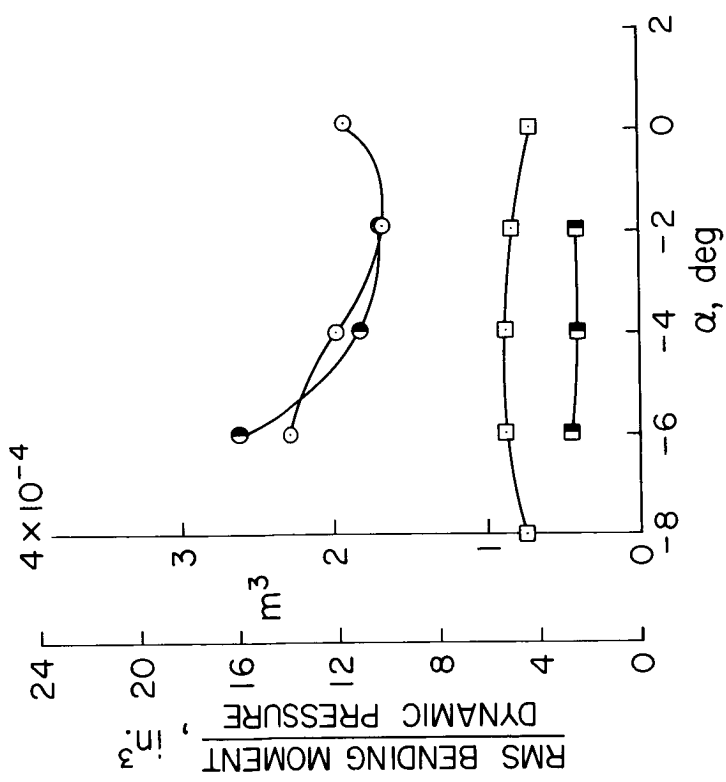
(Figure 8)

Buffet response in the yaw plane is shown in Figure 8. In general, the yaw plane response is very similar to the pitch plane response except for the bodies only configuration. For this configuration, the response decreases significantly for small angles of sideslip. This behavior is not unusual for symmetrical nonlifting bodies.

# BUFFET RESPONSE IN THE YAW PLANE

$M = 0.85$

ORBITER



BOOSTER

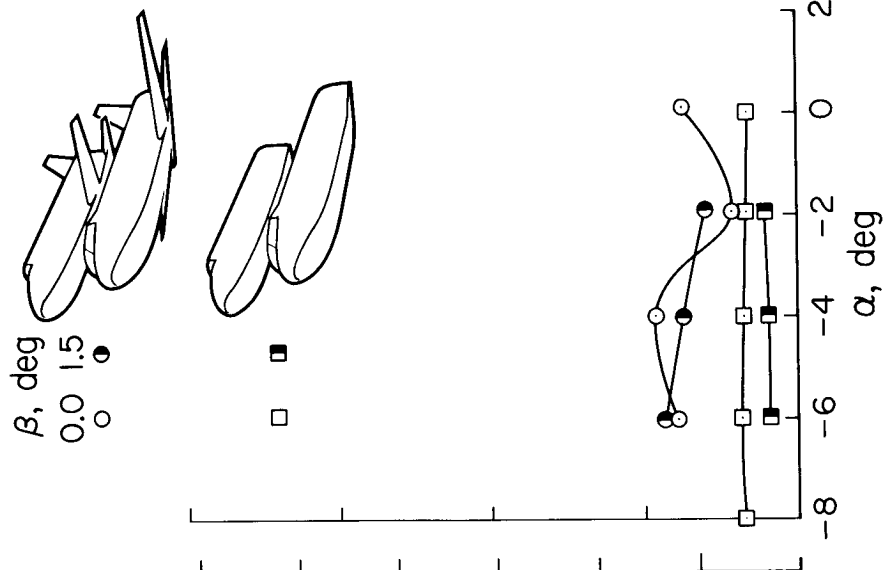


Figure 8

## BUFFET RESPONSE OF DELTA WING MODEL IN PITCH PLANE

(Figure 9)

The wings of the delta wing configuration are not elastically scaled. Therefore, the response of this configuration does not truly represent the response of a practical full scale vehicle and can not be easily scaled to full scale. However, the relative response of this model with changes in attitude and Mach number can provide useful dynamic information. Thus, the bending moment for the delta wing configuration is normalized by the bending moment at 1.40 Mach number. At this Mach number, the response of the model is a very weak function of Mach number and angle of attack.

Figure 9 shows the response of the delta wing configuration as a function of angle of attack at  $M = 0.85$  and  $0.95$ .

The largest response measured on the delta wing configuration occurs at  $\alpha = -2^\circ$ ,  $M = 0.95$ .

This angle of attack corresponds to approximately zero lift on the orbiter.

The response of the delta wing generally remains constant or decreases with small changes in angle of attack from the zero lift condition. This is contrary to the response of the straight wing configuration.

BUFFET RESPONSE OF DELTA WING MODEL IN  
THE PITCH PLANE

$$\beta = 0^\circ$$

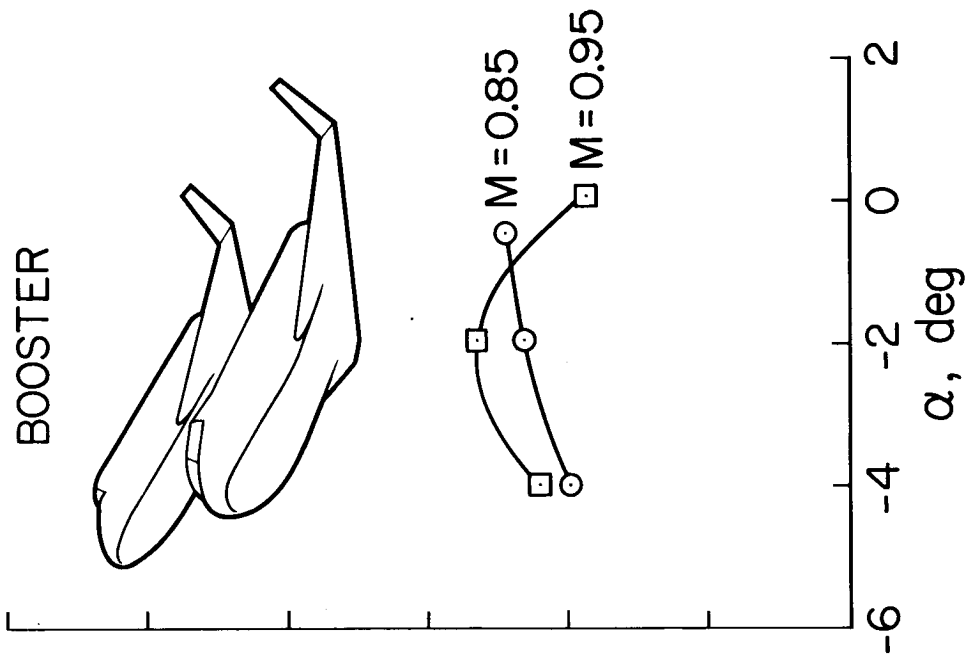
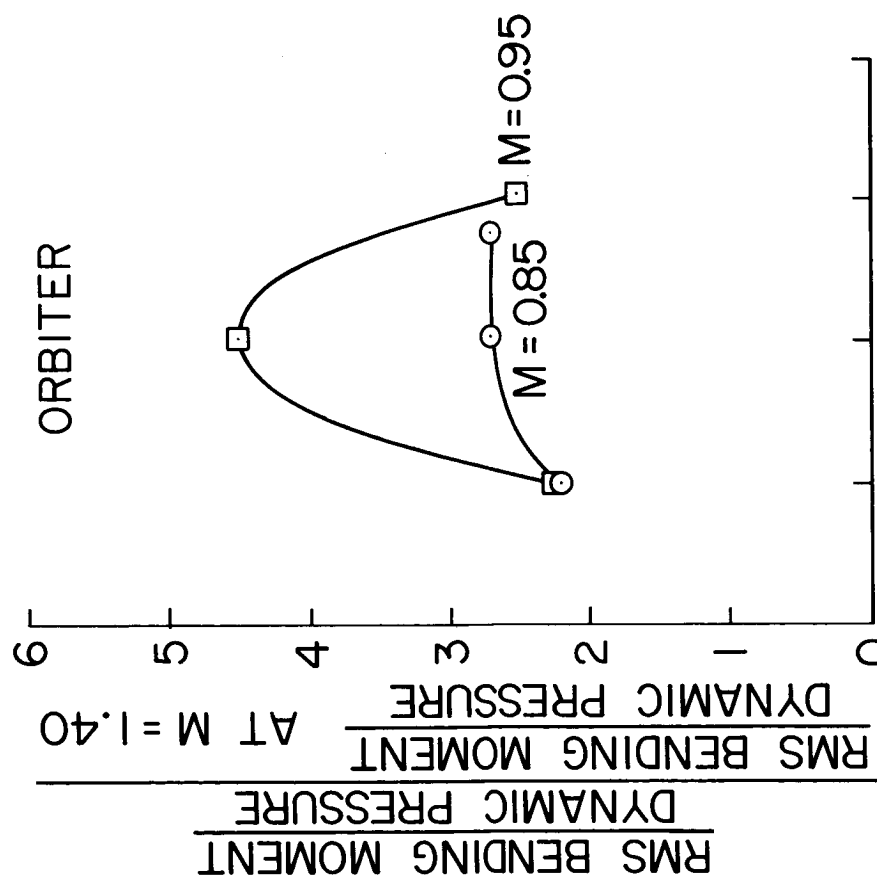


Figure 9

## EFFECT OF MACH NUMBER ON BUFFET RESPONSE IN THE PITCH PLANE

(Figure 10)

The buffet response in the pitch plane as a function of Mach number is shown in Figure 10. The response of the bodies only is a smooth function of Mach number. At high subsonic Mach numbers, the response of the straight wing configuration is four to six times the response of the bodies only. The large response at  $\alpha = 4^\circ$ ,  $M = 0.85$  is close to the booster wing flutter condition previously discussed.

At supersonic Mach numbers, the response of the straight wing configuration is generally less than twice as great as that of the bodies alone.

EFFECT OF MACH NUMBER ON BUFFET RESPONSE  
IN THE PITCH PLANE  
 $\beta = 0.0^\circ$

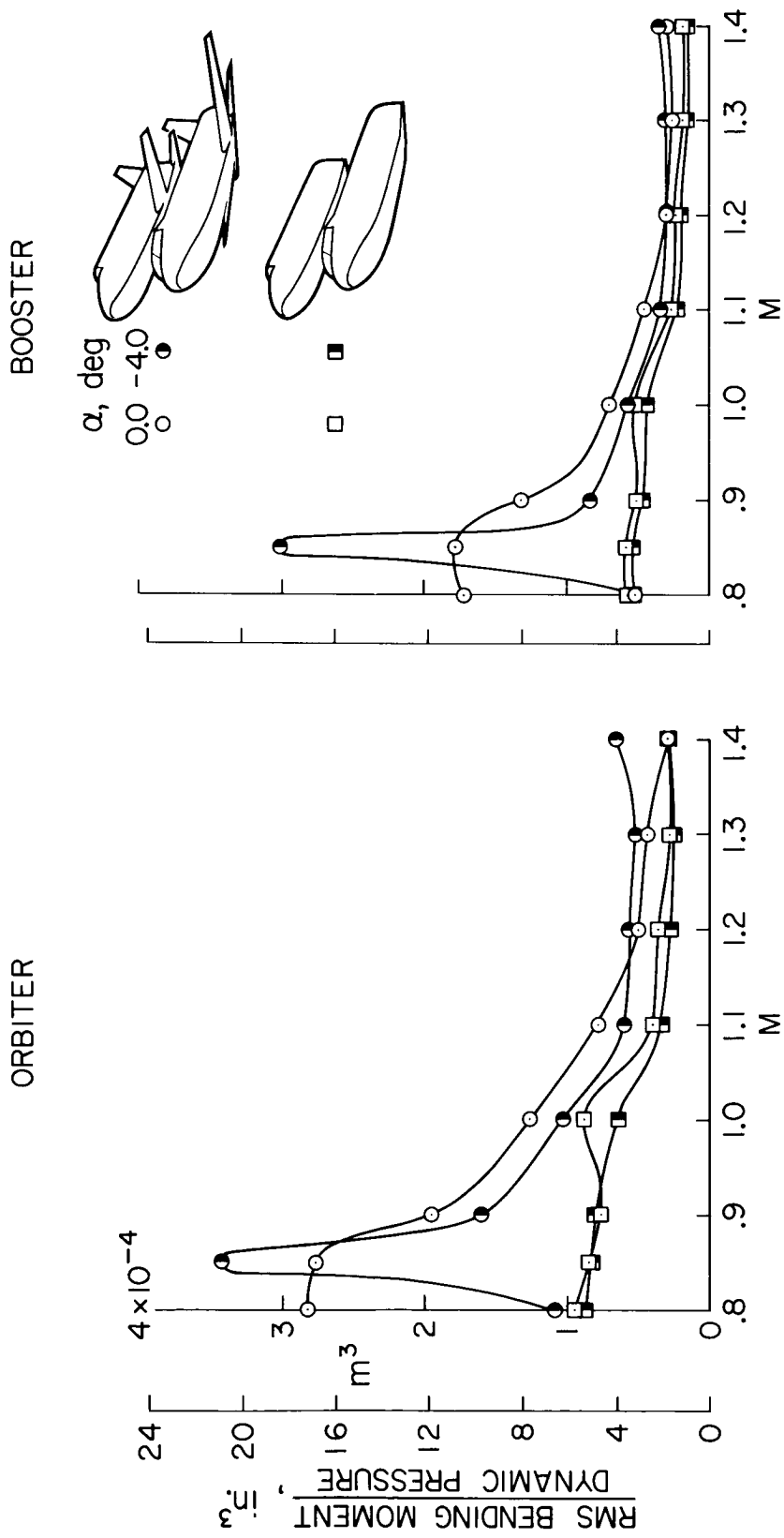


Figure 10

EFFECT OF MACH NUMBER ON BUFFET RESPONSE IN THE YAW PLANE

(Figure 11)

The buffet response in the yaw plane as a function of Mach number is shown in Figure 11. The response is very similar to that observed in the pitch plane except that now a large peak in the response occurs at  $M = 1.0, \alpha = 0^\circ$  and disappears with small changes in angle of attack. At present it is not certain what is the source of this buffet.

EFFECT OF MACH NUMBER ON BUFFET RESPONSE  
IN THE YAW PLANE  
 $\beta = 0.0^\circ$

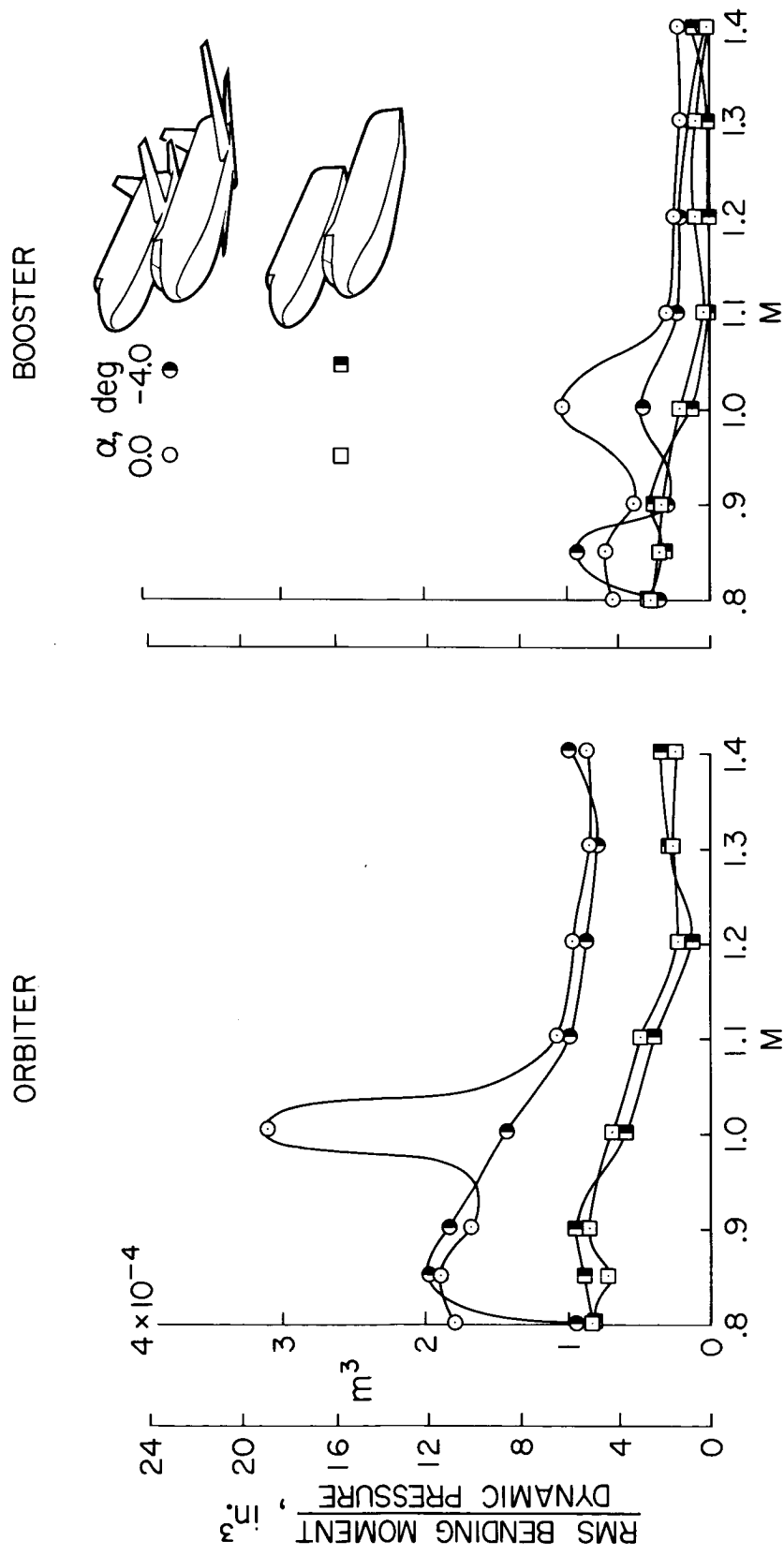


Figure 11

EFFECT OF MACH NUMBER ON BUFFET RESPONSE OF DELTA WING MODEL IN THE PITCH PLANE  
(Figure 12)

The response of the delta wing configuration as a function of Mach number is shown in Figure 12 for two angles of attack. At supersonic Mach numbers, the response is relatively low and constant whereas at high subsonic Mach numbers, the response is much higher and at some Mach numbers, is a strong function of angle of attack.

EFFECT OF MACH NUMBER ON BUFFET RESPONSE OF DELTA WING  
MODEL IN THE PITCH PLANE  
 $\beta = 0.0^\circ$

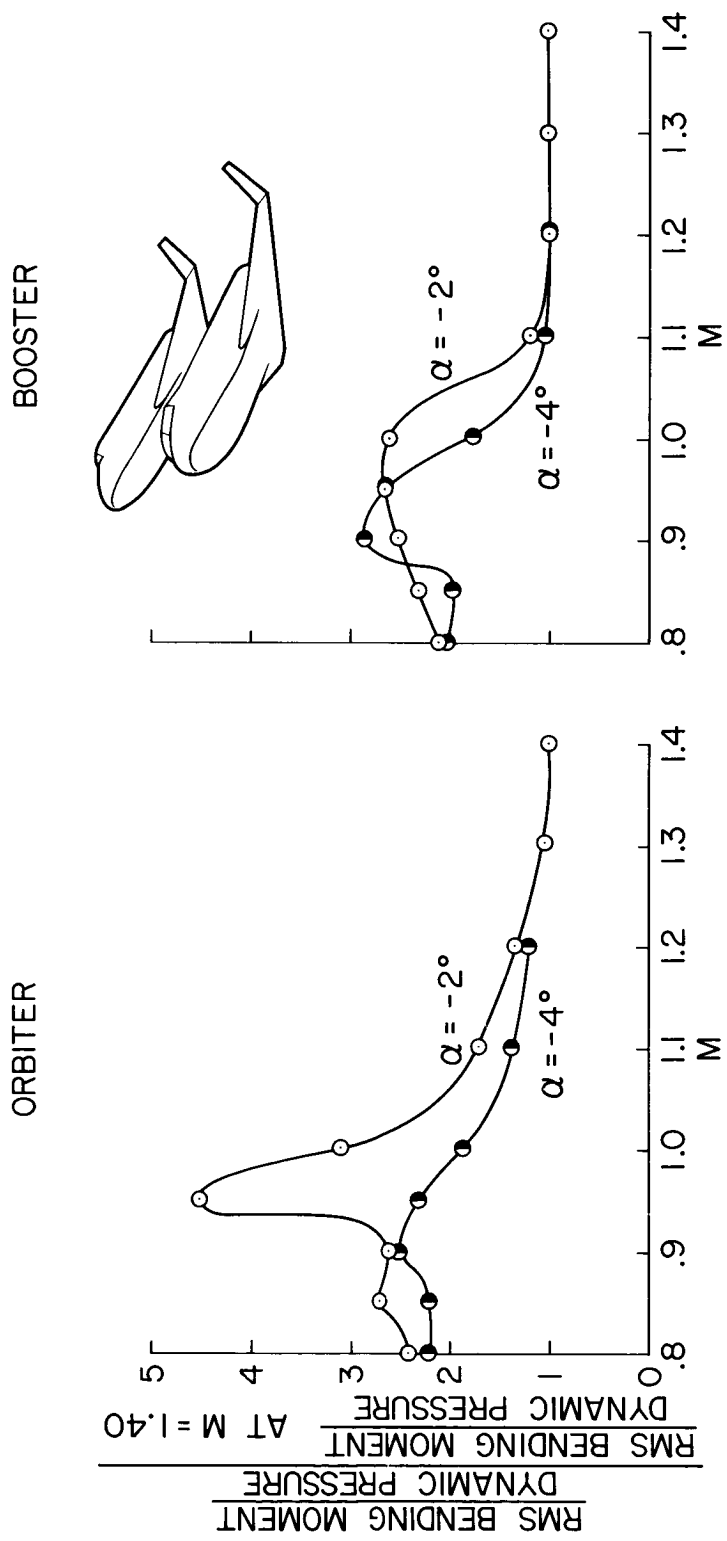


Figure 12

## CONCLUSIONS

It should be again emphasized that these data are very preliminary and that a much more detailed analysis will be performed. However, this preliminary look indicates that there are no major buffet problems produced by coupling the orbiter and booster bodies in parallel in the manner of the configuration tested. However, the addition of airfoils to these bodies can cause significant increases in buffet. With the data currently available, it is not clear that one of the winged configurations is superior to the other with respect to buffet. It should also be pointed out that since many of the buffet producing phenomena are very Mach number and angle of attack sensitive, it will be necessary to do some very careful and detailed testing to be sure that a potentially dangerous condition has not been overlooked.

## SUMMARY

An aeroelastic model was used to determine the response to buffet loads on the launch configurations of a space shuttle vehicle. Tests were conducted from  $M = 0.80$  to  $M = 1.40$  for a series of angles of attack and sideslip. The configurations tested were (1) a straight wing orbiter coupled to a straight wing booster, (2) a delta wing orbiter coupled to a delta wing booster, (3) the coupled bodies without lifting surfaces, and (4) the coupled bodies with the horizontal and vertical tail surfaces.

Results are presented as normalized body bending moments of the orbiter and booster models in the pitch and yaw planes as functions of angle of attack and Mach number.

It is concluded that most of the buffet is produced by lifting and control surfaces. The coupled bodies without lifting or control surfaces do not exhibit any unusual buffet response over the range of conditions of these tests.

## PRELIMINARY MEASUREMENTS AND FLOW VISUALIZATION STUDIES OF PRESSURE FLUCTUATIONS ON SPACE SHUTTLE CONFIGURATIONS

By Charles F. Coe, Jules B. Dods, Jr., Robert C. Robinson  
NASA Ames Research Center, Moffett Field, Calif.  
and William H. Mayes  
NASA Langley Research Center, Hampton, Va.

### INTRODUCTION

In order to specify with confidence the aero-acoustic loads on space shuttle vehicles it is necessary to identify and locate zones of significant turbulence, and then to measure the unsteady pressures in these zones on scale models in wind tunnels. Although such tests will be needed when a final configuration is selected, early tests of candidate configurations have also been needed to gain insight on complexities of flow and to acquire preliminary estimates of fluctuating pressures.

Accordingly, research is in progress at Ames Research Center and at Bolt, Beranek and Newman (on contract to Langley Research Center) to study the flow characteristics and pressure fluctuations on both space-shuttle launch and re-entry configurations. The Ames investigations to date have consisted of pressure fluctuation measurements at transonic speeds on 0.01- and 0.025-scale models of straight-and delta-wing launch configurations and fluorescent oil flow tests of 0.008-scale models of straight-and delta-wing launch configurations over a Mach number range of 0.8 to 2.0. The Bolt, Beranek and Newman tests have been directed to the definition of unsteady pressures for re-entry conditions. They have consisted of flow visualization studies and measurements of pressure fluctuations on both 0.004-scale and 0.0077-scale models of a low-cross-range orbiter configuration at  $\alpha = 60^\circ$  for Mach numbers of 2.5 and 4.0.

## 0.025-SCALE MODELS OF LAUNCH CONFIGURATIONS TESTED IN AMES 11' TWT\*

(Figure 1)

Although flow visualization studies are necessary to detect all regions of severe turbulence on a vehicle, some regions can be anticipated by visual inspection of the geometry. The preliminary measurements of pressure fluctuations on the launch configurations were in fact obtained at Ames Research Center prior to the availability of flow visualization data. Most of the data were obtained during the tests of the 0.025-scale elastic buffet models shown in Figure 1. These models were previously described by Muhlstein in a preceding paper. Transducers were located over the orbiter cockpit, on the orbiter heat shield in the vicinity of flow interference from the booster, and also on the booster in the region of wake flow from the orbiter. The data were obtained in this wake-flow region for both the straight-wing and delta-wing configurations.

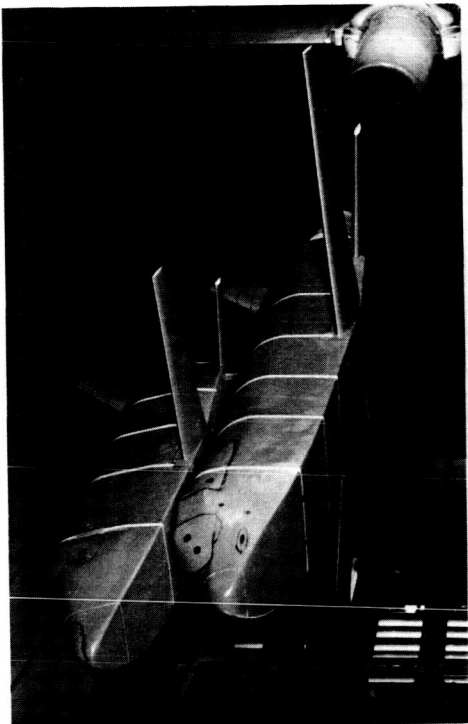
Some earlier data were also obtained on a 0.01-scale model in the region of the orbiter heat shield by Robinson at Ames Research Center.

---

\*TWT - transonic wind tunnel.

0.025-SCALE MODELS OF LAUNCH CONFIGURATIONS  
TESTED IN AMES 11-ft TWT

STRAIGHT WINGS



DELTA WINGS

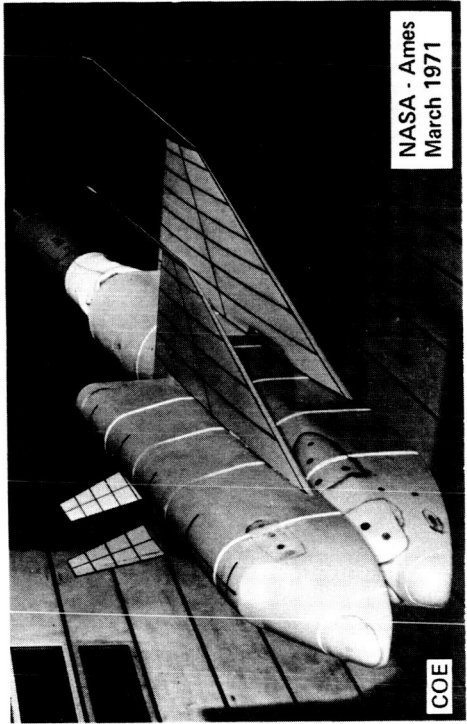


Figure 1

ESTIMATED PRESSURE FLUCTUATIONS DURING ASCENT - ORBITER COCKPIT  
(Figure 2)

Figure 2 shows the estimated pressure fluctuations in the region of the orbiter cockpit during ascent through the Mach number range of 0.8 to 1.4. The data in this figure and in Figures 3, 4 and 5 were scaled to full-scale conditions using standard scaling relationships. The full-scale dynamic pressures and velocities used for the launch configurations are tabulated below. The data in Figures 2, 3 and 4 represent the maximum measurements obtained for the full ranges of angles of attack and sideslip tested. Because of the static load limits on the elastic model the ranges varied with Mach number, but for some test conditions the ranges were from  $\alpha_w = 0^\circ$  to  $\alpha_w = -6^\circ$  and  $\beta = 0^\circ$  to  $\beta = \pm 1\frac{1}{2}^\circ$ .

The maximum overall fluctuating pressure levels (OA FPL) in the region of the orbiter cockpit, 160 dB, occurred at subsonic Mach numbers near 0.8. Representative maximum one-third octave spectra peak at approximately 148 dB. The frequencies at which the peaks occur vary from 5 Hz to 200 Hz and are dependent upon the type of flow and proximity of the transonic shock wave to the measurement location. The lower frequency peaks near 10 Hz are associated with shock oscillations and the higher frequency peaks near 200 Hz with separated flow.

M	.8	.9	1.1	1.4
$q_{FS}$ , N/m <sup>2</sup> (lb/ft <sup>2</sup> )	22,264. (465.)	24,898. (520.)	28,728. (600.)	28,632. (598.)
$U_{FS}$ , m/sec (ft/sec)	243.8 (800.)	274.3 (900.)	333.8 (1095.)	420.6 (1380.)

ESTIMATED PRESSURE FLUCTUATIONS DURING ASCENT  
ORBITER COCKPIT

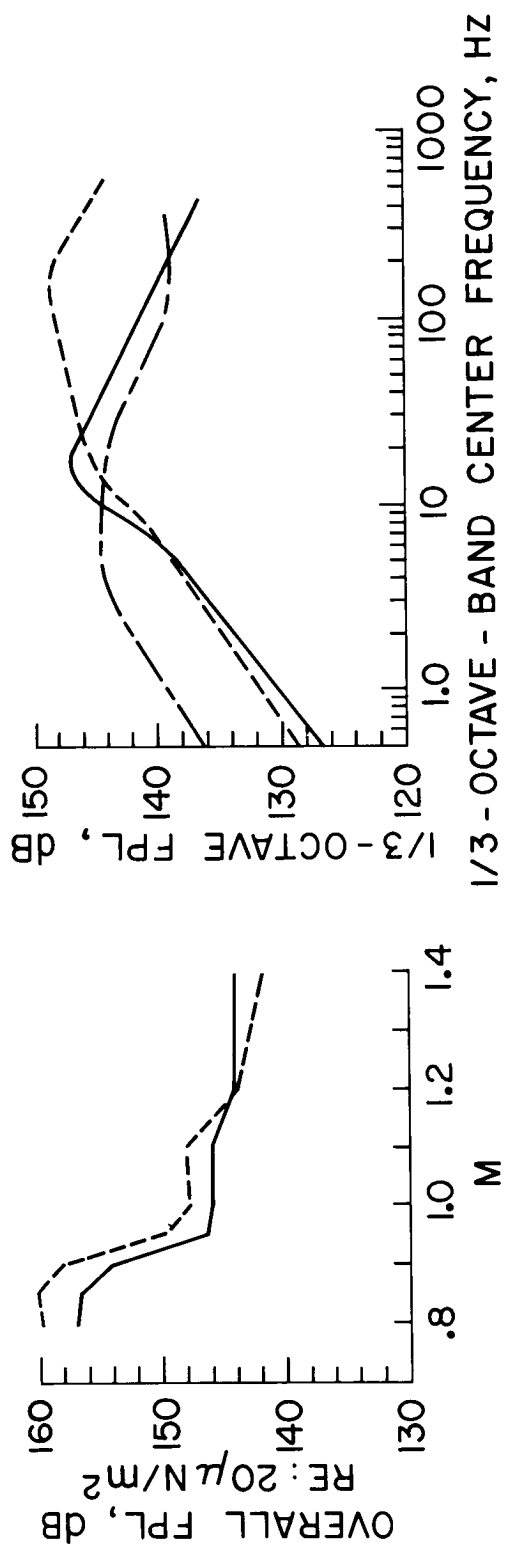
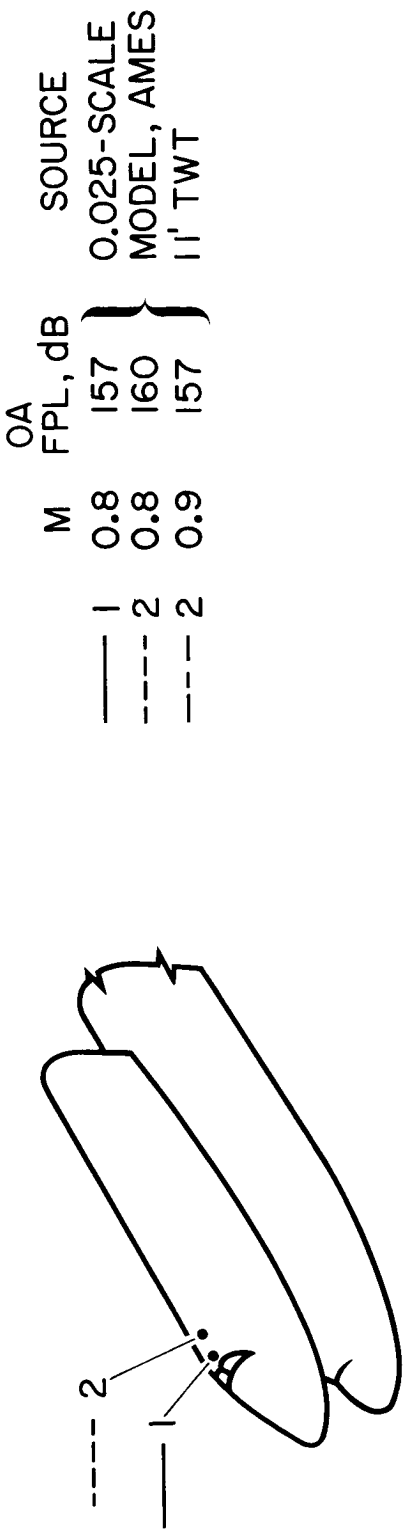


Figure 2

ESTIMATED PRESSURE FLUCTUATIONS DURING ASCENT - ORBITER HEAT SHIELD

(Figure 3)

Estimated full-scale pressure fluctuations on the orbiter heat shield due to flow interference from the booster nose are shown in Figure 3. The maximum overall fluctuating pressure level of 164 dB occurred at the highest test Mach number of 1.4. Corresponding one-third-octave band fluctuating pressure levels peaked at about 153 dB. A comparison of the OA FPL and one-third-octave FPL estimates from the 0.025-scale and 0.01-scale models with Titan III flight data obtained in the interference region from the strap-on solid-propellant rockets and scaled to the SSV\* dynamic pressure shows reasonable agreement. As previously mentioned in connection with the spectra shown in Figure 2, these spectra vary in shape in a manner consistent with the locations of the measurements.

---

\*SSV - space shuttle vehicle.

ESTIMATED PRESSURE FLUCTUATIONS DURING ASCENT  
ORBITER HEAT SHIELD

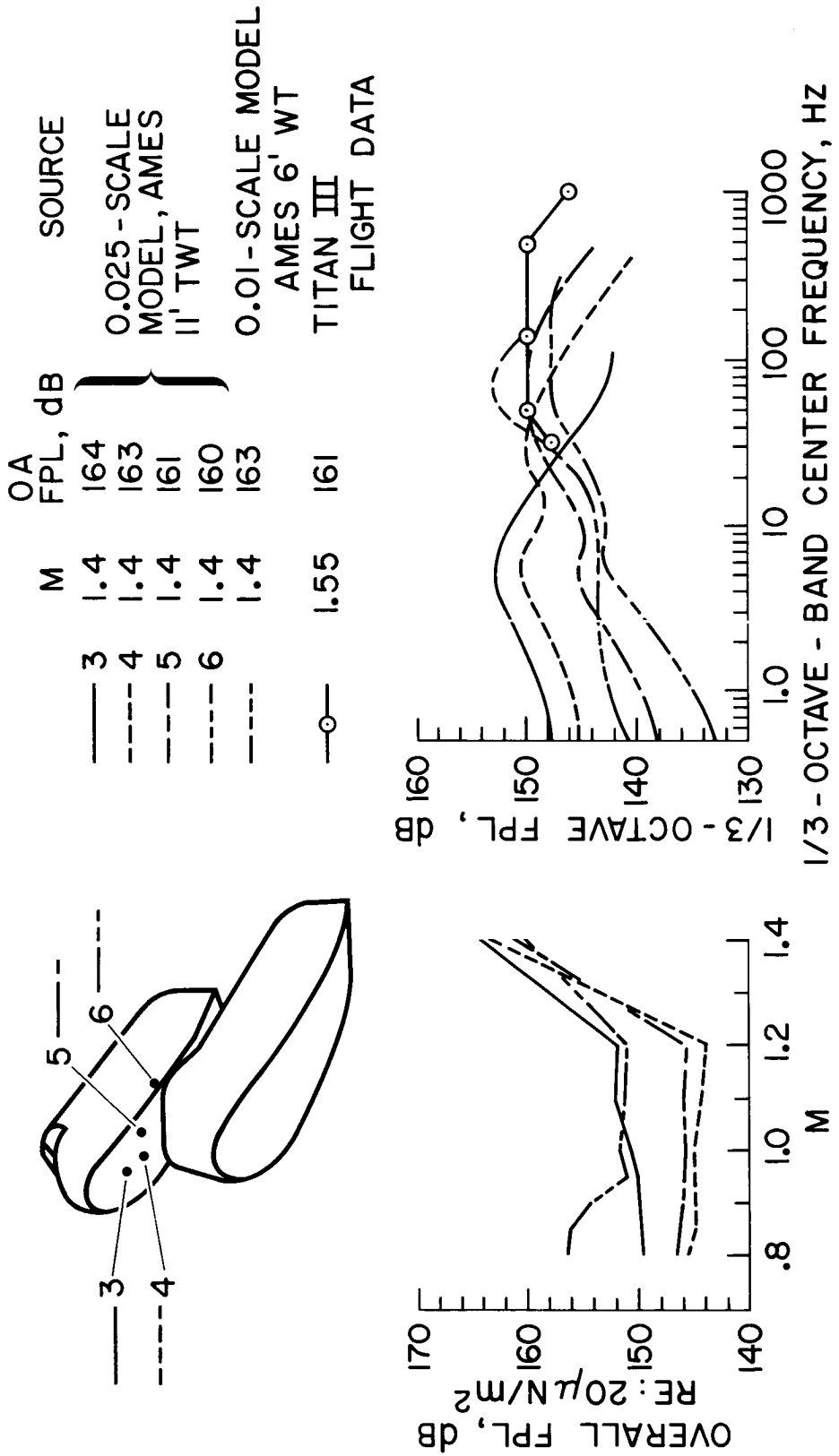
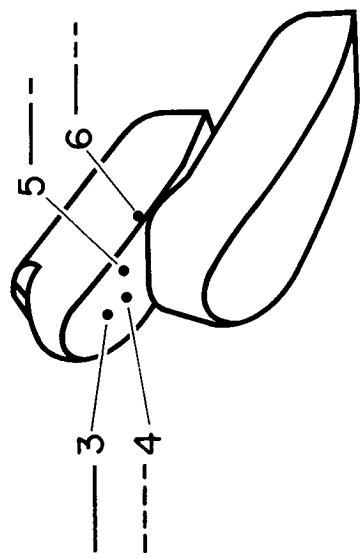


Figure 3

## ESTIMATED PRESSURE FLUCTUATIONS DURING ASCENT - BOOSTER IN WAKE OF ORBITER

(Figure 4)

Figure 4 shows the estimated full-scale pressure fluctuations on the booster in the wake-flow region from the orbiter for configurations with straight and delta wings. The data from each configuration represent the maximum obtained at any of the six measurement locations over the full range of test angles of attack and sideslip. The data show that the overall fluctuating pressure levels may be from 4 dB to 8 dB higher on delta-wing than on straight-wing configurations. The OA FPL with delta wings was about 164 dB. The one-third-octave band fluctuating pressure levels peak at about 152 dB for the delta wings and at about 144 dB for the straight wings.

ESTIMATED PRESSURE FLUCTUATIONS DURING ASCENT  
BOOSTER IN WAKE OF ORBITER

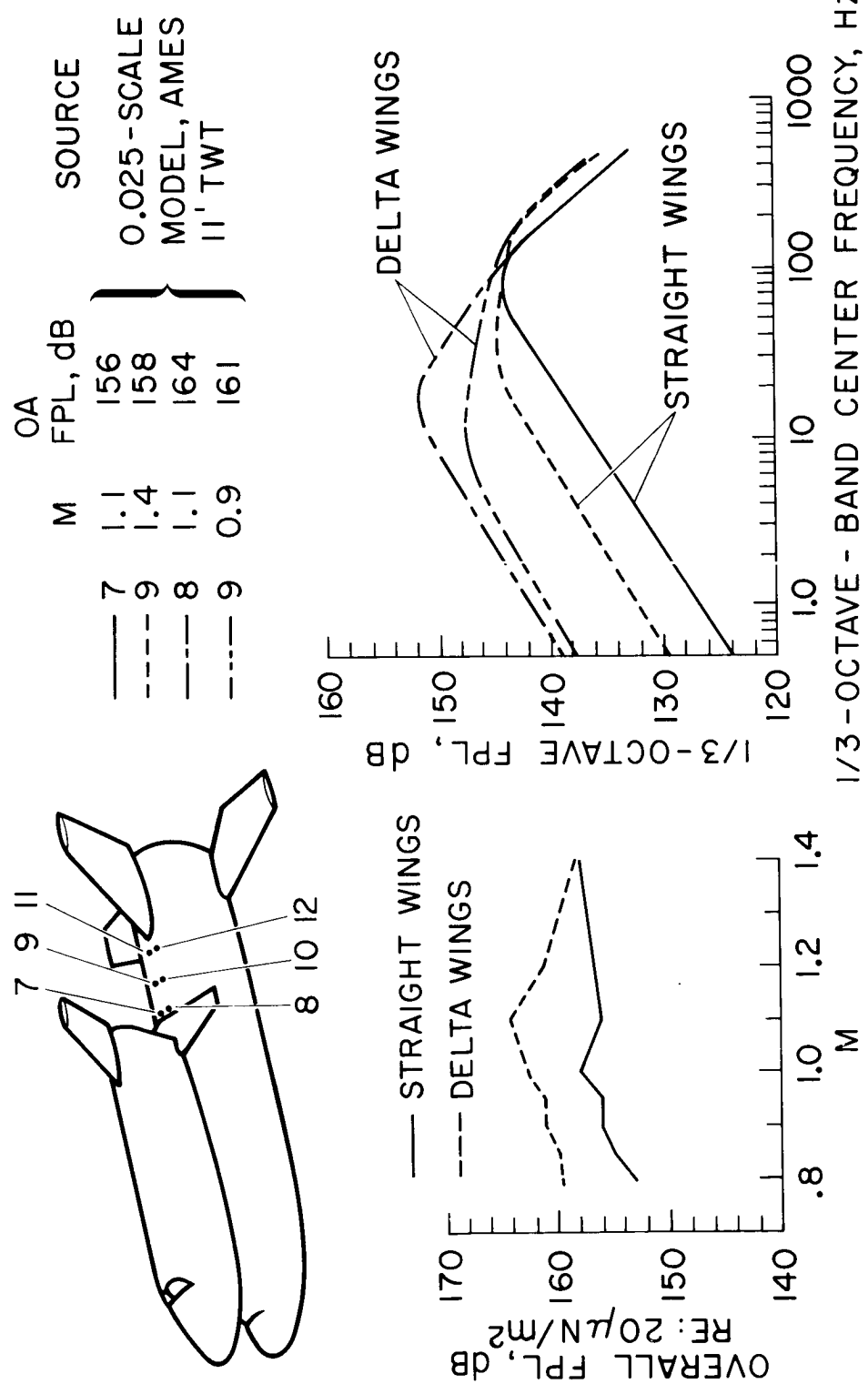


Figure 4

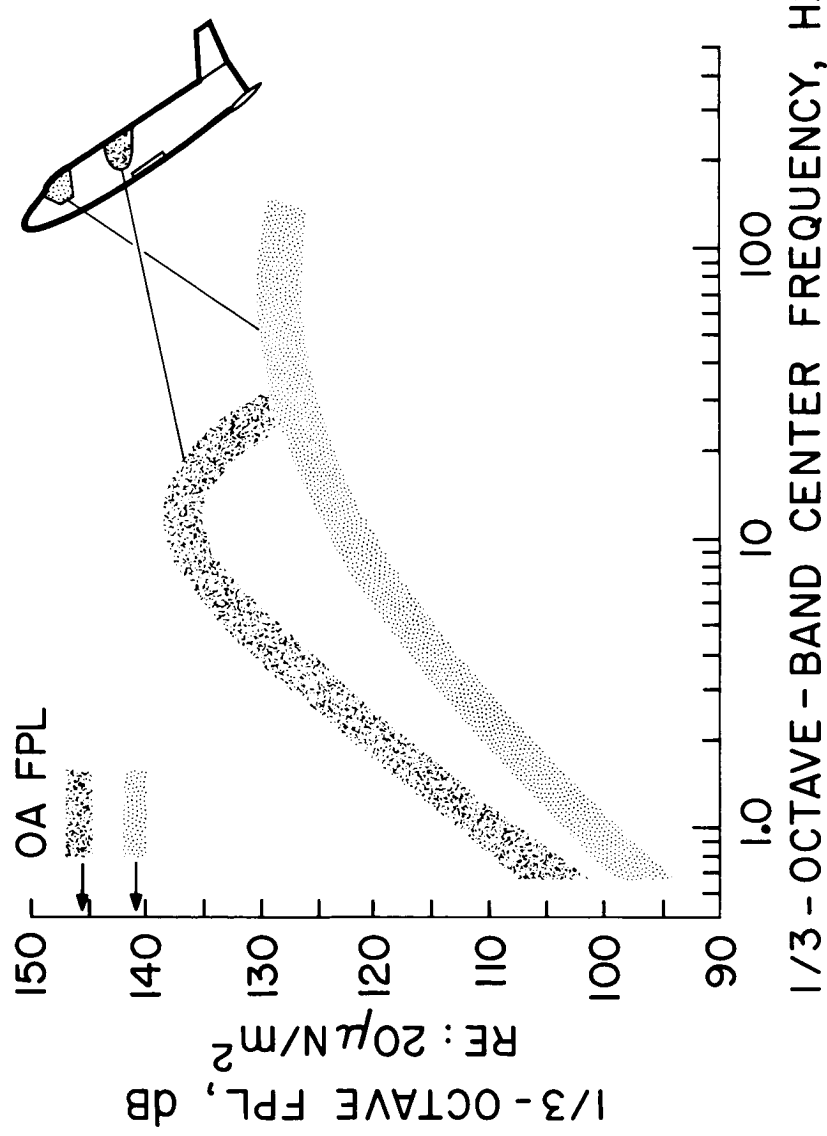
ESTIMATED PRESSURE FLUCTUATIONS DURING REENTRY AT  $\alpha = 60^\circ$ 

(Figure 5)

Some estimations of full-scale pressure fluctuations on a low-cross-range reentry configuration at  $\alpha = 60^\circ$  have been made by Bolt Beranek and Newman, Inc. The results, shown in Figure 5, were obtained as part of a Langley Research Center sponsored contract to investigate boundary-layer noise and base-pressure fluctuations at supersonic Mach numbers. These data were scaled from pressure fluctuations measured in the indicated regions on two models at  $M = 4$ --a 0.004-scale straight-wing model and a 0.0077-scale stub-wing model with most of the wing span removed to enable wind tunnel starting. The indicated zone near the cockpit contained two microphones, and the zone on the fuselage near the wing contained three microphones. The shaded envelopes of the one-third-octave spectra include the data from all the microphones in each zone and also the data from the two different scale models. The data are presented for  $q_{FS} = 4788 \text{ N/m}^2 (100 \text{ lb/ft}^2)$ .

The data show the highest levels in the vicinity of the wing interference--peaking at about 140 dB and 10 Hz. The levels near the cockpit are somewhat lower--peaking at about 130 dB near 100 Hz.

ESTIMATED PRESSURE FLUCTUATIONS DURING RE-ENTRY AT  $\alpha = 60^\circ$   
0.004 - AND 0.0077 - SCALE BBN MODELS  
 $M = 4$ ,  $q_{FS} = 4788 \text{ N/m}^2$  (100 lb/ft<sup>2</sup>)



## 0.008-SCALE MODEL CONFIGURATIONS

(Figure 6)

The preliminary measurements of the pressure fluctuations on the launch configurations were made in a few regions of obvious turbulence selected without the benefit of a prior flow visualization study. Experience has shown, however, that not all regions of high-intensity turbulence are obvious by visual inspection of the geometry. Complex flow patterns involving high-pressure gradients and separated flows can be elusive, particularly in the presence of cross flow due to angles of attack and sideslip. It was for this reason that flow visualization studies of the 0.008-scale models of launch configurations were recently conducted in the Ames 6- by 6-foot wind tunnel. The objective was to gain insight on the complexities of flow on launch configurations and to determine if additional pressure-fluctuation measurements are needed prior to the completion of Phase B shuttle contracts.

The configurations tested are shown in Figure 6. The configurations included the booster and orbiter with straight wings, delta wings with tip fins, and clipped delta wings with the vertical stabilizers of the straight-wing configuration.

The tests were conducted at Mach numbers from 0.8 to 2.0. At  $M = 2.0$  a solid axisymmetric plume simulator was mounted on the sting at the base of the booster to induce flow separation over the rearward part of the booster. The size of the plume was considerably exaggerated for  $M = 2$ . However, an extra large plume representing an unknown higher Mach number was chosen to insure that plume-induced separation effects would be observed.

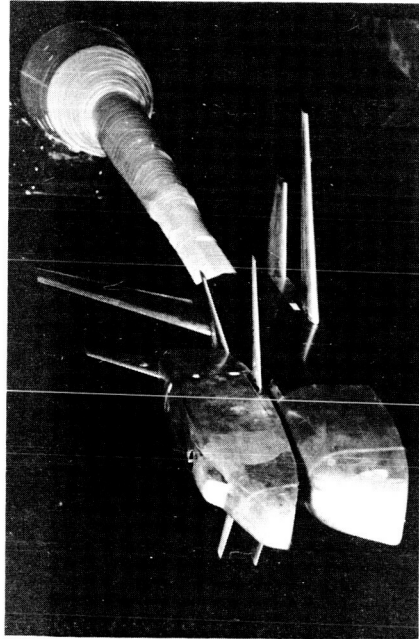
Angle of attack, referred to the wings, was varied from  $-8^\circ$  to  $+8^\circ$  at angles of sideslip of  $0^\circ$  and approximately  $5^\circ$ . Both still and motion pictures<sup>1</sup> were taken of the oil flow.

---

<sup>1</sup>Copies of a film that illustrate the flow of fluorescent oil on each of the model configurations are available on loan from NASA-Ames Research Center.

# 0.008-SCALE MODEL CONFIGURATIONS

## STRAIGHT WINGS



DELTA WINGS, TIP FINS  
STRaight WINGS

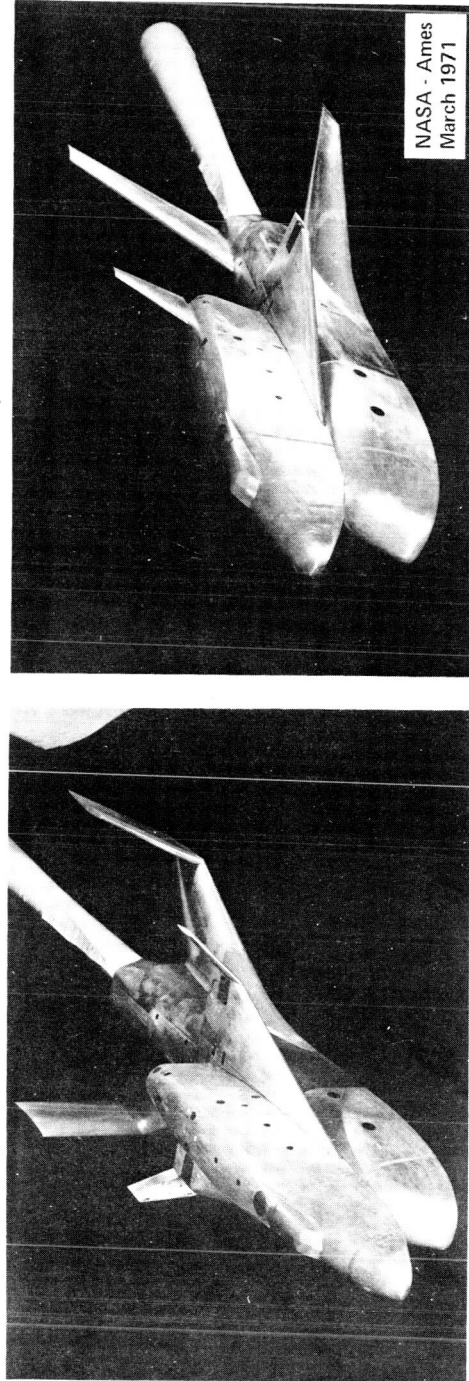


Figure 6

## FLUORESCENT OIL FLOW - STRAIGHT WINGS

(Figure 7)

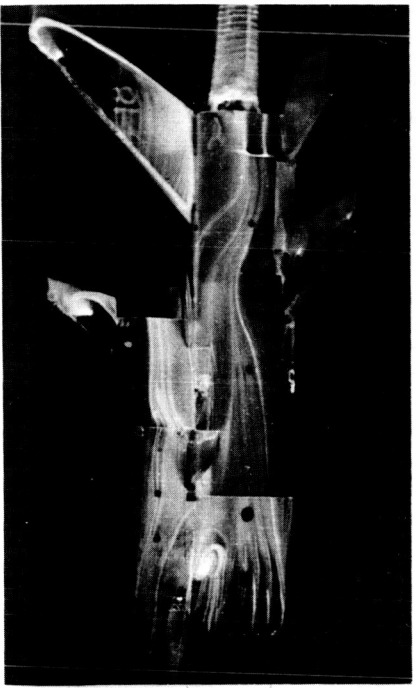
Figure 7 shows some of the photographs taken of the oil flow on the configuration with straight wings. A single picture was selected for each of the Mach numbers shown,  $M = 0.9$ ,  $1.1$ , and  $2.0$ , that was judged to illustrate the most interesting flow characteristic. A photograph of the model is also included in the figure for reference purposes, since portions of the model not wetted by oil are obscure.

At  $M = 0.9$ ,  $\alpha_w = 4^\circ$ , and  $\beta = 5^\circ$  a prominent vortex-like separation pattern can be seen on the booster a short distance downstream from the oil-flow orifices. A flow pattern of this type would be expected to cause high local pressure fluctuations that need to be investigated. The booster and orbiter vertical stabilizers show signs of separated flow, particularly on the orbiter where the overhanging tail appears to be influenced by the wake flow. At  $M = 1.1$ ,  $\alpha_w = -4^\circ$ , and  $\beta = 5^\circ$ , a vortex-like pattern of separation appears to occur on the booster between the trailing edge of the orbiter wing and the leading edge of the horizontal stabilizer. The  $M = 2$  picture shows the simulated plume and resulting flow separation on most of the booster empennage.

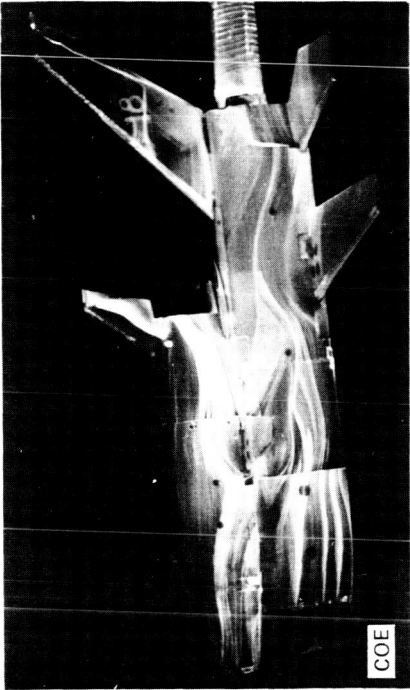
FLUORESCENT OIL FLOW  
STRAIGHT WINGS

MODEL PHOTOGRAPH

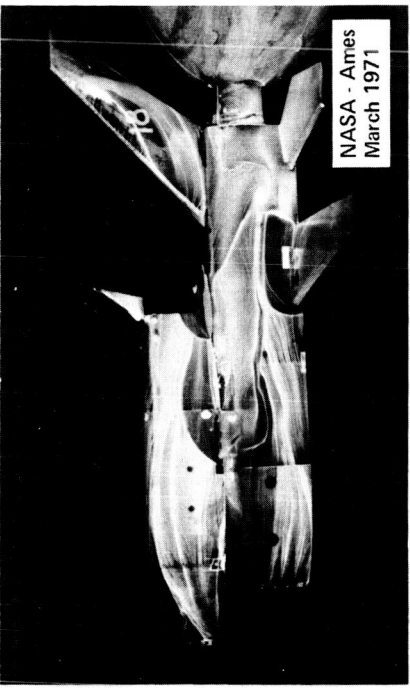
$$M = 0.9 \quad \alpha_w = 4^\circ \quad \beta = 5^\circ$$



$$M = 1.1 \quad \alpha_w = -4^\circ \quad \beta = 5^\circ$$



$$M = 2 \quad \alpha_w = 0^\circ \quad \beta = 5^\circ$$



NASA - Ames  
March 1971

Figure 7

## FLUORESCENT OIL FLOW - DELTA WINGS, TIP FINS

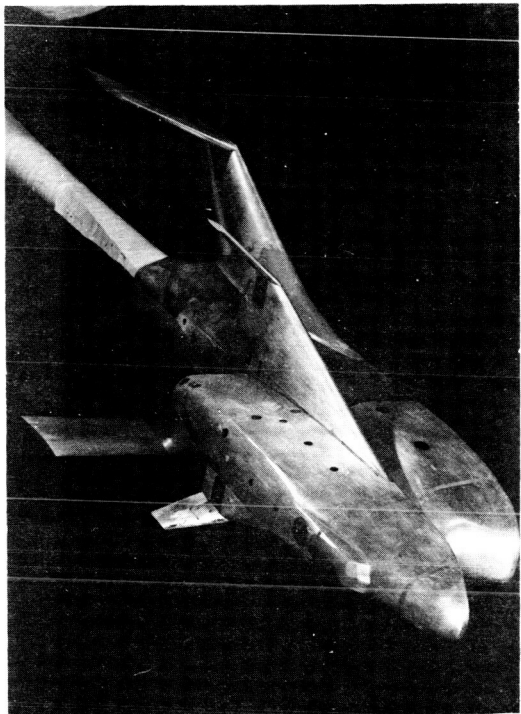
(Figure 8)

Photographs of the fluorescent oil on the configuration with delta wings and tip fins are shown in Figure 8. Generally the same type of flow features occur on the delta configuration as on the straight-wing configuration. At  $M = 0.9$ ,  $\alpha_w = 4^\circ$ , and  $\beta = 5^\circ$  a transonic shock wave can be noted on the booster a short distance downstream from the orifices. At  $M = 1.1$  the vortex-like separation pattern occurred on the booster near the trailing edge of the orbiter delta wing. This more rearward position on the delta configuration than on the straight-wing configuration no doubt accounts for the significantly higher pressure fluctuations measured on the 0.025-scale delta-wing booster.

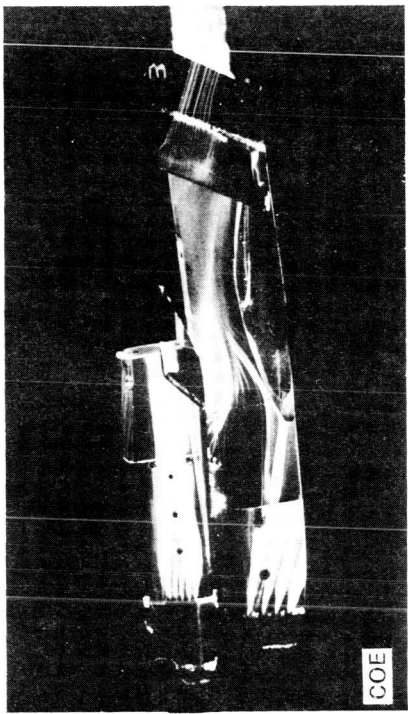
FLUORESCENT OIL FLOW - DELTA WINGS, TIP FINS

MODEL PHOTOGRAPH

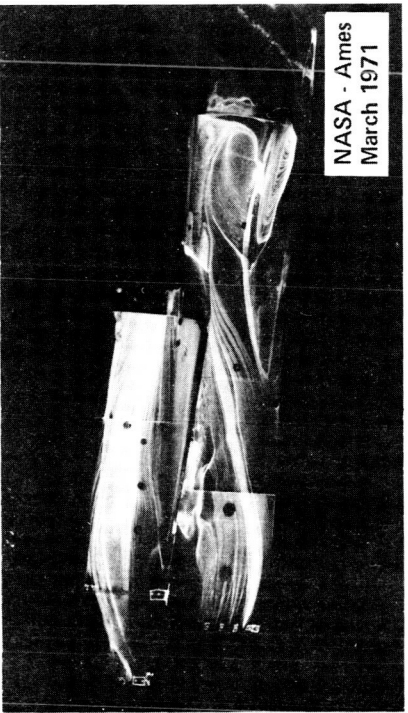
$M = 0.9$      $\alpha_W = 4^\circ$      $\beta = 0^\circ$



$M = 1.1$      $\alpha_W = -8^\circ$      $\beta = 0^\circ$



$M = 2.0$      $\alpha_W = 4^\circ$      $\beta = 5^\circ$



NASA - Ames  
March 1971

## FLUORESCENT OIL FLOW — CLIPPED DELTA WINGS, & VERTICAL STABILIZER

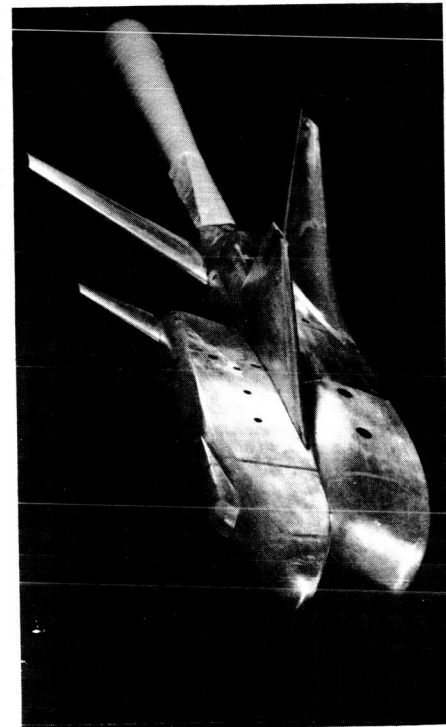
(Figure 9)

Figure 9 contains the illustrative photographs of the oil flow on the configuration with clipped delta wings and centerline vertical stabilizers. These conditions of  $M$ ,  $\alpha$ , and  $\beta$  shown for this configuration are the same as those shown for the straight-wing configuration. Generally it appears that the flow is somewhat more orderly on the orbiter and booster with the delta wings than with the straight wings. The vortex-like separation pattern at  $M = 0.9$  appears in the same location on both the delta- and straight-wing configurations. It therefore does not appear to have been influenced by the flow field near the leading edge of the delta wing.

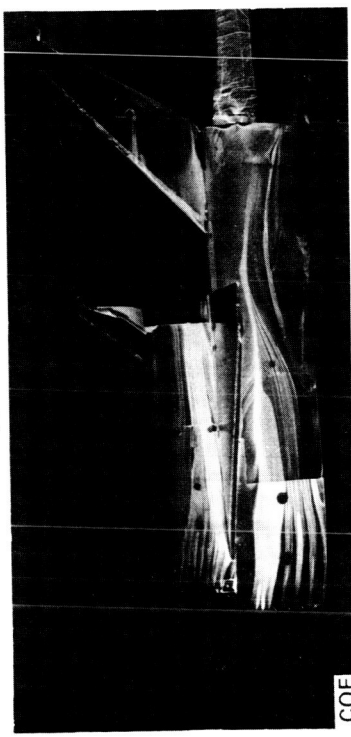
FLUORESCENT OIL FLOW - CLIPPED DELTA WINGS,  
C VERTICAL STABILIZER

MODEL PHOTOGRAPH

$$M = 0.9 \quad \alpha_W = 4^\circ \quad \beta = 5^\circ$$

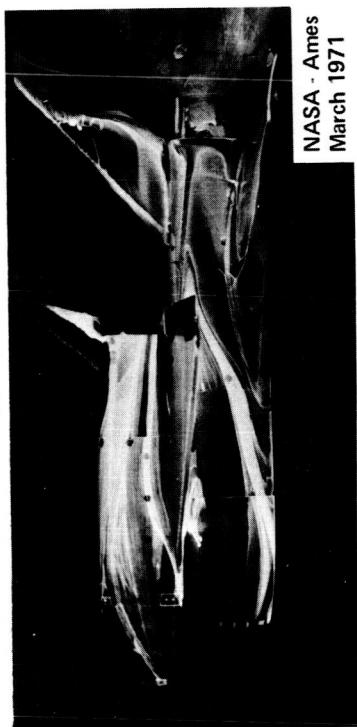


$$M = 1.1 \quad \alpha_W = -4^\circ \quad \beta = 5^\circ$$



COE

$$M = 2 \quad \alpha_W = 0^\circ \quad \beta = 5^\circ$$



NASA - Ames  
March 1971

Figure 9

FLUORESCENT OIL FLOW - DELTA WINGS, TIPS FINS  
(EFFECT OF PLUME)

(Figure 10)

Photographic records of plume-induced flow separation on the S-IC stage of Saturn-V launch vehicle and some corresponding flight measurements of pressure fluctuations<sup>1</sup> indicate a potentially serious problem of plume-induced unsteady loads on space-shuttle boosters. The problem would be especially aggravated by a delta-wing configuration. Figure 10, showing a top view of the delta-wing configuration with and without the plume, illustrates the problem. The plume simulation is not correct for the  $M = 2$  flow; however, the intent here is only to show the extent of wing surface area that can be affected at supersonic Mach numbers approximately in the range from 3 to 5.

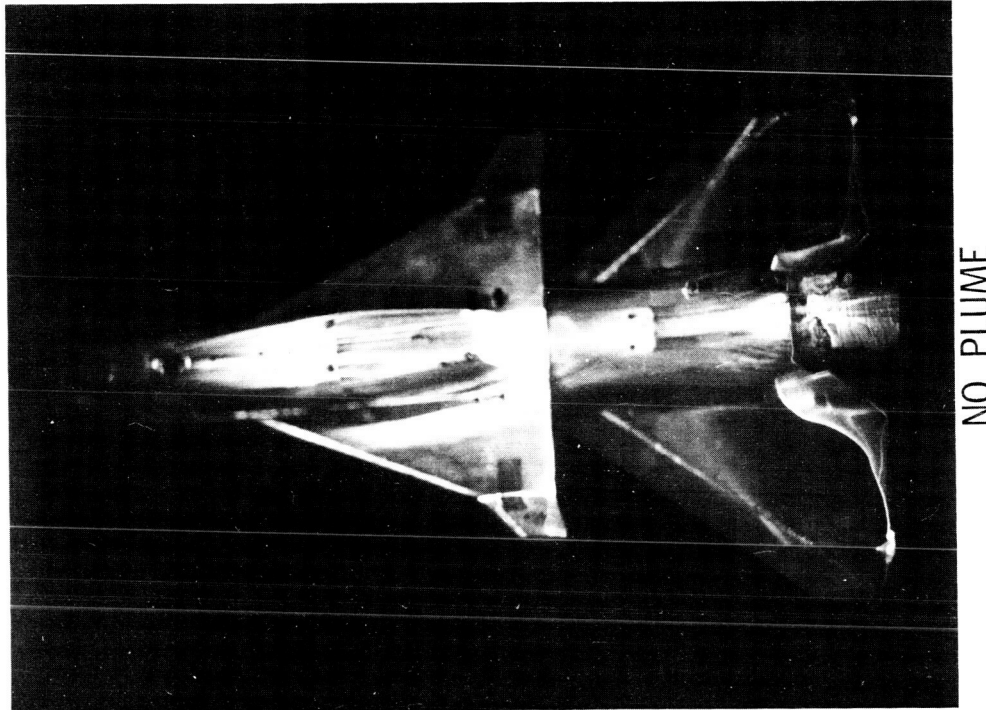
---

<sup>1</sup>Jones, Jess H.: Acoustic Environment Characteristics of the Space Shuttle. NASA TM X-52876, Vol. II, July 1970.

FLUORESCENT OIL FLOW - DELTA WINGS, TIP FINS  
EFFECT OF PLUME

$M = 1.4$     $\alpha_w = 0^\circ$     $\beta = 5^\circ$

$M = 2.0$     $\alpha_w = 0^\circ$     $\beta = 5^\circ$



PLUME

NO PLUME

Figure 10

## CONCLUSIONS

Preliminary measurements of pressure fluctuations have been made on models of launch configurations with straight and delta wings and on a low-cross-range orbiter model at a re-entry angle of attack of  $60^\circ$ . The data presented in this paper showed significant full-scale fluctuating pressure levels at the selected regions of study on the launch configurations. Pressure fluctuations on the booster in the wake-flow region of the orbiter were about 2 times higher for delta wings than for straight wings. The pressure fluctuations measured at  $M = 4$  for a  $60^\circ$  re-entry angle were moderate, based on  $q = 4788 \text{ N/m}^2$  ( $100 \text{ lb/ft}^2$ ). Additional measurements are needed for conditions simulating a high cross range re-entry. Fluorescent oil flow studies of launch configurations were also presented that show regions of expected high-intensity turbulence that should be investigated with quantitative measurements of pressure fluctuations. The studies illustrated the potential problem of plume-induced unsteady loads, particularly on delta-wing boosters.

THE EFFECTS OF PARAMETER VARIATION ON  
INFILIGHT WIND LOADING  
By Alden C. Mackey  
NASA Manned Spacecraft Center, Houston, Texas

## INTRODUCTION

In order to maximize the payload in space shuttle operation, three areas must be investigated. These are performance, controllability, and structural loads. Shown here are the results of a structural loads study on an MSC\* in-house shuttle configuration. This vehicle was straight wing on both orbiter and booster. (See fig. 1.)

---

\*MSC NASA Manned Spacecraft Center.

# THE EFFECTS OF PARAMETER VARIATION ON INFIGHT WIND LOADING

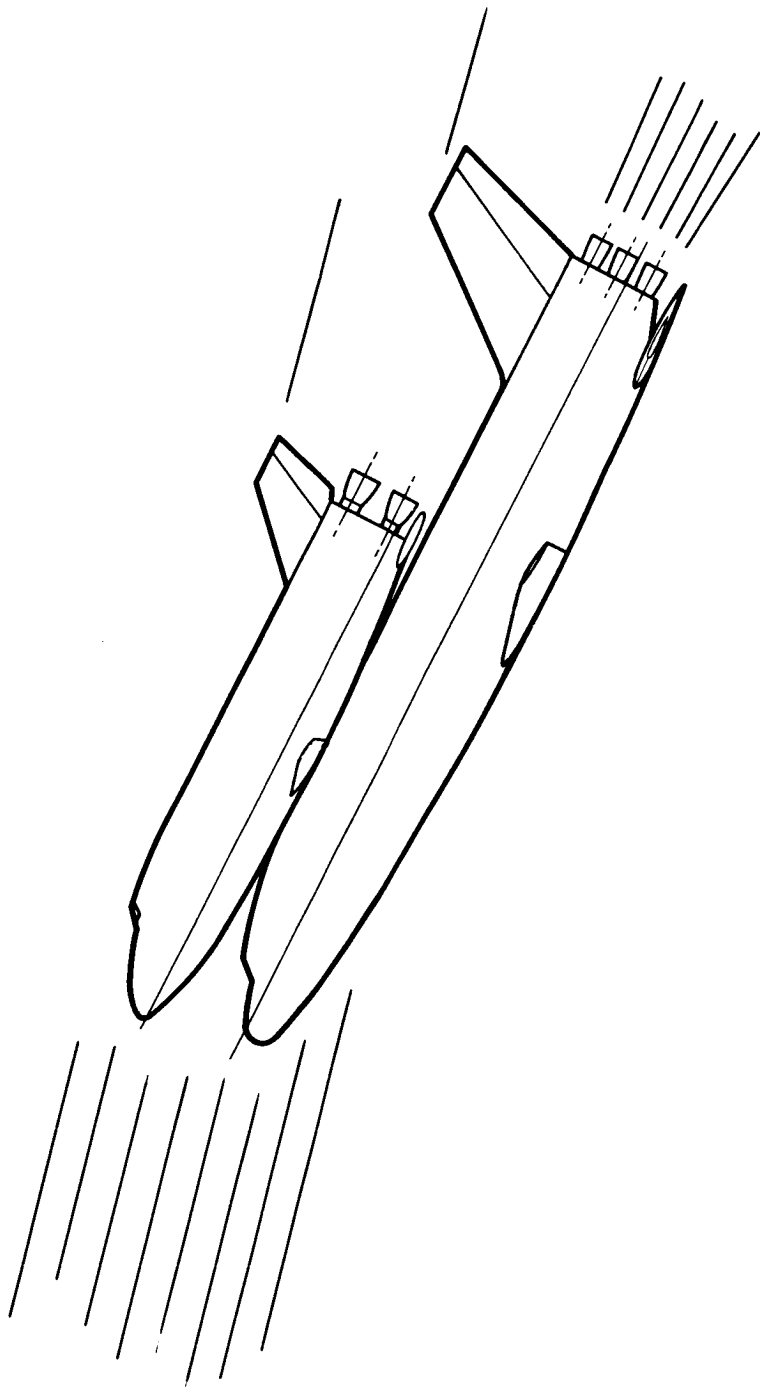


Figure 1

The parameters in figure 2 are ones which have a major effect on the space shuttle structural loads during boost. These parameters will also affect the controllability and performance requirements on the vehicle. Other parameters which must be considered in these studies but are not varied here are engine gimbal angle limits, vehicle launch orientation, and center-of-gravity location and travel.

## **PARAMETERS WHICH AFFECT BOOST LOADS AND PERFORMANCE**

- WING INCIDENCE ANGLE
- CONTROL SYSTEM GAINS
- COMMANDED ATTITUDE HISTORY
- WINDS - MAGNITUDE AND DIRECTION

Figure 2

The MSC shuttle boost was simulated for the first 100 seconds of flight with tail winds defined by the synthetic wind profile. Wind incidence was varied from  $0^\circ$  to  $6^\circ$  for both the orbiter and the booster.

The minimum tailwind  $q_a$  response and maximum head-wind response occurred with a  $1.6^\circ$  wing incidence angle. (See fig. 3.) The maximum and minimum are associated with the  $1.6^\circ$  angle between the booster center line and the balanced thrust line through the center of gravity of the boost configuration at max  $q$ .

# EFFECT OF WING INCIDENCE ON MAXIMUM $q\alpha$

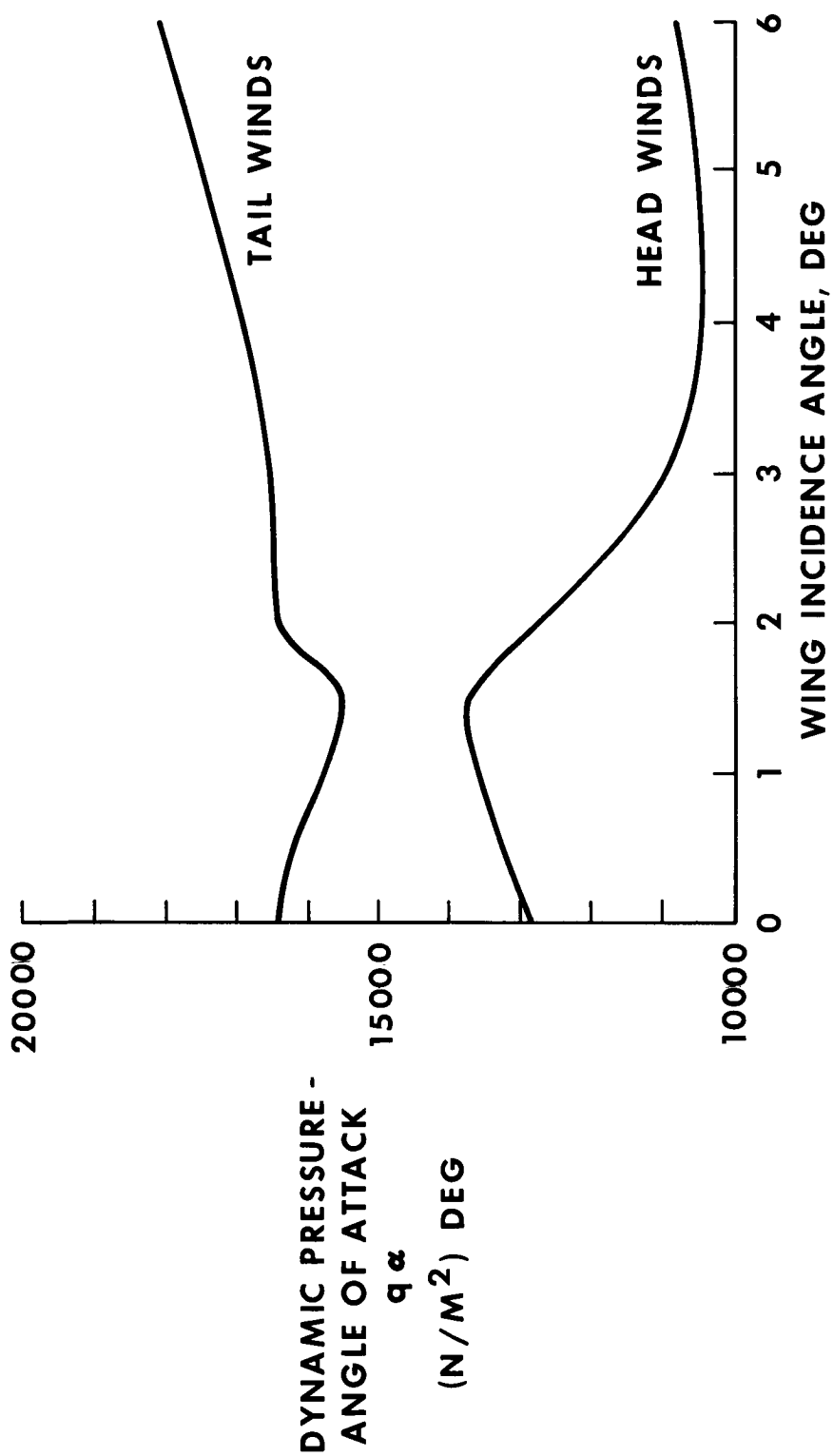


Figure 3

For the synthetic tail wind the difference in response for two attitude control gain histories is shown. The attitude gain in one case is varied linearly from 1.0 at 40 seconds to 0 at 80 seconds and back to 1.0 at 120 seconds. This response is compared with the response of the vehicle with an attitude gain of 1.0 for the first 120 seconds of boost. (See fig. 4.)

The reduction in attitude gain in the high  $q$  region of boost allows the vehicle to "weather cock" into the wind and deviate from the prescribed trajectory. The result is a desirable decrease in the max  $qc$  loading, but a coincident decrease in performance may occur since the vehicle is allowed to deviate from the prescribed commanded trajectory.

## EFFECT OF PITCH ATTITUDE CONTROL GAIN ON $q\alpha$

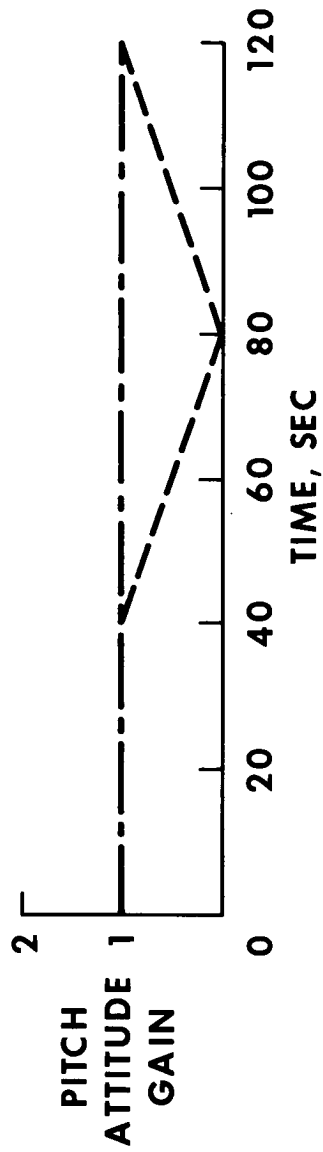
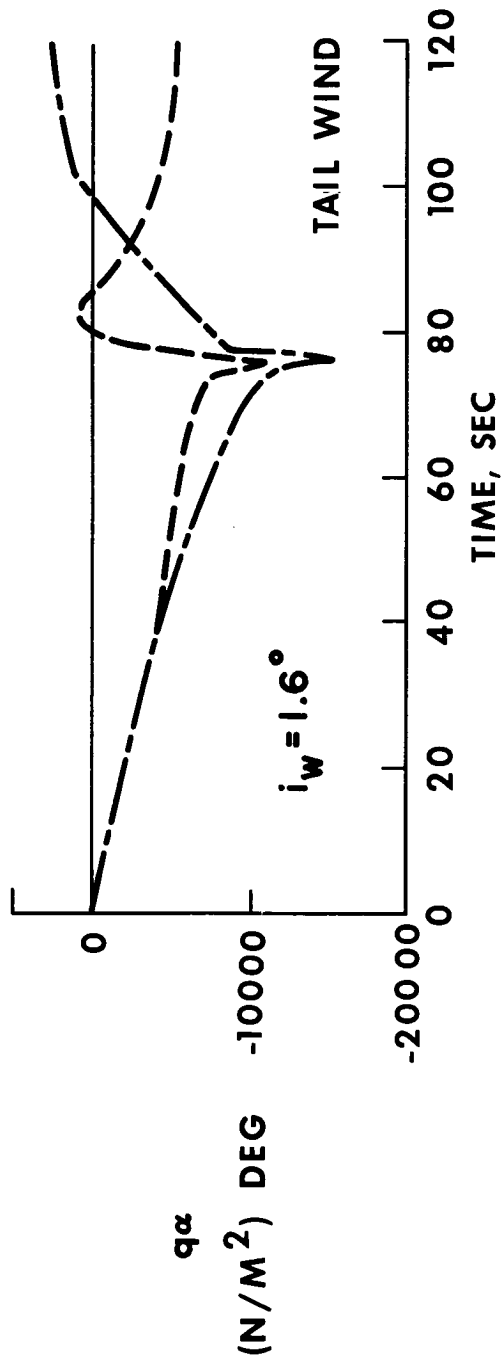


Figure 4

A similar reduction is seen in the  $q\alpha$  response for the head-wind synthetic wind profile.

(See Fig. 5.)

If reduction in attitude control gain is considered as a means of reducing structural loads, a complete parameter variation study of attitude control gain would be required to determine the maximum payload with maximum structural weight saving.

# EFFECT OF PITCH ATTITUDE CONTROL GAIN ON $q\alpha$

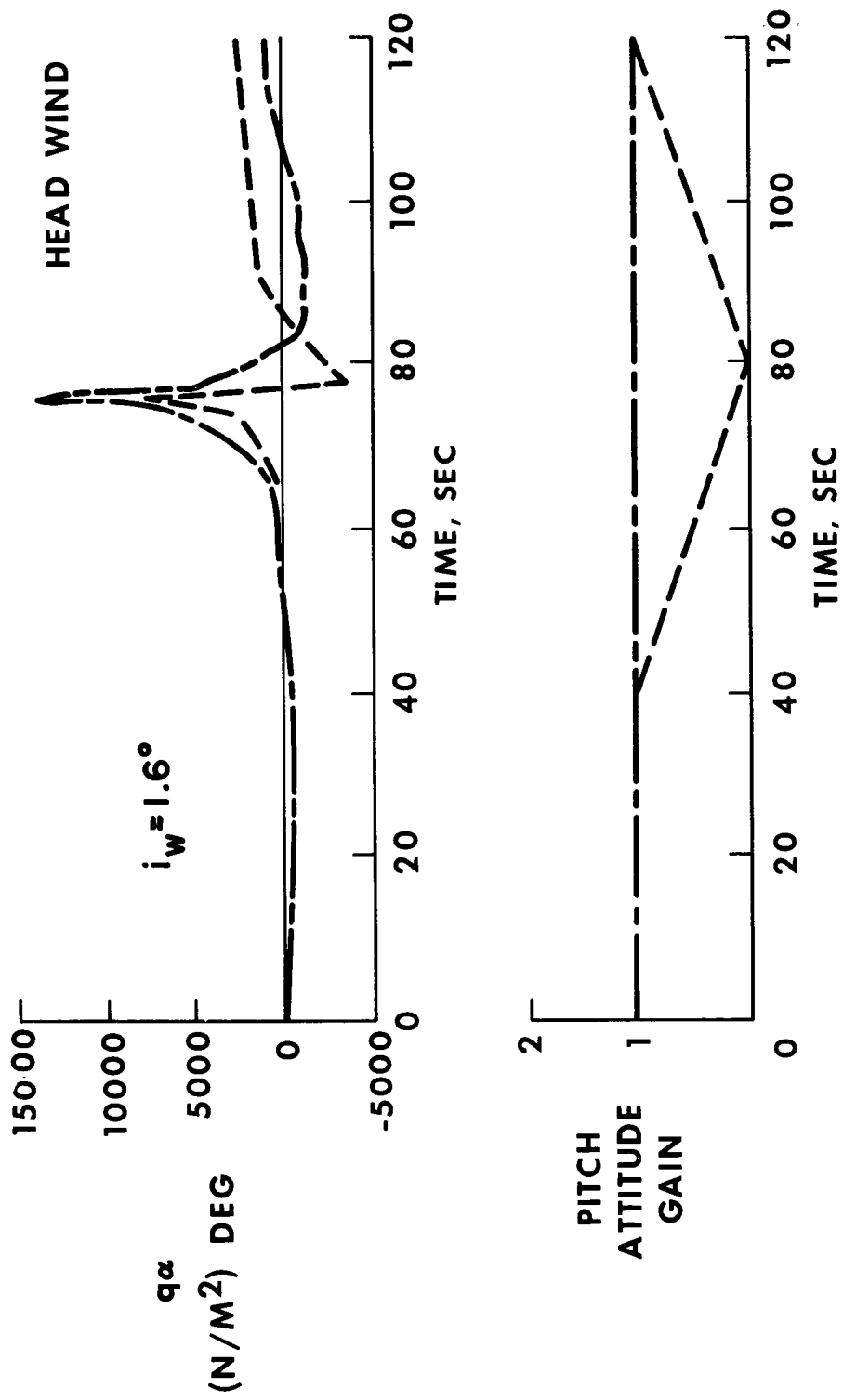


Figure 5

The commanded pitch-attitude history A was one used in baseline studies for the MSC shuttle configuration.

The commanded pitch-attitude history B was one found by investigation to reduce the  $q\alpha$  response for design synthetic wind profile, that is, head and tail winds. (See fig. 6.)

# SPACE SHUTTLE COMMANDED PITCH ATTITUDE

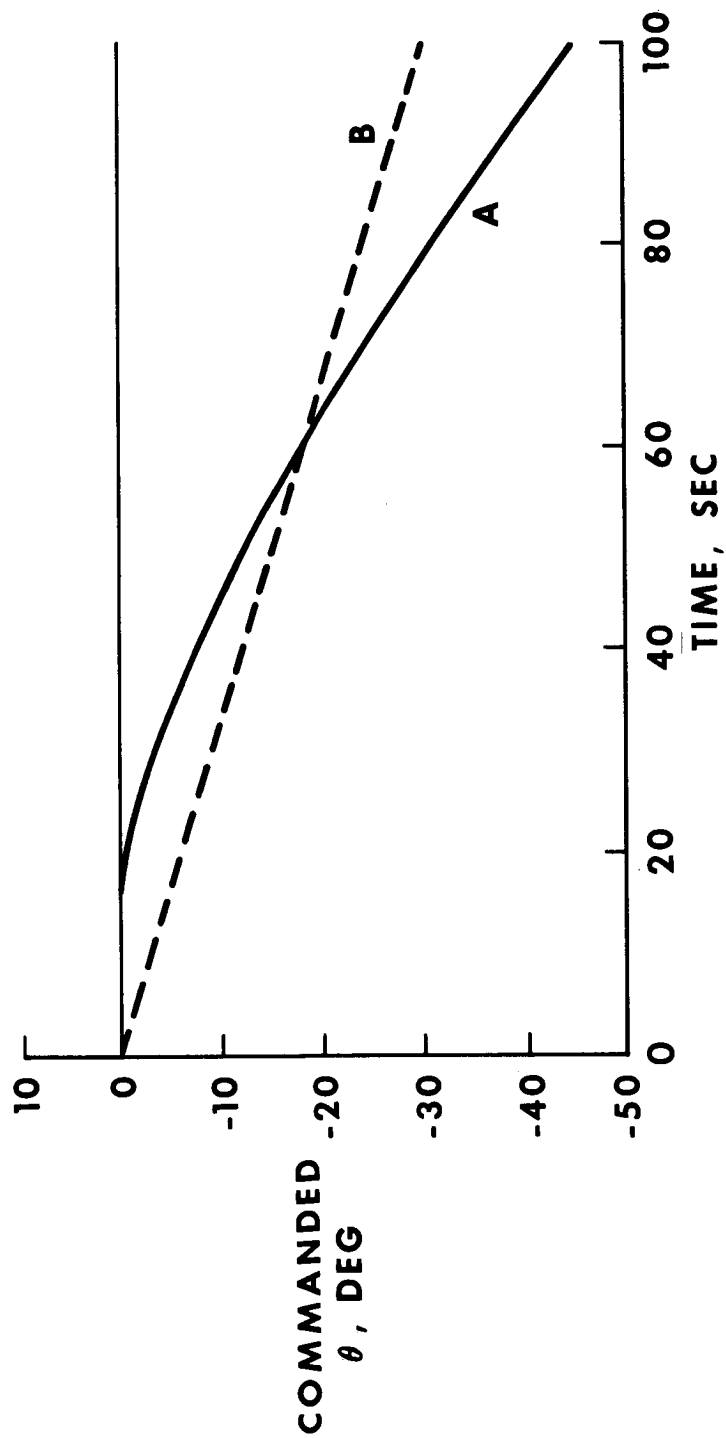


Figure 6

The  $q_a$  responses to trajectory A for no-wind, head-wind, and tail-wind cases are shown. Head and tail winds are 95-percentile wind magnitude with design shears and gust. The no-wind case shows a negative  $q_a$  in the high  $q$  region and the winds induce large variations from the no-wind case for both head and tail winds. (See fig. 7.)

**SPACE SHUTTLE  $q\alpha$   
RESPONSE - TRAJECTORY A  
 $i_w = 1.6^\circ$ ; PITCH-ATTITUDE GAIN, 1**

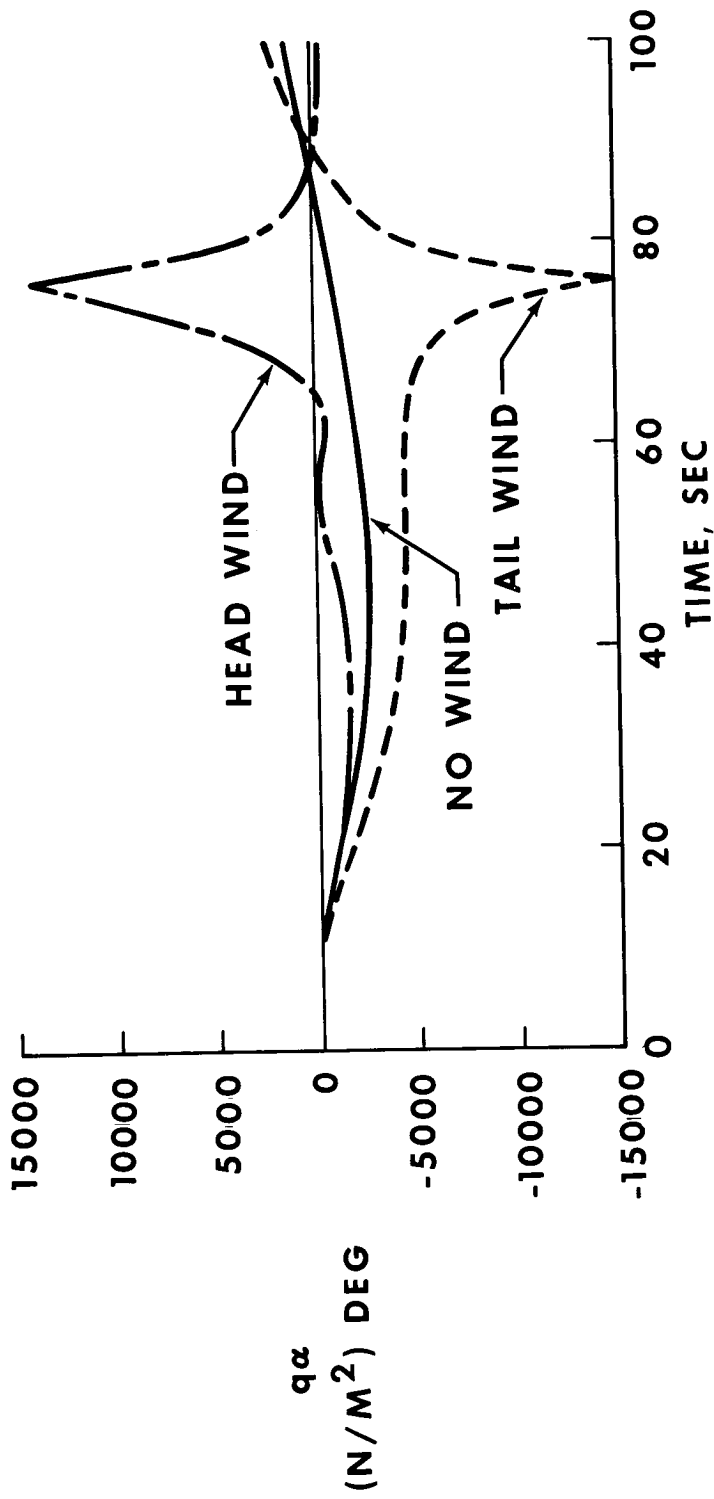


Figure 7

The  $q\alpha$  response for trajectory B is shown for the same winds as applied to trajectory A. Here the no-wind  $q\alpha$  is positive and the variation from the no-wind response to the head-wind response is small, whereas the variation from the no-wind response to the tail-wind response is the same as that for trajectory A. The tail-wind  $q\alpha$  is reduced by 30 percent and the head-wind  $q\alpha$  by 12 percent. (See fig. 8.)

**SPACE SHUTTLE  $q\alpha$   
RESPONSE - TRAJECTORY B**  
 $i_w = 1.6^\circ$ ; PITCH-ATTITUDE GAIN, I

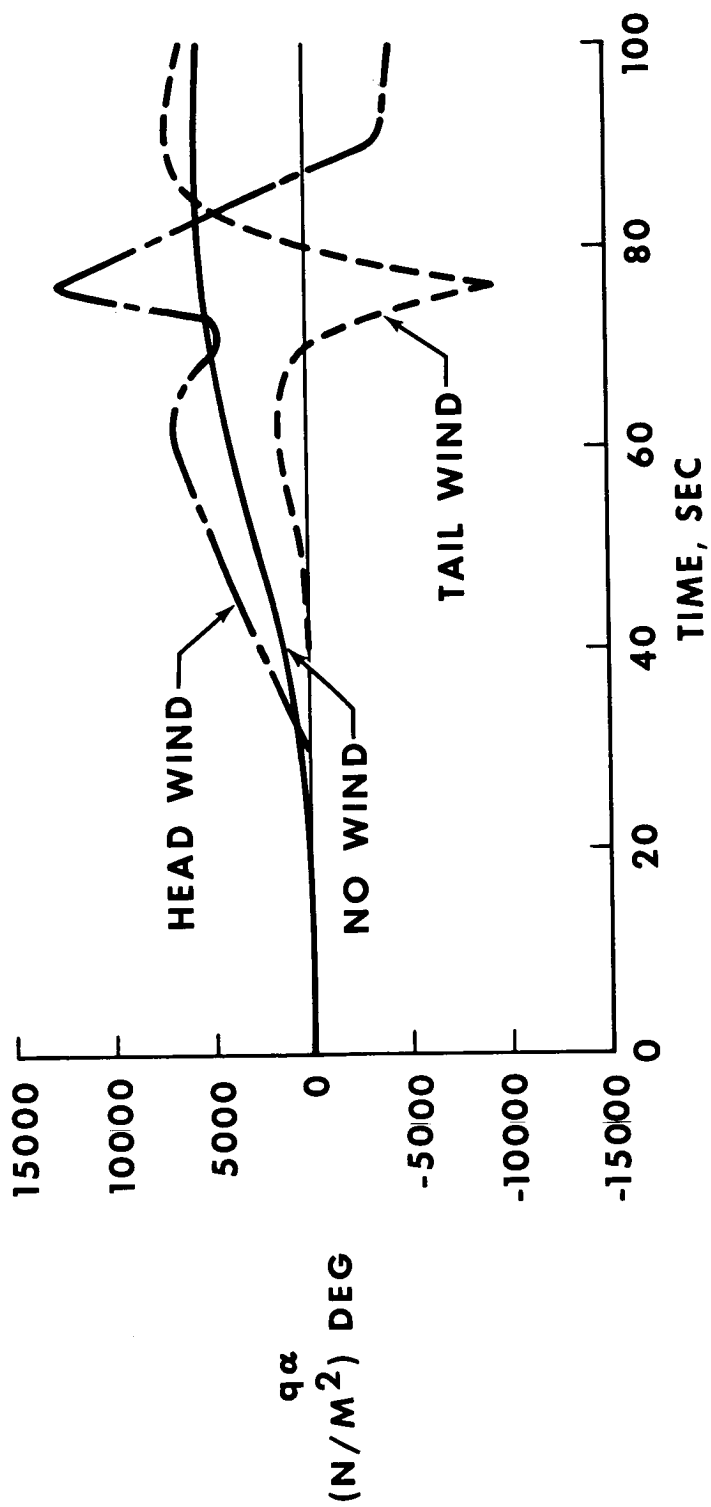


Figure 8

## CONCLUDING REMARKS

- MEANS ARE AVAILABLE TO REDUCE STRUCTURAL LOADS AND HENCE STRUCTURAL WEIGHT
- STRUCTURAL LOADING MUST BE CONSIDERED IN PAYLOAD MAXIMIZATION ANALYSES
- MAXIMUM PAYLOAD TRAJECTORY MUST INCLUDE THESE INTEGRATED EFFECTS
  - CONTROLLABILITY
  - PERFORMANCE
  - AERODYNAMIC HEATING
  - STRUCTURAL LOADS

Figure 9

TECHNOLOGY - PRELIMINARY INVESTIGATION OF LOAD AND MODAL  
SUPPRESSION FOR SPACE SHUTTLE

By

Bernard J. Kuchta

Convair Aerospace Division of General Dynamics, San Diego, California

A study is currently being conducted to determine the potential value of loads alleviation control for Space Shuttle vehicles. This study is being conducted by Convair Aerospace Division of General Dynamics under NASA Contract NAS 9-11191. The technical monitor is Mr. Frank Elam of the NASA -MSC Guidance and Control division. Study objectives are listed opposite. The analysis is being conducted in two phases: Phase 1, rigid body design load reduction; and Phase 2, modal suppression. (See Figure 1.)

# STUDY OBJECTIVES

- DEVELOP RIGID BODY DESIGN LOAD REDUCTION TECHNIQUES
- DETERMINE PERFORMANCE AND WEIGHT PENALTIES ASSOCIATED WITH RIGID BODY LOAD REDUCTION
- DETERMINE THE SENSITIVITY OF STRUCTURAL WEIGHT TO LOAD LEVEL
- DETERMINE THE POTENTIAL STRUCTURAL WEIGHT SAVING OF THE VARIOUS RIGID BODY LOAD REDUCTION TECHNIQUES
- DEVELOP PRELIMINARY LOAD SPECTRA FOR FATIGUE ANALYSIS
- CONDUCT A PRELIMINARY FATIGUE DAMAGE ANALYSIS
- EVALUATE THE NEED FOR MODAL SUPPRESSION
- DEVELOP MODAL SUPPRESSION TECHNIQUES
- ESTIMATE THE WEIGHT PENALTY ASSOCIATED WITH ANY MODAL SUPPRESSION TECHNIQUES

Figure 1

The study, which started in July 1970, selected the North American/Convair Aerospace Phase B baseline configurations of that time. The configurations shown opposite are the straight wing booster, and the low-crossrange, straight wing orbiter. Both vehicles have conventional tails and use thrust vector control on ascent, Attitude Control Propulsion System control in low dynamic pressure, and elevator/stabilizer/aileron/rudder control for conventional flight. The transition for both vehicles was the dynamic subsonic transition. (See Figure 2.)

# MATED VEHICLE SYSTEM - STRAIGHT WING

## Orbiter & Booster

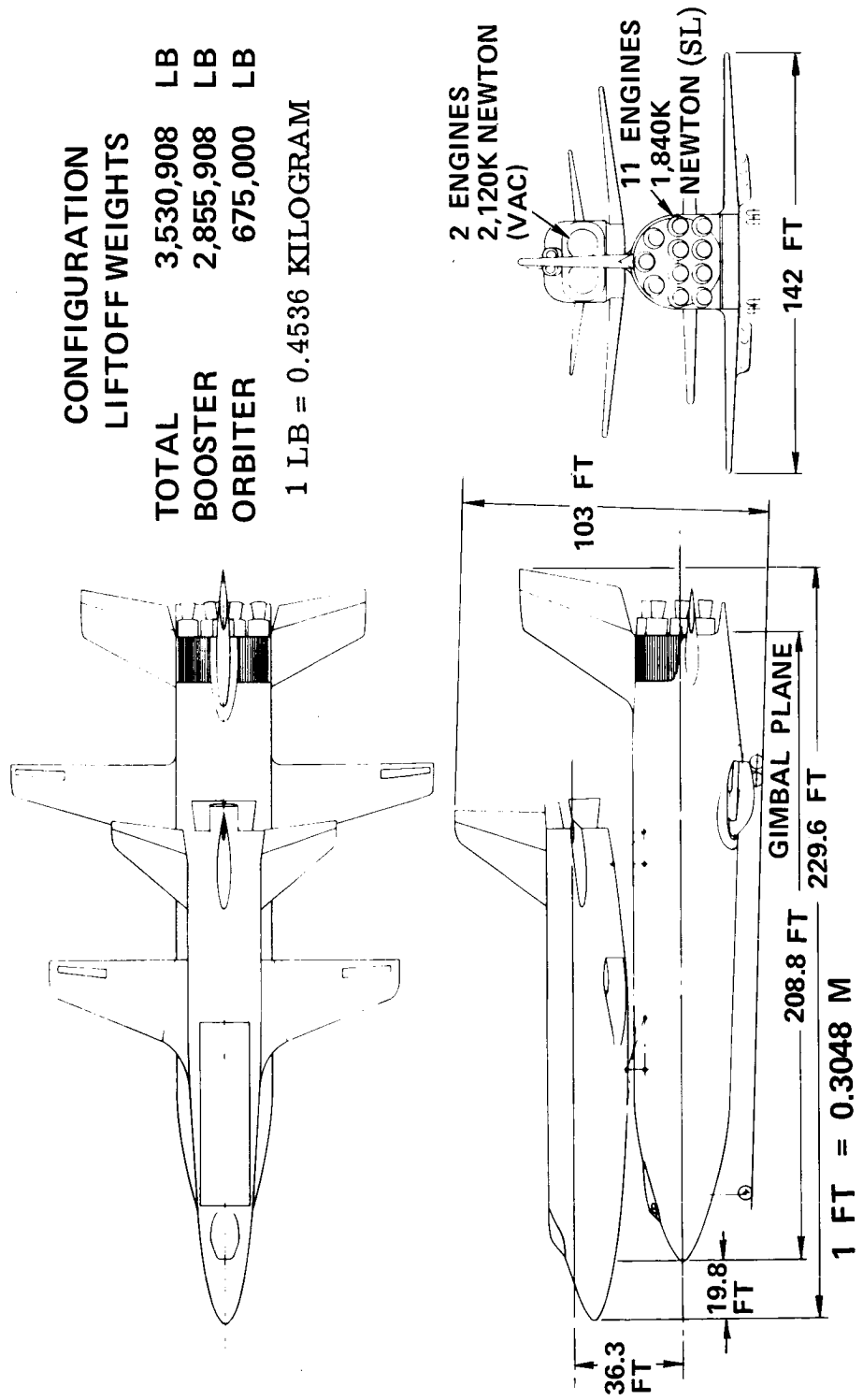


Figure 2

Rigid body load alleviation techniques were investigated for both the pitch and yaw planes. In the pitch plane, gimbal angle limiting, trajectory biasing, and gain scheduling with accelerometer feedback were studied. Gimbal angle limiting was considered a software limit that was scheduled with time. This technique was feasible because of the large static stability of the configuration. As the vehicle encounters the wind, the control moment is overpowered by wind moment and the vehicle "weathercocks" into the wind, which results in reduced loads. Approximately  $\pm 1.0^\circ$  of limit results in the maximum load reduction. At lower values, dynamic overshoot limits the load reduction potential. At higher values the "weathercock" response time is longer. Performance penalties in terms of added propellant are encountered due to the deviation from the optimum no-wind ascent trajectory. (See Figure 3.)

## RIGID BODY ALLEVIATION TECHNIQUES INVESTIGATED

### GIMBAL ANGLE LIMITING (SOFTWARE LIMITING)

- STATICALLY STABLE VEHICLE DURING ASCENT
- LIMITING DURING PEAK LOADS
- POTENTIAL MAXIMUM  $\alpha_Q$  LOAD REDUCTION

$\delta_{\text{max}} = \pm 0.5^\circ$	7% LOAD REDUCTION
$\delta_{\text{max}} = \pm 1.0^\circ$	14% LOAD REDUCTION
$\delta_{\text{max}} = \pm 2.0^\circ$	6% LOAD REDUCTION

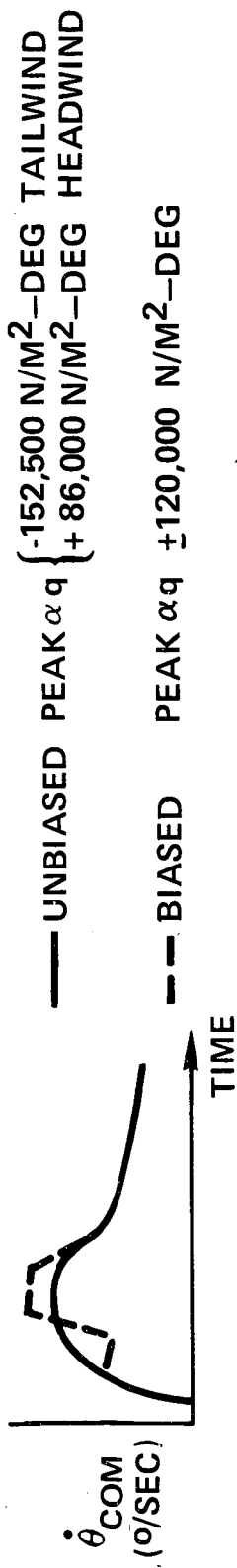
Figure 3

Trajectory biasing has been used to reduce the ascent design loads by shaping the commanded pitch rate (pitch programming). The shaping is based on knowledge of the winds before launch. For headwind conditions, the vehicle is pitched more rapidly into the wind at peak dynamic pressure; for tailwind conditions, the vehicle is allowed to climb more by reducing the commanded pitch rate. For an unbiased trajectory, the maximum tailwind  $\alpha q$  is  $-152,500 \text{ N/M}^2\text{-deg}$ , and the maximum headwind  $\alpha q$  is  $86,000 \text{ N/M}^2\text{-deg}$ . Structural weight saving was realized by reducing the tailwind value at the expense of the headwind load. A good compromise value was  $\pm 120,000 \text{ N/M}^2\text{-deg}$  for both wind conditions. Propellant consumption increased by approximately 4,536 kilograms for this biased trajectory. (See Figure 4.)

## RIGID BODY ALLEVIATION TECHNIQUES INVESTIGATED (Continued)

### TRAJECTORY BIASING – ASCENT

- BIASED SO THAT HEADWIND AND TAILWIND LOADS ARE APPROXIMATELY EQUAL
- BASED ON PREDICTED WINDS (PRIMARILY ALTITUDE OF PEAK WIND)



### GAIN SCHEDULING AND ACCELEROMETER FEEDBACK

- TIME SCHEDULE GAINS
- LINEAR VARIATIONS IN GAINS
- 10% POTENTIAL MAXIMUM  $\alpha q$  LOAD REDUCTION

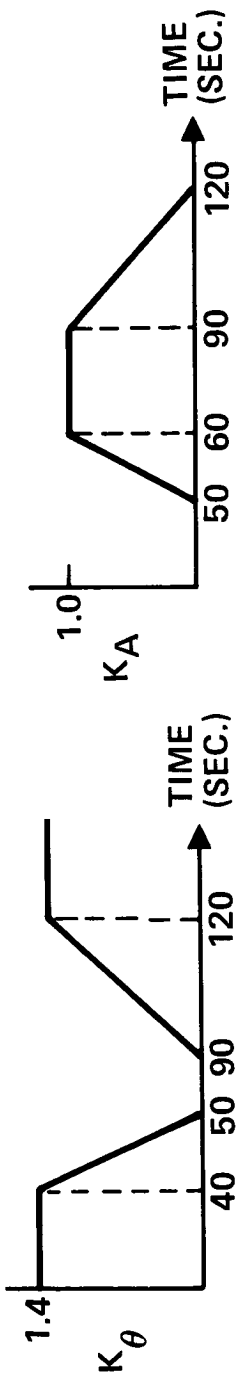
Figure 4

Gain scheduling with accelerometer feedback was analyzed and found to provide a potential 10% maximum  $\alpha q$  load reduction. The pitch attitude and accelerometer gain was scheduled with time. As the load increases, the pitch attitude gain is reduced to allow the vehicle to "weathercock" and the accelerometer gain is increased to provide a control moment in the direction to increase "weathercocking." For stability considerations a first-order filter was applied to the accelerometer signal.

Yaw attitude and sideslip feedback were used to reduce ascent side loads. As sideslip increases, yaw gain is dropped to allow the vehicle to yaw to reduce the sideslip. Yaw attitude gain was scheduled with time while sideslip gain was scheduled with dynamic pressure. A 36% side-load reduction potential exists for this type of load reduction scheme. (See Figure 5.)

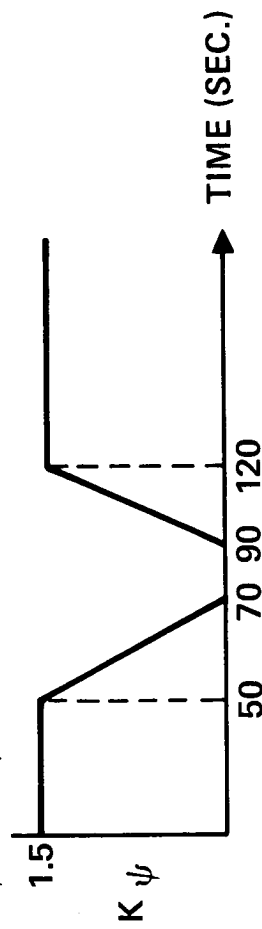
## RIGID BODY ALLEVIATION TECHNIQUES INVESTIGATED (Continued)

$$\bullet \delta_c = 1.0 \dot{\theta} + K_\theta \theta + \frac{0.1 K_A A_{ZCG}}{(s+1)}$$



$$\bullet \beta = \text{FEEDBACK} \quad K_\beta = \frac{1.5 \bar{Q}}{650} \quad \bar{Q} = \text{DYNAMIC PRESSURE}$$

$$\delta_c \text{ YAW} = K_\psi \dot{\psi} + K_\psi \psi + K_\beta \beta$$



• 36% LOAD REDUCTION

Figure 5

To assess the potential of load reduction, the design conditions must be identified and the relative criticality of each condition established. This chart lists design conditions for each major structural component of the booster and orbiter. Note that minimum structural gage (0.762 mm is used in this study), booster burnout, ullage pressure, maximum entry load factor, and maximum thrust are design conditions that cannot be reduced by load alleviation control. For the booster 4g maximum entry load factor, reducing this load would increase the flyback range and thereby nullify any structural weight advantage. (See Figure 6.)

STRUCTURAL DESIGN CONDITIONS

BOOSTER	WING	4g ENTRY/ASCENT WINDS
	VERTICAL TAIL	ASCENT WINDS
	HORIZONTAL TAIL	4g ENTRY/MIN. GAGE
	FUSELAGE	BOOSTER BURNOUT/ASCENT WIND ULLAGE PRESSURE/MAX. THRUST
ORBITER	WING	ENTRY/ASCENT WINDS/MIN. GAGE
	VERTICAL TAIL	ASCENT WINDS
	HORIZONTAL TAIL	ENTRY/ASCENT WINDS/MIN. GAGE
	FUSELAGE	ENTRY/ORBITER BURNOUT/MAX. ACCEL./ASCENT TAILWIND MAX. ACCEL./ASCENT TAILWIND
	LOWER SURFACE	
	UPPER SURFACE	

Figure 6

This chart lists the potential structural weight saving from ascent load reduction — 1,720 kilograms of booster structural weight represents approximately 285 kilograms additional payload capability. Load alleviation has a bigger payoff for the orbiter in that approximately 635 kilograms of structural weight can be saved, representing an additional 635 kilograms of payload. Orbiter structure trades for payload in a 1 to 1 ratio, while booster structure trades for payload by approximately 6 to 1 ratio. Booster propellant trades for payload by approximately 14 to 1 ratio. Approximately 4,500 kilograms of additional propellant is required to compensate for off-optimum trajectory dispersions. (See Figure 7.)

## POTENTIAL STRUCTURAL WEIGHT SAVING FROM ASCENT LOAD REDUCTION

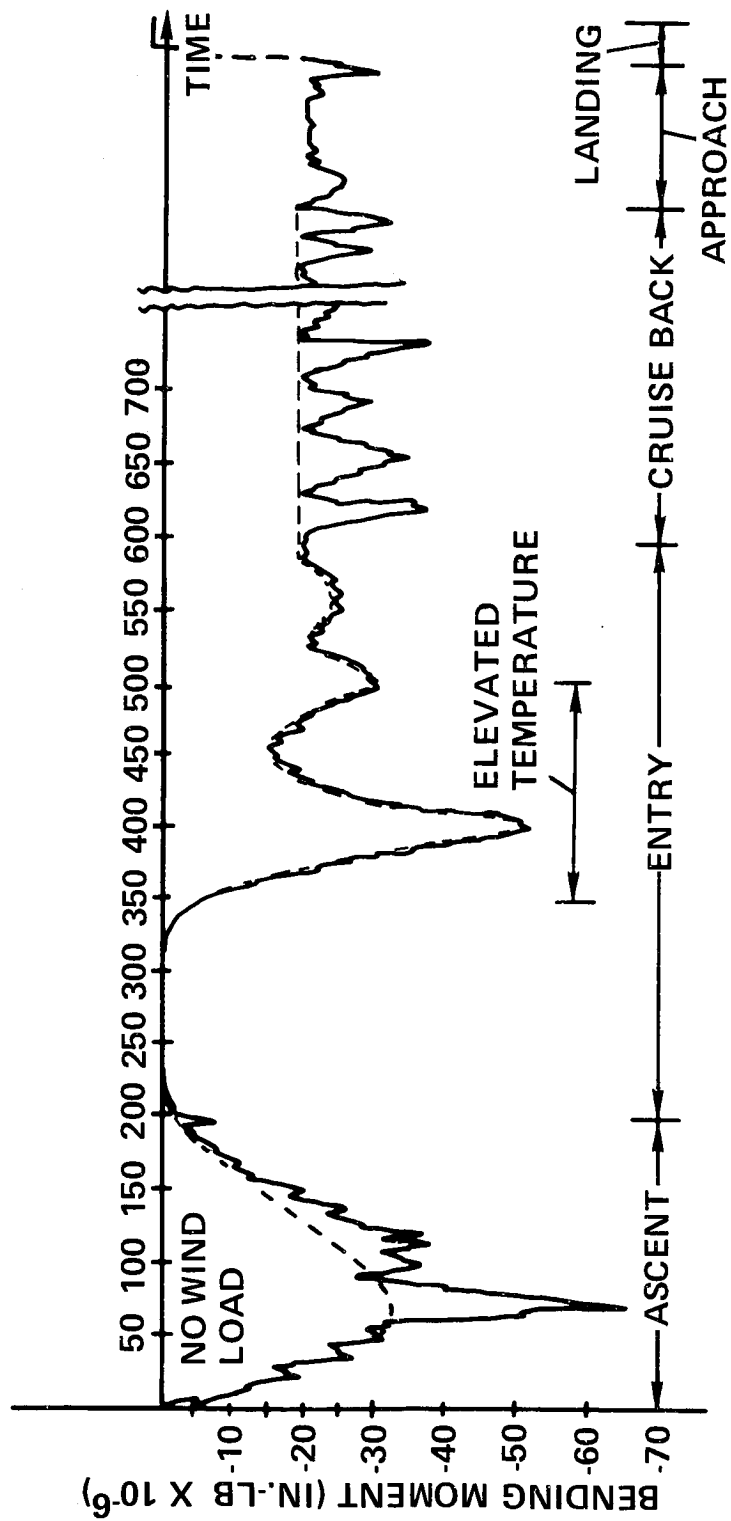
	<u>BOOSTER</u>	<u>ORBITER</u>
WINGS	1,000 LB	400 LB
HORIZONTAL TAILS	100	100
VERTICAL TAIL	1,200	600
FUSELAGE	1,500	300
	<u>3,800 LB</u>	<u>1,400 LB</u>

- 3,800 POUNDS OF BOOSTER STRUCTURAL WEIGHT REPRESENT APPROXIMATELY 630 POUNDS OF ADDITIONAL PAYLOAD
- 1,400 POUNDS OF ORBITER STRUCTURAL WEIGHT REPRESENT 1,400 POUNDS OF ADDITIONAL PAYLOAD
- APPROXIMATELY 10,000 POUNDS OF ADDITIONAL PROPELLANT ARE REQUIRED FOR PERFORMANCE LOSSES ATTRIBUTABLE TO LOAD REDUCTION. THIS REPRESENTS APPROXIMATELY 750 POUNDS OF PAYLOAD.
- LOAD REDUCTION HAS THE POTENTIAL OF INCREASING PAYLOAD FROM 1,000 TO 1,500 POUNDS  
1 LB = 0.4536 KILOGRAM

Figure 7

To determine the need for modal suppression, an estimate must be made of the fatigue damage the vehicle will incur during its lifetime. Fatigue damage analysis is based on an estimated load spectrum. This chart presents a typical booster root bending moment time history. Accumulated load occurrences for 100 flights in the life of the vehicle are being generated. The mission profile has been divided into the regions of: (1) ascent, (2) entry, (3) cruise, (4) approach, and (5) landing. Spectra are being generated for booster wing root, booster fuselage forward of wing, booster horizontal tail root, booster vertical tail root, orbiter wing root, orbiter fuselage forward of wing, and orbiter longitudinal and vertical tail root.  
(See Figure 8.)

## TYPICAL LOAD SPECTRA Booster Wing Root Bending Moment



1 IN-LB = 0.11126 METER-NEWTON

Figure 8

This chart presents the lifetime booster wing root load spectra for the ascent portion of flight. Ascent has been subdivided into nine segments. For each segment, alternating loads and average loads are presented. (See Figure 9.)

# LOAD SPECTRUM FOR BOOSTER WING ASCENT FLIGHT UNAUGMENTED

## Booster Wing Root Bending Moments

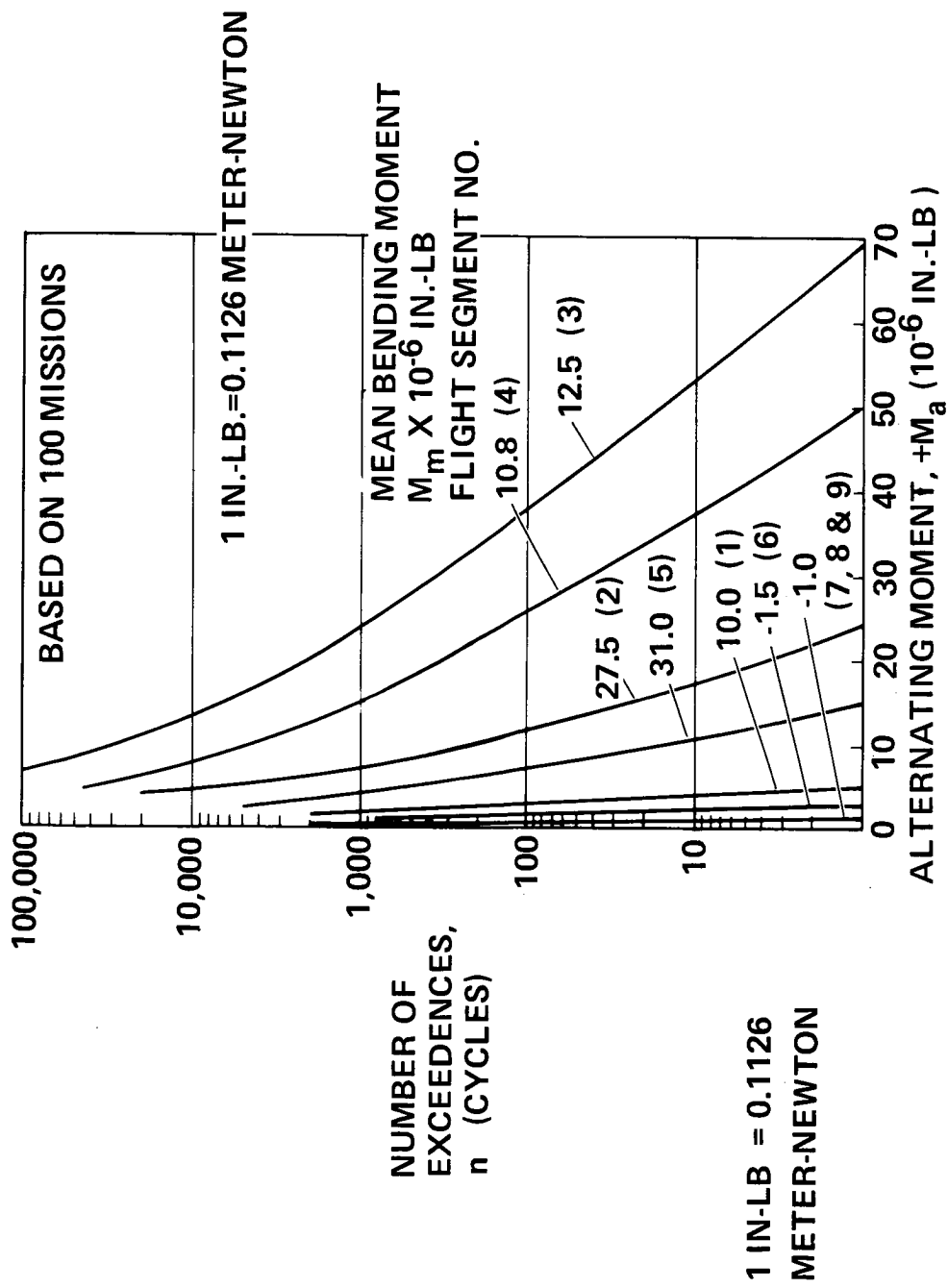


Figure 9

Fatigue damage is being evaluated using Miner's cumulative damage theory with a scatter factor of 4 and a notched factor,  $K_t$ , of 3. S-N data is lacking for the materials being considered for Space Shuttle. Data is needed in the low life cycle, high stress level area. Data used for ascent is in the form of stress oscillation about a mean stress, which corresponds to wind and gust loads being applied about a no-wind load. Data used for entry was of the form of maximum stress above zero; this corresponds to the expected entry load history, which is gust or wind independent. (See Figure 10.)

## BOOSTER WING FATIGUE DAMAGE

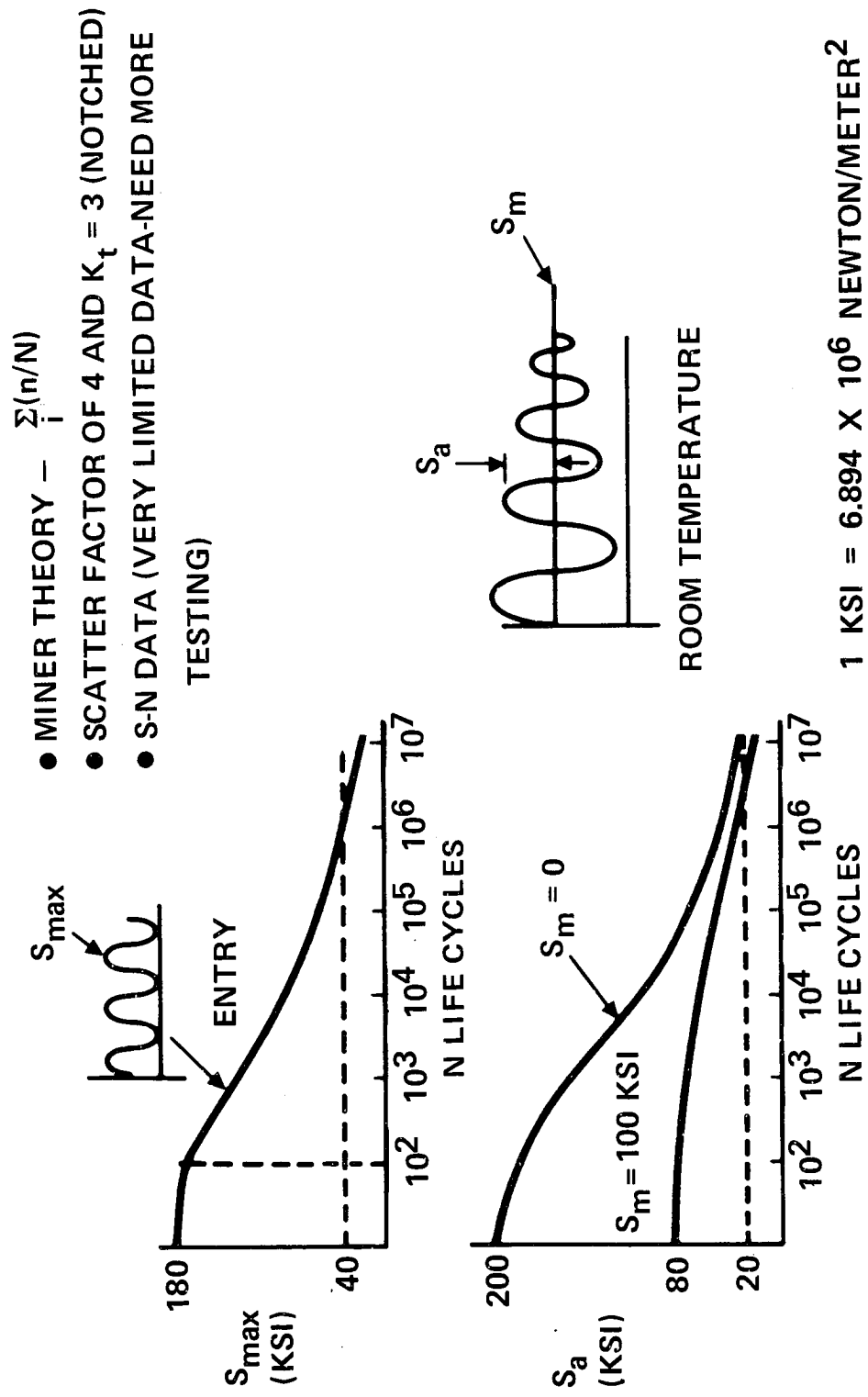


Figure 10

For the booster wing, cruise gust load represents the flight regime which produces most fatigue damage. Based on limited fatigue test data the accumulative fatigue index (with a scatter factor of 4) is 0.48. An index of less than one indicates no fatigue damage. However, there is concern for the effects of temperature during the high entry load condition. This portion of flight may be subjected to creep; the effects of creep and fatigue must be studied in more depth. (See Figure 11.)

## BOOSTER WING FATIGUE DAMAGE

- $\sum(n/N_j) = 0.07$

ASCENT                  ENTRY                  CRUISE

- NOT FATIGUE CRITICAL

$$\sum n/N = 0.19$$

$$4 \times 0.19 = 0.76$$

BUT THIS IS BASED ON LIMITED FATIGUE TEST DATA AND 0.76 DOES NOT PROVIDE A LARGE MARGIN FOR DATA VARIATIONS

- CREEP MAY CHANGE THIS CONCLUSION WHEN COMBINED WITH FATIGUE

Figure 11

Since the fatigue damage index factor is sufficiently high, consideration is being given to reducing the load spectra by active modal suppression. A wing-mounted aileron is the active controller being considered for both the orbiter and booster wing. Sensors under consideration are wing-mounted accelerometers, rate gyros, and strain gages. The fuselage modes will be stabilized by thrust vectoring. The sensors under consideration are fuselage-mounted rate gyros. The distribution of sensors will be to provide maximum damping and reliability. (See Figure 12.)

# MODAL STABILIZATION

- WING AND FUSELAGE
- BOOSTER WING

FREQUENCY (Hz)

3.38	FIRST WING BENDING
4.11	WING BENDING + SECOND BODY BENDING
7.2	WING BENDING + THIRD BODY BENDING
8.65	FIRST WING TORSION
11.34	SECOND WING BENDING

- AILERON CONTROL ON WING FOR MODAL STABILIZATION
- WING-MOUNTED ACCELEROMETERS/RATE GYROS/STRAIN GAGES
- THRUST VECTOR CONTROL FOR FUSELAGE MODAL STABILIZATION
- RATE GYROS DISTRIBUTED ALONG FUSELAGE

Figure 12

## SHUTTLE POGO REVIEW

By John E. Harbison  
George C. Marshall Space Flight Center  
Marshall Space Flight Center, Alabama

### INTRODUCTION

In the Saturn V program, POGO, a regenerative coupling between vehicle structure and propulsion system, has occurred both on the S-IC and S-II stage powered flights.

In the S-IC, a lox preflare in the outboard engine lox line was used as an accumulator and successfully decoupled the structure and line. A fix for the S-II stage has been incorporated and consists of an accumulator in the center engine lox line. This also has proved to be a very effective suppression device.

The approach taken in the shuttle POGO investigation is to use our experience on the Saturn vehicle where possible. At the same time, it is to be recognized that the shuttle vehicle is unique in certain areas and, therefore, the development of new or modification of existing techniques is necessary.

A basic understanding of the structural and propulsion systems dynamic characteristics is necessary to be in a position to "design in" a workable suppression device, in the event one is needed.

This presentation represents a status report of a very preliminary POGO investigation. All data reflected in the slides are considered to be rough estimates.

The significant parameters, their use in POGO analyses, and the ways to obtain these parameters are discussed.

## STABILITY MODEL

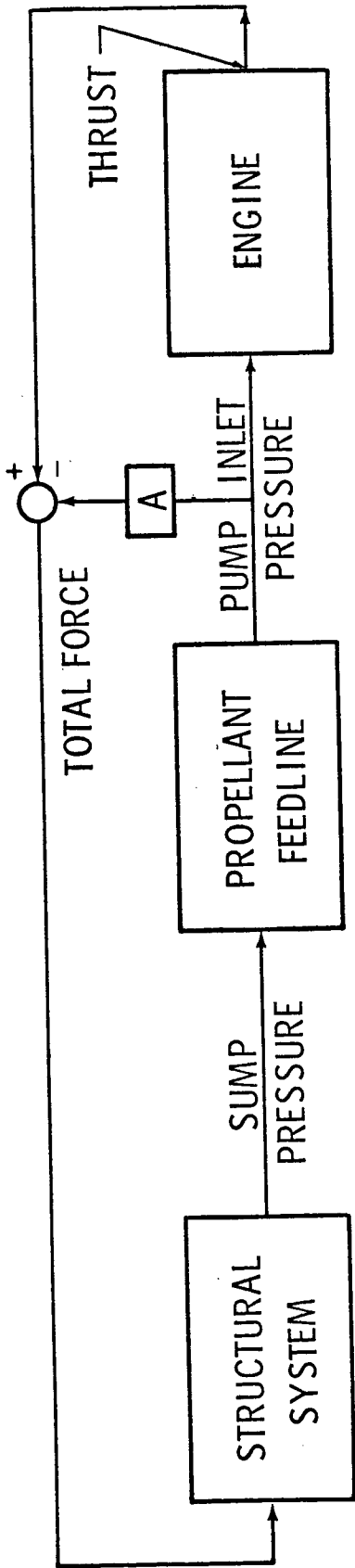
(Slide 1)

This slide presents a POGO loop which shows the transfer function necessary to perform a stability analysis.

The structural and the propellant feedline systems are defined by the frequencies, mode shapes, generalized mass, and damping. The engine system is described by transfer functions relating pressure and flow to thrust.

Since the closed loop gain is dependent upon the product of these three parameters, a change in gain of any one parameter will affect the overall systems gain. In previous vehicle programs where a fix has been required, it has been more feasible to modify the propellant feed system in order to decrease the total loop gain.

# STABILITY MODEL



$$\text{STRUCTURE TRANSFER FUNCTION} = \phi_1 = \frac{\partial g}{\partial F}$$

$$\text{FEEDLINE TRANSFER FUNCTION} = \phi_2 = \frac{\partial P_{OS}}{\partial g}$$

$$\text{ENGINE TRANSFER FUNCTION} = \phi_3 = \frac{\partial T}{\partial P_{OS}}$$

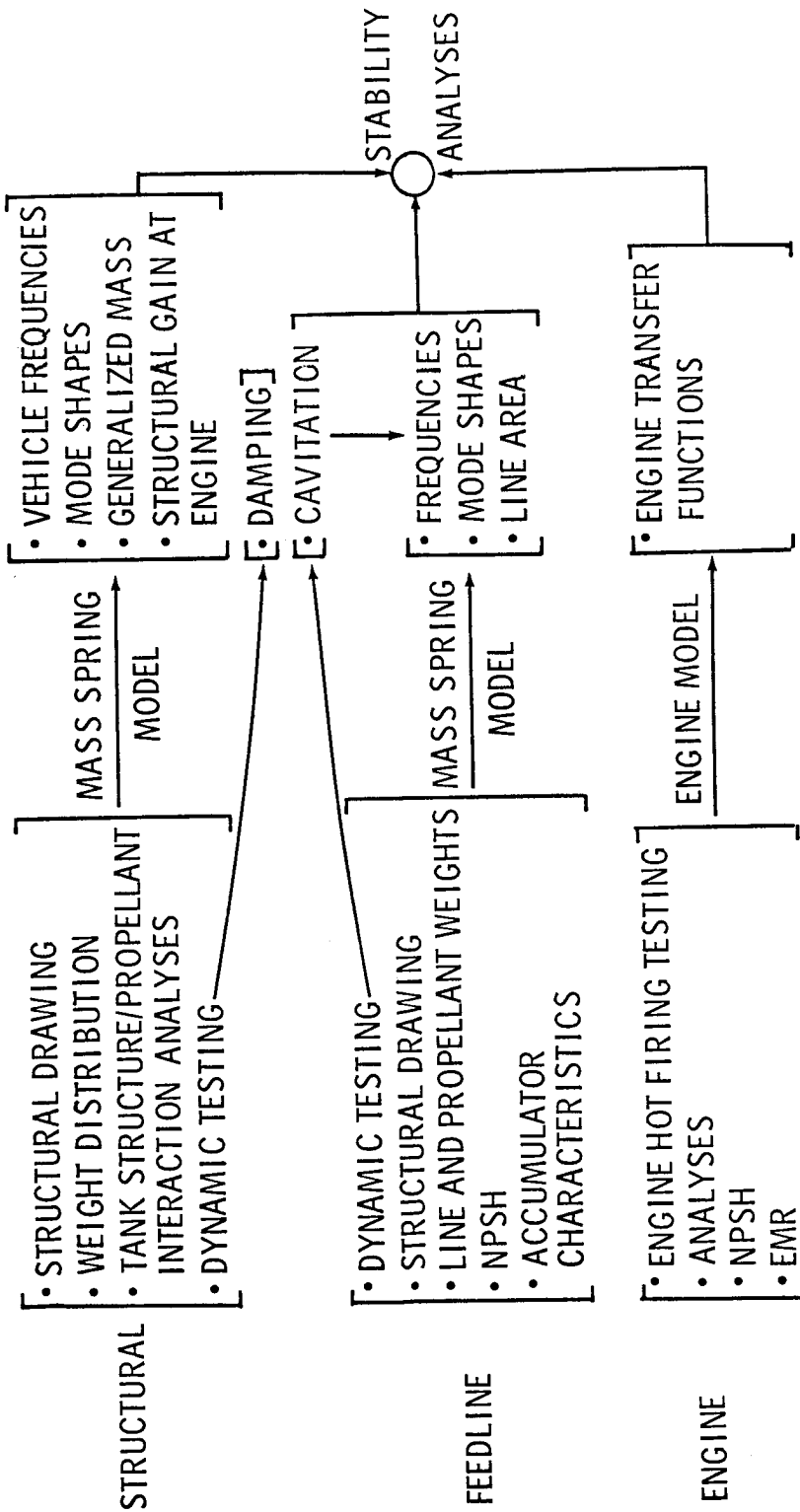
$$T_0 = \phi_3 \phi_2 \phi_1 T_i$$

DATA FLOW DIAGRAM

(Slide 2)

The data flow diagram describes the necessary inputs for deriving the inputs to a POGO stability analysis. In the beginning of a new vehicle program, all data are generated from preliminary type analyses, or from extrapolations of empirical data obtained from tests of other configurations. As vehicle design configuration progresses, more refined analyses are performed and used in conjunction with the available propulsion system and structural test data. An iterative process continues until the vehicles' first flight. If no surprises are found in the flight data, the succeeding vehicles are assessed by configuration changes and how these changes perturbate the baseline stability results.

## DATA FLOW DIAGRAM FOR POGO ANALYSES



Slide 2

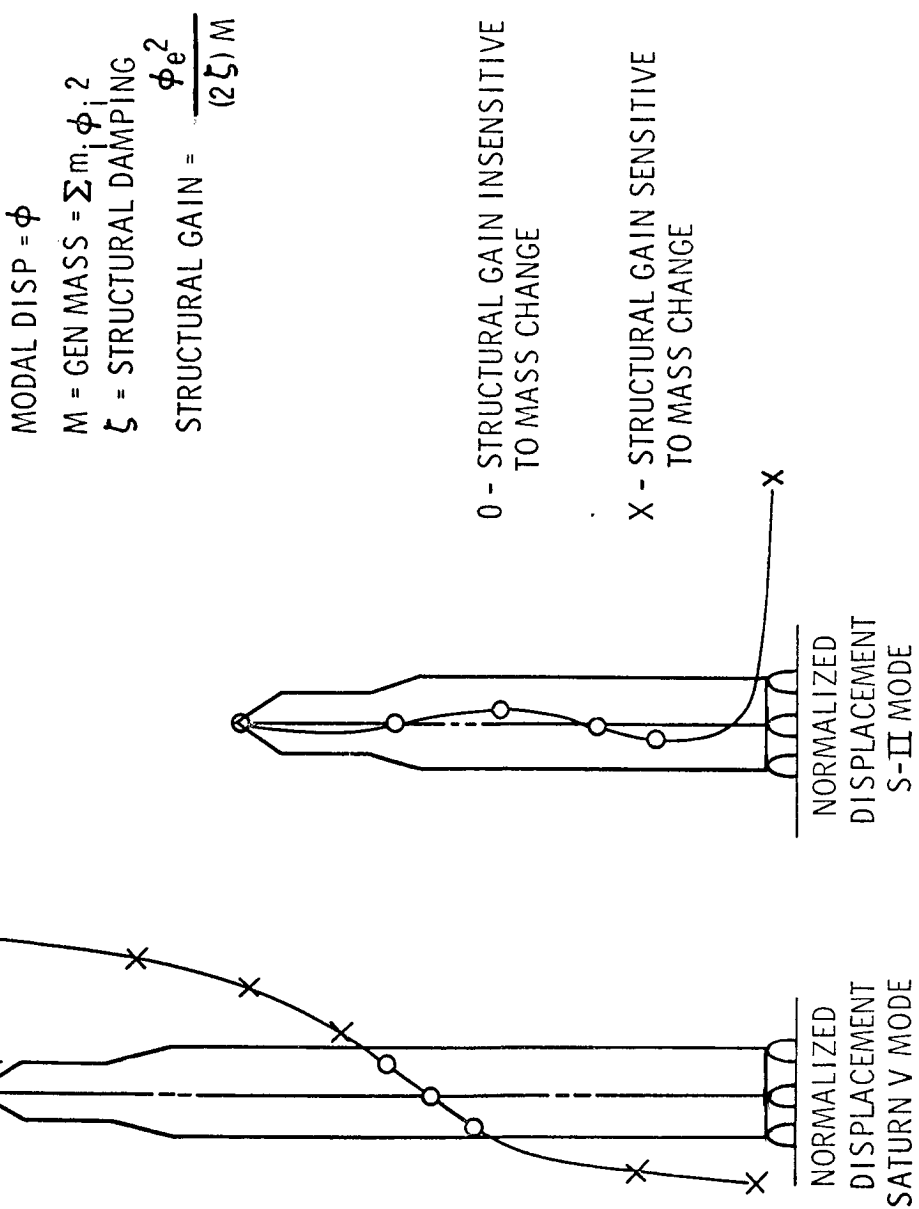
## VEHICLE LONGITUDINAL MODE SHAPES

(Slide 3)

Slide 3 presents two distinct POGO situations which have been observed in flight. The first mode shape is a first longitudinal mode of vibration; this mode has a large structural gain in the engine area. POGO in this mode would transmit oscillations to the payload area. The second mode shape represents a mode with local deflections in the engine area and POGO oscillations would be transmitted to the payload area.

These mode shapes play an important role in determining what to expect in POGO results due to a major or minor configuration change at various locations of the vehicle. For example, it is easy to understand that a mass change for locations showing a small relative displacement of the mode shape would cause only a small change in the energy of that mode. The converse is true for mass changes for locations that show large modal displacements. Assuming no change in other parameters, this type of quick-look procedure at best can only give a trend as to stability changes. Verification of actual stability changes can only result from analyses, where a baseline analysis has been verified.

## VEHICLE LONGITUDINAL MODE SHAPES

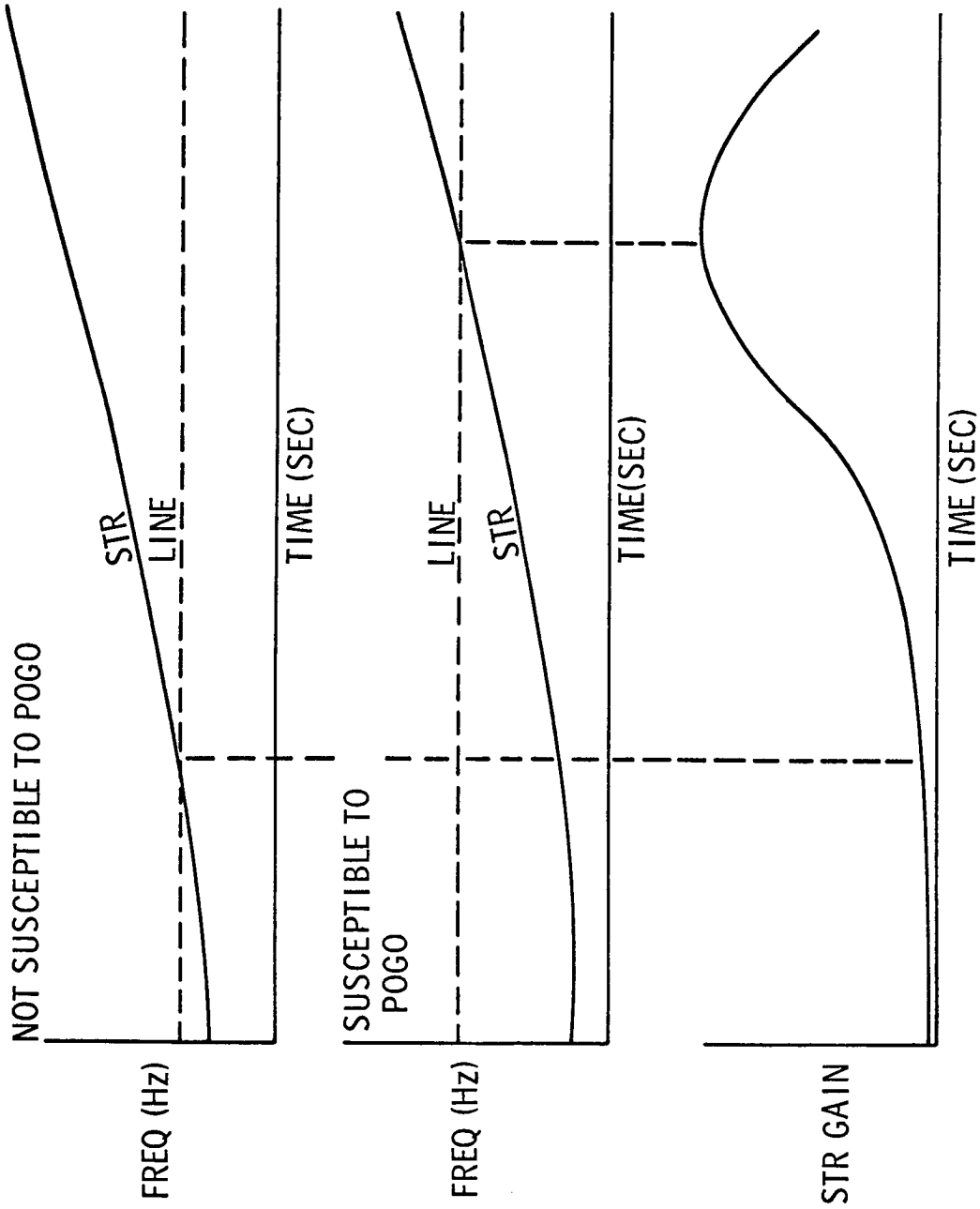


ANALYTICAL POGO INDICATORS

(Slide 4)

An investigation of the propellant feedline and vehicle systems dynamic characteristics will reveal the times of flight of which a concentrated POGO stability analysis is to be performed. The slide shows a propellant line frequency coinciding with a vehicle structural frequency. However, the important parameter is structural modal gain. If the modal gain is very low, there should be no POGO concerns, and conversely, if the particular vehicle mode shows a high gain, then there is a possibility of the existence of POGO at this flight time. There are exceptions to these general rules. In particular, the line and structural frequencies may be well separated, but a high modal gain causes an instability to occur. For this reason, a sufficient number of time points should be investigated by performing stability analyses to establish a stability profile throughout flight.

## ANALYTICAL POGO INDICATORS



PROPELLION DATA ESTIMATES

(Slide 5)

In order to determine potential POGO problems, an estimate of the required data has to be made.

This slide presents that data with variations from different contractors. For example, a significant parameter, engine gain, varied from .3 to .8. A comparison of these shuttle propulsion parameters with Saturn V S-IC and S-II propulsion system parameters are shown in the slide.

# PROPELLSION DATA ESTIMATES

PARAMETER	BOOSTER	ORBITER	SAT. V (S-TC)	SAT. V (S-II)
$\partial P_c / \partial P_s$ ENGINE GAIN (N/m <sup>2</sup> /N/m <sup>2</sup> )	.3 TO .8	.3 TO .8	.33	.5
$\partial P_c / \partial P_s$ ENGINE PHASE (DEG)	0 TO -90.	0 TO -90.	-20.	-20. TO -60.
$\partial T / \partial P_c$ THRUST GAIN (kg/Nm <sup>2</sup> )	$2.4 \times 10^6$	$2.4 \times 10^6$	$17.7 \times 10^6$	$4.9 \times 10^6$
NO. OF ENGINES	12	2	5	5
MAX. LOX INLET PRESS. (N/m <sup>2</sup> )	$14.1 \times 10^5$	$10. \times 10^5$	$8.95 \times 10^5$	$3.1 \times 10^5$
LOX LINE AREA (m <sup>2</sup> )	.041	.05	.146	.032
LOX LINE LENGTH (m)	45	33	13.7	1.5
1ST LOX LINE FREQ. (Hz)	2. TO 3.	3. TO 4.	5.	23.
2ND LOX LINE FREQ. (Hz)	10.	14.	30.	100.
LOX LINE DAMPING (%)	5.		16.	7.

STRUCTURAL SENSITIVITY STUDY

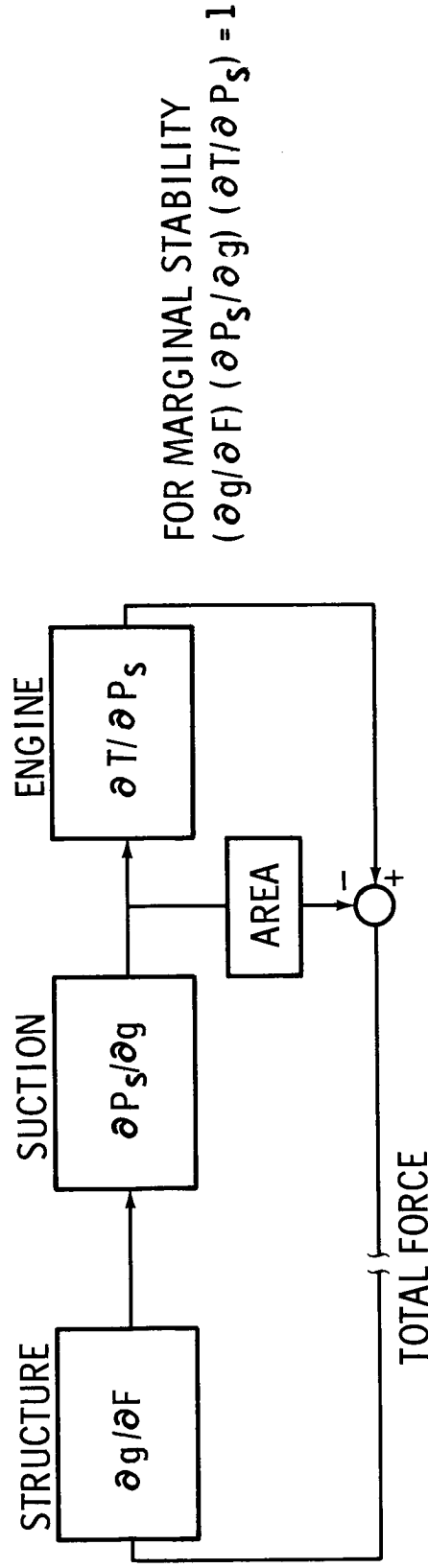
(Slide 6)

In order to determine the necessity for a POGO fix, worst case conditions were assumed. These include a structural/suction resonance, lox system only, and an engine gain of 0.8. A structural gain required to yield marginal stability was then calculated. The results indicated that any structural gain greater than  $2 \times 10^{-5}$  could produce instability. A review of the available structural data showed several modes could be unstable.

After vehicle and engine configurations have been finalized, if any of the several worst case assumptions are valid, then a fix must be considered.

# STRUCTURAL SENSITIVITY STUDY

- ASSUMPTIONS
  - STRUCTURAL/SUCTION RESONANCE
  - LOX SYSTEM ONLY
  - WORST CASE ESTIMATES



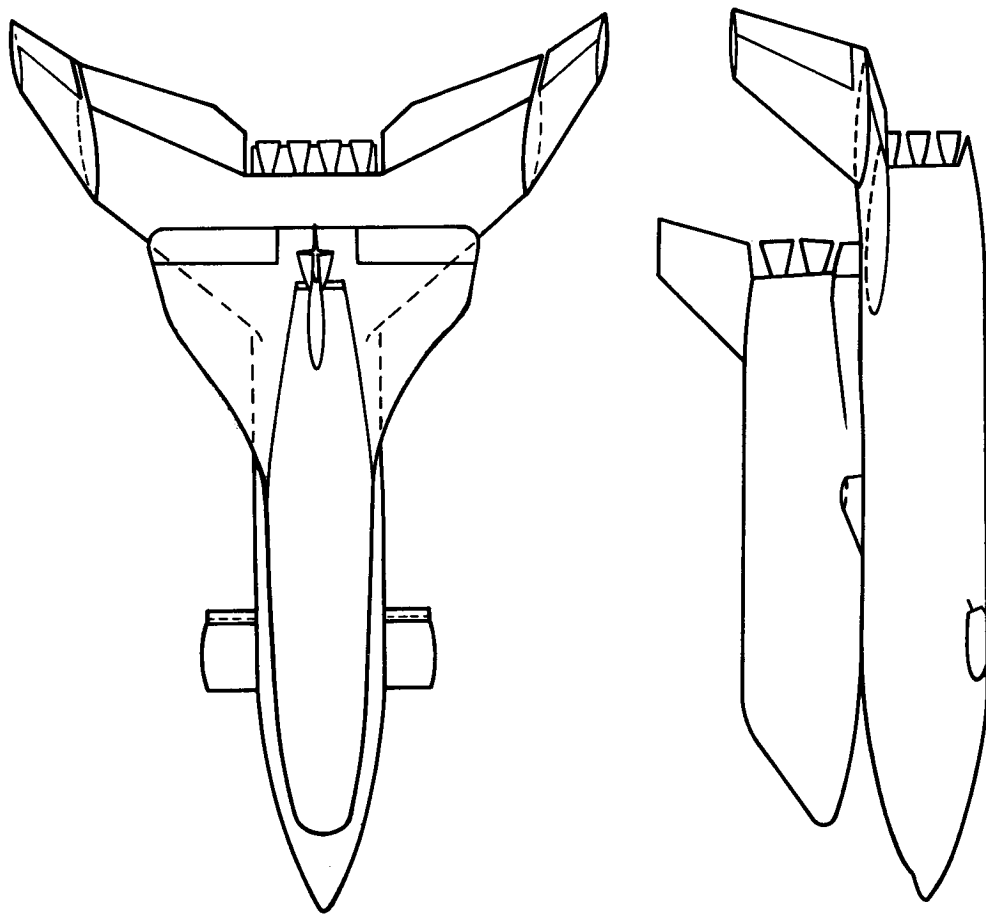
- RESULTS
  - STRUCTURAL GAIN  $> 2 \times 10^{-5}$  IS POTENTIAL POGO PROBLEM
  - FIX MUST BE CONSIDERED SINCE SEVERAL MODES EXCEED THIS

SPACE SHUTTLE CLUSTER CONFIGURATION

(Slide 7)

Longitudinal/lateral modal coupling has in the past been relatively unimportant from a POGO consideration. In this respect, the shuttle vehicle is unique. For this configuration arrangement, it becomes mandatory, in refined POGO analyses, to include the coupled modes. This longitudinal/lateral coupling will result in a high number of low vehicle system frequencies (0 to 30 hertz). This possibly means that the vehicle propulsion system coupling is more likely to occur.

## SPACE SHUTTLE CLUSTER CONFIGURATION



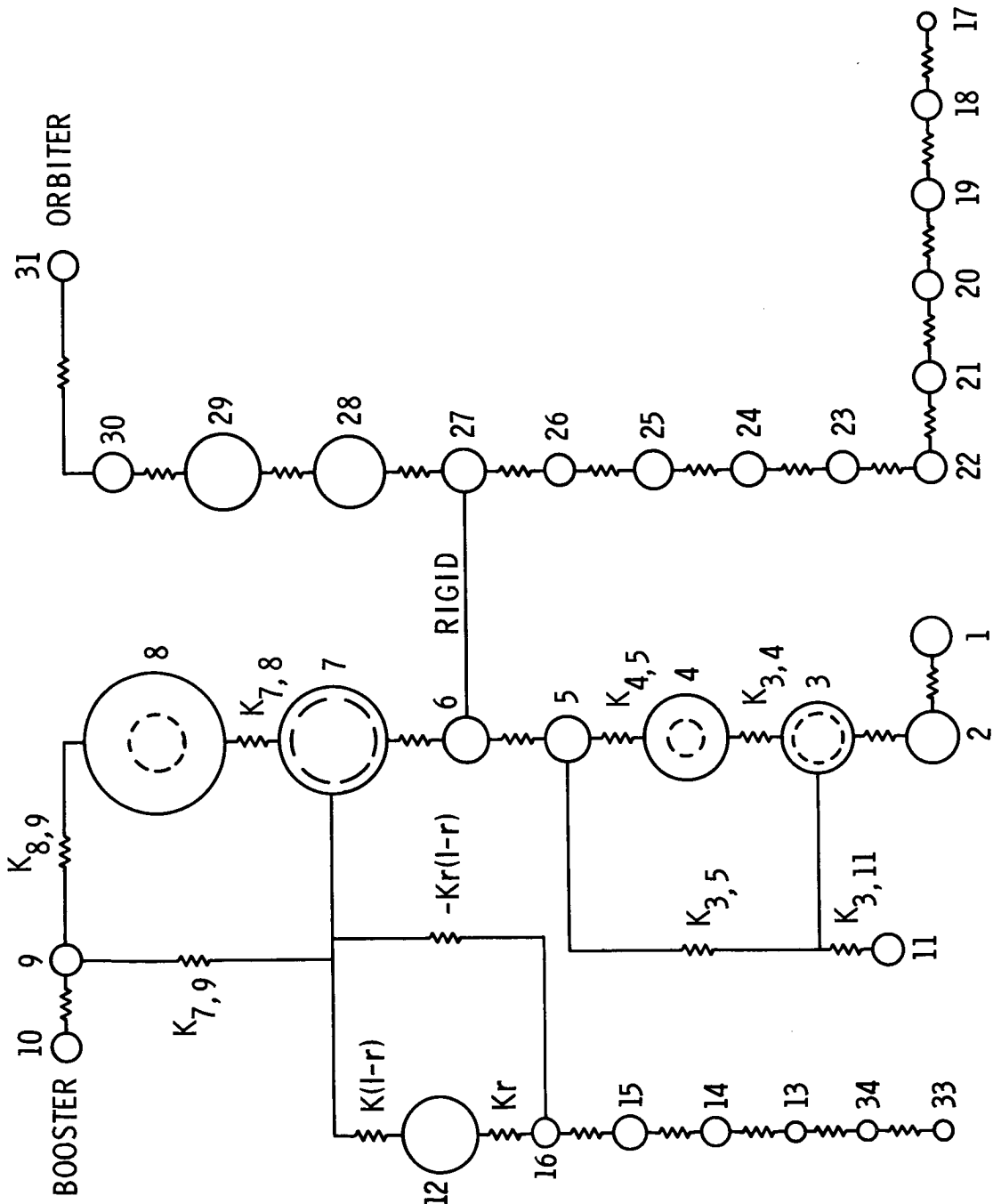
Slide 7

### SHUTTLE MODEL

(Slide 8)

The model in this slide represents a longitudinal model used in the stability analyses to better understand the longitudinal/lateral coupling. Nodes 17 through 31 represent the orbiter, and nodes 1 through 12 comprise the booster. A single degree of freedom model is used for the booster lox tank; therefore, only one tank mode will appear in the modal analyses.

## SHUTTLE MODEL

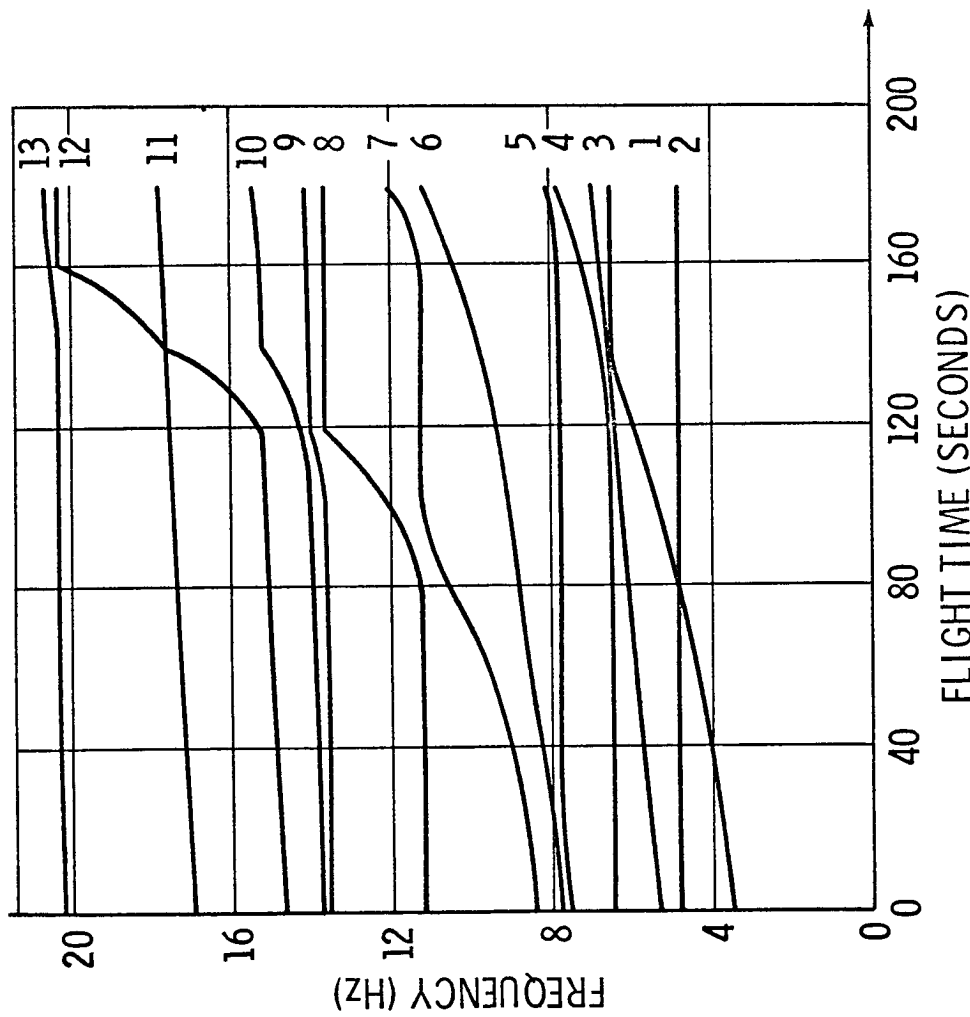


SHUTTLE BOOSTER/ORBITER FREQUENCIES  
VERSUS FLIGHT TIME

(Slide 9)

The structural frequencies versus flight time are shown in this slide. The modes were calculated from the longitudinal model; the first thirteen modes were used in the stability analyses. It is noted that a longitudinal/lateral model will have a first mode lower than the one presented in this slide.

# SHUTTLE BOOSTER/ORBITER FREQUENCIES VERSUS FLIGHT TIME

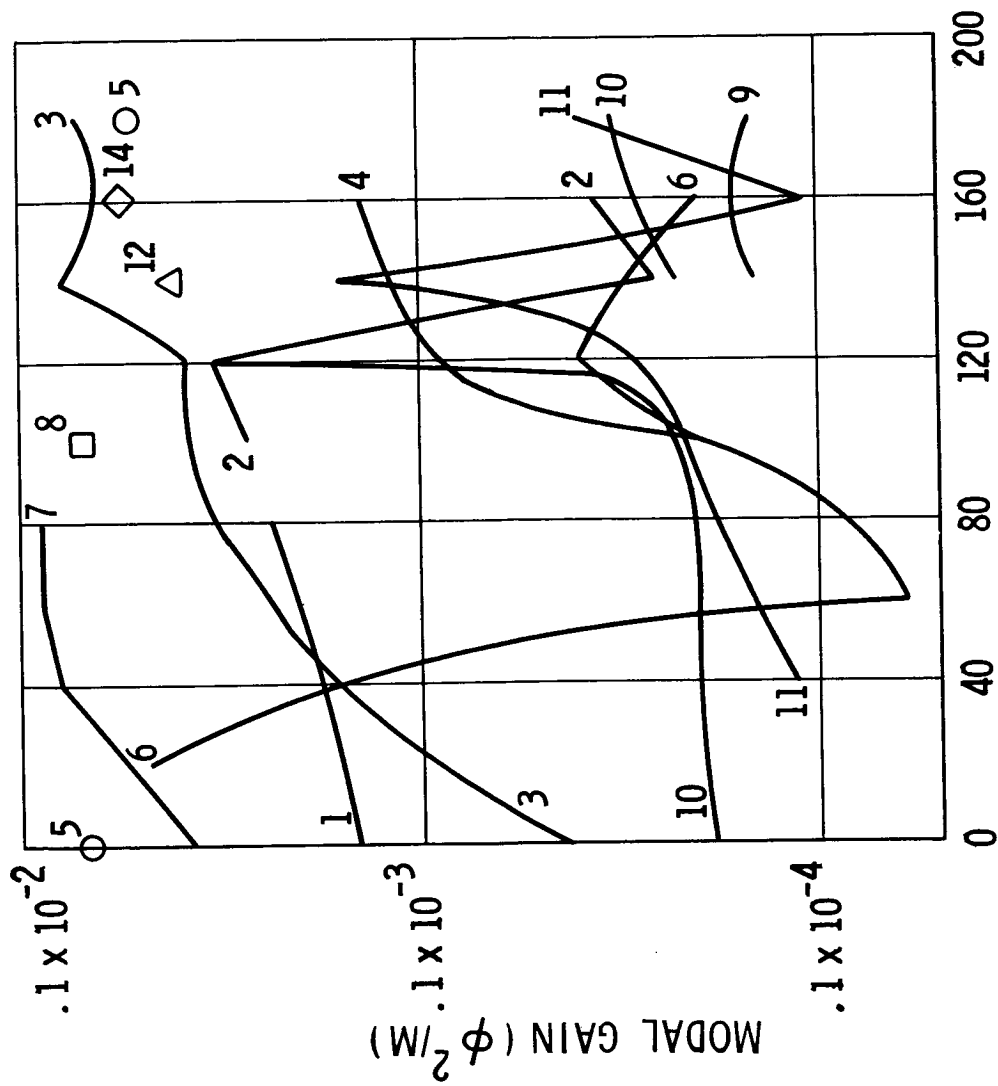


MODAL GAIN FOR SHUTTLE BOOSTER/ORBITER

(Slide 10)

Modal gains were calculated for the longitudinal model and are presented in this slide. It can be seen that several modes exceed the  $2 \times 10^{-5}$  modal gain that results in marginal stability if worst case estimates are used.

# MODAL GAIN FOR SHUTTLE BOOSTER/ORBITER

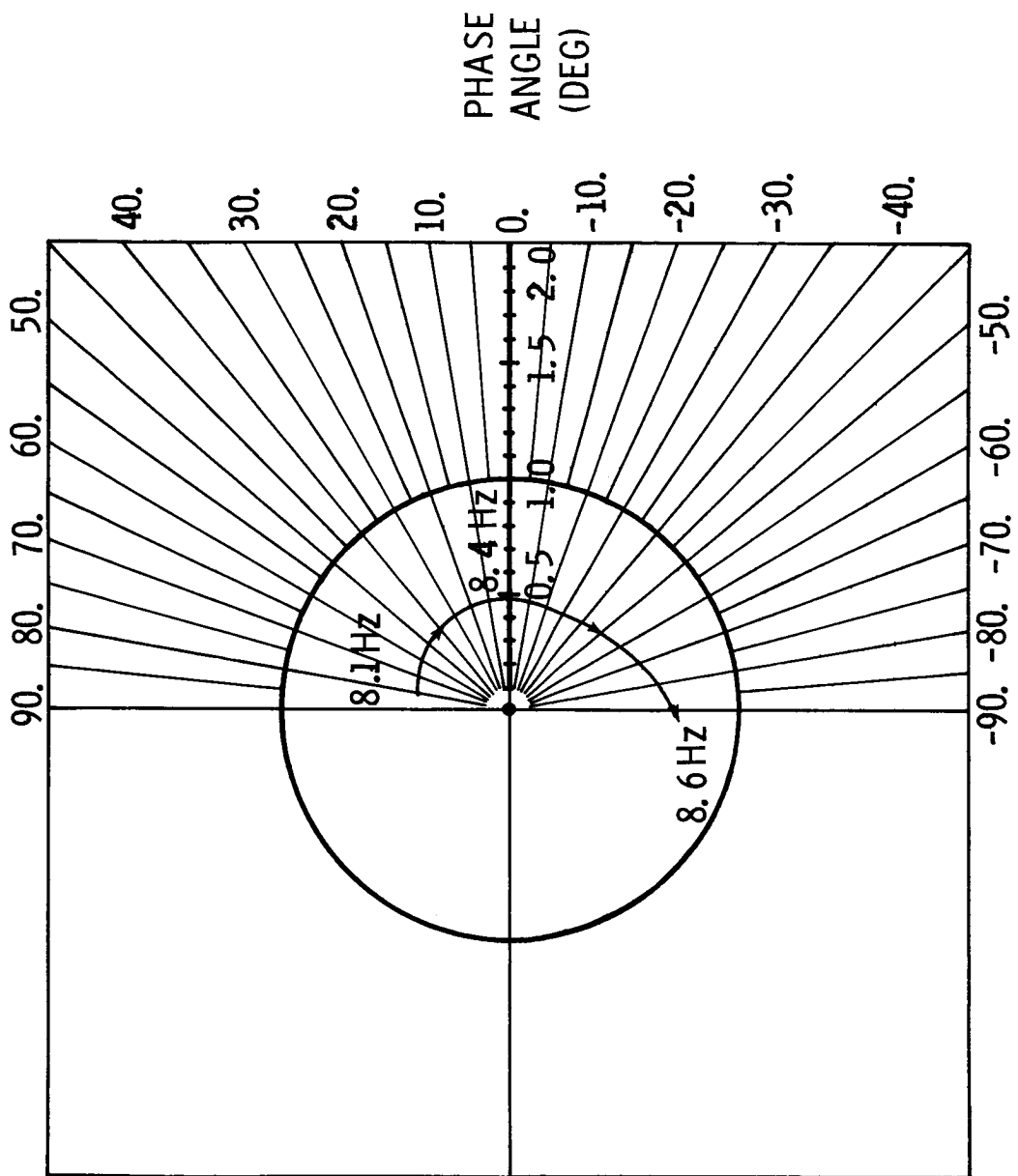


## STABILITY RESULTS

(Slide 11)

These stability results are presented in Nyquist plot form. This plot indicates the open loop gain using nominal structural and propulsion data. This plot represents time point zero, and the in-phase point (8.4 Hz) is the bulkhead mode. The in-phase stability margin is approximately -7 dB stable. The peak gain has a stability margin of -2 dB with a phase angle of 90 degrees.

## STABILITY RESULTS



DYNAMIC CHARACTERISTICS

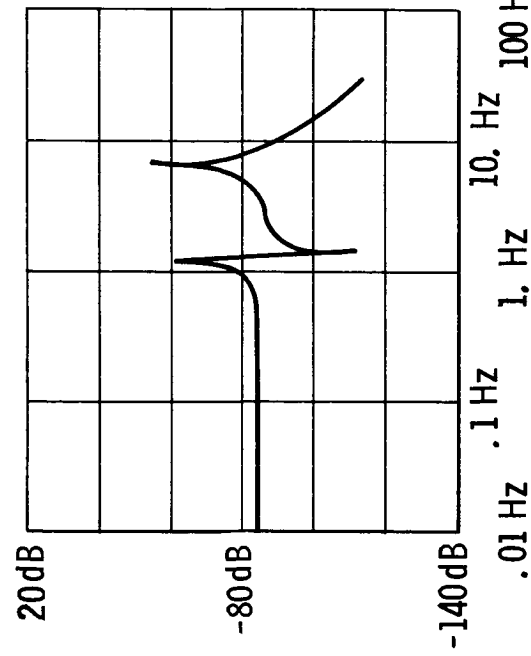
(Slide 12)

This slide presents the structural dynamic characteristics of a longitudinal/lateral model. The right plot is a Bode plot derived from a booster feedline model. Due to the extreme length of the booster lox lines, a modal model was used to represent them. The plot is relating lox pump inlet pressure ( $\partial P_{os}$ ) to lox sump pressure ( $\partial P_s$ ).

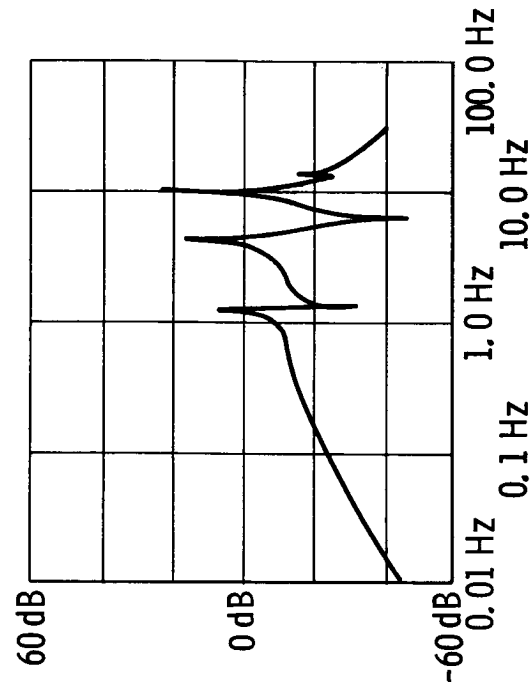
The left plot presents the structural transfer function and relates the deflection ( $\partial X$ ) at the engine to a force ( $\partial F$ ) applied to the engine.

## DYNAMIC CHARACTERISTICS

STRUCTURE TRANSFER FUNCTION ( $\partial X / \partial F$ )



SUCTION TRANSFER FUNCTION ( $\partial P_{OS} / \partial P_S$ )



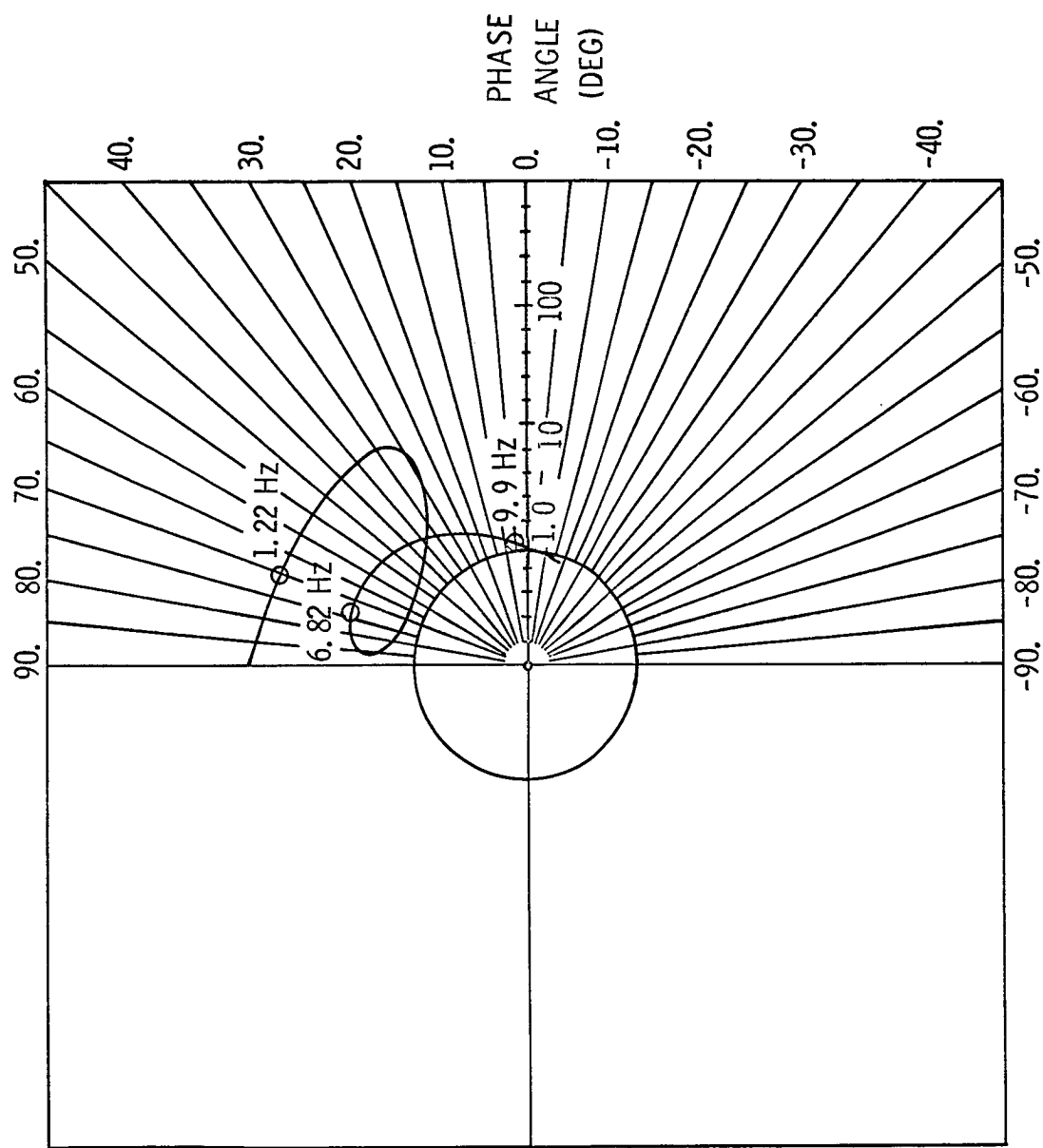
Slide 12

STABILITY ANALYSIS

(Slide 13)

A preliminary stability analysis using a coupled model for the space shuttle booster has been completed. For nominal conditions, two modes were identified as having the potential to provide an unstable POGO condition at 1.22 Hz and 6.83 Hz frequencies. The Nyquist plot presented shows the high gain modes to be phase stabilized. The reason for the phase stabilization is that the pressure times area load acting down on the thrust structure is much greater than the thrust oscillation acting upward. Because of the high gain and the phase sensitivity, relatively small changes in the input data could produce an unstable condition.

## STABILITY ANALYSIS



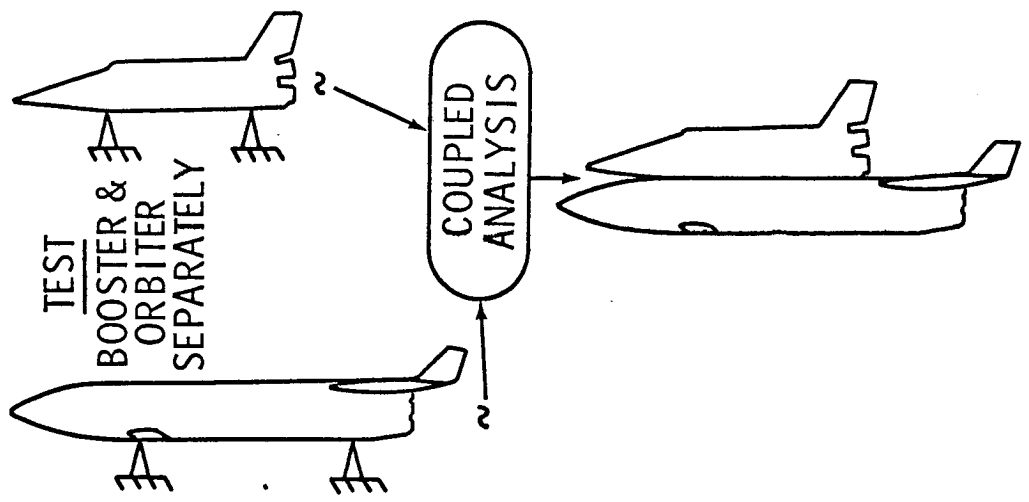
DEVELOPMENT OF COUPLED MODAL ANALYSIS

(Slide 14)

The shuttle dynamic test philosophy incorporates a closely integrated test and analysis concept. Since no cluster test is planned, a technique to verify a POGO math model must be included. This slide presents this test philosophy.

Scale models will be used to verify the modal coupling techniques. The scaled booster and orbiter will be tested separately and then coupled. Each analysis will be verified by test of the model analyzed. Once this is completed, the coupled test must verify the modal synthesis technique used in the analysis.

# DEVELOPMENT OF COUPLED MODAL ANALYSIS



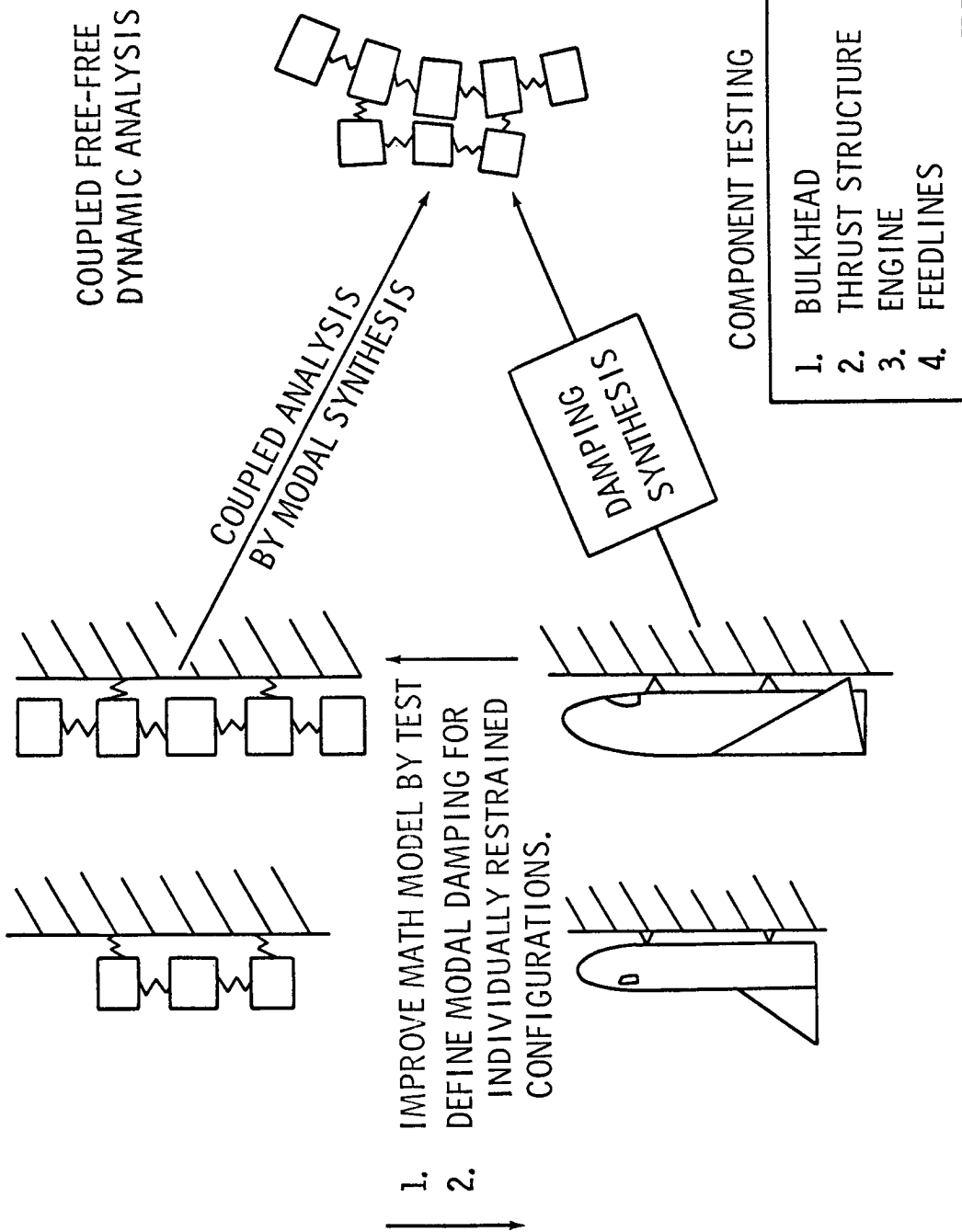
ANALYSIS <sub>(I)</sub>	+	ANALYSIS <sub>(II)</sub>	=	PHASE I TEST	ANALYSIS
					COUPLED ANALYSIS <sub>(III)</sub> = COUPLED ANALYSIS <sub>(III)</sub> EACH ANALYSIS VERIFIED BY TEST OF MODEL ANALYZED

SHUTTLE DYNAMIC ANALYSIS/TEST PROGRAM

(Slide 15)

Full scale test of the booster and the orbiter will be conducted separately to improve the math models. The coupled modal data will be obtained by modal synthesis. Also, a technique to obtain modal damping from a coupled model will be developed. To complete the data needed to perform a stability analysis, component tests will be run on bulkheads, thrust structure, engines, and feedlines.

# SHUTTLE DYNAMIC ANALYSIS/TEST PROGRAM

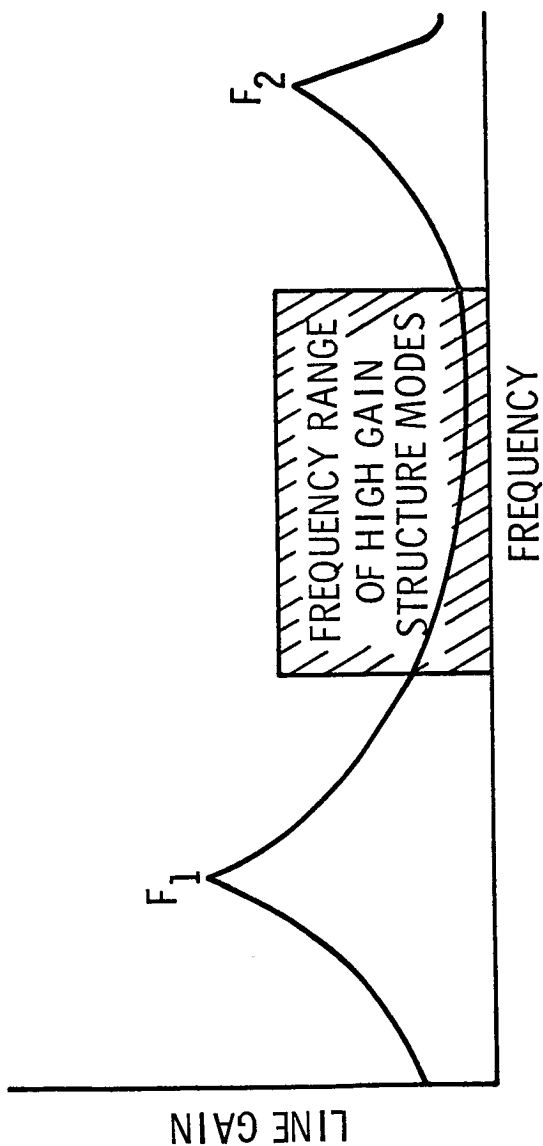


FEEDLINE FIX

(Slide 16)

This slide displays the ideal design for a feedline fix. The crosshatched area represents the frequency range of high gain structural modes. For a feedline fix, one must select a fix which will result in a first line frequency below all structural modes and a second line frequency above the structural modes of concern.

## FEEDLINE FIX



Slide 16

PASSIVE AND ACTIVE FIXES

(Slide 17)

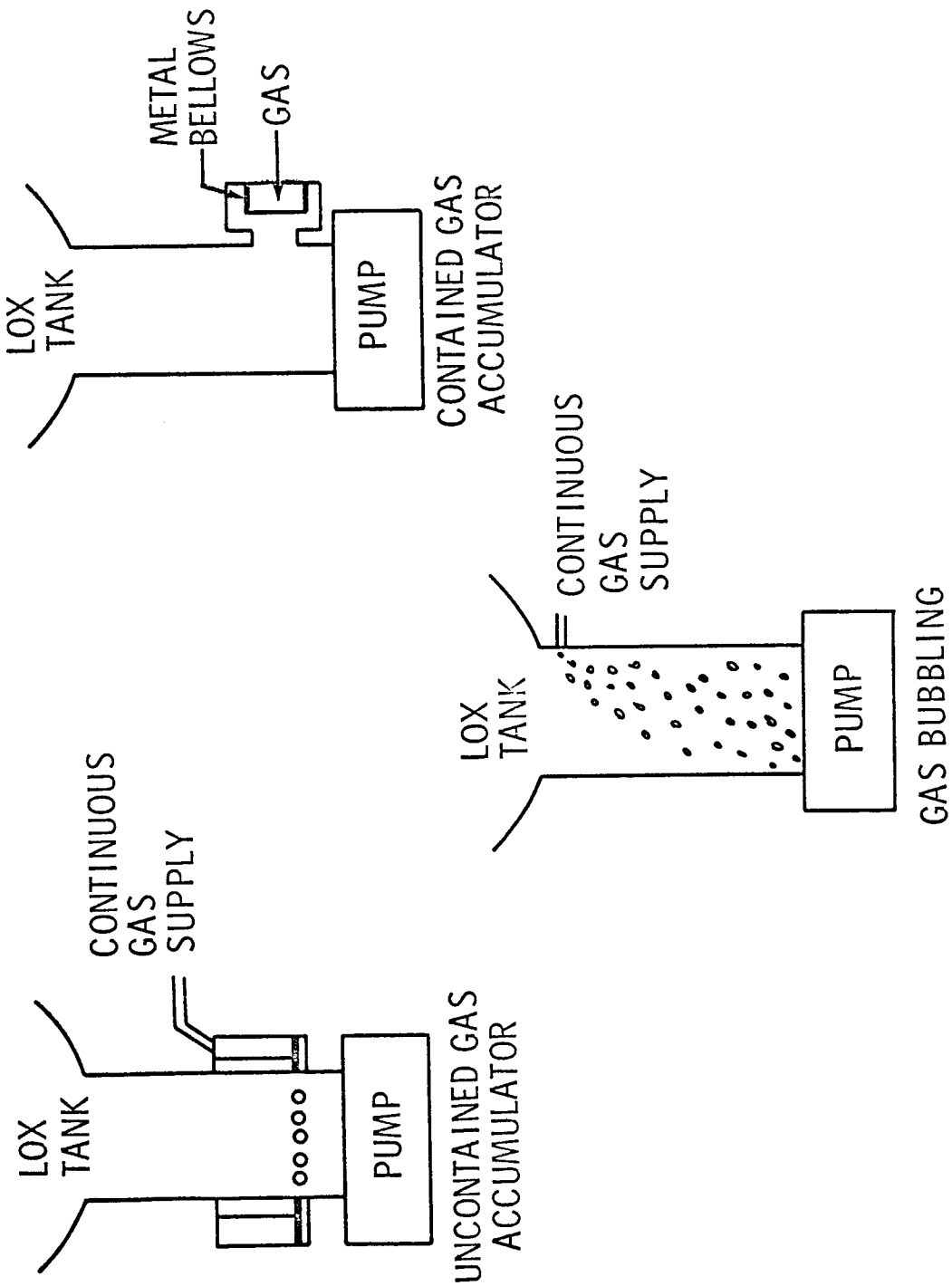
In considering passive fixes, three types have been considered in the past which would apply to the shuttle vehicles. The three are gas bubbling, continuous gas accumulator, and contained gas accumulator. There are advantages and disadvantages with each type; however, the continuous gas accumulator has proved to meet the POGO fix requirement in the past.

Continuous gas accumulator has the advantage of taking less volume than the contained gas accumulator; therefore, the problems of location and installation are reduced. The development cost of the contained accumulator is greater than that of the continuous gas accumulator.

The contained gas accumulator requires a larger volume due to the frequency range within which it must be operative. Gas bubbling requires no additional space, but extensive analysis must be performed to study the higher modes.

There are at present two active fixes under investigation. These include a turbine speed control and a line volume-acceleration compensator.

## PASSIVE FIXES



EXISTING TECHNOLOGY CONTRACTS

(Slide 18)

There are at present several technology contracts under way which could aid in the POGO stability analysis. These include pump cavitation modeling, pump self-induced oscillations, tank structure-propellant modeling, and suction line modeling.

## EXISTING TECHNOLOGY CONTRACTS

- PUMP CAVITATION MODELING
- PUMP SELF-INDUCED OSCILLATIONS
- TANK STRUCTURE-PROPELLANT MODELING
- SUCTION LINE MODELING

Slide 18

SUMMARY

(Slide 19)

Some of the problem areas have been discussed concerning the stability analyses. The structure for the shuttle will be more complicated to analyze due to the longitudinal/lateral coupling. An all-up dynamic test appears to be too expensive so a technique to obtain a coupled model has been derived. The present line configuration (manifold system) complicates both test and analysis.

In performing stability analyses more structural modes will need to be considered and the high line modes will be important because of the very long lines. The number of engine sets to describe the stability has not been determined; however, because of the thrust structure design, four engines may need to be in each set. As more data become available, the baseline stability model will be updated.

## SUMMARY

- STRUCTURE MUCH MORE COMPLICATED TO ANALYZE
- ALL-UP VEHICLE DYNAMIC TEST TOO EXPENSIVE
- PRESENT LINE CONFIGURATION (MANIFOLD SYSTEM) COMPLICATES
  - BOTH TESTS AND ANALYSIS
- MORE STRUCTURAL MODES WILL NEED TO BE CONSIDERED IN
  - STABILITY ANALYSIS
- HIGHER LINE FREQUENCIES MAY BE IMPORTANT BECAUSE OF VERY LONG LINES
- ANALYSIS MAY NEED TO INCLUDE AS MANY AS FOUR ENGINE GROUPS
  - BECAUSE OF THRUST STRUCTURE DESIGN

Slide 19

CONCLUSIONS

(Slide 20)

The results of the stability analysis indicate that POGO must be considered in early structure and propulsion system design. The feasibility of passive and active POGO suppression systems will be investigated. In order to establish a baseline configuration, analytical investigations must be used in conjunction with test data. In selecting a fix to eliminate a specific POGO problem, care must be taken to avoid creating another problem because of implementing a fix.

# CONCLUSIONS

- ELIMINATION OF POGO MUST BE CONSIDERED IN EARLY STRUCTURE AND PROPULSION SYSTEM DESIGN
- FEASIBILITY STUDIES OF BOTH ACTIVE AND PASSIVE POGO SUPPRESSION SYSTEMS WILL BE INVESTIGATED
- DETAILED ANALYTICAL INVESTIGATIONS OF STRUCTURE AND PROPULSION SYSTEMS IN CONJUNCTION WITH TESTS ARE REQUIRED TO DESCRIBE BASELINE CONFIGURATION
- IF A POGO SUPPRESSION DEVICE IS REQUIRED TO ELIMINATE A SPECIFIC POGO PROBLEM, CARE MUST BE TAKEN TO AVOID CREATING ANOTHER PROBLEM BECAUSE OF IMPLEMENTING THIS DEVICE

Slide 20

## SPACE SHUTTLE ACOUSTICS

By Stanley H. Guest

George C. Marshall Space Flight Center  
Marshall Space Flight Center, Alabama

### INTRODUCTION

The space shuttle as now envisioned will be one of the most powerful flying vehicles in the world. With  $6.6 \times 10^6$  lb ( $29.4 \times 10^6$  N) of thrust the booster produces enough mechanical power to energize more than one/half billion 100 watt light bulbs or enough Christmas tree lights to string almost 400 times around the world! However, about two and one/half of these light strings are lost to acoustic energy generation by the exhaust plume. This is an unwanted expenditure in addition to the fact that the acoustic energy can be potentially damaging to structure and to personnel, e.g., metal skin panels of airplane type structures are excited into high vibration states in certain sound fields and the panels can be ruptured or after a time "fatigued" to failure or rivet joints fail with cracks around rivet holes. Personnel can be injured in extreme sound fields; the auditory system of course, is among the most acoustically sensitive organs of the body, along with other organs that are sensitive to energy in various frequency ranges. In severe environments nausea or lack of self-controlled movements can result. In lesser environments communication with others is aggravated. Interference soon produces annoyance or in many other forms exaggerates itself as an unwanted bi-product of progress, a pollutant. Communities far from actual site operations can be influenced; homes or other private property can be damaged, i.e. plaster walls cracked, etc. This effect is certainly recognized and much effort is expended to reduce this bi-product or reduce its effects on the public or community and on the controlled areas near the test or launch operation of a rocket or jet flow system.

## SPACE SHUTTLE ACOUSTIC ENVIRONMENTS

(Slide 1)

The two basic regions of concern here are the farfield area, technically more than 3 to 5 wave-lengths from the source, and in the nearfield area, the vehicle itself. The farfield environments due to both launch and static test will be considered along with the vehicle environments induced by the supersonic exhaust flow. Some of the terminology utilized in describing farfield environments are discussed in the next two paragraphs.

Farfield acoustic environments are dependent on the power of the source commonly defined in terms of acoustic efficiency which is the ratio of acoustic power to the total mechanical power produced by the rocket.

$$\text{Acoustic efficiency } \eta = \frac{\text{Acoustic power, } W_a}{\text{Mechanical power, } W_m}$$

In watts the mechanical power is 0.918 TV, where T is thrust in newtons, V is effective exhaust velocity in meters per second. The acoustic power then is given by

$$W_a = \eta 0.918 TV \text{ watts}$$

The acoustic power level, PWL, is given by

$$PWL = 10 \log_{10} \left( \frac{W_a}{W_0} \right) \text{ or } 10 \log_{10} \left( \frac{\eta W_m}{W_0} \right)$$

where  $W_0$  = Reference power, 10<sup>-12</sup> watt (metric system related). PWL is related to sound pressure level, SPL, by

$$\overline{PWL} = \overline{SPL} + 10 \log_{10} A + K$$

The bar denotes root mean square or average values, A is the area through which sound energy is radiated, and K is a constant which involves impedance ratios.

## **SPACE SHUTTLE ACOUSTIC ENVIRONMENTS**

- **FARFIELD**
- **VEHICLE NEARFIELD**

Slide 1

TOTAL ACOUSTIC POWER FOR VARIOUS VEHICLES

(Slide 2)

The Saturn V ( $7.5 \times 10^6$  lb thrust -  $3.33 \times 10^7$  N) with 0.4% acoustic efficiency, and  $1.78 \times 10^8$  watts acoustic power, is surpassed by the shuttle if the efficiency is 0.3% or more. The single high  $P_c$  engine test produces  $2.4 \times 10^7$  watts of acoustic power at 0.5% efficiency which is very near the total power output of the Saturn IB ( $1.5 \times 10^6$  lb thrust -  $6.66 \times 10^6$  N) with  $2.7 \times 10^7$  watts or 193.8 dB OA PWL and 195.0 dB OA PWL, respectively.

**TOTAL ACOUSTIC POWER FOR  
VARIOUS VEHICLES**

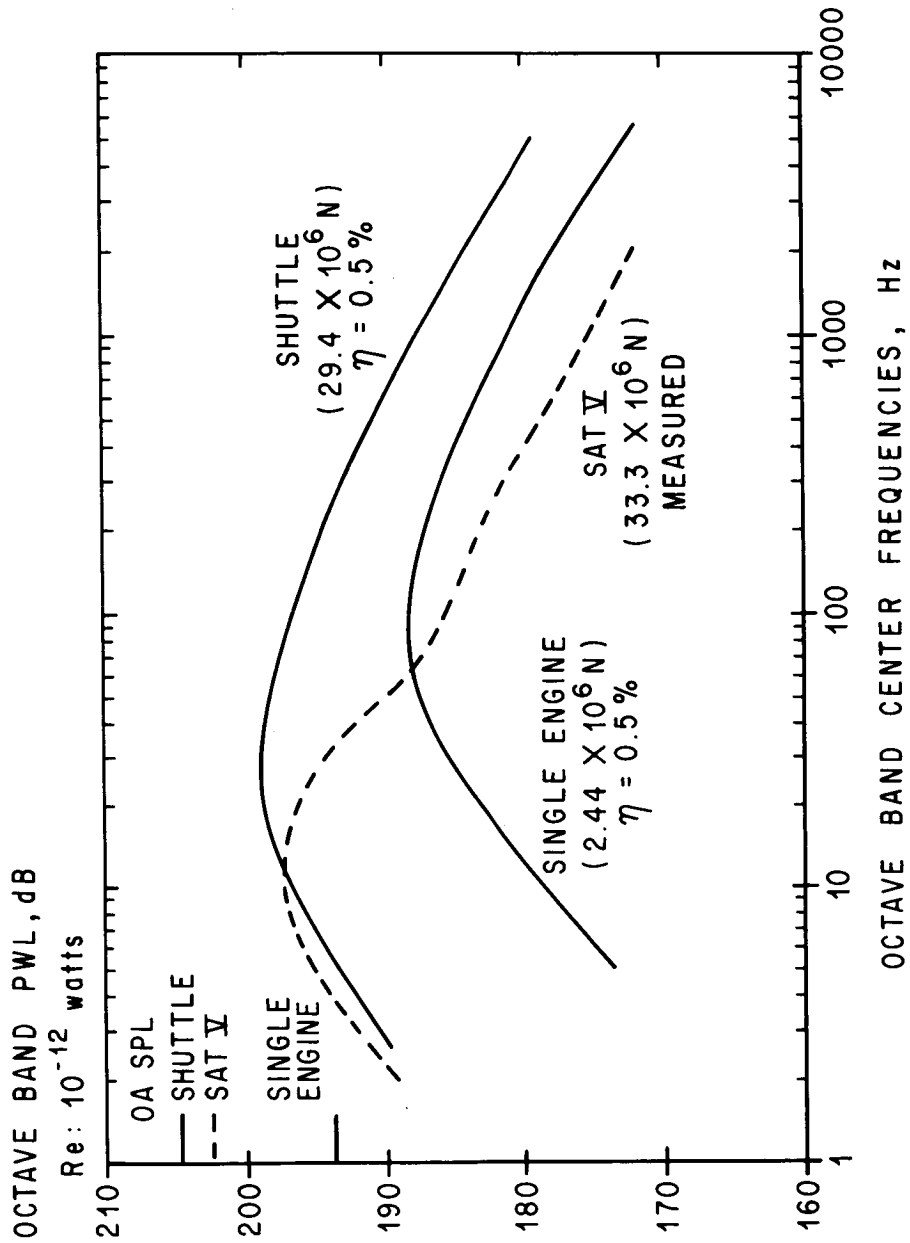
VEHICLE	ACOUSTIC POWER		ACOUSTIC EFFICIENCY (percent)
	(watts)	dB (Re: 10 <sup>-12</sup> watts)	
SATURN IB	$2.70 \times 10^7$	195.0	0.3
SATURN V	$1.78 \times 10^8$	202.5	0.4
SPACE SHUTTLE (12 550K ENGINES)	$\{ 2.89 \times 10^8$ $5.78 \times 10^8 \}$	204.6 207.6	0.5 1.0
550K SINGLE ENG	$2.40 \times 10^7$	193.8	0.5

## ACOUSTIC POWER SPECTRA

(Slide 3)

The power spectrum is the acoustic energy per frequency band, that is, a definition of the available acoustic power at the source, and is given here in octave bands. Indicated here are the shuttle, Saturn V, and single high  $P_c$  engine acoustic power spectra. The Saturn V produces more acoustic power below 10 Hz than the shuttle; however, above 10 Hz the shuttle generally produces up to 11 dB more power per octave band than does the Saturn V. This power spectrum is a source characteristic however, and the resulting field environments are modified in the propagation process by nonlinear energy losses with respect to frequency, i.e., basically due to the frequency dependent absorption phenomena in the atmosphere. Observation of the power spectrum differences would lead one to conclude, with all other factors equal, that extreme farfield environments for the Saturn V would exceed that of the shuttle, and the shuttle's higher energy in the upper frequency range would indicate that the environments for the shuttle would exceed that of the Saturn in the more adjacent farfield, i.e., at lesser radii.

## ACOUSTIC POWER SPECTRA



Slide 3

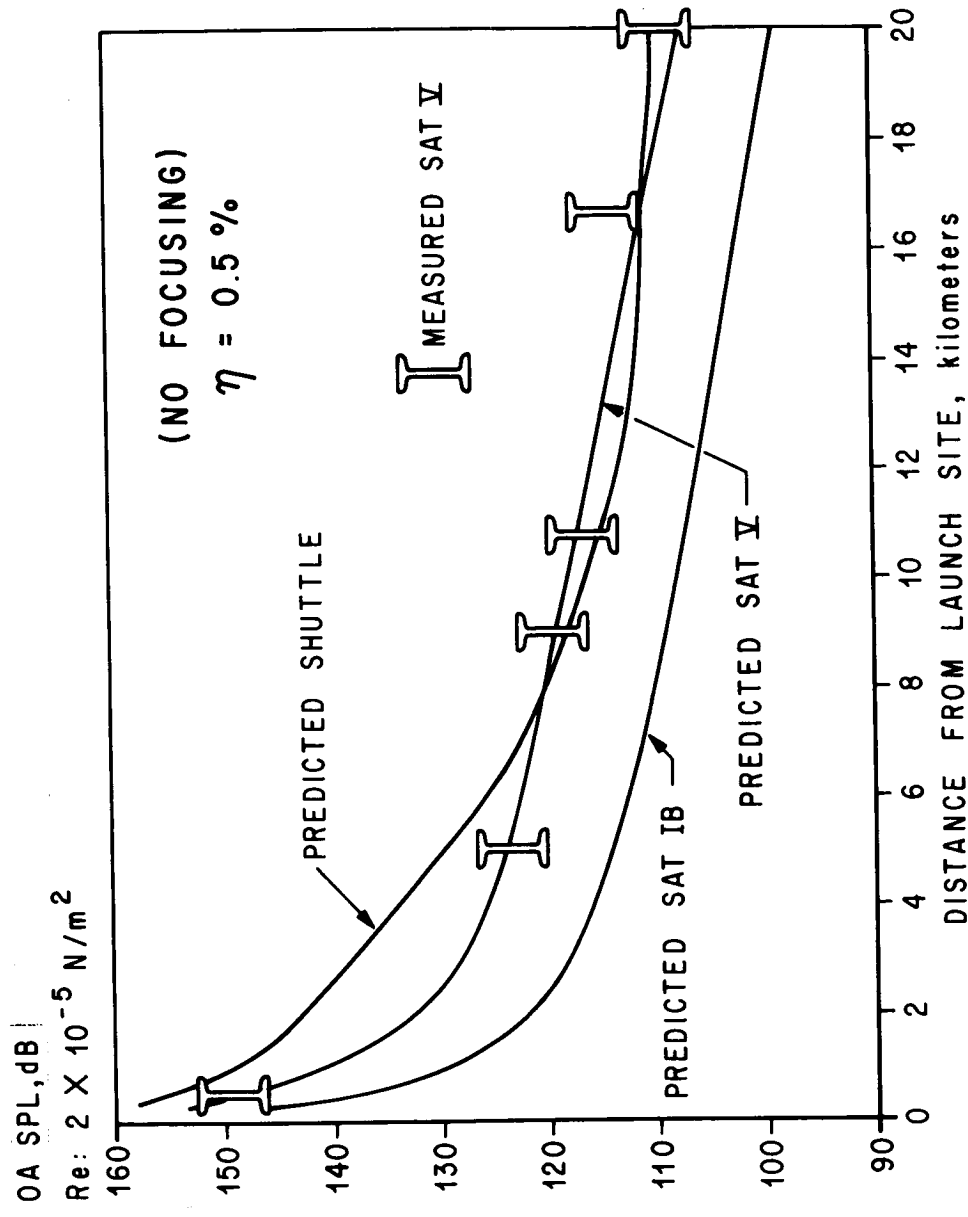
## MAXIMUM OVERALL SOUND PRESSURE LEVEL VS. DISTANCE FROM LAUNCH SITE

(Slide 4)

The indications of higher environments for the more adjacent farfield during shuttle launch is evidenced in the maximum OA SPL vs. distance from the launch site predicted for the shuttle in comparison with the measured data from Saturn V. The environments due to Saturn V do appear to dominate over that of the shuttle between 6 and 18 km. This fact is due partially to the relative power spectra, to the propagation effects (as previously indicated), and to the trajectory differences, e.g., the shuttle trajectory apparently deviates from the vertical more rapidly than that of the Saturn V and essentially aids in inducing higher SPL's because of the reorientation of the source with respect to the ground. This is expected when the directional properties of the source are considered. At farther distances from the launch site the absorption effects become more dominate and the directivity for the Saturn and shuttle both tend to coalesce as do the environments at the more distant farfield beyond 20 km. For equal trajectories environments from the shuttle would exceed those of the Saturn V by 1 to 2 dB in adjacent areas and then approach similar levels in the more distant farfield.

The maximum level observed will not be symmetrical all around the launch site unless the ascent is totally vertical and meteorological conditions are not conducive to focusing. The launch azimuth and particular trajectory for the shuttle will thereby determine where the levels will be maximum as indicated.

# MAXIMUM OA SPL VS DISTANCE FROM LAUNCH SITE

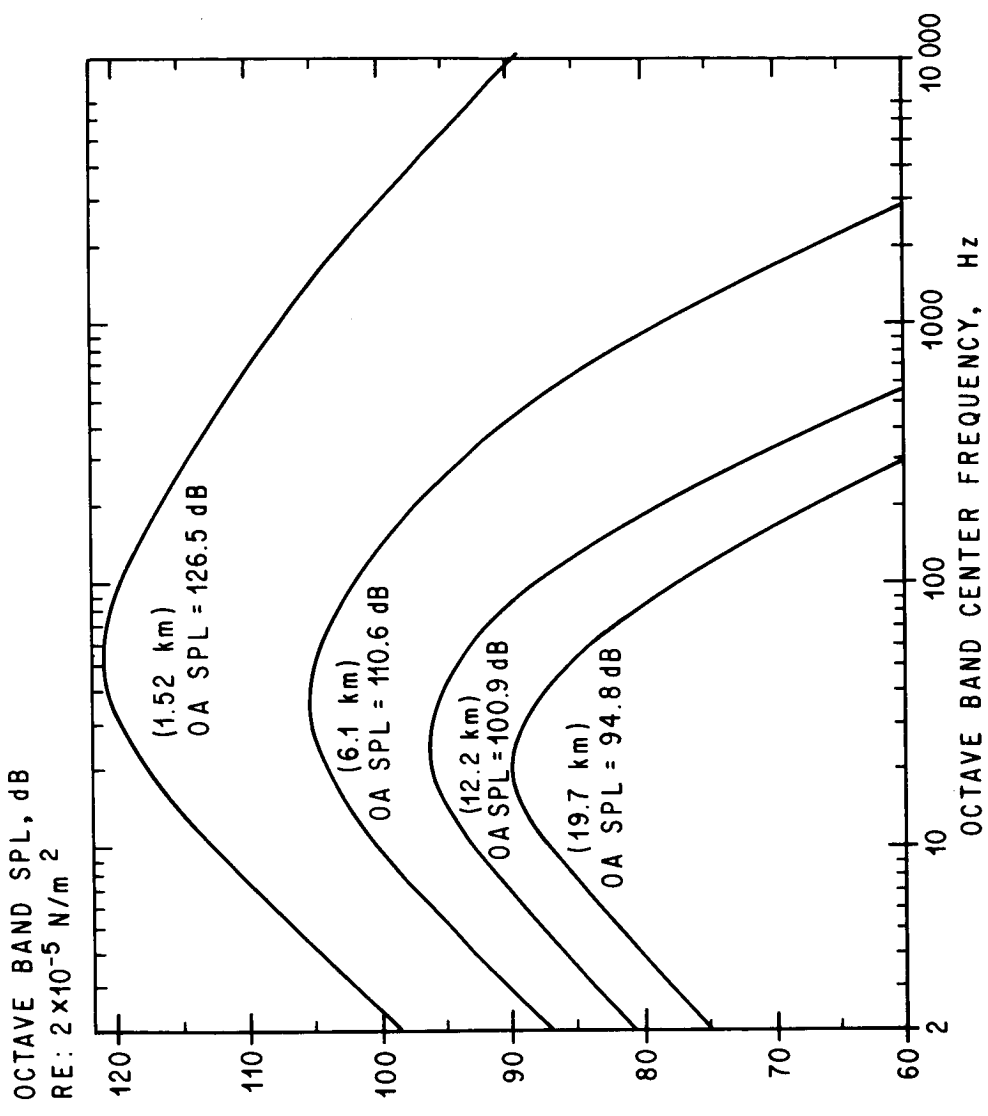


Slide 4

MAXIMUM GROUND PLANE OCTAVE BAND SPECTRA FOR STATIC TEST OF A SINGLE HIGH P<sub>c</sub> ENGINE  
(Slide 5)

The octave band sound pressure levels at various distances from the static test site show the combined losses due to spherical spreading and absorption. The spectrum given for 1.5 km, with an OA SPL of 126.5 dB, peaks in the 50 Hz octave band, and at 6.1 km (110.6 dB) the peak is down to about 35 Hz, likewise at 12.2 km (100.9 dB) peaking at 25 Hz; and at approximately 20 km (94.8 dB) peaking at 20 Hz. The spectrum for 6.1 km is considered acceptable for exposing the public or community areas and is not felt to be excessive for the normal static firing schedules.

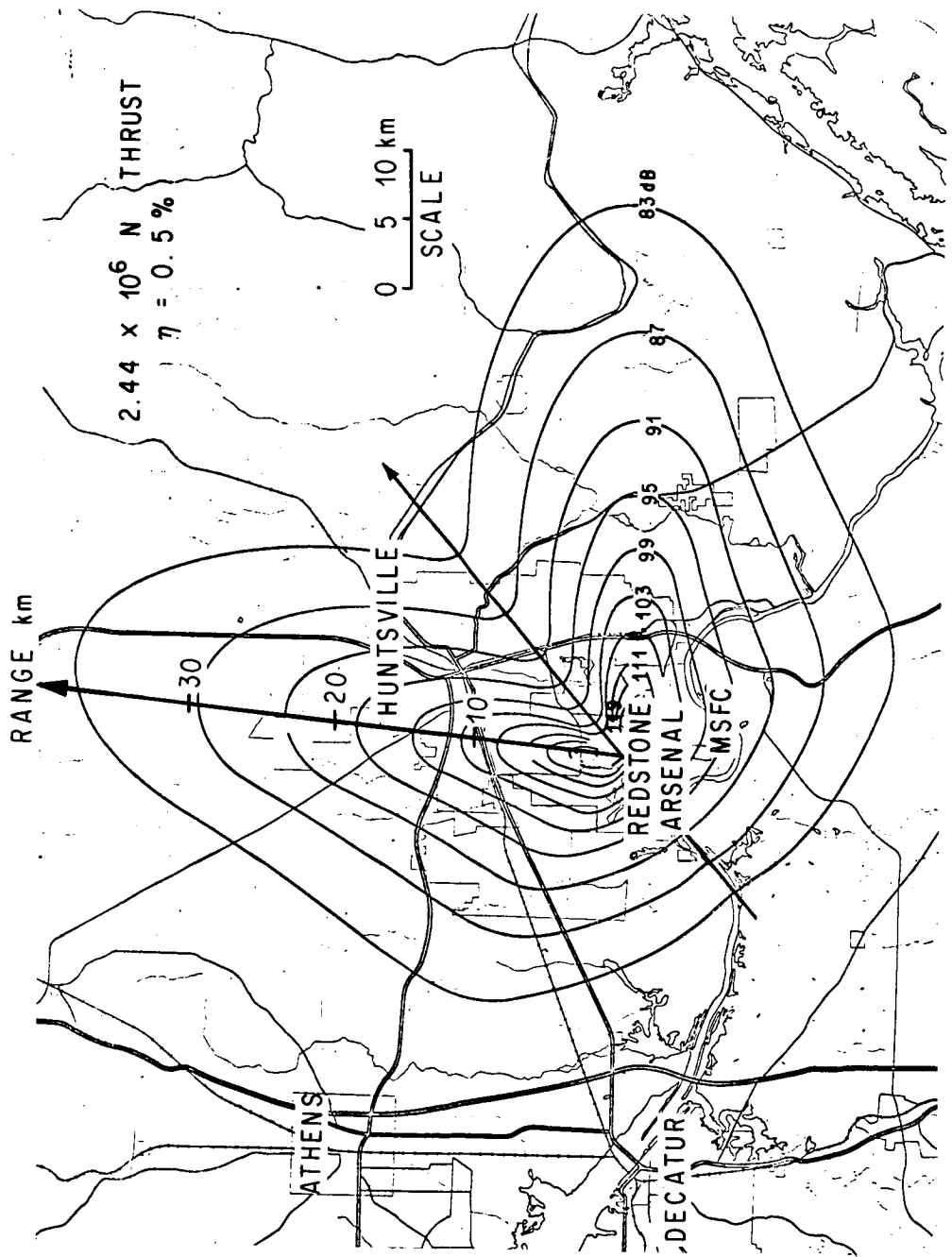
**MAXIMUM GROUND PLANE OCTAVE BAND SPECTRA**  
**STATIC TEST SINGLE ENGINE**  
 $(2.44 \times 10^6 \text{ N})$     $\eta = 0.5\%$



OVERALL SOUND PRESSURE LEVEL CONTOURS FOR SINGLE SHUTTLE ENGINE STATIC FIRING  
(Slide 6)

The sound pressure level contours, lines of equal OA SPL, indicate the effects of directivity or selective spatial directability of the source and are influenced by deflectors or suppressors, etc. The arrow indicates the exhaust flow direction from a bucket deflector exiting approximately parallel with the ground plane. This example showing MSFC is without regard to meteorological conditions which should be considered in making refined estimates of farfield environments since the refractive phenomenon (focusing) can change the sound pressure levels with respect to the test site by changing the relative direction of maximum energy propagation or by extending or decreasing the range where given SPL's are produced.

OVERALL SPL CONTOURS AT MSFC  
STATIC TEST - BUCKET DEFLECTOR



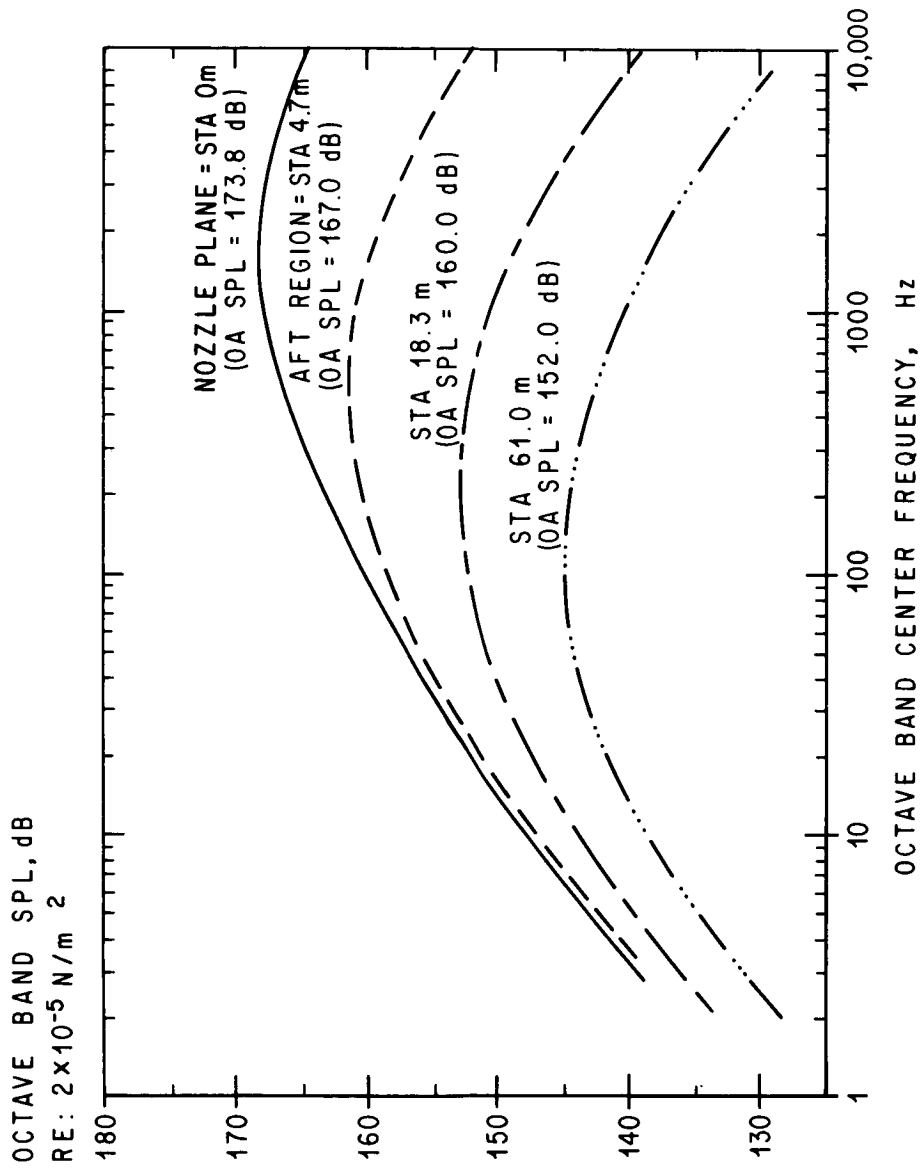
## OCTAVE-BAND SOUND PRESSURE LEVEL SPECTRA FOR VARIOUS VEHICLE STATIONS

## Holdown Conditions

(Slide 7)

The acoustic environments for the vehicle itself during holdown (firing down vertically onto a deflector) are denoted for four stations: the engine exit nozzle plane (Station 0 m) through Station 61 m. The OA SPL's range from approximately 174 dB to 152 dB with peak octave-band levels from 2000 Hz to approximately 100 Hz at the aft and forward stations, respectively.

HOLDDOWN CONDITION  
 OCTAVE BAND SOUND PRESSURE LEVEL  
 SPECTRA FOR VARIOUS VEHICLE STATIONS  
 $29.4 \times 10^6$  N THRUST



Slide 7

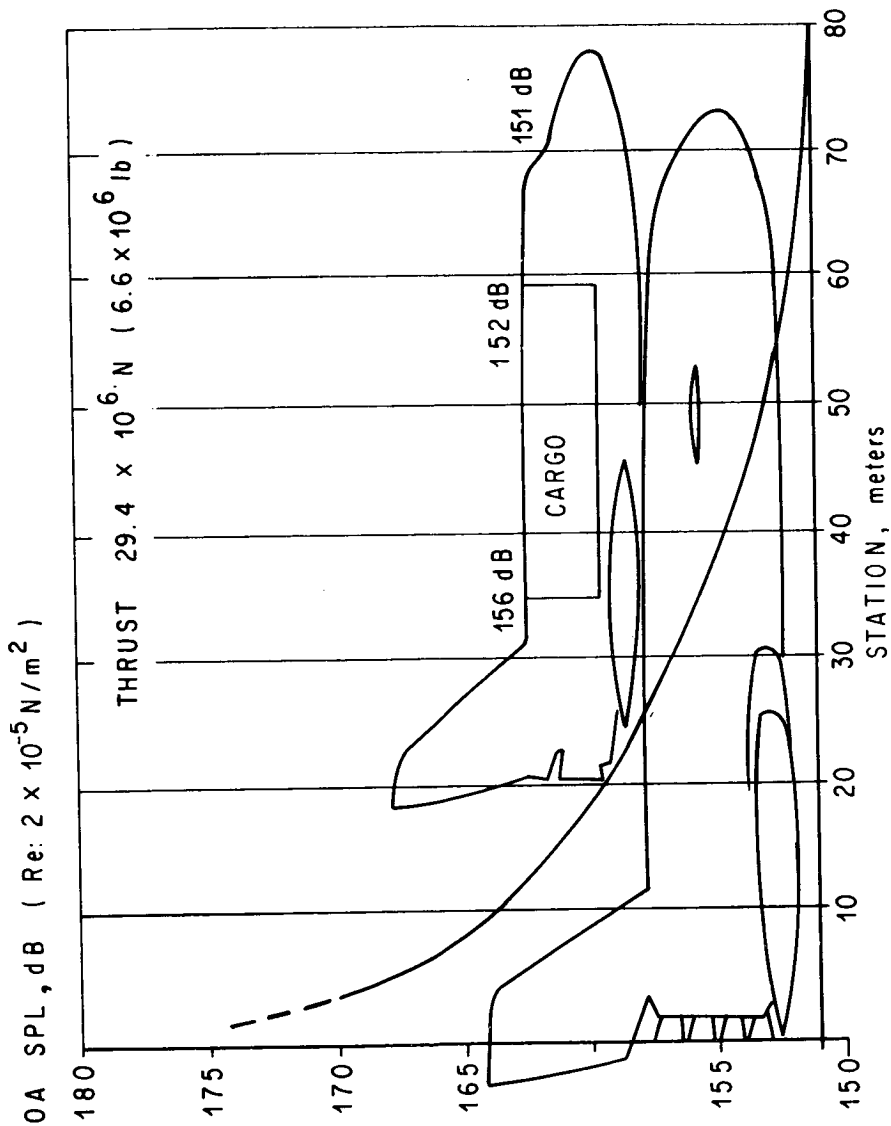
OVERALL SOUND PRESSURE LEVEL VS. SHUTTLE STATION

(Slide 8)

The OA SPL values range from approximately 174 dB at the booster nozzle plane to 160 dB at the orbiter's nozzle plane (still due to booster firing) and 156 to 152 dB for the cargo compartment.

The forward crew areas appear to be in the 151 to 152 dB range. Heat shields, wing panels, thermal coverings on upper body, and electronic equipment must be considered in such severe dynamic environments where fatigue can be a major problem in a reusable system.

OVERALL SOUND PRESSURE LEVEL  
VS  
SHUTTLE STATION



Slide 8

COMPARISON OF CREW/COMPARTMENT AREAS ENVIRONMENTS (EXTERNAL) DURING HOLDDOWN

(Slide 9)

The shuttle crew areas are exposed to environments that are 152 dB, approximately 5 to 6 higher on the shuttle than on Saturn IB or Saturn V. This is due to differences in the power spectra of each vehicle and also to the relative location of the crew areas on these vehicles. Consideration of this difference should be reflected in the design to reduce internal crew environments for adequate crew safety, communications, and relative comfort. The cargo compartment area, which will house electronic equipment and other items which are sensitive to severe dynamic environments, will have exposures as high as 156 dB external.

**EXTERNAL SOUND PRESSURE LEVELS  
FOR THE  
CREW/COMPARTMENT AREA  
DURING HOLDOWN**

	SPL (dB)
SATURN IB VEHICLE	146
SATURN V VEHICLE	147
SPACE SHUTTLE	152 / 156

Slide 9

## CONCLUDING REMARKS

(Slide 10)

The comments on the farfield environments are as follows:

- (1) 0.5% acoustic efficiency is anticipated for current planning purposes.
- (2) The OA PWL is 204.6 dB (with  $\eta = 0.5\%$ ).
- (3) The shuttle environments for the adjacent farfield exceed those of Saturn V.

Trajectory changes and meteorological conditions, of course, can influence these environments.

- (4) Still the effects of the high  $P_c$  system are not known. Farfield environments depend on the directivity and efficiency of the sound source.

Vehicle Environments

- (1) Booster base region - 175 dB OA SPL
- (2) Orbiter base region - 160 dB OA SPL
- (3) Cargo compartment (aft region) - 156 dB OA SPL
- (4) Crew compartment (forward) - 152 dB OA SPL
- (5) Fatigue of aircraft type structures and with thermal coatings and attachment is potentially a major problem along with the crew environments (interference in crew communications, physical discomfort, or possible performance shift under exposure to elevated SPL's).
- (6) Again the effects on the acoustic nearfield is dependent on the flow system of the high  $P_c$  engine and variations can be expected.

## CONCLUDING REMARKS

### FARFIELD ENVIRONMENTS

- $\eta \approx 0.5\%$
- OA PWL  $\approx 204.6$  dB ( Re:  $10^{-12}$  Watts )

### LAUNCH ENVIRONMENTS

- UP TO 10 dB HIGHER THAN SATURN V FOR RADIUS UP TO 6 km
  - UP TO 3 dB LOWER THAN SATURN V FOR RADIUS FROM 6 TO 18 km
- STATIC TEST
- MAX OA SPL FOR 6 km  $\approx 110$  dB ( STD. MET. CONDITIONS )

### UNKNOWN

- EFFECTS OF HIGH  $P_c$  SYSTEM

### VEHICLE ENVIRONMENTS

	OA SPL	PEAK OCTAVE
• BOOSTER BASE REGION	174 - 175 dB	2000 - 3000 Hz
• ORBITER BASE	160 dB	200 - 400 Hz
• CARGO ( AFT ) STA.	156 dB	100 - 200 Hz
• CREW ( FWD ) STA.	151 - 152 dB	80 - 100 Hz

- GENERAL  
FATIGUE POTENTIAL IS HIGH  
CREW ENVIRONMENTS HIGH
- UNKNOWN  
EFFECTS OF HIGH  $P_c$  SYSTEM

## INFORMATION FOR DESIGN IMPACT

### Progress

Two engine contractors have or are performing tests with full-scale hardware and acoustic data are being obtained; however, use is limited.

### Recommendations

Design considerations for severe acoustic environments must be given as soon as possible.

**Method:** Provide for dynamic sub-scale model studies.

**Investigate:** Deflector effects on efficiency

Cluster effects

Directivities

Vehicle environments

Interface with launch facilities

Source amplitude and phase correlation properties

Source locations

PRELIMINARY VIBRATION DESIGN AND TEST CRITERIA CONSIDERATIONS

FOR THE SPACE SHUTTLE

By Harry J. Bandgren  
NASA George C. Marshall Space Flight Center  
Marshall Space Flight Center, Ala.

INTRODUCTION

This paper presents some Marshall Space Flight Center preliminary vibration design and test criteria considerations for the space shuttle. The discussion is primarily concerned with the formulation of vibration criteria for the design and testing of the equipment installations on the shuttle. A recommended criteria format is presented with a discussion of when the vibration environment has to be considered in design and testing.

A semiempirical method of predicting the vibration criteria for the shuttle from vibroacoustic structural data banks is presented.

Some preliminary vibration criteria predictions are presented for the orbiter and booster equipment bays and for the main shuttle engine.

A research testing program to determine the vibroacoustic transfer through a typical shuttle thermal protection system (TPS) panel configuration is described.

## VIBRATION CRITERIA FORMAT FOR THE SPACE SHUTTLE

(Figure 1)

Figure 1 shows the vibration criteria format that MSFC is presently pursuing. Deviations from this format will be made, when necessary, as in the main engine area.

The vehicle dynamics are low frequency cyclic transients resulting from the vehicle responding in its modes of vibration during certain transient events, such as launch release, engine cutoff, and orbiter/booster separation.

The last three phases of the criteria format are broadband random vibrations resulting from the engine-generated noise during lift-off and the aerodynamic-generated noise during the transonic boost and reentry periods. The lift-off sequence and boost trajectories for the space shuttle are similar to those for the Saturn vehicles. A review of the Saturn vehicle acceleration time histories shows the lift-off environment to be present down 6 dB from its maximum level for a period of 10 seconds, and the transonic environment to be present down 6 dB from its maximum level for a period of 40 seconds. Reliable estimates of the reentry acoustic environments are not available; however, preliminary indications are that the levels will be lower and present for longer periods of time than either the lift-off or transonic environments.

**VIBRATION CRITERIA FORMAT  
FOR THE SPACE SHUTTLE**

- SINUSOIDAL VEHICLE DYNAMICS
- LIFT-OFF RANDOM
- TRANSONIC RANDOM
- REENTRY RANDOM

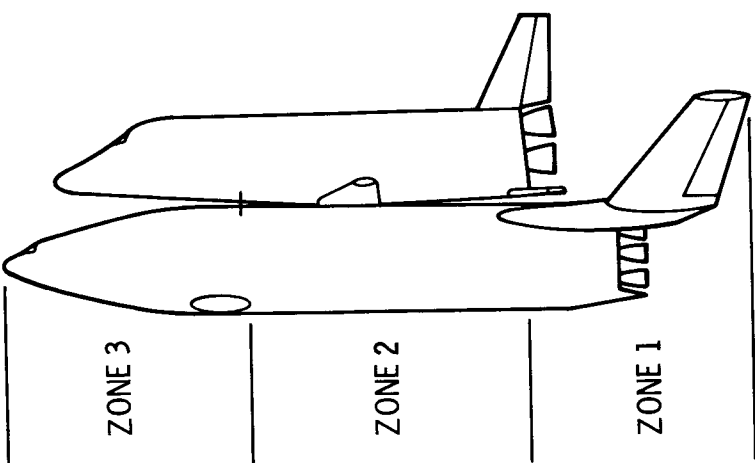
Figure 1

## SHUTTLE VEHICLE DYNAMIC ACCELERATIONS

(Figure 2)

The vehicle dynamics criteria are determined from forced vibration analyses of the vehicle using 3 sigma probability level forcing functions. Extrapolations from Saturn V vehicle analyses were used as the basis for the preliminary shuttle vehicle dynamics shown in figure 2. The shuttle vehicle is divided into 3 zones. The composite low frequency vehicle dynamic accelerations are given for lift-off, engine cutoff, and booster/orbiter separation in both the longitudinal and lateral axes. The lift-off transients are for quick release, which is the reason for the high composite accelerations of  $\pm 8$  g's in the flight direction for zone 1. These composite accelerations are a summation of the modal accelerations at the time when the sum is maximum. The laboratory simulation for this criteria will be a 3 octave/minute sinusoidal sweep for a single shuttle mission.

## SHUTTLE VEHICLE DYNAMIC ACCELERATIONS



LIFT-OFF ACCL. ( $\pm g$ 's PEAK)			
	LONGITUDINAL	35-50 Hz	LATERAL
ZONE	0-35 Hz	35-50 Hz	0-35 Hz
1	8.0	2.0	1.5
2	3.0	1.0	1.0
3	2.0	1.0	1.0

ENGINE CUTOFF/SEPARATION ACCL. ( $\pm g$ 's PEAK)			
	LONGITUDINAL	35-50 Hz	LATERAL
ZONE	0-35 Hz	35-50 Hz	0-35 Hz
1	3.5	1.5	1.0
2	3.0	2.0	2.0
3	3.0	1.0	2.0

Figure 2

TYPICAL MOBILE ACOUSTIC RESEARCH LABORATORY (MARL) TEST CONFIGURATION

(Figure 3)

The acoustically induced broadband random vibration criteria for the shuttle vehicle are being determined from vibroacoustic structural data banks. These data banks were developed from the more than 3,000 pieces of vibration and acoustic data taken from static firings and flights of the Saturn vehicles and from the MARL testing program.

The MARL is a forty-foot platform on wheels. Various large flight and development structures, such as instrument units, skirts, and interstages are installed on the MARL. Figure 3 shows a typical MARL test configuration. It shows the MARL with the S-IVB stage aft skirt and thrust structure installed. The MARL and test structures are located in the acoustic near and midfields and subjected to static firings of the various Saturn stages and engines at MSFC and Mississippi Test Facility. The MARL test structures are instrumented and vibration and acoustic data are recorded during the static firings.

**TYPICAL MOBILE ACOUSTIC  
RESEARCH LABORATORY  
(MARL) TEST CONFIGURATION**

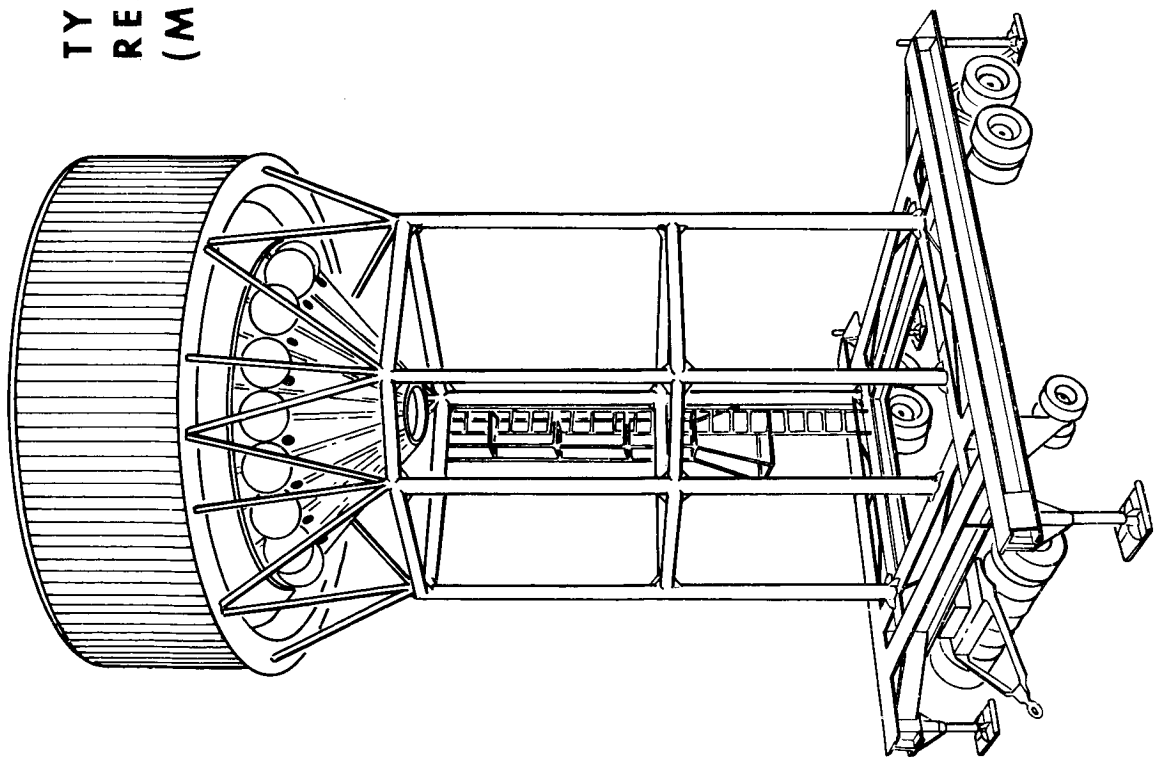


Figure 3

## VIBROACOUSTIC STRUCTURAL DATA BANK

(Figure 4)

A vibroacoustic structural data bank is a statistical compilation of vibration and acoustic data which are categorized according to definite structural parameters, such as skin, stringer, ring frame, honeycomb, etc. In simple words, a vibroacoustic data bank indicates the vibration level for a given sound-pressure level acting on a particular structural configuration.

Figure 4 shows an example of a vibroacoustic data bank. This is a skin-stringer-ring-frame data bank and represents the response of the unloaded ring frames. The data that went into the formulation of this data bank were taken from the S-II stage forward skirt. This is a 10.06-meter (33-foot) diameter skin-stringer-ring-frame cylindrical shell structure. The stringers are spaced 21.92 cm (8.63 in.) apart and weigh 0.70 kg/m (0.47 lbm/ft). The skin is 7075-T6 aluminum and is 0.10 cm (0.04 in.) thick. The ring frames are spaced approximately 76.2 cm (30 in.) apart and weigh 1.70 kg/m (1.14 lbm/ft).

Each of the ring-frame vibration spectrums with its associated acoustic spectrum was normalized to the reference acoustic spectrum shown in figure 4. The reference acoustic spectrum has no special meaning other than that it is a typical Saturn V lift-off acoustic spectrum. The normalized vibration spectrums were statistically analyzed to determine the mean and the 97.5 percent probability level spectrums. Vibroacoustic data banks for many structural configurations are being determined. Several skin-stringer-ring-frame data banks have been determined for different structures. The S-II forward skirt data were used to formulate data banks for the unloaded skin and for the unloaded stringers as well as for the ring-frame data bank shown in figure 4. The data banks are being developed for both the lift-off and transonic environments which take into account the differences in the spatial correlation of the random acoustic pressure fields.

When these data banks are utilized for determining vibration criteria for the shuttle, the data bank that is closest to the shuttle structural configuration is selected. The proper mass and sound pressure level adjustments are made to determine the vibration criteria for the unloaded shuttle structure. Component vibration criteria for varying weight ranges can be determined from conventional mass attenuation techniques.

VIBROACOUSTIC STRUCTURAL DATA BANK  
RING FRAME

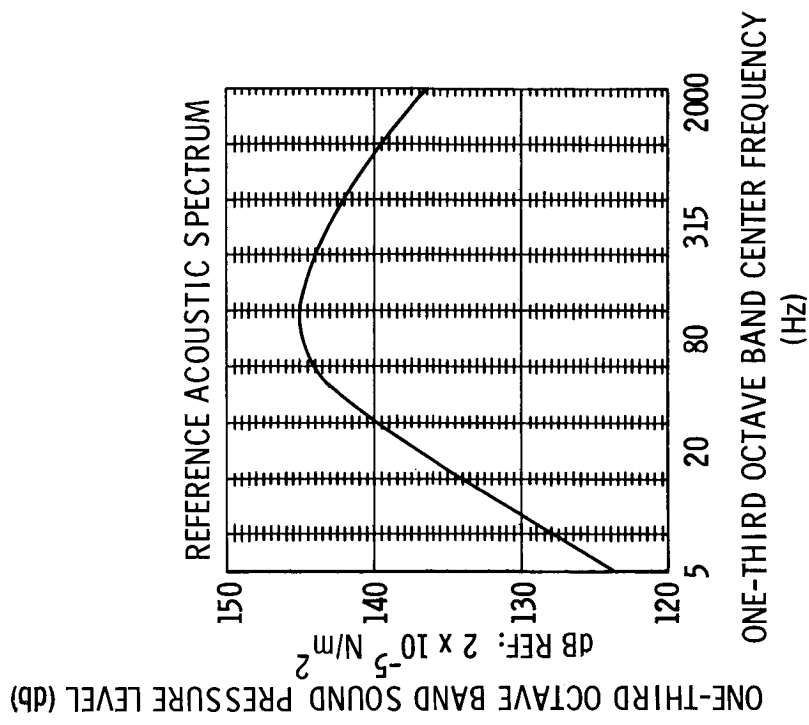
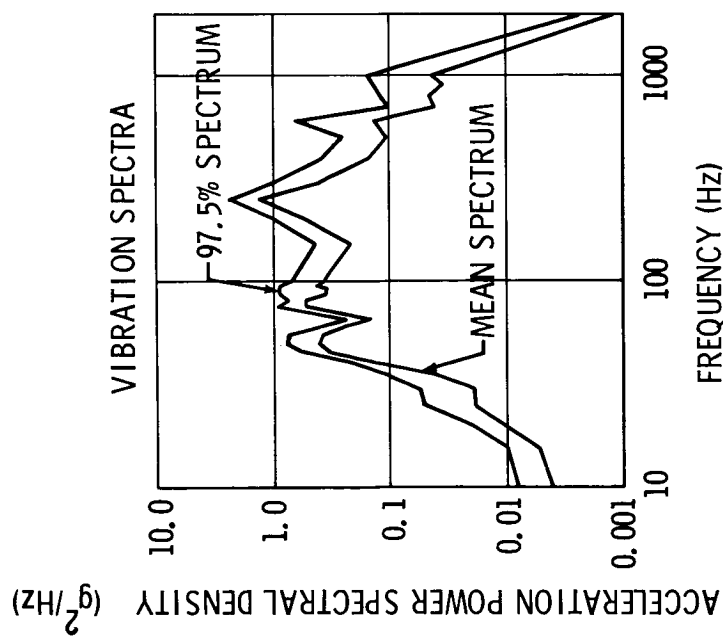


Figure 4

SHUTTLE BOOSTER AND ORBITTER VIBRATION ZONES

(Figures 5 and 6)

Preliminary estimates of the transonic and lift-off acoustic environments for the space shuttle are reasonably accurate. Reliable estimates of the reentry acoustic environment and detailed local structural definition are needed before better vibration criteria predictions can be made.

Figure 5 shows the preliminary vibration criteria zoning for the shuttle booster. The booster is divided into six major vibration zones. These major zones are further divided into subzones. Major zone 1 is divided into four subzones; the nose cone, crew compartment, forward equipment bay, and the main LOX tank. When the local detailed structural definition becomes available, these subzones will be further subdivided to include vibration criteria for components mounted to the skin, stringers, ring frames, etc., throughout the component weight ranges.

## SHUTTLE BOOSTER VIBRATION ZONES

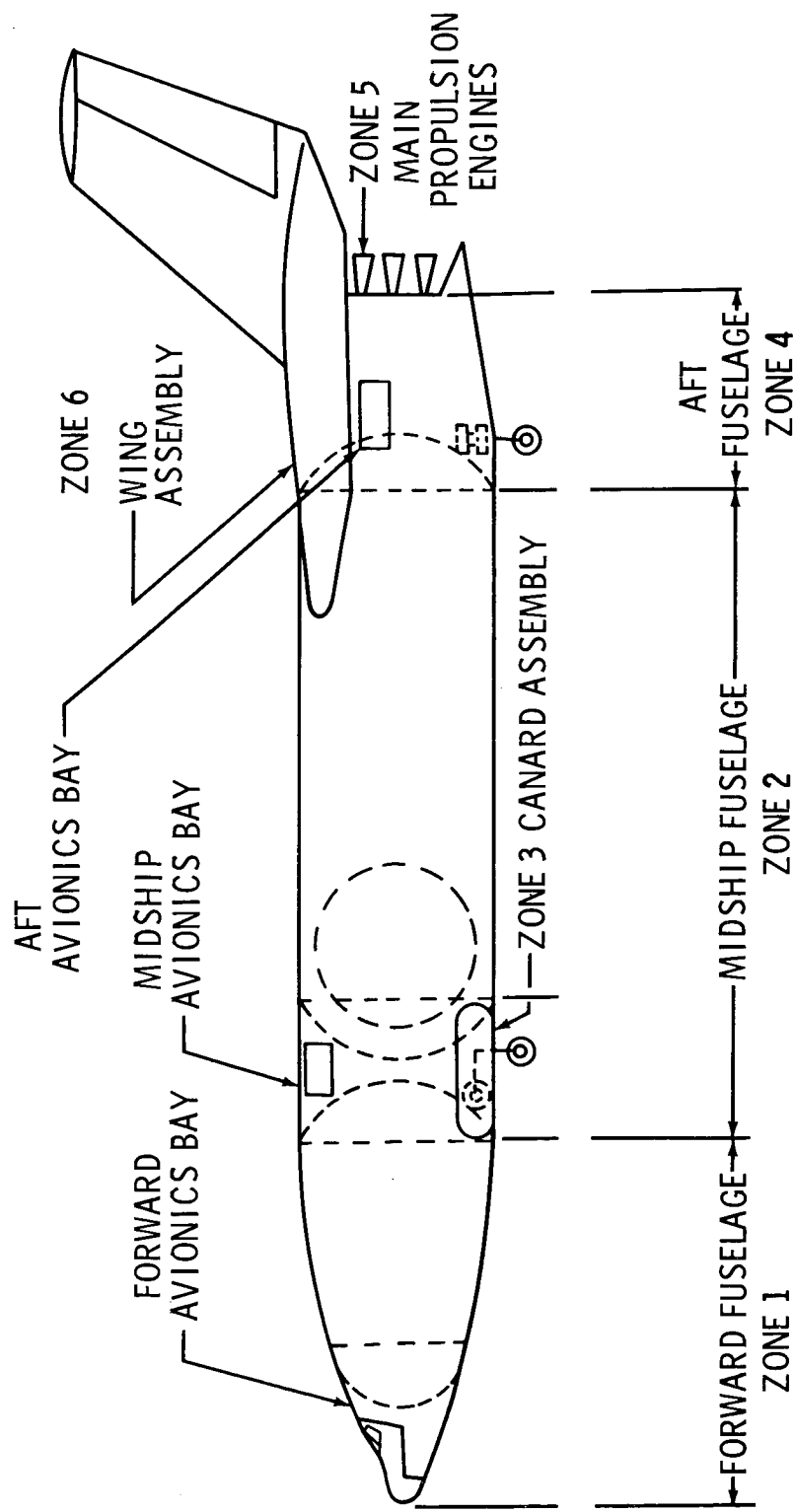


Figure 5

Figure 6 shows the preliminary vibration criteria zoning for the shuttle orbiter.

## SHUTTLE ORBITER VIBRATION ZONES

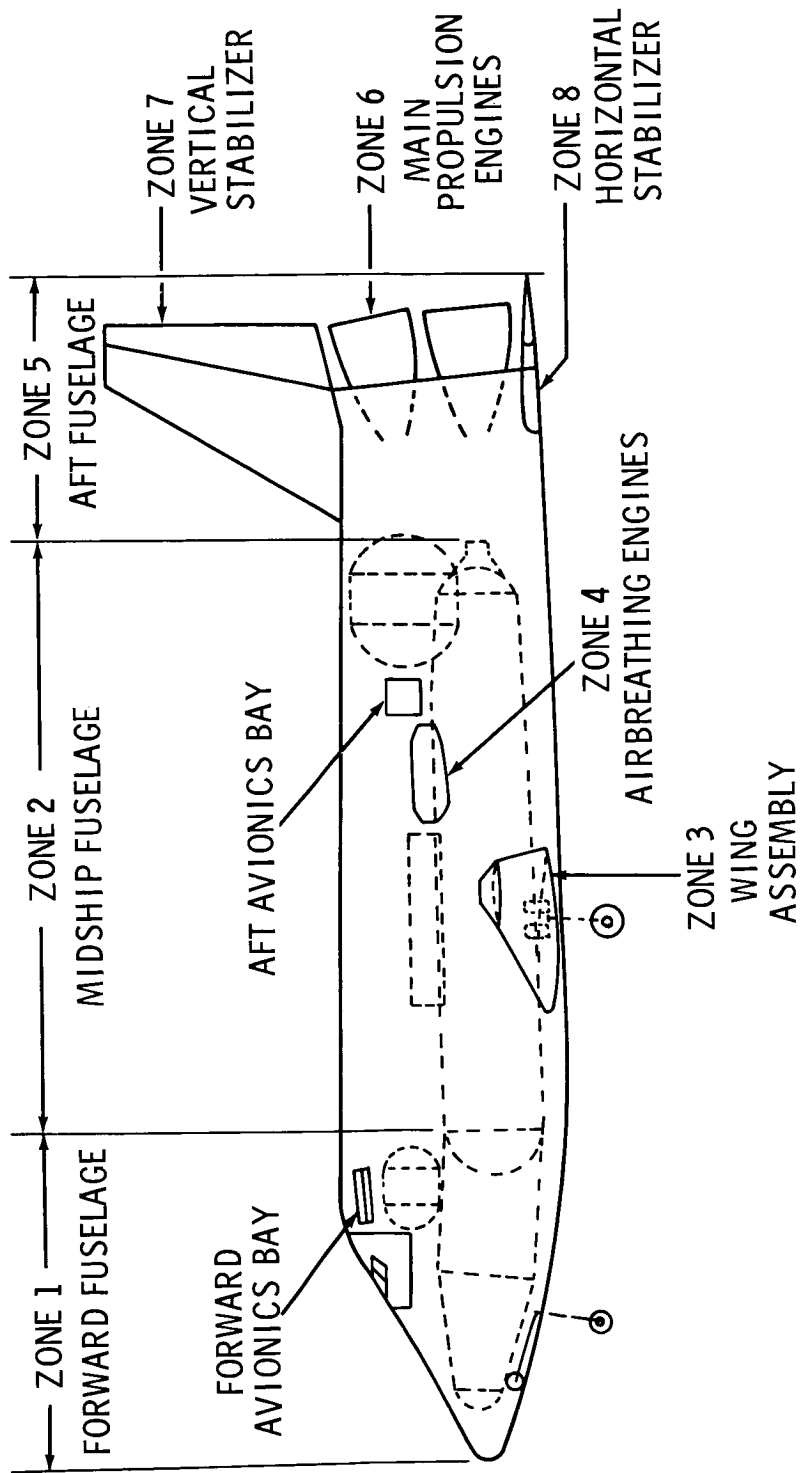


Figure 6

THERMAL PROTECTION SYSTEM PANEL,

(Figure 7)

The Astrionics Laboratory at MSFC is conducting a study to determine the feasibility of using selected avionics equipment for the shuttle, which were developed for other aerospace programs. In support of this study, preliminary vibration criteria for the avionics equipment bays shown in figures 5 and 6 were determined. The structure for these equipment bays is shown in figure 7. The thermal protection system consists of 0.051-cm (0.020-in.) thick outer corrugated and stiffened titanium panels, attached to the load-carrying structural ring frames on 43.18-cm (17-in.) centers by alternate flexible clips and rings. A 1.27 cm (0.50 in.) layer of microquartz insulation is attached to the backup plate external to the ring frames. The proposed equipment racks with the components installed weigh approximately 90.72 kg (200 lb) and attach to alternate ring frames.

MSFC is sponsoring an in-house research program to evaluate in the laboratory the dynamic response characteristics and vibroacoustic transfer through three thermal protection system (TPS) panel configurations. One of these TPS test panels is constructed as shown in figure 7. The other two panels have similar geometry but are constructed from different materials. Each of the test panels will be installed in a test fixture and located between the reverberation and anechoic chambers at MSFC's acoustic test facility. The test panels will be subjected to 150 acoustic/thermal mission cycles. An acoustic/thermal mission cycle will consist of: lift-off acoustics, 10 seconds; transonic acoustics, 40 seconds; reentry thermal profile; reentry acoustics, 5570 seconds.

The results of these TPS panel tests will be threefold: (1) the acoustic/thermal fatigue life of the TPS panels will be determined, (2) the sound transmission loss through the panels will be determined, and (3) the vibratory response characteristics of the load carrying structural ring frames will be determined.

## THERMAL PROTECTION SYSTEM PANEL

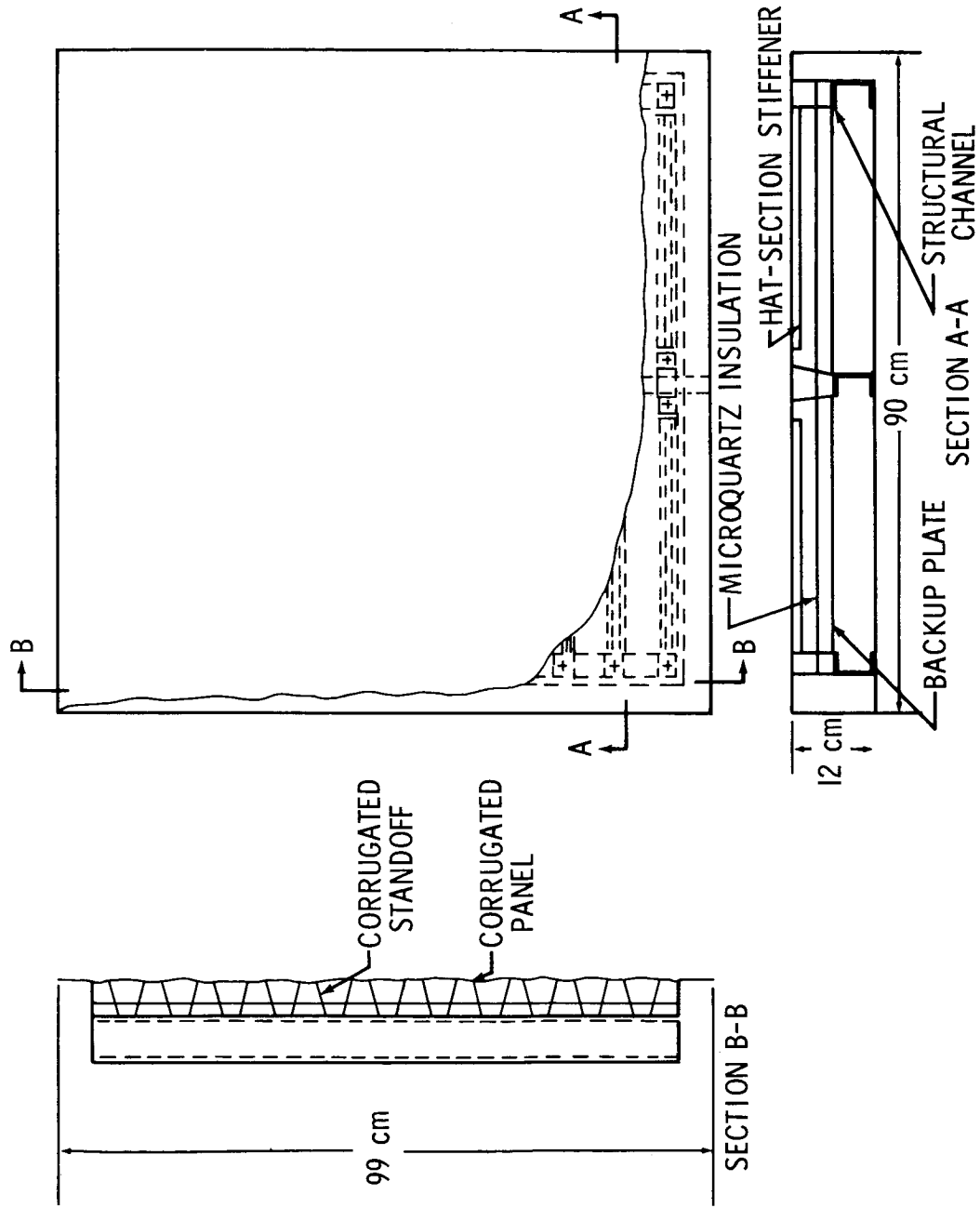


Figure 7

BOOSTER AND ORBITER AVIONICS EQUIPMENT BAYS  
(90.72 kg (200 lb) RACK-MOUNTED COMPONENTS)

(Figures 8 and 9)

Figure 8 shows the lift-off and transonic vibration criteria predictions for the forward avionics equipment bay in the booster. The transonic estimate was based on an envelope of the acoustic environment for turbulent boundary layer flow and flow separation. When wind-tunnel data become available to define the transonic flow patterns in these regions the transonic vibration criteria can probably be revised downward.

**BOOSTER FWD. AVIONICS EQUIPMENT BAY**  
(90.72 kg (200 lb) RACK-MOUNTED COMPONENTS)

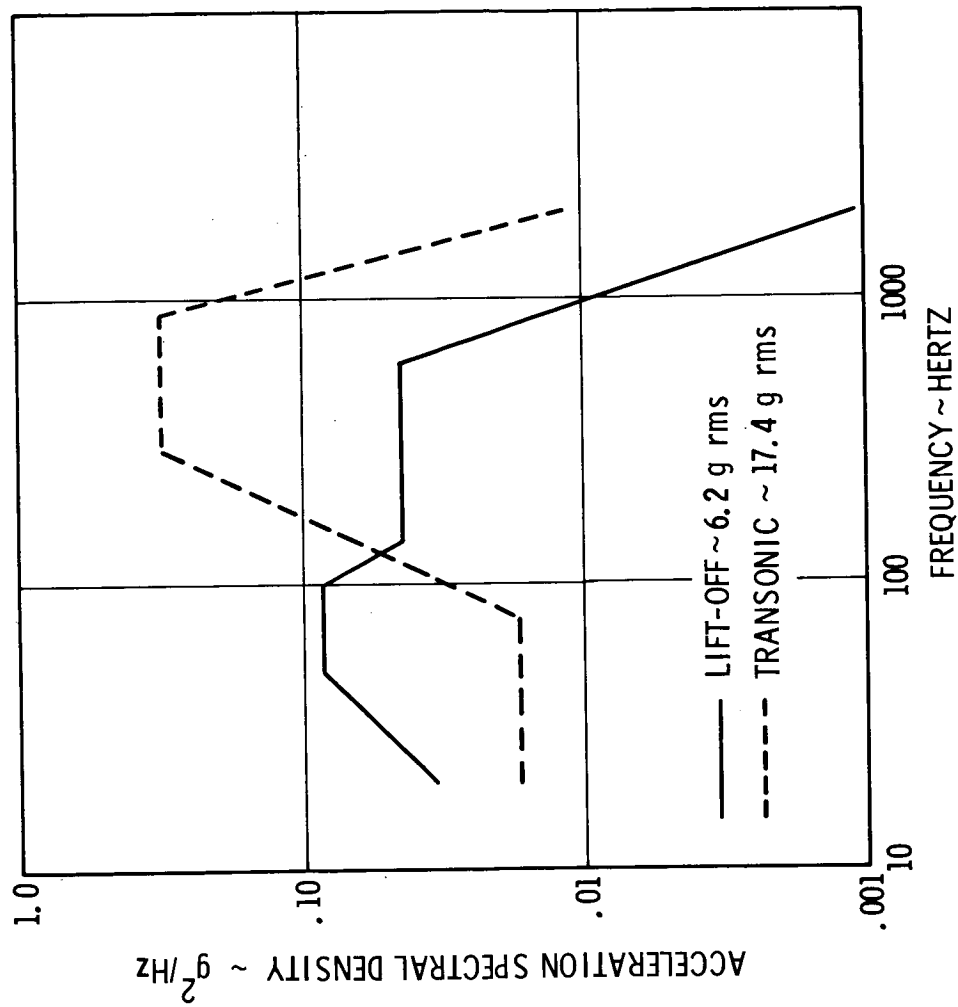


Figure 8

Figure 9 shows the lift-off and transonic vibration criteria predictions for the midship equipment bay in the booster and the forward equipment bay in the orbiter.

**BOOSTER MIDSHIP AND ORBITER FWD. AVIONICS EQUIPMENT BAYS**  
(90.72 kg (200 lb) RACK-MOUNTED COMPONENTS)

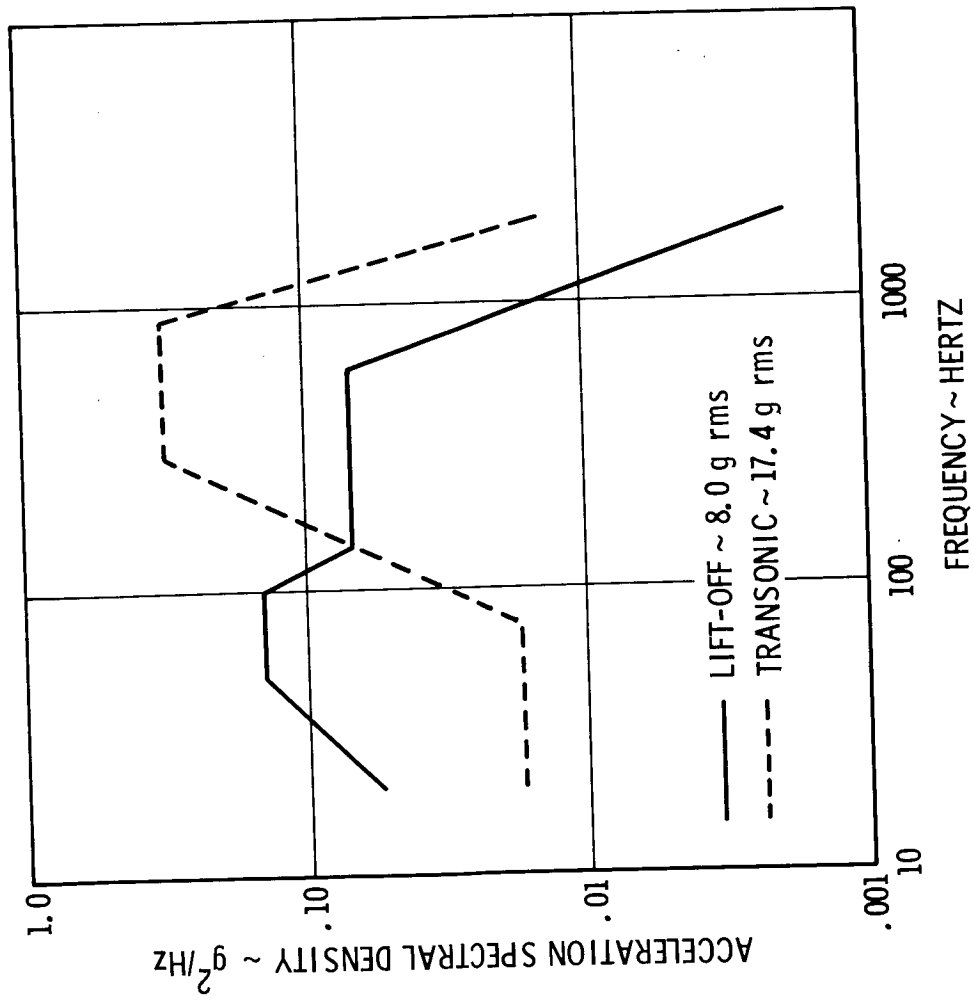


Figure 9

BOOSTER AND ORBITER AFT AVIONICS EQUIPMENT BAYS  
(90.72 kg (200 lb) RACK-MOUNTED COMPONENTS)

(Figure 10)

Figure 10 shows the lift-off and transonic vibration criteria predictions for the booster and orbiter aft avionics equipment bays. The lift-off criteria reflects the close proximity of these equipment bays to the main shuttle booster engines.

The vibroacoustic structural data bank that was used to formulate the vibration criteria for the shuttle equipment bays, was developed from vibration and acoustic data taken on the S-IVB stage forward skirt. This is a 6.71-m (22-ft) diameter skin—stringer—ring-frame cylindrical shell structure.

Efficient vibration transmission through the thermal protection system to the ring frames was assumed throughout the frequency range in determining the criteria for the equipment bays.

**BOOSTER AND ORBITER AFT AVIONICS EQUIPMENT BAYS**  
(90.72 kg (200 lb) RACK-MOUNTED COMPONENTS)

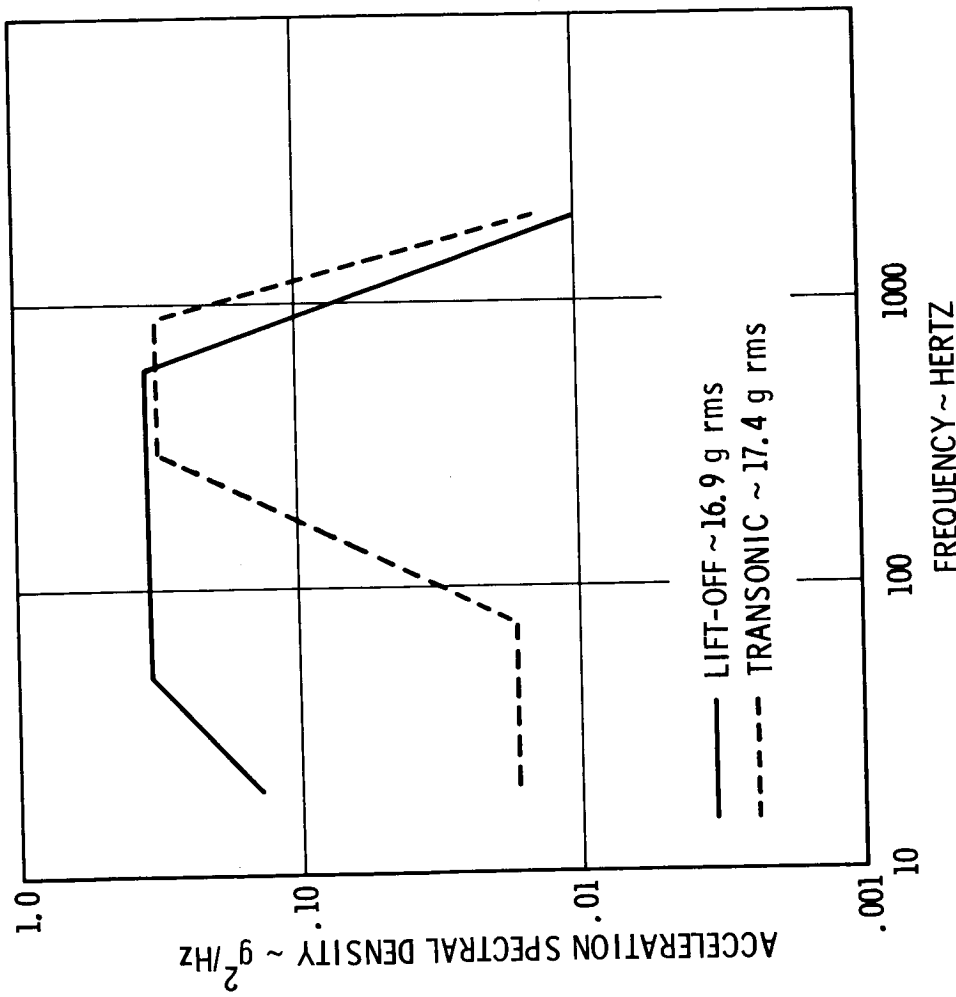


Figure 10

ENGINE PARAMETERS AND VIBRATION ZONING

(Figures 11 and 12)

Vibration criteria for a configuration of the main shuttle engine were determined by scaling J-2 engine vibration data using the scaling parameters suggested by Barrett (ref. 1). The engine parameters and scaling equation are shown in figure 11. The J-2 engine is a good engine to scale from since it is also a large hydrogen/oxygen engine having an approximate specific impulse of 300 seconds.

## ENGINE PARAMETERS

### J-2 ENGINE (SEA LEVEL)

- THRUST - 720,000 N (162,000 LB)
- EXHAUST VELOCITY - 2,900 M/SEC (9,600 FT/SEC)
- WEIGHT FLOW RATE - 250 Kg/SEC (540 LB/SEC)
- ENGINE DRY WEIGHT - 1,600 Kg (3,500 LB)
- THRUST - 2,440,000 N (550,000 LB)
- EXHAUST VELOCITY - 4,000 M/SEC (13,000 FT/SEC)
- WEIGHT FLOW RATE - 640 Kg/SEC (1,400 LB/SEC)
- ENGINE DRY WEIGHT - 2,900 Kg (6,400 LB)

### SCALING EQUATION

$$g_n(f) = g_d(f) \frac{(VT)_n W_d}{(VT)_d W_n} F$$

- SUBSCRIPT  $n$  DENOTES NEW ENGINE
- SUBSCRIPT  $d$  DENOTES DATA ENGINE
- $g(f)$  = ACCELERATION POWER SPECTRAL DENSITY
- $V$  = EXHAUST GAS VELOCITY
- $T$  = ENGINE THRUST
- $W$  = ENGINE WEIGHT
- $F$  = ATTENUATION FACTOR FOR COMPONENT LOADING

### SHUTTLE MAIN ENGINE (SEA LEVEL)

Figure 11

Figure 12 shows the preliminary vibration criteria zoning for the main shuttle engine.

## EXPANDED VIEW OF MAIN SHUTTLE ENGINE

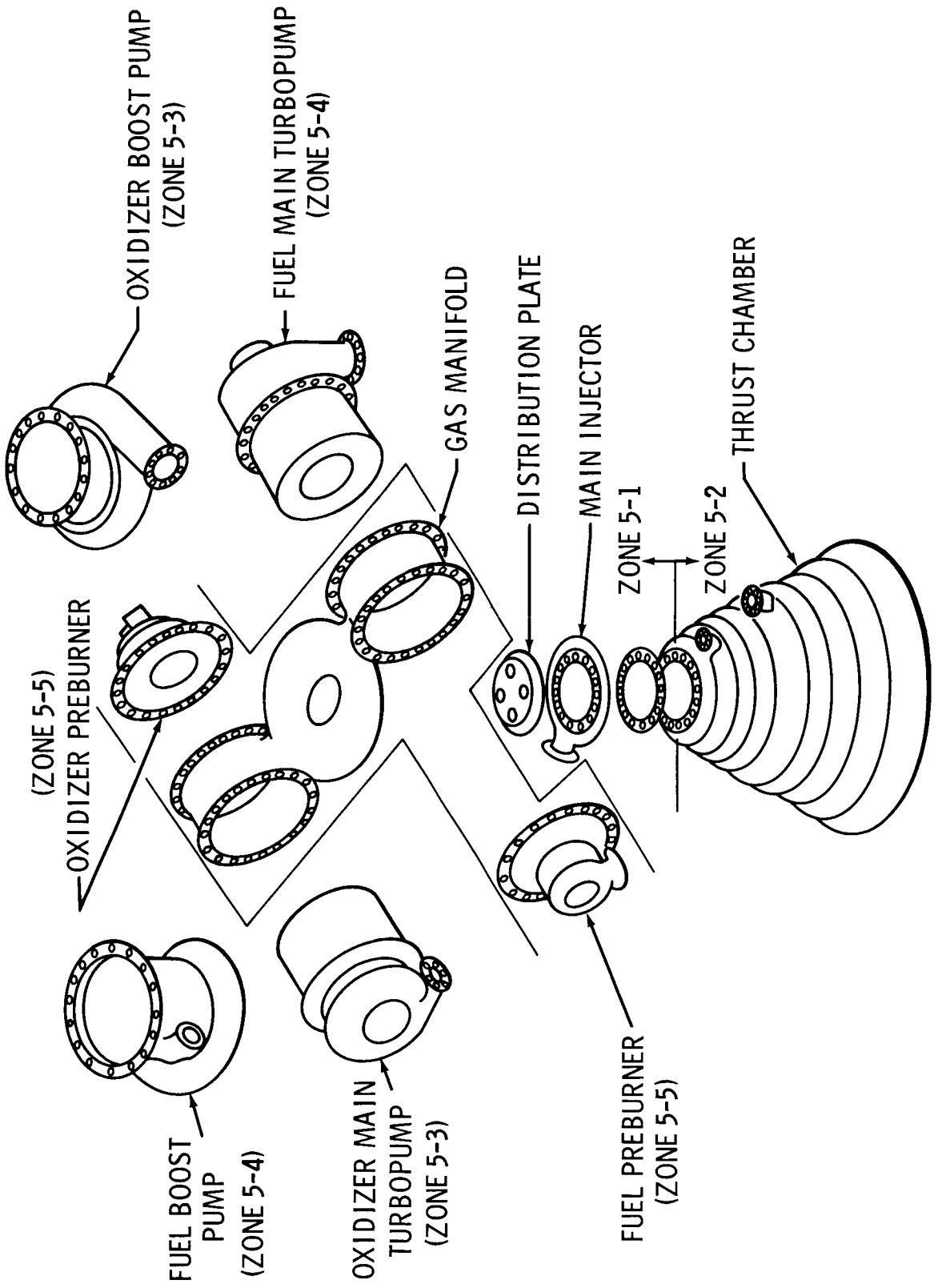


Figure 12

## MAIN SHUTTLE ENGINE VIBRATION CRITERIA

(Figure 13)

Figure 13 shows the preliminary vibration criteria for the main shuttle engine combustion chamber and turbopumps. These criteria represent the vibratory response of the engine systems and are applicable to components mounted to them.

Superimposed sinusoids will be added to the broadband random criteria when their frequency and level becomes known. The sinusoids are a function of the operating speeds and harmonics of the rotating machinery.

## MAIN SHUTTLE ENGINE VIBRATION CRITERIA

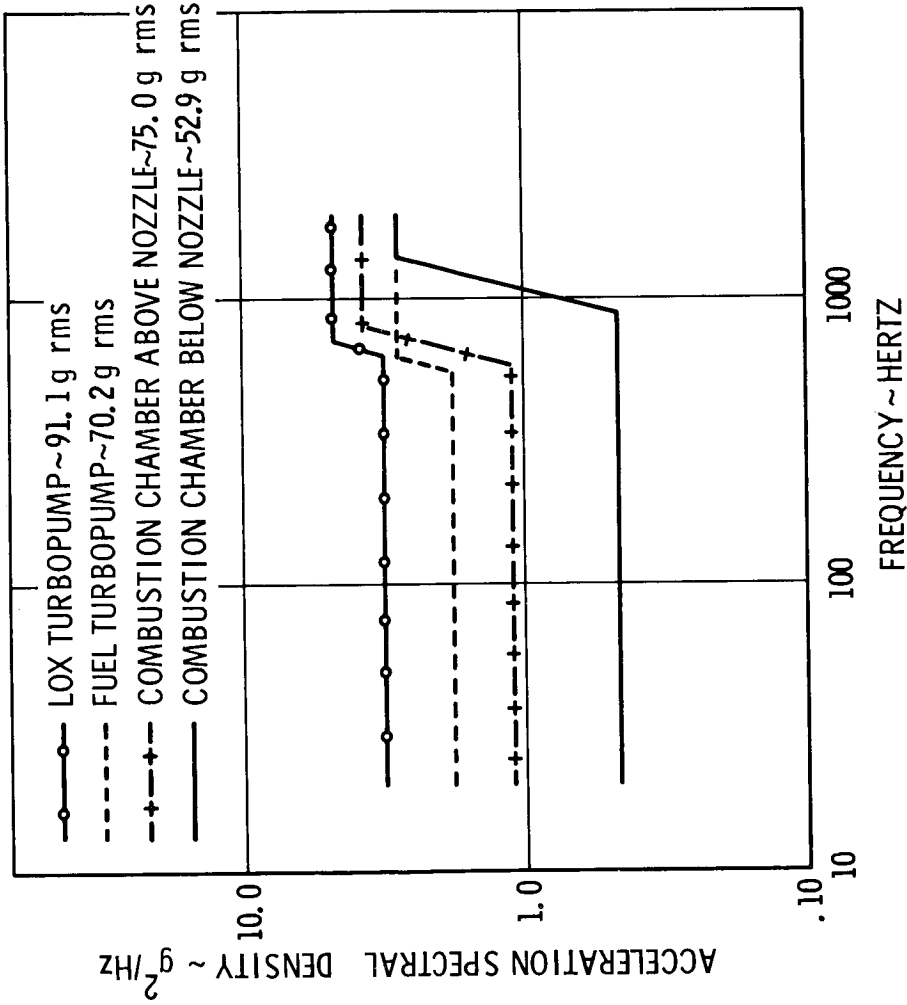


Figure 13

## CONCLUSIONS

A preliminary vibration design and test criteria format for the space shuttle has been determined. The development of vibroacoustic structural data banks for use in formulating random vibration criteria for the shuttle is continuing.

Preliminary vehicle dynamics criteria for the shuttle have been extrapolated from Saturn V vehicle analyses.

Preliminary vibration criteria in support of shuttle design analyses are being determined.

Research programs in support of shuttle vibration design and test criteria predictions are in progress.

## REFERENCE

1. Barrett, R. E.: Techniques For Predicting Localized Vibratory Environments of Rocket Vehicles.

NASA TN D-1836, October 1963.